

University of Dundee

DOCTOR OF PHILOSOPHY

Ultrasound mediated Targeted Drug Delivery In Vitro: design, evaluation and application

Gourevich, Dana

Award date:
2013

Awarding institution:
University of Dundee

[Link to publication](#)

General rights

Copyright and moral rights for the publications made accessible in the public portal are retained by the authors and/or other copyright owners and it is a condition of accessing publications that users recognise and abide by the legal requirements associated with these rights.

- Users may download and print one copy of any publication from the public portal for the purpose of private study or research.
- You may not further distribute the material or use it for any profit-making activity or commercial gain
- You may freely distribute the URL identifying the publication in the public portal

Take down policy

If you believe that this document breaches copyright please contact us providing details, and we will remove access to the work immediately and investigate your claim.

Download date: 17. Feb. 2017

DOCTOR OF PHILOSOPHY

Ultrasound mediated Targeted Drug
Delivery In Vitro: design, evaluation and
application

Dana Gourevich

2013

University of Dundee

Conditions for Use and Duplication

Copyright of this work belongs to the author unless otherwise identified in the body of the thesis. It is permitted to use and duplicate this work only for personal and non-commercial research, study or criticism/review. You must obtain prior written consent from the author for any other use. Any quotation from this thesis must be acknowledged using the normal academic conventions. It is not permitted to supply the whole or part of this thesis to any other person or to post the same on any website or other online location without the prior written consent of the author. Contact the Discovery team (discovery@dundee.ac.uk) with any queries about the use or acknowledgement of this work.

Ultrasound Mediated Targeted Drug Delivery *In Vitro*: Design, Evaluation and Application

Dana Gourevich

Doctor of Philosophy

University of Dundee, January 2013

This page was intentionally left blank

Table of Contents

Acknowledgments.....	7
Certification.....	8
Author Declaration.....	9
List of Figures.....	10
List of Tables.....	14
List of Equations.....	14
List of Symbols and Abbreviations.....	15
Abstract.....	21
CHAPTER 1 INTRODUCTION.....	22
1.1 Targeted Drug Delivery and Ultrasound	22
1.2 Motivation.....	24
1.3 Contributions to Knowledge	25
1.4 Outline of the Thesis	26
1.5 List of Publications	27
1.6 References	28
CHAPTER 2 BACKGROUND.....	31
2.1 Introduction	31
2.2 Drug Delivery Systems	31
2.2.1 Traditional Delivery Systems.....	31
2.2.2 Colloidal Carriers.....	33
2.2.3 Cyclodextrins.....	35
2.3 Targeted Drug Delivery	44
2.3.1 Targeting Principles.....	45
2.3.2 Targeting Moieties	45
2.3.3 Cyclodextrins in Targeted Drug Delivery.....	45
2.4 Ultrasound	50
2.4.1 Principles of Ultrasound.....	50
2.4.2 Ultrasound in Materials: Properties of Ultrasound Propagation.....	52
2.4.3 Cavitation	54
2.4.4 Biomedical Ultrasound Applications.....	57
2.4.5 Magnetic Resonance guided Focused Ultrasound Surgery	59
2.4.6 Magnetic Resonance guided Focused Ultrasound Surgery Systems in Drug Delivery.....	63

2.5	Summary.....	63
2.6	References.....	64
CHAPTER 3 DEVELOPMENT AND CHARACTERIZATION OF A CYCLODEXTRIN- BASED DRUG CARRIER.....		75
3.1	Introduction.....	75
3.1.1	Chemical Modification and Cyclodextrin Derivatives.....	75
3.1.2	Production Methods of Complexes.....	78
3.1.3	Characterization of Cyclodextrins and Their Complexes.....	79
3.1.4	Aims and Objectives.....	83
3.2	Materials and Methods.....	84
3.2.1	Materials.....	84
3.2.2	Methods.....	85
3.3	Results.....	88
3.3.1	Synthesis.....	88
3.3.2	Chemical and Structural Analyses of the Carrier and the Complexion with Dox.....	88
3.4	Discussion.....	105
3.5	Conclusions.....	110
3.6	References.....	111
CHAPTER 4 ADAPTATION OF CLINICAL MRgFUS SYSTEM FOR IN-VITRO APPLICATION OF FUS: DESIGN AND EVALUATION.....		117
4.1	Introduction.....	117
4.1.1	Ultrasound.....	118
4.1.2	Magnetic Resonance guided Focused Ultrasound Surgery.....	120
4.1.3	Additional Thermal Evaluation Techniques.....	125
4.1.4	Aims and Objectives.....	127
4.2	Materials and Methods.....	128
4.2.1	Materials.....	128
4.2.2	Methods.....	128
4.3	Results.....	146
4.3.1	Thermal Evaluation.....	146
4.3.2	US Evaluation.....	156
4.4	Discussion.....	167
4.5	References.....	171

CHAPTER 5	FOCUSED ULTRASOUND APPLICATION ON CELLS – AN IN-VITRO STUDY.....	176
5.1	Introduction	176
5.1.1	Therapeutic Ultrasound and Cells.....	176
5.1.2	Aims and Objectives.....	182
5.2	Materials and Methods.....	182
5.2.1	Materials	182
5.2.2	Methods.....	183
5.3	Results.....	189
5.3.1	Sonoporation with UF System	189
5.3.2	Sonoporation with Conformal Bone System.....	193
5.3.3	Sonoporation and Heating Influence on Encapsulated Drug Uptake and Cell Viability.....	196
5.4	Discussion.....	205
5.5	Conclusions	211
5.6	References	212
CHAPTER 6	CONCLUSIONS AND IMPLEMENTATION OF RESEARCH: TOWARDS CLINICAL TRIALS.....	216
6.1	Introduction	216
6.2	Conclusions of Research	216
6.3	USmTDD In vivo.....	221
6.3.1	Aim and Objectives	222
6.3.2	Materials and Methods.....	222
6.3.3	Results.....	224
6.3.4	Discussion and Conclusions	227
6.4	References	230
Appendices		
i.	Diffusion Coefficient (D) Calculations.....	232
ii.	Dimensions of 96-well plate (Greiner Bio-One, UK).....	233
iii.	Beam dimensions calculations.....	234
iv.	The Efficiency (Eff) and the Uniformity (Uni) calculations.....	234
v.	Hydrophone Calibration constants β_H (V ² cm ² /W) and α_H (V/Pa) and calculations.....	235
vi.	Attenuation of Ultrasound Waves in Tissues.....	235

Only of Myself I Knew How to Tell

Only of myself I knew how to tell.
 My world is as narrow as the ant's,
 Also my burdens I carried like her
 Too many, too heavy for my thin shoulder.

Also my path - like hers to the treetop -
 path of pain, and path of toil,
 Giants' hand, malicious and securing,
 teasing hand lay over all.

All my ways trembled and wept
 constant fright of the giants' hand.
 Why have you called me, shores of wonder?
 Why disappointed me, distant lights?

Rachel the Poetess,
 4.3.1930

רק על עצמי לספר ידעתי

רק על עצמי לספר ידעתי.
 צר עולמי כעולם נמלה,
 גם משאי עמסתי כמוה
 רב וכבד מכתפי הדלה.

גם את דרכי – כדרכה אל צמרת –
 דרך מכאוב ודרך עמל,
 יד ענקים זדונה ובוטחת,
 יד מתבדחת שמה לאל.

כל ארחותי הליז והדמיע
 פחד טמיר מיד ענקים.
 למה קראתם לי, חופי הפלא?
 למה קזבתם, אורות רחוקים?

רחל המשוררת,
 ד' אדר תר"ץ.

Acknowledgments

First and foremost I would like to thank my supervisor, Prof. Sandy Cochran, for making my dream come true. Thank you. I simply could have not done any of this without all your help and guidance. As it was indeed a tough journey, yet I would have not changed it a bit.

Additional gratitude should be expressed to my other supervisors: Prof. Andreas Melzer and Dr. Maya Thanou, and also to Dr. Michael Wright who contributed his comments on this thesis, and Dr. Jallal Gnaim, who I owe special gratitude for sending me on this lonely quest, yet always being there, in the shadows, guiding and shielding me. A special thank you goes to Alex and Osnat Volovick, without whom much of this could not have been achieved. Thank you goes to Dr. Lijun Wang and Dr. Fabian Arditti, for their much appreciated inputs on the biological aspects of the work. I would also like to acknowledge other wonderful people I met on my way, which taught me so much both professionally and personally, some of them are: Dr. Eyal Neria, Prof. Yoav Medan, Mrs. Doudou Xu, Dr. Dun Liu, Dr. Limor Frish, Mr. Stefan Chulski, Dr. Clare Hoskins, Mr. Bjoern Gerold, Dr. Ritu Malik, Dr. Mariana Bobeica, Dr. Paul Prentice, Mr. Muhammad Athama, Dr. Yoni Hertzberg, Dr. Eihab Kabha as well as the support staff in the Institute of Medical Science and Technology (IMSaT) and InSightec staff including Dr. Shuki Vitek, Mr. Javier Grienfield, Mr. Oleg Prus and Mr. Yaron Shafran.

Personal thanks goes to Mrs. Lauren Patterson and the lovely Norris family, which made me feel at home a million miles away, to Mr. Tsion Ohaion, for his unlimited patience, and Miss Natali Mislivtsev for her mental encouragements.

More than anyone, I would like to thank my tiny precious family for carrying the burden while stubbornly trying to hide it- this belongs to you as much as it belongs to me. Last but not least, I want to thank my partner, Mr. Alexey Shamov, for not giving up on me.

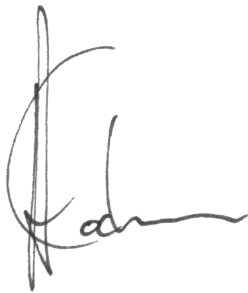
Thank you all.

The research presented in this manuscript received funding from the European Community's Seventh Framework Programme (FP7/2007-2013) under grant agreement n°230674 (Nanoporation project).

CERTIFICATION

This is to certify that Dana Gourevich has complied with all the requirements for the submission of this Doctor of Philosophy thesis to the University of Dundee,

Signature:

A handwritten signature in black ink, appearing to read 'Dana', written over a horizontal line.

Date: 15.3.13

**DECLARATION CONCERNING THESIS PRESENTED FOR
THE DEGREE OF**

DOCTOR OF PHILOSOPHY

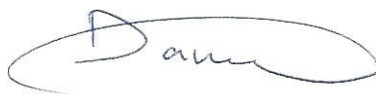
I Dana Gourevich

solemnly and sincerely declare, in relation to the thesis entitled:

**Ultrasound Mediated Targeted Drug Delivery *In Vitro*: Design,
Evaluation and Application,**

that I am the author of this thesis, that all references cited have been consulted by me; that the work of which the thesis is a record has been done by me, and that the material has not previously been accepted in whole, or in part, for any other degree or diploma.

Signature:

A handwritten signature in black ink, appearing to read 'Dana', enclosed within a large, loopy oval flourish.

Date: 15.3.13

List of Figures

Figure 2.1 - Amphiphilic molecule and a micelle structure	32
Figure 2.2- (a) Chair conformation of D-glucopyranose in a CD and (b) a 3D structure of a D-glucopyranose unit, where the atoms C,O,H marked with grey, red and white, respectively ...	36
Figure 2.3- (a) Schematic representation of CD 3D conformation and (b) γ CD	37
Figure 2.4- Illustration of 1:1 inclusion complex of a guest molecule in a CD	39
Figure 2.5- Diagram of phase solubility behaviour.....	41
Figure 2.6- Focusing of acoustic waves	51
Figure 2.7- Schematic representation of sound velocity in different liquids	52
Figure 2.8- Snell's law	54
Figure 2.9- <i>In-vivo</i> liver ablation through the ribcage (InSightec, Ltd.).....	58
Figure 2.10- A schematic representation of M_0 under the influence of B_1	60
Figure 3.1- Doxorubicin (Dox).....	78
Figure 3.2- Transition between orbitals	80
Figure 3.3- Synthesis of carriers Ca-1688 and Ca-1709.....	85
Figure 3.4- HPLC measurement of the carrier.....	89
Figure 3.5- (a) Fluorescence spectrum of Dox with increasing carrier concentrations and (b) Dox fluorescence at 592 nm as a function of carrier concentration.....	89
Figure 3.6- Benesi-Hildebrand plot of Dox fluorescence.....	90
Figure 3.7- $^1\text{H-NMR}$ spectrum of γ CD in D_2O	90
Figure 3.8- $^1\text{H-NMR}$ spectrum of γ CD in DMSO.....	91
Figure 3.9- $^1\text{H-NMR}$ spectrum of the carrier in D_2O	91
Figure 3.10- $^1\text{H-NMR}$ spectrum of the carrier in DMSO.....	92
Figure 3.11- $^1\text{H-NMR}$ spectrum of γ CD (top) and carrier (bottom) in D_2O	92
Figure 3.12- $^1\text{H-NMR}$ spectra of the carrier in D_2O (top) and DMSO (bottom).....	93
Figure 3.13- $^1\text{H-NMR}$ spectrum of Dox in D_2O	94
Figure 3.14- $^1\text{H-NMR}$ spectrum of Dox in DMSO.....	94
Figure 3.15- Comparison between $^1\text{H-NMR}$ spectra of 2 mM Dox in D_2O (top) and DMSO (bottom)	95
Figure 3.16- $^1\text{H-NMR}$ spectra of Dox in D_2O at 2 mM (top) and 10 mM (bottom).....	96
Figure 3.17- $^1\text{H-NMR}$ spectrum 1:10 Dox:carrier complex in D_2O	98
Figure 3.18- $^1\text{H-NMR}$ spectra of Dox (top), carrier (middle) and 1:1 Dox:carrier complex (bottom) in D_2O	98
Figure 3.19- $^1\text{H-NMR}$ spectra of 1:10 Dox:carrier complex (in red) and 1:1 Dox:carrier complex (in blue) in D_2O	99
Figure 3.20- $^1\text{H-NMR}$ Spectra of Dox (top), carrier (middle) and 1:1 Dox:carrier complex (bottom) in DMSO	100
Figure 3.21- $^{13}\text{C-NMR}$ spectrum of the carrier	100
Figure 3.22- $^1\text{H-NMR}$ sel-NOE of 1:10 Dox:carrier in D_2O	102
Figure 3.23- $^1\text{H-NMR}$ (a) COSY and (b) NOESY spectra of 1:1 Dox:carrier complex in D_2O	102
Figure 3.24- Subtraction of the COSY and NOESY spectra presented in Figure 3.23	103
Figure 3.25- 5-6 ppm $^1\text{H-NMR}$ (a) COSY and (b) NOESY spectra and (c) their subtraction of 1:1 Dox:carrier complex in D_2O	103

Figure 3.26- 6.8-8ppm ¹ H-NMR (a) COSY and (b) NOESY spectra and (c) their subtraction of 1:1 Dox:carrier complex in D ₂ O.....	104
Figure 3.27- Signal decay in diffusion measurements of Dox, carrier and the complex	104
Figure 3.28- Carrier and Dox prior to encapsulation (a) ball shaped and (b) space filling style	109
Figure 3.29- Carrier and Dox in a suggested encapsulated form (a) ball shaped primary face view, (b) space filling style primary face view, (c) ball shaped primary side view, (d) space filling style side view, (e) ball shaped secondary face view and (f) space filling style secondary face view.....	109
Figure 4.1- Schematic representation of a secondary focus in a well	119
Figure 4.2- ExAblate main components: (a) cradle, (b) operator console and (c) equipment cabinet	122
Figure 4.3- Bath components.....	123
Figure 4.4- Drawing of UF transducer dimensions	123
Figure 4.5- ExAblate 2100 conformal bone system (CBS): (a) connected to a MRI (b) the transducer filled with degassed water and (c) the dimensions of the transducer	124
Figure 4.6- Schematic structure of a copper (Cu)- constantan (C) (T type) thermocouple	126
Figure 4.7- Sealed plate (a) before and (b) after sonication.....	129
Figure 4.8- Diagram of sonication pattern and order in the UF sonoporation arrangement...	129
Figure 4.9- Initial UF sonoporation arrangement in MR environment.....	130
Figure 4.10- Plate holder rings (a) separated and (b) stacked.....	130
Figure 4.11- UF sonoporation arrangement covered by a polystyrene box.....	131
Figure 4.12- Spot planning in (a) coronal and (b) sagittal images of a plate	131
Figure 4.13- Deformation in a single well due to FUS (marked in red).....	133
Figure 4.14- Final UF sonoporation arrangement: (a) designed model, key: 1- water bath containing FUS source; 2- FUS source; 3- degassed water container; 4- the plate; 5- ultrasound absorber material, and (b) real imaging	134
Figure 4.15- Focus within a single well in an inverted plate.....	135
Figure 4.16- CBS sonoporation arrangement: (a) designed model, key: 1- FUS source; 2- degassed water container; 3- the plate; 4- ultrasound absorber material, and (b) real imaging	136
Figure 4.17- Diagram of sonication pattern in the CBS arrangement	137
Figure 4.18- Heating arrangement without FUS: (a) designed model, key: 1- 75°C heater, 2- 75°C heating block, 3- plate, 4- top block, 5- 50°C heater, 6- 50°C heating block, and (b) real imaging.....	138
Figure 4.19- Diagram of heating pattern in the heating arrangement without FUS	138
Figure 4.20- UF heating arrangement: (a) designed model, key: 1- water bath containing FUS source; 2- FUS source; 3- degassed water container; 4- the plate; 5- ultrasound absorber material 6 and 7 - lower and upper tissue mimicking phantoms, respectively, and (b) real imaging.....	139
Figure 4.21- Diagram of sonication pattern and order in the UF heating arrangement	140
Figure 4.22- PRF temperature measurement via the ExAblate software.....	140
Figure 4.23- Positioning of thermal camera on the UF table.....	141
Figure 4.24- Altair software for thermal evaluation via FLIR IR thermal camera	142
Figure 4.25- Thermocouples attached to the (a) base and (b) sealing film on a plate.....	142
Figure 4.26- (a) thermocouples attached to a plate and (b) placed over a phantom	143

Figure 4.27- Thermocouples attached to a plate in the UF Sonoporation arrangement.....	144
Figure 4.28- Special plates with (a) only a sealing film or (b) base attached to the plate frame	144
Figure 4.29- (a) the hydrophone positioner (b) scanning base part of a plate (c) hydrophone position over the plate	145
Figure 4.30- (a) US field measurements (b) positioning of the hydrophone above the plate (c) interpretation of the data using dedicated software.....	145
Figure 4.31- Coronal images of a plate between two DQA phantoms.....	146
Figure 4.32- (a) sagittal and (b) axial images of a plate between two DQA phantoms.....	147
Figure 4.33- Schematic representation of the combined sonication mode.....	147
Figure 4.34- Thermal Monitoring by MRI: (a) axial MR image showing FUS induced heating arrangement, with a white and orange crosses marking the chosen pixel for temperature measurement in the lower and upper phantoms, respectively, (b) temperature graph measurement during sonication in the (i) lower and (ii) upper phantoms and (c) a thermal map, with a white and orange crosses marking the chosen pixel for temperature measurement in the lower and upper phantoms, respectively	148
Figure 4.35- Thermal camera measurement of the well perimeter temperature of a plate....	149
Figure 4.36- Thermal camera imaging of the well perimeter temperature of a plate at the powers (a) 1, (b) 2, (c) 5, and (d) 10 Wa	149
Figure 4.37- Black thick base plate	150
Figure 4.38- Thermal camera measurement of the well base temperature of a black thick base plate.....	150
Figure 4.39- Thermal camera imaging of the well base temperature of a black thick base plate at powers of (a) 1, (b) 2, (c) 5, and (d) 10 Wa.....	151
Figure 4.40- Thermocouple measurements of (a) regular and (b) inverted positioning of the plate.....	152
Figure 4.41- Thermocouple measurements in a heating process of an inverted plate	152
Figure 4.42- Thermocouple measurements of FUS induced heating in (a) regular and (b) inverted plates.....	153
Figure 4.43- Thermocouple measurements of FUS induced heating at (i) 0.5 s on, 2.5 s off mode and (ii) 0.5 s on, 3 s off in a Plate	154
Figure 4.44- Thermocouple measurements in the UF sonoporation arrangement.....	155
Figure 4.45- XY Slice of acoustic measurements (a) without and (b) with the base of a plate.	156
Figure 4.46- Acoustic measurements in XZ plane (a) without and (b) with base and in YZ plane (c) without and (d) with base of a plate	156
Figure 4.47- Focus cross-sections in main axes and schematic representation of the focal point without (a and b respectively) and with (c and d respectively) base of a plate.....	157
Figure 4.48- XY slice of acoustic measurements (a) without and (b) with sealing film.....	158
Figure 4.49- Acoustic measurements in XZ plane (a) without and (b) with sealing film and in YZ plane (c) with and (d) without sealing film.....	158
Figure 4.50- Focus cross-sections in main axes and schematic representation of the focal point with (a and b respectively) and without (c and d respectively) sealing film	159
Figure 4.51- XY slice of acoustic measurements of (a) 100% Tr (b) annulus (c) 50% Tr (d) 20% Tr (e) 50% Tr random phases and (f) 100% Tr random phases	160

Figure 4.52- Acoustic measurements in sagittal plane at (a) 100% Tr (b) donut (c) 50% Tr (d) 20% (e) Tr 50% Tr random phases and (f) 100% Tr random phases.....	160
Figure 4.53- Pressure graphs with X and Y axes represented by the green and blue lines, respectively, at (a) 100% Tr (b) annulus (c) 50% Tr (d) 20% Tr 50% Tr (e) random phases and (f) 100% Tr random phases.....	161
Figure 4.54- XY slice of acoustic measurements at FD of (a) 92, (b) 97, (c) 102, and (d) 106 mm	163
Figure 4.55- Acoustic field measurements over a plate in XY plane (a) without and (b) with a DQA phantom, in XZ plane (c) without and (d) with DQA phantom and focus cross-sections in main axes (e) without and (f) with DQA phantom below the plate	164
Figure 4.56- Single point acoustic measurement in (a) XY plane, (b) the focus cross-sections in main axes X and Y, green and blue, respectively, and the (c) XZ plane and (d) YZ plane	165
Figure 4.57- Acoustic measurement of 16- well multi-focal pattern in (a) XY and (b) XZ plane	166
Figure 5.1- Sonovue MBs	177
Figure 5.2- 5 Wa continuous sonication for 20 s (a) prior to sonication, (b) after sonication (c) after 20 Wa continuous sonication.....	179
Figure 5.3- Bespoke cell sonicator (a) without and (b) with a plate.....	180
Figure 5.4- (a) uptake of Dox and (b) viability of MCF7 cells without and with FUS	180
Figure 5.5- MCF7 cells (a) control without FUS (b) FUS plate #1 and (c) FUS plate #2.....	181
Figure 5.6- Uptake of Dox into MCF7 Cells at Various Sonication Parameters	190
Figure 5.7- Uptake of Dox into A375m cells at 1 Wa for 10 s	191
Figure 5.8- Location dependence of Dox uptake into MCF7 cells at 2 Wa for 25 sec	191
Figure 5.9- High power viability assessment in MCF7 cells 24 h after sonication	192
Figure 5.10- Viability of (a) MCF7 and (b) A375m cells immediately and 24 h after sonication	192
Figure 5.11- Membrane integrity due to FUS in (a) MCF7 and (b) A375m cells.....	193
Figure 5.12- Uptake of Dox into (a) MCF7 and (b) A375m cells with a multi-focal sonication.	194
Figure 5.13- Average within each well of Dox uptake into (a) MCF7, (b) A375m cells and (c) the MI, with 20 Wa multi-focal sonication.....	195
Figure 5.14- Viability of (a) MCF7 cells after 20 Wa multi-focal sonication and A375m cells (b) immediately and (c) 24 h after multi-focal sonication at various powers.....	196
Figure 5.15- Dox uptake into (a) MCF7 and (b) A375m cells in the presence of Ca-1709.....	197
Figure 5.16- Dox uptake into MCF7 cells in the presence of Ca-1709 at (a) 1 Wa for 33 s, (b) 1 Wa for 50 s and (c) 2 Wa for 25 s.....	198
Figure 5.17- Uptake of Dox into MCF7 cells in different rows after 3 min heating of a non-inverted plate.....	199
Figure 5.18- Uptake of Dox into MCF7 cells after (a) 3 and (b) 6 min and (c) into A375m cells after 3 min heating	200
Figure 5.19- Viability of MCF7 cells after 24 h as a result of (a) 3 and (b) 6 min heating.....	201
Figure 5.20- Viability of A375m cells after 24 h as a result of 3 min heating in 5 plates.....	201
Figure 5.21- Uptake of Dox into MCF7 cells after FUS induced heating with (a) 30 Wa for 30 s and (b) 30 Wa for 20 s.....	202
Figure 5.22- Uptake of Dox into A375m cells after FUS induced heating (see text for Mode details).....	203

Figure 5.23- Viability of MCF7 cells 24 h after FUS induced heating.....	204
Figure 5.24- Viability of A375m cells 24 h after FUS induced heating (a) 30 Wa for 30 s followed by a pulsed sonication of 30 Wa, (b) 20 Wa for 45 s followed by a pulsed sonication of 20 Wa, and (c) 15 Wa for 60 s followed by a pulsed sonication of 15 Wa	204
Figure 5.25- A375m cells viability plate following FUS induced heating.....	205
Figure 6.1- Deceased mice (a) on their arrival, (b) covered with Veet shaving cream, and (c) after the second fur removal.....	223
Figure 6.2- Arrangement for FUS application <i>ex-vivo</i> and <i>in-vivo</i>	223
Figure 6.3- Positioning of mice (a) inside breast coil (b) covered with a glove full of warm water	223
Figure 6.4- DQA phantom arrangement.....	224
Figure 6.5- Spot location of the (a) continuous and (b) pulsed sonication	225
Figure 6.6- Sonication at 4 Wa in (a) continuous and (b) pulsed sonication.....	225
Figure 6.7- PRF thermometry measurement at the (a) normal and (b) annular foci in DQA phantom at a power of 4 Wa	226
Figure 6.8- PRF thermometry measurement at the (a) normal and (b) annular foci in DQA phantom at a power of 16 Wa	226
Figure 6.9- Spot location of the (a) normal and (b) annular foci.....	227
Figure 6.10- PRF thermometry measurement at the (a) nominal and (b) annular shaped spots in <i>ex-vivo</i> tissue	227

List of Tables

Table 2.1- Dimensions of α -, β - and γ CD	37
Table 2.2- Water solubility characteristics of α -, β - and γ CD	38
Table 3.1- Equipment and chemicals	84
Table 3.2- HPLC elution solvents	87
Table 3.3- ^1H -NMR chemical shifts of γ CD and the carrier	93
Table 3.4- ^1H -NMR chemical shifts of Dox	97
Table 3.5- ^{13}C -NMR chemical shifts of the carrier	101
Table 3.6- Diffusion coefficients	105
Table 4.1- Equipment and consumables	128
Table 4.2- Summary of measured beam forms	162
Table 4.3- Acoustic pressure measurements of the 16 points focal pattern per well inside the plate	167
Table 5.1- MBs deformation dependance on the MI	177
Table 5.2- Materials for <i>in-vitro</i> work	182
Table 5.3- Fluorescence measurement parameters	184
Table 5.4- Applied US powers in Dox uptake studies	190
Table 5.5- Average acoustic pressure and MI for different powers	194
Table 6.1- Materials for <i>ex-vivo</i> work	222

List of Equations

Equation 2.1- Complex equilibrium	40
Equation 2.2- Equilibrium constant calculation	40
Equation 2.3- A_L solubility equation.....	41
Equation 2.4- Slope of A_L	41
Equation 2.5- Intensity at focal point	51
Equation 2.6- General acoustic wave equation	52
Equation 2.7- Sinusoidal wave equation.....	53
Equation 2.8- Acoustic impedance	54
Equation 2.9- Reflection coefficient	54
Equation 2.10- Mechanical index.....	55
Equation 2.11- Stability of a cavitation bubble.....	56
Equation 2.12- Thermal dose	58
Equation 2.13- Larmor equation	59
Equation 2.14- Angle of M_0 tilt	60
Equation 3.1- K_{binding} calculation via Benesi-Hildebrand method	81
Equation 4.1- Image phase and chemical shift correlation	121
Equation 4.2- Chemical shift relation to temperature.....	121
Equation 4.3- Stefane-Boltzmann law of energy emission as a function of temperature	125
Equation 4.4- Electro-motive force (EMF) as a function of thermal change	126
Equation 5.1- Uptake calculation.....	184
Equation 5.2- Cell viability calculation	185
Equation 5.3- Membrane permeability calculation	185
Equation 5.4- Weight dependence on concentration and volume	187
Equation 5.5- Correlation between volumes and concentrations.....	187

List of Symbols and Abbreviations

A375m	Human Melanoma Cells
AcN	Acetonitrile
B_0	External Magnetic Field
B_1	Secondary Pulse (transverse to B_0)
BBB	Blood Brain Barrier
BCA	Bicinchoninic Acid
BCS	Biopharmaceutical Classification System
BSA	Bovine Serum Albumin
c	Velocity of Sound
C18	Octadecyl Carbon Chain Bonded Silica
CBS	Conformal Bone System
CD	Cyclodextrin

CGTases	Cyclodextrin Glucosyltransferases
CH ₂ Cl ₂	Dichloromethane
CM	Complete Medium
CMC	Critical Micelle Concentration
COSY	Correlation Spectroscopy
CPC	Control Personal Computer
CT	Computed Tomography
D _n	Natural Focal Distance
D	Diffusion Coefficient
D ₂ O	Deuterated Water
DC	Duty Cycle
DCC	<i>N,N</i> -Dicyclohexylcarbodiimide
DMAP	4,4-Dimethylaminopyridine
DMEM	Dulbecco's Modified Eagle Medium
DMF	Dimethylformamide
DMSO	Dimethyl Sulphoxide
DMSO _{d6}	Deuterated Dimethyl Sulphoxide
DOSY	Diffusion Ordered Spectroscopy
Dox	Doxorubicin
DQA	Daily Quality Assessment
<i>Eff</i>	Efficiency
EMF	Electro-Motive Force
<i>f</i>	Frequency of an Acoustic Field
FBS	Fetal Bovine Serum
FD	Focal Distance
FDA	Food and Drug Administration
FID	Free Induction Decay
FOV	Field of View
FUS	Focused Ultrasound
GE	Gradient Echo
GIT	Gastrointestinal Tract
GS	Gerchberg- Saxton
h	Hours
HIFU	High Intensity Focused Ultrasound

HOBT	1-Hydroxybenzotriazole
HPLC	High-Performance Liquid Chromatography
HP- β CD	Hydroxypropyl- β Cyclodextrin
IM	In Muscle
IR	Infrared
J	Joule
J	Coupling Constant
K	Equilibrium Constant
K_{binding}	Binding Constant
LC	Liquid Chromatography
LDH	Lactate Dehydrogenase
LED	Longitudinal Eddy-current Delay
M_0	Net Magnetization
MBs	Microbubbles
MCF-7	Human Breast Cancer Cells
MI	Mechanical Index
min	Minutes
MPa	Megapascal
MRgFUS	Magnetic Resonance guided Focused Ultrasound Surgery
MRI	Magnetic Resonance Imaging
MTT	3-(4,5-Dimethylthiazol-2-yl)-2,5-diphenyltetrazolium Bromide
M_w	Molecular Weight
NEX	Number of Excitations
NMR	Nuclear Magnetic Resonance
NMRI	Nuclear Magnetic Resonance Imaging
NOESY	Nuclear Overhauser Enhancement Spectroscopy
ONs	Oligonucleotides
PBS	Phosphate Buffered Saline
P_D	Pharmacodynamics
PD	Proton Density
PEG	Polyethylene Glycol
P_K	Pharmacokinetics
<i>PNP</i>	Peak Negative Pressure
ppm	Parts Per Million

PRF	Proton Resonance Frequency
PRT	Pulse Repetition Time
RF	Radio Frequency
RPMI	Roswell Park Memorial Institute
ROS	Reactive Oxygen Species
RP-HPLC	Reversed Phase HPLC
rpm	Revolutions Per Minute
RT	Room Temperature
RTD	Resistance Temperature Detector
SBE- β CD	Sulphobutyl Ether β Cyclodextrin
SC	Subcutaneously
Sd	Standard deviation
SDS	Sodium Dodecyl Sulphate
Se	Standard error
SE	Spin Echo
s	Seconds
SF ₆	Sulphur Hexafluoride
SNR	Signal-to-Noise Ratio
T ₁	Spin-Lattice Relaxation
T ₂	Spin-Spin Relaxation
T ₂ *	The 'Apparent' Relaxation
TDD	Targeted Drug Delivery
TE	Echo Time
TFA	Trifluoroacetic Acid
TLC	Thin-Layer Chromatography
TMS	Tetramethylsilane
T _p	Pulse Duration Time
TR	Time Repetition
Tr	Transducer Rings
UF	Uterine Fibroids
USmTDD	Ultrasound mediated Targeted Drug Delivery
<i>Uni</i>	Uniformity
US	Ultrasound
USCA	Ultrasound Contrast Agent

W	Watt
Wa	Acoustic Watt
WR	Working Reagent
Z	Acoustic Impedance
α CD	α -Cyclodextrin
β CD	β -Cyclodextrin
γ CD	γ -Cyclodextrin
α	Tilt Degree
α_H	Hydrophone Calibration Constant 1
β_H	Hydrophone Calibration Constant 2
δ	Chemical Shift
γ	Gyromagnetic Ratio
λ	Wavelength
ρ_0	Density
τ_c	Correlation Time
ω	Angular Frequency
ω_0	Precessional Frequency
ψ	Wave Function
3D	Three Dimensional

This page was intentionally left blank

Abstract

Background Targeted Drug Delivery (TDD) is a therapeutic modality which allows an increase in the medication dose at a treatment site, while simultaneously avoiding effects in the rest of the human body. This can be achieved via different types of delivery vehicles or carriers which encapsulate the free drug and release it only at the needed location. There are various methods of drug release, one of which is ultrasound, as in ultrasound-mediated TDD (USmTDD). The combination of focused ultrasound (FUS) and magnetic resonance imaging (MRI) provides a controllable system of drug release and impact assessment.

In the work reported here, a novel drug carrier was synthesized and assessed. Ultrasonic drug release from the carrier was evaluated *in vitro* using a clinical MRI-guided Focused Ultrasound Surgery (MRgFUS) system. As there was no properly controllable research environment for *in-vitro* studies available prior to the investigation of the carriers, such an environment was built and characterized.

Methods MCF7 and A375m human cancer cell lines were subjected to FUS using the ExAblate 2000 and 2100 systems (InSightec, Haifa, Israel). The experiments were conducted in a specially designed research environment, which was comprehensively evaluated to ensure both cell sterility and proper FUS propagation. Various sonication parameters were applied, in conjunction with a commercially available ultrasound contrast agent (USCA), to achieve maximal cellular uptake of Doxorubicin (Dox) with minimal decrease in cell viability. A novel cyclodextrin (CD) based drug carrier was synthesized, chemically evaluated, and investigated *in vitro* via two release mechanisms: heating and physical effects.

Results Two clinical MRgFUS systems were adapted for *in-vitro* work, showing controllable and repeatable results. Both of the assessed release mechanisms showed their competency: the application of FUS in the presence of USCA increased the cellular drug uptake of Dox by an average factor of 3 ± 0.9 , and up to a factor of 4 due to heating. The Dox release from the CD-based carrier was around 100% with both mechanisms.

Conclusions Adaptation of a clinical MRgFUS system for *in-vitro* research allows the use of a single system starting from *in-vitro* studies, through the pre-clinical stage to clinical trials. This gives physicians the ability to be a part of a wider USmTDD research group, from the beginning of the product definition, bringing real meaning to the term “from bench to bedside”. The baseline studies reported here have verified that intracellular drug uptake is increased through heating and sonoporation processes. The release mechanisms from the carriers were also observed, validating the concept of USmTDD from CD-based carriers.

CHAPTER 1 INTRODUCTION

1.1 Targeted Drug Delivery and Ultrasound

Targeted drug delivery (TDD) has been a subject of investigation for many research groups worldwide (Barannon-Peppas and Blanchette, 2012). Imaging technologies such as magnetic resonance imaging (MRI), ultrasound (US) and computed tomography (CT), gave a further drive in this research field, introducing the possibility for real time image guided TDD. The potential of targeting drugs to a site-specific location in the body, while maintaining a toxin-free environment in the vital organs e.g. heart, lungs, liver etc., has been a possibility that is now becoming more likely for millions of patients (Corti et al., 2012; Rösler et al., 2012). Still, there are many steps from a promising idea, through a suitable model, to a fully functioning and reliable remedy.

One of the most crucial steps in the development of TDD treatments is the *in-vitro* studies. In the *in-vitro* stage the core of the principal is investigated in all its aspects, including not only the basic questions of cytotoxicity, but also its efficiency in comparison to existing treatments and its potential to reach the clinic. Here, one must present an outcome far better than the currently used treatments and demonstrate potential to become economically viable. An important factor at the *in-vitro* stage is its possible applicability to the pre-clinical and subsequent clinical studies. Therefore, the *in-vitro* arrangement must be not only accurate in terms of statistical significance, but also have a clear affinity to its practical application in the clinic.

There are various methods of TDD, both physical, e.g. focused ultrasound (FUS), laser etc., and chemical, e.g. various drug carriers, each of which has its own benefits and drawbacks. In the work presented here, a combination of both the physical and the chemical methodologies was investigated in order to combine the best features of each approach to create a better drug delivery tool (Gao et al., 2004).

In the medical field, US is divided into two major streams: diagnostic and therapeutic. The diagnostic stream mainly refers to imaging, while the therapeutic stream introduces a wider spectrum including lithotripsy, phacoemulsification, FUS and assorted TDD. US-mediated TDD (USmTDD) can be achieved via two different mechanisms, or their combination, the first being generation of local temperature rise (Grüll, and Langereis, 2012) and the second is by application of mechanical force, e.g. generation of cavitation and micro streaming. Both of these applications can potentially increase cell membrane permeability via different mechanisms.

Heat treatments are known to increase *in-situ* drug uptake in cancer cells (Yudina et al., 2012) and can be generated in a relatively straightforward way. Cavitation on the other hand is a more problematic tool in USmTDD. Acoustic cavitation can be defined as acoustically-driven bubble oscillations and collapse (Morfeý, 2001). In general, natural occurring cavitation bubbles and their oscillations and collapse, form a spontaneous and rather unpredictable phenomenon which is difficult to control. Nonetheless, it is possible to generate stable and controllable cavitation using engineered cavitation nuclei, e.g. microbubbles (MBs). Under specific acoustic parameters, MBs are widely utilised for investigation of USmTDD (Yudina et al., 2010) for generation of controlled cavitation to increase cell membrane permeability by sonoporation (Pitt et al., 2004) and cellular massage (Wu and Nyborg, 2008). One of the accelerating research areas is the utilization of FUS to facilitate *in-situ* drug release from various carriers (Kilbanov et al., 2010).

In the present study, the source of FUS was a clinical MRI guided focused ultrasound surgery (MRgFUS) system, CE marked and FDA approved for treatments of uterine fibroids and bone metastases. The utilization of such a system is beneficial not only in providing a highly monitored research tool, but also in gaining an easier transition platform to pre-clinical *in-vivo* studies (Chen et al., 2010), and potentially up to the clinical stages.

From the chemical point of view, a novel nanocarrier was synthesized and evaluated for the work reported here. The nanocarrier is based on a cyclodextrin (CD) unit, which is responsible for complexation with the drug, covalently bonded to an amino-acid-based functional group. CDs are natural, water soluble, sugar based, cone structured molecules with lipophilic inner cavities (Singh et al., 2010). Their ability to form complexes with a wide variety of molecules has been studied for over a century (Schmid, 1989). They have been proven to enhance solubility of non-soluble drugs, contribute to the stability of the guest molecules, reduce volatility, and even mask odours. Another important feature of CDs, especially in TDD applications, is that the created drug-CD complex is in a constant dynamic equilibrium (Brewster and Loftsson, 2007). Consequently, it must be properly targeted to reach the intended location. Targeting the CD-based formulation is usually achieved by creating a chemical derivative, with a functional group as the targeting tool (Van de Manakker et al., 2009). In this work, a newer approach is shown, in which FUS was introduced to a cell monolayer in order to enhance membrane permeability, both through mechanical and thermal mechanisms, in conjunction with a chemically modified CD.

Doxorubicin (Dox) is an antibiotic substance discovered over fifty years ago and is currently classified as the most potent treatment for many malignancies and especially for

solid tumours (Frederick et al., 1990). The main drawback in treatment with Dox is the high cardiotoxicity associated with the cleavage of the Dox molecule and creation of free radicals (Šimůnek et al., 2009). Although many efforts have been applied in order to decrease the unwanted side effects of Dox, e.g. by encapsulation of the Dox into liposomes (O'Brien et al., 2004), the challenge of efficient Dox delivery without harming the surrounding tissues, still exists. It was recently shown that CDs can potentially aid in the prevention of the Dox cleavage and hence decrease their cytotoxicity (Anand et al., 2012; Swiech et al., 2012). In this study, the CD-based carrier was chemically modified in a way that resulted in a successful Dox delivery vehicle. The CD-Dox complex was tested *in vitro*, with the application of FUS as the drug release mechanism.

In this work, it is proposed that the combination of FUS from an arrangement based on a clinical system with a novel nanocarrier based on the CD technology, not only will allow a wide range of possible encapsulated drugs in an *in-vitro* research environment, but also non-invasive, site-specific drug delivery with a faster track to reach the patients.

1.2 Motivation

Even though USmTDD has been a focus of study for some time, there are still many unanswered questions, with the most important being the exact mechanism for increased drug uptake. Moreover there is a constant quest for improved drug carriers. For these reasons it is very important to start research from the *in-vitro* stage, since there, under correct research environment, fundamental questions will be answered. In the present work, the possibility to combine such arrangements with a novel drug carrier presented an opportunity to investigate a well-studied field in a new way.

Using a clinical FUS system gave the work another challenging aspect. While on the one side the system led to an easier path to reach potential *in-vivo* studies, considerable work was needed to adapt it to serve as a purely research tool. The quest for an optimal arrangement was not the only goal. A crucial part of the research lay in the interaction of the novel nanocarriers with FUS, in all its aspects. The possibility to be the first to investigate a CD-based nanocarrier with a state-of-the-art clinical device in order to improve the delivery of drugs was significant.

The core of the presented work is the investigation of the carriers and FUS in the *in-vitro* environment. Due to the fact that *in-vitro* studies involve fragile yet hazardous research materials, they need to be carried out in a biologically strongly controlled setting with specific protocols in place, to protect both the high level sterility of the experiments as well as the

health and safety of the staff. Therefore, the created arrangement for introducing FUS to cells had to utilize standard biological consumables that could then be analysed in common biological lab apparatus. This presented a major challenge of this work: the design and evaluation of a biologically compatible arrangement for FUS application to cancer cell lines. The possibility to establish a bridge between complex biological issues and robust FUS mechanisms was the strongest motivation for this work.

1.3 Contributions to Knowledge

- a. This manuscript presents the successful adaption of a clinical magnetic resonance imaging guided FUS surgery (MRgFUS) system to cell culture work. The utilization of a clinical system allowed more flexibility as compared to even specially designed laboratory sonicators, delivering the possibility to control various parameters, including phase manipulations and variable transducer apertures, in addition to collecting and recording ultrasonic spectra during sonication. Moreover, the establishment and thorough evaluation of the arrangements that were created presents the opportunity for effective repetition of the *in-vitro* experiments by other research groups worldwide.
- b. In this study the outcome of the iterative Gerchberg- Saxton (GS) algorithm for ultrasound beam design was validated for the first time against acoustic field measurements. The novel use of a multi-focal sonication pattern in TDD *in-vitro* experiments was proved to be highly beneficial. A single sonication procedure at 16 points simultaneously significantly reduced the procedure time, resulting in accurate and repeatable results and eliminating the effect of time delay between different treatment groups.
- c. In the presented work, the widely used drug Doxorubicin (Dox) was successfully encapsulated within a novel CD-based carrier. The carrier was synthesized and evaluated by spectroscopic and chemical means including nuclear magnetic resonance (NMR), fluorescence measurements and high performance liquid chromatography (HPLC). Moreover, the created complex between the carrier and Dox was investigated under various NMR methodologies: $^1\text{H-NMR}$, 3D measurements (nuclear Overhauser enhancement spectroscopy (NOESY) and correlation spectroscopy (COSY)) and diffusion coefficient (D) measurements via diffusion ordered spectroscopy (DOSY).
- d. Hyperthermia was shown to be highly beneficial in the drug release and cellular uptake increase of free and encapsulated drug. Although some thermo-sensitive CD-based

polymers have been demonstrated in the past, this is the first *in-vitro* validation of the heat sensitivity of a CD-based drug vehicle with FUS as the heating source.

- e. The drug uptake results have confirmed that the use of FUS and microbubbles (MBs) enhances the membrane permeability of the cancer cells, as was also confirmed by membrane integrity studies. The cell viability results have validated that the membrane rupture is a reversible and non-permanent process which does not lead directly to cell necrosis. Moreover, the combination of MBs with the CD carrier in the presence of FUS has produced significant drug uptake within cancer cells. The presented work is the first *in-vitro* examination of FUS-induced drug delivery from a γ CD-based carrier with the aid of USCA.

1.4 Outline of the Thesis

The field of USmTDD is a multidisciplinary biotechnological field, combining topics in chemistry, biology, physics and medicine. In order to make this thesis as useful as possible for readers with potentially different backgrounds, this manuscript is intended to be thorough and informative but also succinct.

Chapter Two is a literature review on each of the subjects presented in this work. It is divided into two parts. The first part describes the field of drug delivery, with different existing drug carriers, and then focuses on the chosen delivery vehicle - the CDs. A broad description of CDs is presented, including their biocompatibility and physicochemical properties, the formation of CD inclusion complexes and their advantages as drug delivery vehicles. TDD is introduced next, followed by a more specifically relevant delivery system, FUS. The second part of Chapter Two provides a technical background to the technologies in use and focuses on the description of the physics behind US, followed by biomedical ultrasound applications. The chapter closes with the imaging modality in use in this work, MRI, and an overview of MRgFUS is provided, as an introduction to the system used in this work.

The next three chapters deal with the core of the thesis which is the synthesis and chemical evaluation of the novel nanocarriers, the design and calibration of *in-vitro* arrangements for FUS application and the conducted *in-vitro* research. Each of these chapters includes a brief introduction, materials and methods section, the achieved results and their discussion, and conclusions.

Chapter Three is dedicated to the creation of the nanocarriers. This chapter includes a focused introduction to the potential modifications of CDs, alongside possible evaluation methodologies for the CDs and their complexes. The synthesis of the carrier in use in this work

is provided, with a full description of the materials and methods and the analytical measurements. Spectroscopic evaluation of the yield, as well as its encapsulation of the guest molecule, Dox, is also detailed.

Chapter Four describes the arrangement for introducing cells to FUS, giving a more fundamental introduction to US and MRgFUS, describing the materials and methods in use and the logic behind their choice. In the results section, a description of the final arrangement can be found, with proper thermal and acoustic evaluations.

Chapter Five represents the combination of the biological, chemical and physical work that has been done. This chapter depicts the *in-vitro* applications of the apparatus that was established for introducing cells to FUS, as presented in Chapter Four. Opening with a preface on US application to cell culture, and the possible effects on cells, a description of the biological protocols and experimental layout follows. The outcomes of application of FUS to cells in various arrangements and conditions are detailed.

Chapter Six is assigned to the conclusions and future outcomes of the work presented in this manuscript. Here a summarized output is presented of the overall data from the *in-vitro* and *ex-vivo* experiments conducted as preparation for the *in-vivo* stage. Furthermore, in correspondence with the possible *in-vivo* studies, the discussion of this chapter presents the future work suggested to be performed on this topic.

1.5 [List of Publications](#)

Peer Reviewed

- **D. Gourevich**, Y. Hertzberg, A. Volovick, Y. Shafran, G. Navon, S. Cochran, and A. Melzer (2012) Ultrasound mediated Targeted Drug Delivery generated by Multifocal Beam Patterns: An in-vitro Study. *Ultrasound Med Biol*, Accepted 24.10.12.
- **D. Gourevich**, O. Dogadkin, A. Volovick, L. Wang, J. Gnaim, S. Cochran, A. Melzer (2013) Ultrasound-mediated Targeted Drug Delivery with a Novel Cyclodextrin-based Drug Carrier by Mechanical and Thermal Mechanisms. Submitted to *J Control Release*

Conference Proceedings

- **D. Gourevich**, B. Gerold, F. Arditti, D. Xu, D. Liu, A. Volovick, L. Wang, Y. Medan, J. Gnaim, P. Prentice, S. Cochran, and A. Melzer (2012) Ultrasound Activated Nano-Encapsulated Targeted Drug Delivery and Tumour Cell Poration In E. Zahavy et al. (Eds.), Nano-Biotechnology for Biomedical and Diagnostic Research, Advances in Experimental Medicine and Biology 733 (pp.135-144). DOI 10.1007/978-94-007-2555-3_13, Springer Science+Business Media.

- B. Gerold, **D. Gourevich**, D. Xu, F. Arditti, P. Prentice, S. Cochran, J. Gnaim, M. Yoav, L. Wang and A. Melzer (2011) Applicator for *In-vitro* Ultrasound-activated Targeted Drug Delivery, In R. Muratore and E. Konofagou (Eds.) Proceedings of the 11th International Symposium on Therapeutic Ultrasound, New York, NY, USA, American Institute of Physics.

Conference Presentations

- Oral
D. Gourevich, A. Volovick, O. Dogadkin, R. Malik, L. Wang, Y. Medan, J. Gnaim, S. Cochran and A. Melzer (2012) "Ultrasound Facilitated Targeted Drug Delivery: An in-vitro study of drug uptake with a clinical MRgFUS system". 9th Interventional MRI Symposium, Boston, USA, September 22-23, 2012.
- Slide Presentation
D. Gourevich, A. Volovick, O. Dogadkin, R. Malik, L. Wang, Y. Medan, J. Gnaim, S. Cochran and A. Melzer (2012). "An in-vitro study of ultrasound facilitated drug uptake with clinical MRgFUS system". 1st European MRgFUS Symposium, Rome, Italy, September 22, 2011.
- Poster
D. Gourevich, A. Volovick, O. Dogadkin, R. Malik, L. Wang, S. Cochran and A. Melzer (2012) "Towards In-Vivo: Ultrasound Mediated Targeted Drug Delivery to Cancer Cells In-Vitro Via A Clinical MRgFUS System". 3rd International Symposium on Focused Ultrasound, Bethesda, Maryland, USA, 14- 17 October, 2012.
D. Gourevich, O. Dogadkin, R. Malik, A. Volovick, B. Gerold, D. Xu, Y. Vachutinsky, F. Arditti, L. Wang, P. Prentice, Y. Medan, J. Gnaim, S. Cochran, A. Melzer. "An in-vitro study of increased drug uptake with MRI-guided focused ultrasound surgery". 28th Annual Scientific Meeting of the European Society for Magnetic Resonance in Medicine and Biology (ESMRMB), Leipzig, Germany, October 6-8, 2011.
D. Gourevich, F. Arditti, A. Volovick, J. Gnaim, A. Melzer, S. Cochran. "The Nanoporation project: A potential new application of Magnetic Resonance guided Focused Ultrasound (MRgFUS)". 22nd International Conference of Society for Medical Innovation and Technology, Trondheim, Norway, September 2-4, 2010.

1.6 References

- Anand, R. et al.** (2012) A close-up on doxorubicin binding to α -cyclodextrin: an elucidating spectroscopic, photophysical and conformational study. *RSC Advances*, 2, pp. 2346- 57.
- Brewster, M.E. and Loftsson, T.** (2007) Cyclodextrins as pharmaceutical solubilizers. *Adv Drug Deliver Rev*, 59, pp.645- 66.

- Chen, L. et al.** (2010) MR-guided focused ultrasound: enhancement of intratumoral uptake of [3H]-docetaxel in vivo. *Phys Med Biol*, 55, pp.7399- 410.
- Corti, A. et al.** (2012) Targeted drug delivery and penetration into solid tumors. *Med Res Rev*, 32 (5), pp. 1078- 91.
- Frederick, C.A. et al.** (1990) Structural comparison of anticancer drug-DNA complexes: adriamycin and daunomycin. *Biochemistry*, 29, pp.2538- 49.
- Gao, Z. et al.** (2004) Ultrasound-enhanced tumor targeting of polymeric micellar drug carriers. *Mol Pharmaceut*, 1 (4), pp. 317-30.
- Grüll, H. and Langereis, S.** (2012) Hyperthermia-triggered drug delivery from temperature-sensitive liposomes using MRI-guided high intensity focused ultrasound. *J Control Release*, 161, pp. 317-27.
- Klibanov, A.L. et al.** (2010) Ultrasound-triggered release of materials entrapped in microbubble-liposome constructs: A tool for targeted drug delivery. *J Control Release*, 148, pp. 13- 17.
- Morfey, C.L.** (2001) *Dictionary of acoustics*. Great Britain: Academic Press.
- O'Brien, M. E. R. et al.** (2004) Reduced cardiotoxicity and comparable efficacy in a phase III trial of pegylated liposomal doxorubicin HCl (CAELYX™/Doxil®) versus conventional doxorubicin for first-line treatment of metastatic breast cancer. *Annals of Oncology*, 15, pp. 440- 9.
- Pitt, W.G. et al.** (2004) Ultrasonic drug delivery- a general review. *Expert Opin Drug Deliv*, 1(1), pp.37–56.
- Rösler, A. et al.** (2012) Advanced drug delivery devices via self-assembly of amphiphilic block copolymers. *Adv Drug Deliv Rev*, 64 p. 270- 9.
- Schmid, G.** (1989) Cyclodextrin glycosyltransferase production: yield enhancement by overexpression of cloned genes. *TIBTECH*, 7, pp.244- 8.
- Šimunek, T. et al.** (2009) Anthracycline-induced cardiotoxicity: overview of studies examining the roles of oxidative stress and free cellular iron. *Pharmacol Rep*, 61, p.154- 71.
- Singh, R. et al.** (2010) Characterization of cyclodextrin inclusion complexes – a review. *J Pharm Sci Tech*, 2 (3), pp.171- 83.
- Swiech, O. et al.** (2012) Intermolecular interactions between doxorubicin and β -cyclodextrin 4-methoxyphenol conjugates. *J Phys Chem B*, 116, pp.1765- 71.
- Van de Manakker, F. et al.** (2009) Cyclodextrin-based polymeric materials: synthesis, properties, and pharmaceutical/biomedical applications. *Biomacromolecules*, 10(12) pp.3157- 75.

Wu, J. and Nyborg, W.L. (2008) Ultrasound, cavitation bubbles and their interaction with cells. *Adv Drug Deliver Rev*, 60, pp.1103- 16.

Yudina, A. et al. (2010) Evaluation of the temporal window for drug delivery following ultrasound-mediated membrane permeability enhancement. *Mol Imaging Biol*, 13, pp.239- 49.

Yudina, A. et al. (2012) In vivo temperature controlled ultrasound-mediated intracellular delivery of cell-impermeable compounds. *J Control Release*, doi:10.1016/j.jconrel.2012.04.018.

CHAPTER 2 BACKGROUND

2.1 Introduction

In this chapter a general scientific introduction will be given on each of the research fields combined in this work. Because this is a multidisciplinary study that has brought together techniques from various fields and backgrounds, the presented scientific overview is deliberately broad and deals with various subjects. Thorough description and explanations on specific procedures are provided in each following chapter.

2.2 Drug Delivery Systems

Administration of drugs in order to heal or prevent illness has been utilised for millennia. Humans have always been intrigued by the possible beneficial effects of various substances on their bodies and minds, and so the pharmaceutical industry, as we address it today, was developed. Substances that used to be labelled as ‘witchcraft’ can be found these days in every pharmacy (Saltzman, 2001). Despite the life-changing developments in the biological, chemical and medical fields in the past centuries, drug discovery is likely to always remain a relevant research topic. While there is still a significant lack in treatment of existing diseases, new health hazards constantly arise. Moreover, even if a certain drug is available for therapy, there can be various problems with its administration, biocompatibility, formulation stability and most importantly, accessibility to the necessary body location (Allen and Cullis, 2004). Another concerning issue is that, with time, cells and viruses can mutate and become immune to established treatments, as often happens in cancer treatments. These reasons define the constant quest for innovative, more efficient drug delivery methodologies.

2.2.1 Traditional Delivery Systems

A typical cell in the human body consists of about 80% water. It can thus be assumed that most of the biological interactions with drugs within the human body occur in water-based environments, meaning that given drugs should be able to interact in aqueous media. Moreover, the delivery of drugs to the cells is mostly done in aqueous media as well, e.g. the blood stream. This presents the challenge of introducing hydrophobic drugs into aqueous solutions.

The rather straightforward way to overcome the problem of dissolving hydrophobic drugs in aqueous solutions is to have a secondary solvent (co-solvent) present in the solution.

A co-solvent can be as simple as another layer of hydrophobic liquid (Liu and Venkatraman, 2012) or surfactants or emulsions.

Surfactants can be described as a mixture of amphiphilically-structured molecules in a solution or suspension. Amphiphilic molecules have a hydrophilic head and a lipophilic tail. They tend to create micelles according to the nature of the surrounding media (Figure 2.1) (Torchilin, 2001). Surfactants can be used in drug delivery to enhance solubility of insoluble drugs and to stabilize them in aqueous environments.

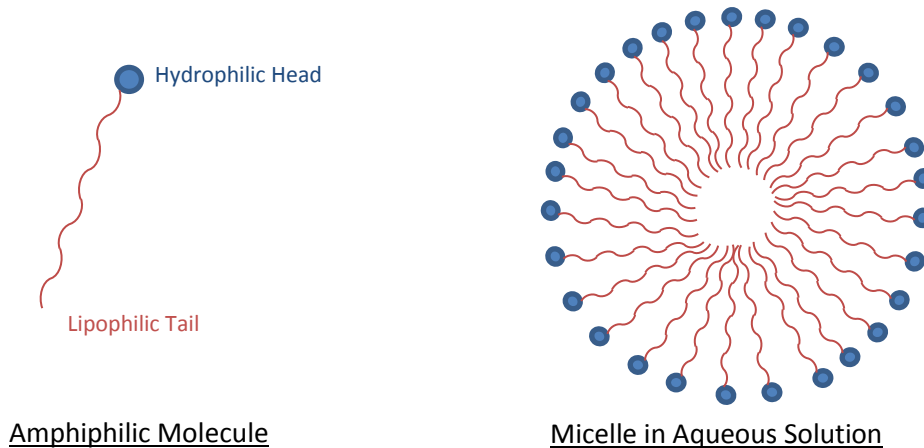


Figure 2.1 - Amphiphilic molecule and a micelle structure

Surfactants can be divided into three types according to the electric charge of the hydrophilic group: cationic, anionic or amphoteric (Fainerman et al., 2001). Charged surfactants can stabilize each other by electric repulsion from the neighbouring molecule charge. Moreover, large structured molecules can create a steric interference which can stabilize the drug and prevent precipitation. The combination of the mentioned two stabilization methods is also known as 'Electrosteric stabilization' (Tadros, 2005). Amphiphilic molecules are known to reduce surface tension of liquids, which can aid in dissolving bulk aggregated drug in aqueous solutions. When constructing a surfactant for drug stabilization, special care should be taken to ensure the uniformity of the solution created. Surfactants can also be used to decrease the rate of drug clearance from the blood through the phagocytic system (Karsa et al., 1996). Since surfactants are basically the building blocks for creating micelles, they are also often used in the creation of emulsions.

Emulsions are the liquid phase of colloids; therefore they can also be described as a mixture of two immiscible liquids (e.g. water and oil). Emulsions and micro-emulsions can be used to immerse hydrophobic drugs, e.g. Lidocaine, into aqueous solutions. Usually the drug is dissolved in an oil-based liquid and then added to the aqueous layer. In this case the oil creates droplets of drug in the water (Tadros, 2010). The main cause of unwanted separation of

emulsions is gravity. Because of the polarity and the surface tension of the droplets and the suspension, as well as the earth's gravity, the droplets may accumulate, causing creaming. To avoid this situation, large structured polymers, also known as thickeners, can be added. Gum based or high percentage oil in water emulsions are often used for dermal drug delivery. On the contrary, for parenteral delivery, the emulsion should have as low viscosity as possible to pass through the needle easily (Tadros, 2005).

The main limitations of emulsions are the cloudiness of the suspensions and their lack of stability and tendency to separation. Micro-emulsions on the other hand, do not face these difficulties and offer a more stable drug delivery method with a transparent appearance which is important for pharmaceutical applications (Lawrence and Rees, 2000).

2.2.2 Colloidal Carriers

Drug wrapping within individual carriers (Prodrugs) was developed as a technique for drug delivery in order to succeed where general administration failed (Kulkarni, 2010). Unfortunately, while solvent-based drug delivery provides a solution to the solubilisation of lipophilic drugs, it can assure neither triggered drug release nor targeting to a specific body location. Moreover, surfactants might disturb the binding of the drug to the needed receptor and alter its metabolic activity and there is also the concerning possibility of interaction between the surfactant and the cell membrane (Karsa et al., 1996). Today, there is an enormous range of drug carriers designed and manufactured worldwide. Because of the rapid development rate of science, particularly nanotechnology (Caruthers et al., 2007), new technologies for drug delivery constantly emerge. Most of these new technologies focus on the best functionalities of each delivery system. Therefore, it is becoming hard to describe the existing drug carriers under individual titles. What follows is a brief introduction to the popular types of drug carriers; it should be noted that today's research usually combines two or more of these methods to create the desired drug carrier.

Polymers The term polymer generally refers to high molecular weight (M_w) molecules, e.g. > 5 KDa, consisting of covalently bonded monomers. The size of the polymers usually depends on the number of repeated monomers. Polymers were developed early in the drug delivery field and can be used in various forms, e.g. to transform from liquid to gels (Tadwee et al., 2011). The basic structure of a polymer is a backbone with a drug covalently bonded or attached in another form, e.g. absorbed, a solubilizing moiety and a possible targeting group (Larson and Ghandehari, 2012). Polymers are considered to be a good drug delivery method for anticancer drugs. They can reach specifically into solid tumours due to the tumour extended vascular activity and increased endocytosis. Moreover, some polymers have

been shown to enhance the paracellular permeability of certain drugs within cancer cells (Thanou et al., 2007).

In drug delivery today, polymeric drug carriers describe a wide spectrum of chemically modified molecules containing biodegradable and non-biodegradable structures with an average size of 10 - 1000 nm (Torchilin, 2006). Such structures may include purely organic molecules or a combination of organic molecules with non-organic elements, e.g. conjugation of gold nanoparticles with polymers (Bergen et al., 2006). Furthermore, unique antibodies can be attached to polymers to guide the drugs to a specific location (Pasut and Veronese, 2007).

A well-known polymer often used in drug delivery is polyethylene glycol (PEG). PEG is a FDA-approved substance which can be combined with all types of drug carriers by either spherical encapsulation around the carrier or chemical conjugation to it (Greenwald et al., 2003). The combination of drug carriers with PEG has many benefits which depend on the individual needs of the designed carrier; e.g. it could prolong a certain carrier blood circulation time. PEG is present in all the commercially available drug carriers. Similarly to any chemical substance used in medical applications, there are pros and cons regarding the wide use of PEG in drug delivery, but at present it seems that the benefits PEG offers outweigh its disadvantages (Knop et al., 2010).

Micro-emulsions As previously explained, amphiphilic molecules can form micelles, Figure 2.1, and potentially carry drugs within them. The size of such micelles varies from 5 to 100 nm (Schäfer-Korting, 2010). Micelles are the essence of micro emulsions, and although they are mainly considered to be spherical in structure, as shown in Figure 2.1, they may have various structures such as tubes and hexagonal rods (Lawrence and Rees, 2000). The principle of drug delivery via micelles or micro-emulsions is similar to that of emulsions. Surfactants are normally used to stabilize micro-emulsions (Aboofazeli et al., 1994).

Despite the great potential of micro-emulsions to serve as drug carriers, there is a potential limitation concerned with their dissolution due to dilution (Owen et al., 2012). When introduced into large volumes of aqueous environment, e.g. the blood stream, they tend to separate and release the drug rather quickly, in order to maintain the ratio of water to surfactant. The dissociation rate depends on the critical micelle concentration (CMC); the point from which the surfactants become micelles (Narang et al., 2007). This fact allows optimisation of the rate of dissociation by pH, temperature and ionic charge. In general, anionic micro-micelles tend to dissolve faster than non-ionic ones, but this depends on the aqueous environment and surfactants chemistry.

In conclusion, micelles have the capability to serve as successful drug carriers and therefore to be of use for certain *in-vivo* applications (Julianto et al., 2000). Yet various parameters should be considered when using micro-emulsions for drug delivery, such as the difficulty to control the drug release, their major stability issues, and their cytotoxicity.

Liposomes Liposomes are spherical organic vesicles composed mostly of amphiphilic molecules in a lipid bilayer. The size of liposomes used in drug delivery varies from 80 - 1000 nm. The liposomes' lipid bilayer is somewhat similar to the cellular one and so there could be an interaction between the two (Mayer et al., 1986). The duality of the liposome composed of amphiphilic molecules offers the possibility for delivery of both lipophilic drugs, in the lipid layer, and hydrophilic drugs, in the core (Al-Jamal and Kostarelos, 2011). Most liposomes are eliminated from the blood by liver cells within 15 - 30 min after administration. The procedure of elimination is in correlation with the liposomes' size; the bigger the liposomes, the faster they will be removed (Harashima and Kiwada, 1996). Postponement of the liposome elimination from the blood circulation can be achieved by protective coating, e.g. PEG coating, as used clinically in Doxil[®]. Moreover, shell-protected liposomes can also have a targeting moiety that can aid in accumulation of the drug in the right location, e.g. the use of site-specific antigens integrated within the liposome or its coating (Juergen et al., 2012). The drug release from the liposome can be achieved by either a chemical reaction such as in pH change sensitive liposomes (Karanth and Murthy, 2007) or a physical method such as triggered release by US (Huang, 2006; Schroeder et al., 2009).

Additional Types of Drug Carrier As mentioned previously, a significant number of drug carriers and prodrugs is currently under development. Some of these novel carriers for drug transportation include DNA based vehicles (Bagalkot et al., 2006), colloidal gold nanoparticles (Paciotti et al., 2006), carbon nanotubes (Elhissi et al., 2012) and dendrimers, i.e. highly branched molecules (Gillies and Fréchet, 2005). The drug carriers presented here are just a fraction of the drug delivery vehicles investigated at various research levels worldwide and although many of them might never reach the market, the list of clinically approved prodrugs is constantly growing: a summary of FDA approved nanoparticles for cancer therapy can be found in Wang and Thanou (2010).

2.2.3 Cyclodextrins

CDs were first discovered in 1891 by the French scientist A. Villiers, who isolated them from starch which was digested by bacteria. After classifying the substance as dextrin, Villiers named it 'cellulosine', which was identified as β CD a decade later by the Austrian microbiologist, Franz Schardinger (Schmid, 1989). Schardinger distinguished between two

types of CD: α CD and β CD, which he had derived from potato starch using a microbe called *Bacillus Macerans*. In 1935, Freudenberg and Jacobi discovered γ CD. Together with Carmer and their co-workers they established γ CD physicochemical profiles, structural features and their capability to create various complexes with other substances (Brewster and Loftsson, 2007).

Up until the 1970s, although more types of CDs were discovered, there was an inability to manufacture substantial amounts of pure, affordable CDs. It was the advancement in the biotechnological field throughout the 1970s that brought a revolution in CD production. The ability to (almost) selectively create specific subtypes of CD became possible using CD glucosyltransferases (CGTases), starch converting enzymes (Maarel et al., 2002; Schmid, 1989). Currently, a purifying process in conjugation with those enzymes can produce significant quantities of highly pure (>99%) specific CD subtypes (Manakker et al, 2009).

2.2.3.1 Physicochemical Properties

Structural Features CDs, also known as cyclic oligosaccharides, are D-glucopyranose units linked by α -(1, 4)-glucosidic bonds (Figure 2.2) (Li et al., 2007). The number of the D-glucopyranose units, n , (Figure 2.2a) may vary from 6 (fewer do not exist because of steric interference) to 10 or more, although the latter are problematic to purify. Therefore the main CDs utilized are the 6 D-glucose units (α CD), 7 D-glucose units (β CD) and 8 D-glucose units (γ CD) (Singh et al., 2010).

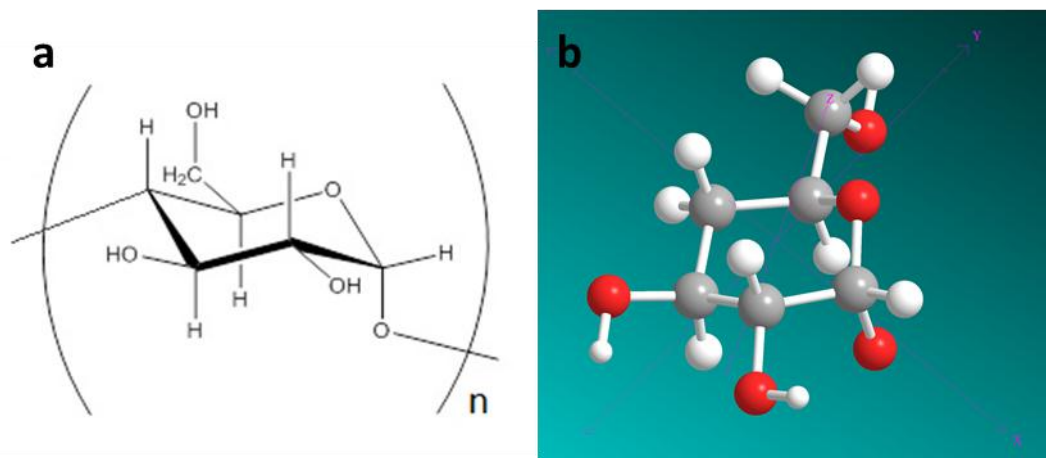


Figure 2.2- (a) Chair conformation of D-glucopyranose in a CD and (b) a 3D structure of a D-glucopyranose unit, where the atoms C,O,H marked with grey, red and white, respectively

The D-glucopyranose units in their chair conformation form a truncated cone. The hydroxyl groups are orientated to the outer surface of the cone, with the primary hydroxyls located on the narrow edge of the cone and the secondary hydroxyls on the wider edge (Tafazzoli and Ghias, 2009), as presented in Figure 2.3.

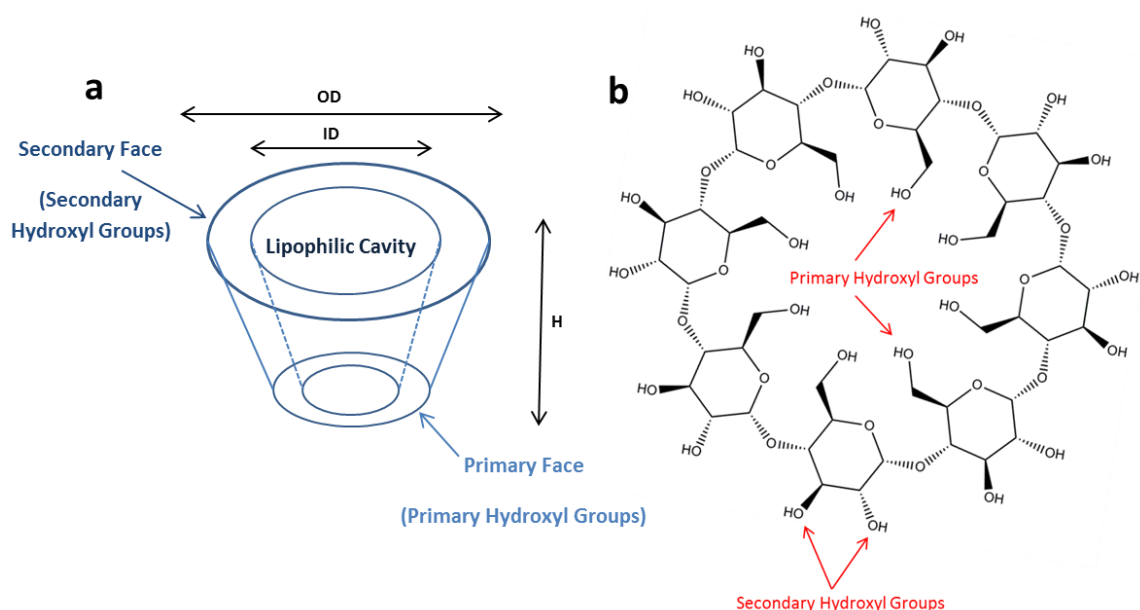


Figure 2.3- (a) Schematic representation of CD 3D conformation and (b) γ CD

This arrangement creates an inner cavity with a relatively lipophilic nature and an outer hydrophilic surface, which enables the CD to form complexes with hydrophobic drugs while simultaneously to be water-soluble (Bibby et al., 2000). A schematic representation of the truncated cone shape of CD is presented in Figure 2.3a. The size of the cavity and other dimensions of the natural, also referred to as 'parental', CDs are presented in Table 2.1.

Table 2.1- Dimensions of α -, β - and γ CD

CD Type	Number of Glucose Units	Dimensions (nm)		
		H	OD	ID
α -Cyclodextrin (α CD)	6	0.78	1.37	0.57
β -Cyclodextrin (β CD)	7	0.78	1.53	0.78
γ -Cyclodextrin (γ CD)	8	0.78	1.69	0.95

As can be seen in Table 2.1, the height of the CD remains the same and only the cavity size enlarges with addition of glucose units.

Solubility & Stability Despite the fact that parental CDs possess hydroxyl groups located on the outer surface of the cone, they have relatively poor solubility in water. Therefore, introducing a CD with a drug in an aqueous solution may result in a solid precipitation of the CD-drug complex (Loftsson and Brewster, 1996).

Table 2.2- Water solubility characteristics of α -, β - and γ CD

Characteristics/ CD	α	β	γ
No. of Glucopyranose Units	6	7	8
Molecular Weight (M_w)	972	1135	1297
Water Solubility at 25 °C (g/100 mL)	14.5	1.85	23.2

Table 2.2 shows that β CD has a particularly low solubility. A possible explanation is that the secondary OH groups form intramolecular hydrogen bonds, reducing their ability to react with the water molecules. This phenomenon usually occurs in CDs with non-even numbers of D-glucose units (Zhou and Ritte, 2010). A remarkable increase in the solubility can be achieved by replacing any of the hydroxyl groups, even with hydrophobic functions, in order to reduce the intramolecular hydrogen bonds. Nevertheless, the substitution degree should be carefully considered as it may cause a steric hindrance which can subsequently prevent the creation of complexes (Frömming and Szejtli, 1993). It can also be noticed that γ CD, Figure 2.3b, has the highest water solubility factor among the CDs, which makes it the most potentially valuable natural CD for drug encapsulation.

Although, in alkaline solutions, the CDs' glycosidic bonds are quite stable, strong acids will hydrolytically cleave those bonds, resulting in linear oligosaccharides. The ring-opening ratio due to such hydrolysis is proportional to the CD's cavity size, therefore it will increase with larger cavity sizes (α CD < β CD < γ CD). Various factors can decelerate the ring-opening rate; e.g. adding guest molecules to β CD inhibits the access of the oxonium ions to the glycosidic bonds. Against enzymatic hydrolysis, by substituting the hydroxyl groups in the CD, it is possible to slow down the degradation process (Uekama et al., 1998).

2.2.3.2 Biocompatibility

The proven high stability of hydroxypropyl- β CD (HP- β CD) against enzymatic hydrolysis indicates that it will not be significantly degraded by the body's metabolism (Szente and Szejtli, 1999). The same is true for natural α CD and β CD. These are not hydrolyzed in the blood flow or in the metabolic system of rats, dogs or humans, and are excreted unaltered in the urine (Brewster and Loftsson, 2007). Unlike β CD and α CD, γ CD is hydrolyzed by the human pancreatic and salivary α -amylase because of its larger cavity (Uekama et al., 1998).

From the toxicological point, all of the CD subtypes are generally defined as non-toxic and are widely used in pharmaceutical applications by various administration routes, as well as in the food and cosmetics industries (Bilensoy, 2011).

2.2.3.3 Cyclodextrin Inclusion Complexes

The CD's notable ability to form complexes has been widely recognized and investigated since 1980 and continues today. In principle, CDs are able to form inclusion complexes with practically any type of molecule (Dodziuk, 2006). The possibilities vary from natural or ionic organic/inorganic compounds up to noble gases. The only condition for such interaction is the guest's ability to fit inside the CD's cavity, even just partially (Li and Purdy, 1992). A 1:1 complex formation is represented in Figure 2.4.

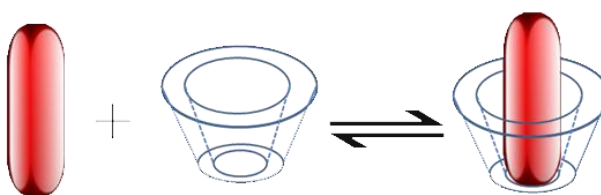


Figure 2.4- Illustration of 1:1 inclusion complex of a guest molecule in a CD

According to Vyas et al. (2008), there are some suggested parameters that can indicate if a certain molecule is suitable for encapsulation within a CD:

- The backbone of the molecule consists of at least 5 atoms (mostly C, N, S and P).
- The melting point of the molecule is below 250°C.
- The molecule should have no more than 5 aromatic rings.
- The solubility of the guest molecule in H₂O is less than 10 mg/ml.
- The Mw of the guest molecule should be preferably between 100 and 400 g/mol.

Although these are practical guidelines for choosing a possible guest molecule, these conditions often change for specific cases and have many exceptions (Dick et al., 1992).

The main driving force behind the creation of the CD-based complexes is the displacement of the water molecules, with relatively high enthalpy, from the CDs cavity, with a more preferable, less polar, guest molecule (Szejtli, 1989).

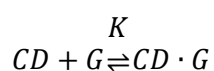
Factors Influencing Formation and Stability of Inclusion Complexes There are four main factors that can determine the stability of a created complex:

- The geometric capability: This is by far the most critical influencing factor. Although it is possible for a CD to form a complex with a significantly larger guest than the cavity size, it will only bind to a certain group or a side chain whilst overly small molecules will pass through the cavity, resulting in no bonding at all (Zhou and Ritte, 2010).

- The polarity of the guest molecule: In order to form a complex with a CD, the guest molecule must have a hydrophobic tendency. Moreover, there is a linear correlation between the guest's hydrophobic character and the stability of the complex created, resulting in hydrophilic guest molecules creating weak complexes or none at all.
- The medium: Although the formation of these complexes is possible in solution or in the crystalline state, it is most commonly carried out in a water solution.
- The temperature: There is an inverse correlation between temperature and the formation of the complex: an increase in temperature will decrease the stability of the complex (Liu and Purdy, 1992).

Determination of Binding Constant When complexation occurs between CDs and different guest molecules, many types of complexes can be created. Even if the molecular ratio between the CD and the guest is 1:1 (1 molecule of CD: 1 guest molecule), the resulting complex can be 1:2; 2:2; 2:1 and even higher (Arun et al., 2008). The variation in the order of the complexation is dependent on many features of the guest molecule, such as the structure, stereochemistry and polarity, and its interaction with the specific CD in use. The most commonly investigated interaction, and the one investigated in the present work, is the 1:1 inclusion ratio (Szejtli, 1998; Davis and Brewster, 2004).

The formation of a guest (G) and CD complex (CD·G), in 1:1 binding ratio, can be described by the following equilibrium:



Equation 2.1- Complex equilibrium

The equilibrium constant (K) is defined by Equation 2.2:

$$K = \frac{[CD \cdot G]}{[CD][G]}$$

Equation 2.2- Equilibrium constant calculation

When considering a poorly soluble guest molecule, with intrinsic solubility G_0 , for complexation within the CD, a typical manner of studying the solubility behaviour of the created inclusion complexes is by the phase-solubility approach (Kurkov et al., 2011), as presented in Figure 2.5.

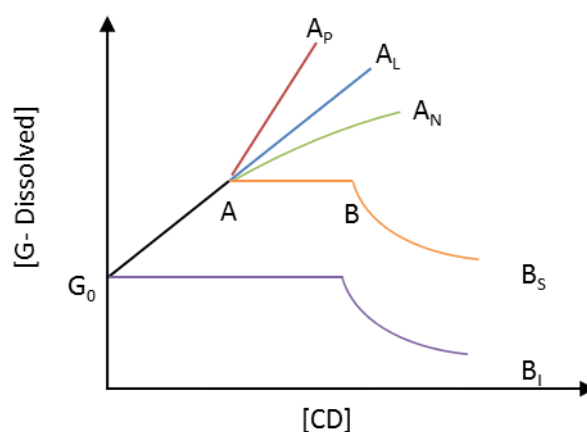


Figure 2.5- Diagram of phase solubility behaviour

This schematic representation of the guest molecule solubility, free and encapsulated guest i.e. $G_0 + G \cdot CD$, as a function of the CD concentration is achieved by introducing increasing concentrations of CD to a high excess constant amount of the guest. The solubility of a guest molecule as shown can be divided into two types, referred to as 'Type A' and 'Type B' (Szejtli, 1989). Type A indicates that the created complex is soluble and Type B clearly represents low solubility inclusion complexes.

The solubility behaviour of 'Type A' has three common trends: A_L , A_P and A_N . In the case of A_L , there is a linear correlation between the amount of CD added and the solubility of the guest molecule. This can be represented by:

$$G_{Total} = G_0 + \frac{KG_0[CD_{Total}]}{KG_0 + 1}$$

Equation 2.3- A_L solubility equation

where G_0 is the intrinsic solubility of the guest molecule (no CD added), G_{Total} is the guest total solubility, and $[CD_{Total}]$ is the total concentration of CD added. This equation shows that a rise in the CD concentration will result in greater solubilisation of the guest, where the slope of such growth is:

$$Slope = \frac{KG_0}{KG_0 + 1}$$

Equation 2.4- Slope of A_L

Therefore the influencing factors on the guest solubility are the guest's intrinsic solubility (G_0), the equilibrium constant (K) and the concentration of the added CD ($[CD_{Total}]$).

In the case of A_p , at higher concentrations of CD the solubility of the guest will be greater than linear, usually as a result of a higher order complex creation such as $G \cdot CD_2$, $G \cdot CD_3$ etc. (Brewster and Loftsson, 2007). In the final case, A_n , at higher concentrations of CD the solubility of the guest will increase in a lower rate. This may occur for various reasons, e.g. changes in the characteristics of the solution or the formation of CD-CD complexes (Dell Vale, 2004; Davis and Brewster, 2004).

The solubility behaviour of 'Type B' has two common trends: B_s and B_i . In the B_s trend, the complexes created have limited solubility. At first there is a linear increase in the guest solubility (up to point A) at which the guest creates a complex with the CD resulting in a solution of both G_0 and the created complex $CD \cdot G$. The complex created with the CD added after point A precipitates. Due to equilibrium, while the complex precipitates, free guest molecules dissolve (according to their G_0). Hence, the concentration of the guest in solution remains the same between points A and B. At point B, when there are no free guest molecules in the solid state, the remaining complexes precipitate as well. In the B_i trend, the complexes created are insoluble. Since the complexes create precipitates, the concentration of dissolved guest in the solution remains G_0 at a plateau phase until there are no free guest molecules left in the solid state (Kurkov et al., 2011).

Dissociation of Drugs from Inclusion Complexes CD-based complexes are very stable in their dried form, with long shelf life. Once the complex is introduced back into water, the various activation forces in the CD inclusion formation reappear. In the aqueous solution many factors can influence the formation (and hence the dissociation) of complexes, examples include hydrogen bonding with the hydroxyl groups and thermodynamic considerations. However, the main binding criterion between the CD and its guest is considered to be van der Waals/ hydrophobic interactions (Arun et al., 2008). Accordingly, there is no covalent bonding between the CD and the guest molecule, meaning that the host-guest complex is in a constant dynamic equilibrium state (Rozou et al., 2005). Due to the rapidity of the transit between association and dissociation of complexes, this equilibrium is considered to be a 'rapid equilibrium', with the most significant *in-vivo* dissociation factor of the CD-guest complex being dilution (Stella and Quanren, 2008).

2.2.3.4 Cyclodextrins in Pharmacology and Drug Delivery

As previously stated, there are numerous applications for CDs and the inclusion complexes they create. Although, in this work, the main focus is on their pharmaceutical exploitation, they are currently widely used in the food and beverage, cosmetics and chemical industries (Boer et al., 2000).

Control of Drugs Solubility The major reason for creating CD-based complexes is their ability to increase the solubility of guest molecules. As demonstrated in Figure 2.5, the increase in solubility of a guest molecule can be determined using phase-solubility analysis. The mentioned increase in solubility can usually be described as linear. In addition to the toxicological benefit, this gives the CDs an advantage over organic solvents. Organic solvents often behave in a log-linear way; therefore, the complex might precipitate once introduced into an aqueous solution (Brewster and Loftsson, 2007; Davis and Higson, 2011). The increased solubility as a result of the complexation can enable a certain drug to become suitable for parenteral administration or enhance its oral bioavailability. The latter is specifically applicable to class II drugs (insoluble yet permeable through the gastrointestinal tract (GIT)), as defined by the Biopharmaceutical Classification System (BCS) (Davis and Brewster, 2004).

In-Situ Drug Release from CD-Based Complexes As mentioned previously the main dissociation factor of the CD-drug complex is dilution. This factor is extremely important when discussing the stability of encapsulated drugs *in vivo*. Relatively small amounts of drugs encapsulated in CDs, with $K < 1 \times 10^5 \text{ M}^{-1}$, will be completely dissolved in the human body, e.g. 1 ml injected in a 70 kg subject will result in about a 1: 4,200 dilution factor considering only the extracellular water, being about 30% of the body weight (Stella and Rajewski, 1997).

After administration other factors can contribute to the drug release. Such factors include binding of the drug to various proteins, competitive displacement of the drug, and drug uptake into the tissues. These processes can all result in an equilibrium shift towards the dissociation of the complex, according to Equation 2.1. However, in certain circumstances one may desire to keep the drug encapsulated. A good example is in application of encapsulated drugs in muscle (IM) or subcutaneously (SC) when an unwanted precipitation of the drug can result in tissue damage. A possible solution is the utilization of chemically modified CDs, such as sulphobutyl ether β CD (SBE- β CD) (Stella and Quanren, 2008). Through chemical modifications it is possible to control the time and location of the drug release from encapsulation. A description of the modifications needed as a function of the time and release location can be found in Uekama et al. (2006).

Stabilization of Drugs CDs may greatly improve the stability of various molecules via the complexation process. It has been proven that CDs not only stabilize a lipophilic drug in an aqueous environment, but can also stabilize it in the solid state and hence create a complex that can be orally administered (Terao et al., 2006). CDs are not only able to physically stabilize the guests by inhibition of crystal growth, but also to suppress the guest's chemical reactivity (Davis and Higson, 2011).

Directing of Physical and Chemical Reactions The complexation ability of CDs can be utilized in directing chemical reactions. One example is selectively protecting functional groups on molecules in order to perform regioselective reactions (Breslow, 1980). Inclusion complexes are also able to translate liquid or oily compounds into a crystalline form. For example, the combination of CDs with greasy coffee aroma concentrates creates a stable complex in the microcrystalline form, which can be then be added to instant coffee products (Cabral Marques, 2010). Another controllable parameter available to manoeuvre chemical reactions is the ability of the CD to accelerate or decelerate the reactivity of a guest molecule, as a result of the complex creation. Usually, in complexes where the functional group of the guest molecule is located inside the CD's cavity, it will result in an inhibition effect. However, if the active moiety is partially or fully outside the cavity, acceleration may occur.

Reduction of Volatility An important application of CD-based complexes is the reduction of volatility of different compounds. The formed inclusion complex can stabilize highly volatile substances, and increase their boiling point in a solution (sublimation point in the solid state). Moreover complexation with CD can transform volatile liquids into stable solid crystals (Szejtli, 1985). This function is especially useful in the food and cosmetic industries, where it is used to preserve flavours, colours, aromas and vitamins during storage periods, which later can be released upon contact with water (Astray et al., 2009).

Masking of Organoleptic Properties of Drugs A further application of the CD inclusion complexes is the ability to mask odours and tastes of different substances. The modification or elimination of certain tastes and odours can be achieved at low temperatures and at high concentrations of CD. The possibility to mask drug odour or bitterness without altering its functionality is of great interest, especially in orally administered drugs. Recent clinical studies proved reduction in the bitterness of antihistaminic drugs using β CDs (Ono et al., 2011).

2.3 Targeted Drug Delivery

The delivery of drugs into a specific location within the body refers not only to the arrival of the drug close to a certain organ, but also to its penetration into the cells or even into their nuclei. In order to design a drug delivery vehicle, the mechanisms of drug absorption *in situ* must be thoroughly understood.

Drug penetration within cells usually occurs through binding receptors on the surface of the cell. Hence the amount of absorbed drug is proportional to the amount of drug bound to receptors (Golan et al., 2008). Once the drug has entered the cell, it can alter various

processes to cause cell destruction. Such processes include changes related to mRNA creation and degradation or/and alteration of various enzymatic behaviours. More on cell structure and behaviour in the presence of various substances can be found in Lu and Øie (2004).

2.3.1 Targeting Principles

The methodology of targeting drugs within the human body can be divided into three main pathways as follows: directing of the drug via chemical modification, e.g. encapsulation within a drug carrier with a targeting function; application of an external stimulus, e.g. hyperthermia, magnetophoresis, *in-situ* injection etc.; and the combination of the two methods, e.g. US triggered drug release from liposomes, thermal application to heat-sensitive nanocarriers etc. (Tadwee et al., 2011). While this chapter mainly focuses on the chemical approach of TDD as a general background for the chemical and biological work, the mechanisms of TDD via US and the effects of US on cell membrane, together with current research in USmTDD, are reported in Chapter 5.

2.3.2 Targeting Moieties

Drug targeting with pharmaceutical carriers which can survive long enough in the blood circulation to reach the target region, can be achieved via the following mechanisms (Schäfer-Korting, 2010):

- Passive diffusion by spontaneous penetration into the cells
- *In-situ* drug release due to environmental changes (pH, temperature etc.)
- Targeting ligands (antigens, proteins)

When designing drug carriers, there are various targeting possibilities to choose from. The decisive parameters for the delivery method are determined by the nature of the targeted region.

2.3.3 Cyclodextrins in Targeted Drug Delivery

The proven advantage of CDs over traditional drug systems such as co-solvents and surfactants is that the pharmacokinetics (P_K) and pharmacodynamics (P_D) of the encapsulated drug generally remain unaltered due to complexation (Stella et al., 1999).

CDs, in their nature, are not capable of crossing cell membranes easily and their effect on membrane permeability highly depends on the composition of the membrane barrier and the properties of the encapsulated drug (Loftsson et al., 2007). This must be taken into consideration when designing a CD-based drug vehicle as the complex formation can potentially aid in delivery of drugs to the cells by manipulation of the aqueous diffusion

barriers or obstruct the absorption of drugs through lipophilic membrane barriers (Rasheed et al., 2008). In addition, CD complexes can enhance drug availability in specific locations by re-complexation with competing agents from the cell components and so releasing high doses of drugs only *in situ*, which results in a promising TDD vehicle (Uekama, 2006).

2.3.3.1 Routes of Administration

CDs can be administered into the body by most of the conventional drug delivery routes. Full explanations on drug absorption mechanisms and *in-situ* drug activation within each organ, via all administration routes presented here can be found in Jain (2008).

Oral Drug Delivery The utilization of CDs in oral drug delivery has dual benefits: the improvements of the drug characteristics due to complexation, e.g. bioavailability, solubility, stability etc. and the possibility of taste/ odour masking (Brouwers et al., 2008; Terao et al., 2006). The complex created with CDs often acts like a shield with the purpose of carrying the drug to the target location. Once the target is reached, the released drug penetrates the biomembranes. Moreover, CDs can aid in the creation of stable tablets for oral administration of oily drugs (Motoyama et al., 2009). The CD is considered to be non-toxic for oral administration; especially due to the CD's low penetration ability through the GIT (Moses et al., 1999). CDs can be used not only to deliver therapeutic drugs orally but also lipophilic vitamins with relatively low bioavailability, as was shown for vitamin E *in vivo* by Miyoshi et al. (2011).

Parenteral Drug Delivery The major release mechanism in parenteral administration of drugs encapsulated by CD is dilution. As previously discussed, when introducing the complex into the blood stream, it is likely to dissociate due to the high dilution factor. In addition, the drug can also dissociate from the CD due to the CD encapsulation of competing agents and covalent binding to proteins or functional groups (Stella et al., 1999). The most commonly used CDs in parenteral drug delivery are HP- β CD and SBE- β CD, which are considered non-toxic with high aqueous solubility.

The main benefits from the usage of CDs in parenteral drug delivery are solubilisation and stabilization of drugs in an aqueous environment. Moreover, they can be used to minimize irritation that may be caused by the drug at the administration location (Challa et al., 2005).

Ocular Delivery Similar to the parenteral administration, the HP- β CD and SBE- β CD show great potential in ocular drug delivery. The main reason is that they are well tolerated in aqueous eye drop solutions. Beyond the usual utilization of CDs in enhancement of drug solubility and stability, in ocular administration they are used to reduce the drug irritation and to enhance its permeability.

In ocular drug delivery, it is crucial for both the drug and the potential delivery vehicle to be non-irritating to the ocular surface. This will avoid rapid washout of the drug due to tearing and blinking reflexes (Davies, 2000). The key difficulty in ocular drug administration is the maintenance of large drug amounts. A possible solution was suggested through gel administration but was rejected in the clinical phase due to patient dissatisfaction. Consequently, eye drops remain the most acceptable form of ocular drug delivery. CDs do not penetrate the ocular biological membranes; therefore they can enhance the uptake of ophthalmic drugs by keeping them in solution on the eye surface. As dilution usually does not occur in the precorneal area, the dissociation factors are the displacement of the drug by the precorneal liquids and the binding and absorption of the drug by the ocular tissues (Stella and Rajewski, 1997).

Nasal Drug Delivery Regarding nasal drug delivery, one should always assess the possible impacts of the drugs on the mucociliary system. CDs are proven to be clinically non-toxic in nasal drug formulation, making them useful drug carriers in nasal delivery. The absorption of the drug is improved by the CD's ability to open tight junctions and enhance the cell membrane permeability (Pires et al., 2009). CDs can also be used in conjunction with other drug enhancers or can be coupled with other polymers. A recent *in-vivo* study presented a novel delivery method for insulin via nasal administration using a HPG-conjugated CD (Zhang et al., 2011).

Rectal Drug Delivery The main benefit from CD-based rectal drug delivery is the enhancement of drug release from the suppository base. This enhancement occurs because the complex created between a lipophilic drug and the hydrophilic CD is not soluble in the suppository base. This leads not only to enhancement of drug uptake from the melted vehicle, but also to inhibition of the reverse diffusion into the base. The influencing factors on CD-enhanced rectal drug diffusion are mainly the partition coefficient of the drug and the complexes' stability constant. Accordingly, three important facts must be noted: firstly, there might be no effect on the drug release if the complex dissociates in the suppository base; secondly, the partition coefficient of the CD-drug complex is highly significant as part of the drug might be absorbed while still in complex; and thirdly, once the CD-drug complex is released from the suppository base, it usually dissociates leaving a free drug for absorption (Matsuda and Arima, 1999; Challa et al., 2005).

Rectal drug delivery based on CD complexes has been studied for its promising ability to enhance morphine drug uptake from the suppository base, an extremely important clinical need in advanced cancer patients. While the release rate of the drug from the suppository

base was not greatly influenced, the CD increased the morphine permeability into the mucosal membrane (Rajewski and Stella, 1996; Uekama et al., 1998).

Dermal Drug Delivery In dermal drug delivery, CD-based complexes can sustain the drug release from solution; improve the drug stability/solubility; increase the absorbance *in situ* due to enhancement of membrane permeability of the skin cells, e.g. increase in the diffusion into the stratum corneum; and lower the side effects such as irritation. By enhancing the thermodynamic activity of drugs within the vehicle, the CD can increase the drug release rate. A dual advantage of CD-based dermal drug delivery can be achieved by enhancement of drug uptake *in situ*, e.g. drug release due to displacement of the drug by components of an ointment-based vehicle, while decreasing irritation effects caused by application of the free drug (Matsuda and Arima, 1999). Although, typically, CDs cannot penetrate biological membranes, in their free form they may interact with some compounds of the skin (Loftsson et al., 2007). This intriguing feature allows the CDs to remove some parts of the membrane and thereby to increase the local absorption of drugs, especially hydrophilic ones.

Currently CDs are used for dermal administration of anti-aging and anti-wrinkle substances. The complexation of CDs in anti-aging creams is done in order to protect the active substances from oxidation and for controlled release (Buschmann and Schollmeyer, 2002).

Colon Specific Drug Delivery In the case of colon-specific drug delivery, the equilibrium of the CD-drug complex is regarded as a disadvantage. The nominal dissociation rate of drugs from CDs is not compatible with the extended time it takes a drug to reach the colon by oral administration, i.e. about 8 h in humans, which indicates a different approach should be adopted. The suggested solution is to bind the CD covalently to the drug, rather than creating an inclusion complex (Hirayama and Uekama, 1999). It is well known that CDs are rarely affected by hydrolysis in the stomach and the small intestine, meaning they will be enzymatically degraded specifically in the colon (Uekama, 2004). A prodrug for colon-specific drug delivery is based on the conjugation between a drug and a CD by an ester or amide linkage on one of the CDs' primary hydroxyl groups.

Protein & Gene Delivery Absorption difficulties through the biological membranes, unstable chemical structures and fast disposal by the plasma are just some of the reasons that make peptide and protein drug delivery extremely difficult. CDs are able to enhance intracellular absorption of peptides and protein by lowering the cells' barrier function (Vyas, et al., 2008). In addition, their relatively non-toxic nature offers a potential approach for peptide, protein and gene delivery (Kihara, 2003). Although CDs are able to identify the structural features of amino acids, proteins may be too big to be included in the CD's cavity, meaning

only parts or side-chains will be encapsulated. Nonetheless, this is enough to stabilize and solubilize certain peptides and proteins, e.g. growth hormones. An additional option for protein and gene delivery via CD-based complexes is with CD-conjugated supramolecular hydrogels (Li and Loh, 2008). Other applications of CDs involve triggering folding and re-folding of proteins, inhibition of efflux pumps, and interactions with the membranes in the nasal epithelium in order to enhance drug absorbance (Huang et al., 2010).

The many difficulties in chronic therapy with peptide and protein-based drugs can cause major discomfort to the patients, e.g. daily injections. Controlled release of drugs over a certain time period offers a possible solution. One example is the combination of CDs with injectable oil-based suspensions. CDs offer an alternative to limited cell membrane penetration of viral based gene and oligonucleotides (ONs). Moreover, the CD is also able to inhibit the ON's degradation by endonucleases. Both neutral and charged CDs are used in development of novel gene delivery mechanisms (Davis, 2009).

Brain Drug Delivery Because of the blood brain barrier (BBB), it is hard to deliver drugs to the brain. One of the methods to overcome this is by conjugating the active drugs with highly lipophilic prodrugs. CDs are used in this situation as a solubilizing agent for the lipophilic prodrugs. Moreover, when utilising CDs for solubilisation of lipophilic prodrugs, it allows the possibility of combining two or more types of drug in one treatment (Hirayama and Uekama, 1999).

2.4 Ultrasound

2.4.1 Principles of Ultrasound

Although ultrasound (US) has been in practical use only over the past century, its theoretical principles can be traced to the 6th century BC. The first practical application for US is known as SONAR (SOund Navigation And Ranging) and its idea emerged a hundred years ago with the sinking of Titanic in 1912 (Szabo, 2004). The possibility of knowing the location of underwater icebergs, and later on submarines, was so stimulating that by the end of WWI the first hydrophone was created. The technology in use was mainly based on the 'The Theory of Sound' by Lord Rayleigh (1877) and the discovery of piezoelectric materials to generate and detect US waves by the Curie brothers in 1880. Within a few decades US had found various additional applications, such as sonochemistry and medicine (Luque de Castro and Capote, 2007) and by the nineteen forties the commonly used ultrasonic device was invented - the diagnostic US imaging system. Since then, US has been broadly in use in medical environments for both diagnosis and therapy (National Academy of Sciences, 2003).

US can be defined as a pressure wave propagating through a medium. These waves create what is referred to as an 'acoustic field' (Azhari, 2010). The 'ultra' prefix in US refers to the frequency of the wave, which in this case is above the human hearing threshold (>20 kHz). The frequency of an ultrasonic wave can be defined as the velocity of the sound divided by the wavelength, which is temperature dependent. The effect of US waves on the surrounding environment, i.e. the propagation of US, results in compression at the high pressure points and rarefaction at low pressure points (Seegenschmiedt et al, 1995). This occurs due to shifting of the particles under the application of US from their equilibrium positions. Therefore, the propagation of the acoustic field depends on the elasticity of the medium it is propagating through. Full equations for homogenous and inhomogeneous environments are given in Section 2.4.2.

US can be generated and detected by a piezoelectric material, most commonly crystal or ceramic. The deformation of the material due to an electric field produces pressure waves that are distributed in the surrounding media and, *vice versa*, where under a mechanical force the piezoelectric material produces electrical voltage (Jaffe and Berlincourt, 1965). The piezoelectric principle lies in the presence of dipoles. The net dipole moment of a specific non-conductive material is altered due to applied mechanical force. This change results in a charge density difference that can then be measured.

Ultrasonic waves can be directed in order to create a focused beam (Zanelli et al., 1993). Focused ultrasonic fields are implemented in various devices, partially in diagnostic US but mainly in therapeutic applications (see Section 2.4.4.2). The most common methods to create focused beams are either via a bowl-shaped transducer or with a phased array. The principle of focusing acoustic waves is similar to optical focusing by lenses. The spherical shell resembles the optical lens when a ray of light is passing through it (Mueller and Adam, 2012). Due to lens geometry, at a specific distance a focus will occur. The same is true for an acoustic field created by a curved piezoelectric bowl (Huo and Chen, 2001). The shape of the focus is an ellipsoid structure, usually described as a ‘cigar shape’.

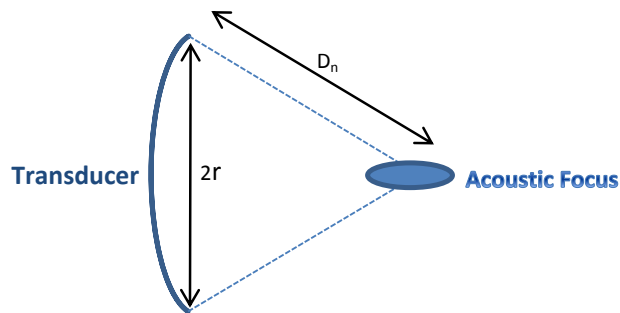


Figure 2.6- Focusing of acoustic waves

The intensity at the focal point can be represented by

$$I_R = I_0 \cdot \left(\frac{2 \cdot \pi \cdot r^2}{\lambda \cdot D_n} \right)^2$$

Equation 2.5- Intensity at focal point

where I_0 represents the transducer's surface average intensity, r is the flat radius of the transducer and D_n is the natural focal distance (Figure 2.6). According to Equation 2.5 the intensity at the focal point is in inverse correlation to the wavelength (λ), and therefore it is also dependent on the frequency (Duck et al., 1998).

A phased array transducer is a more complicated device which consists of many small ultrasonic elements that need to be coherently driven in order to create a focus (Bai et-al., 2009). Such a transducer can be spherically shaped similar to a single element bowl transducer; this way, it will have a natural focus, but the multiple transmitting elements also allow flat surface geometry. The great benefits of using a relatively high number of focusing elements are the variability in the focal distance and the possibility of creating multi-focal patterns (Hertzberg et al., 2010). Both of these benefits are important in the present work.

2.4.2 Ultrasound in Materials: Properties of Ultrasound Propagation

2.4.2.1 Acoustic Fields in Homogenous Environments

As mentioned previously there is a correlation between the type of the medium and the velocity of the sound wave propagation (c [m/s]). Moreover, c is also dependent on the state of matter and the temperature. In gas, the velocity of sound increases as a function of temperature; in ideal gases, the rise is approximately $60 \text{ cm}/(\text{sec}\cdot^\circ\text{C})$. On the other hand, in liquids, there is an inverse correlation between the temperature and c , with a decrease of about $2 - 6 \text{ m/s}\cdot^\circ\text{C}$. It should be noticed that c in gas is about one order of magnitude lower than in liquids, e.g. c_{Nitrogen} in its gas form (20°C) $\approx 351 \text{ m/s}$ while in the liquid form (-197°C) $c_{\text{Nitrogen}} \approx 869 \text{ m/s}$. In other words, there is an increase in c according to $c_{\text{gas}} < c_{\text{liquid}} < c_{\text{solid}}$ (Shutilov, 1988).

The dependence on temperature as described previously is true for most liquids, except water and some liquid metals. H_2O is well known for its anomaly, and in this case it is expressed by a nonlinear relation between temperature and the sound velocity. This behaviour is presented in Figure 2.7, in comparison with standard behaviour of liquids.

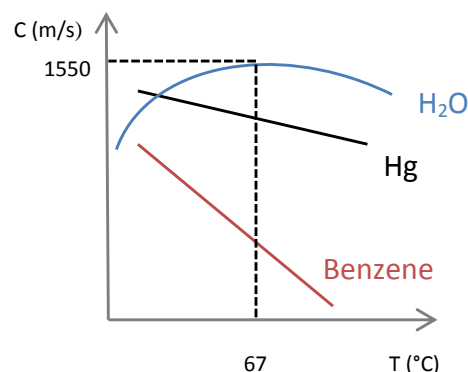


Figure 2.7- Schematic representation of sound velocity in different liquids

As presented in Figure 2.7 there is a rise in c of about $2.5 \text{ m}/(\text{sec}\cdot^\circ\text{C})$ up until the maximum at 67°C at which $c = 1550 \text{ m/s}$. After reaching the maximum, the dependence on the temperature reverses and decreases as in the rest of the liquids.

The Acoustic Wave Equation The general acoustic wave equation can be represented by

$$\Delta\Psi = \left(\frac{1}{c^2}\right) \cdot \left(\frac{\partial^2\Psi}{\partial t^2}\right)$$

Equation 2.6- General acoustic wave equation

where Δ is the Laplace operator (second order differential operator), ψ is the wave function and t is the time (Azhari, 2010).

In homogenous environments the wave function can be described as a harmonic sinusoidal wave:

$$\psi_{(x,t)} = \psi_{max} \cdot \sin(\omega t - kx)$$

Equation 2.7- Sinusoidal wave equation

where ψ_{max} is the amplitude of the wave, $\omega = 2\pi f$ is the angular frequency, where f is the oscillation frequency, $k = \omega/c$ is the wave number, and x is the distance the wave has travelled. Most of the theoretical and mathematical models describing waves, e.g. Equation 2.6 and Equation 2.7 refer to a one dimensional planar propagating wave. In practice, this is only partially correct for gas and liquid and especially solids, where shear waves may occur (Szabo, 2004).

Acoustic Field of a Phased Array Focused Beam As previously mentioned, a phased array transducer consists of many elements that, by manipulation of their transmission phase, can create a focused acoustic beam (Yu et-al., 2011). The acoustic beam created equals the superposition of the acoustic wave created from each element, e^{ikx} or $\sin(kx)$, where x is the distance from the element to the focal point. This can be calculated by the Rayleigh-Sommerfeld integral (Ebbini and Cain, 1989). Exact calculations for the phased array transducers in use in the present work can be found in Hertzberg et al. (2010).

2.4.2.2 Acoustic Fields in Inhomogeneous Environments

Although the model of an homogenous environment represents well the physical principles of US, many materials, including the human body, are inhomogeneous; therefore the mathematical and physical assumptions must be adjusted. While in an acoustically transparent medium, such as water, there is almost no attenuation of the acoustic field, in a body, not only is the energy partially absorbed, but it is also scattered and reflected (Laugier and Haiat, 2011). There is a wide range of scattering surfaces in the body, from as small as the nucleus within an individual cell up to the margins of the organs (Webb, 1988). The interface of ultrasonic waves with boundaries, i.e. sudden changes in the medium, is governed by acoustic impedance, Z , whose principles can be derived from Snell's law. According to Snell's law, when a wave is incident on a surface, it is partially transmitted and partially reflected, as illustrated in Figure 2.8.

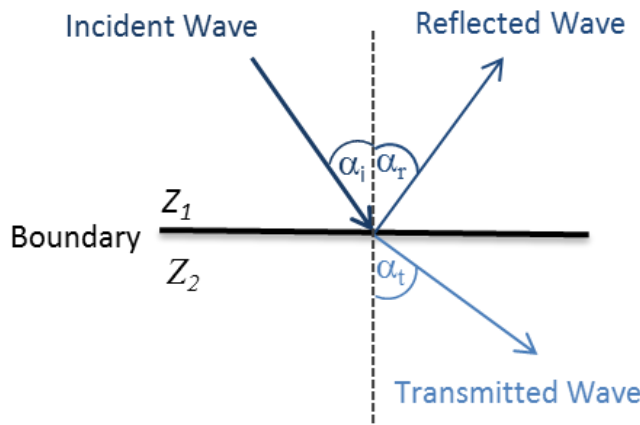


Figure 2.8- Snell's law

This reflection may occur even within the same tissue due to inhomogeneity on a microscale. The reflection, mostly known as scatter reflection, may contribute to measurable amplitudes of acoustic wave, causing interference (Suetens, 2002). Z can also be derived from the density of the medium, ρ_0 , and c according to

$$Z = \rho_0 \cdot c$$

Equation 2.8- Acoustic impedance

Once Z is known, it is possible to calculate the ratio between the transmitted, T_i , and reflected, R_i , wave's intensity travelling between different media (Seegenschmiedt et al, 1995). R is defined by

$$R_i = \left(\frac{Z_2 \cdot \cos \alpha_i - Z_1 \cdot \cos \alpha_t}{Z_2 \cdot \cos \alpha_i + Z_1 \cdot \cos \alpha_t} \right)^2 = 1 - T_i$$

Equation 2.9- Reflection coefficient

where the various symbols are defined in Figure 2.8. The described reflection of the acoustic waves from boundaries can also create standing waves. Standing waves occur in a specific case where the reflected waves are exactly in the same phase as the incident wave, resulting in an increase in the amplitude of the acoustic wave (Crocker, 1998).

2.4.3 Cavitation

Cavitation is "the growth and collapse of gas bubbles in a liquid in response to pressure fluctuations in the liquid" (Morfeý, 2001). These bubbles usually consist of gas, such as air, or vapour and form under very low pressure, which can be explained by classical thermodynamics (Feng et al., 2010). There are various reasons for their creation, and a broad investigation of their behaviour has been on-going since 1950 (Noltingk and Neppiras, 1950).

Although there are several conditions under which cavitation may be generated, such as acceleration of a solid surface in a liquid environment and hydrodynamic flow in a narrow passage (Jean-Pierre and Jean-Marie, 2004), the focus in this work is on the oscillation of air bubbles as a result of an applied acoustic field, which is referred to as ‘acoustic cavitation’ or ‘ultrasonic cavitation’ (Duck et al., 1998). While there are several detailed categories of cavitation, they can be generally divided into the oscillation of bubbles without bursting, i.e. stable cavitation, and the collapse of gas bubbles due to applied pressure, i.e. inertial cavitation (Leighton, 1994).

Inertial Cavitation Inertial cavitation was first described at the beginning of the 20th century by Lord Rayleigh and was suggested as an explanation for damage that occurred to ship propellers. It was considered that air bubbles surrounding the propellers were isothermally enlarged, and then rapidly collapsed. This is still considered to be the mechanism of inertial cavitation (Lecoffre, 1997). Moreover, the bursting of bubbles not only generates high temperature gas but may also create free radicals (Birkin et al., 2001), which can generate light (Luque de Castro and Capote, 2007). This procedure is called ‘sonoluminescence’ and it is of great experimental interest as it could indicate the presence of inertial cavitation (Taleyarkhan et al., 2002). The use of sonoluminescence as a cavitation indicator has been shown in various studies (Taleyarkhan et al., 2004).

Inertial cavitation is threshold dependent, as is the creation of stable cavitation, meaning that a bubble needs to be a certain size under the influence of an acoustic field with specific amplitude and frequency in order to collapse. The threshold for occurrence of cavitation can be predicted via the mechanical index (MI). MI is based on the calculations of Apfel and Holland (1991), and is in wide use in all aspects of ultrasonic applications (Jong, 2002).

$$MI = \frac{PNP}{\sqrt{f}}$$

Equation 2.10- Mechanical index

where *PNP* is the peak negative pressure (MPa) and *f* is the acoustic frequency (MHz). The MI itself is referred to without units (Duck et al., 1998). MI is a useful tool for assessment of cavitation occurrence and needs to be taken into account while working with US signals.

The inertial collapse of the bubble, also called Rayleigh collapse, depends on the pressure of the surrounding liquid and the geometry of the collapse (Ashokkumar, 2011). There are various mechanisms of bubble implosion, e.g. continuous eruptions and regeneration cycles or a jetting effect near a boundary (Leighton, 1994) or even a single cell (Prentice et al., 2005).

Stable Cavitation Although, even in a perfectly homogenous medium, the pressure applied by an acoustic field may create cavitation bubbles, the pressure required for such a process is substantial (1000 - 10,000 atm). Pressures of such magnitudes are far higher than the ones created in normal experimental arrangements, yet cavitation occurs regularly in various lab conditions. This can be explained by the fact that liquids are imperfect. Most laboratory liquids, especially water, are saturated with air, gases, and various dissolved substances, which act as cavitation nuclei (Shah et al., 1999).

After the creation of a bubble, a new question arises regarding its stability. The answer is driven from the same source as the previous one, the saturation of the medium with various impurities. One hypothesis claims that ions created by dissolved salts may stabilize the bubble structure and prevent its implosion, and another that a collection of molecules which are absorbed from the medium into the bubble's surface will create a monolayer and decrease the surface tension (Shutilov, 1988).

The stable bubble state can be described by the following equation:

$$P_O = P_T - \frac{2 \cdot \sigma}{r}$$

Equation 2.11- Stability of a cavitation bubble

where P_O is the outer static pressure; P_T is the sum of saturated vapour pressure in the medium, P_s , and the pressure of the diffused gas within the bubble, P_B ; σ is the surface tension; and r is the radius of the bubble (Neppiras, 1980). Equation 2.11 shows an inverse correlation between the radius of the bubble and the pressure. The lower the pressure, the bigger the bubble and *vice versa*. In other words an applied pressure can expand and contract the bubbles (Crocker, 1998). In the stable state, the gas cavities oscillate in a linear manner at the acoustic field frequency, its harmonics and its sub-harmonics. This movement is also referred to as 'resonant oscillations'. Groups of oscillating bubbles can also create coherent 'bubble clouds' (Gerold, 2011) and micro-streaming.

Enhancement of stable cavitation can be achieved by introducing microbubbles (MBs) into a specific US field. The use of MBs with US beams has been found useful, in slightly different ways, in diagnostic and therapeutic fields (Dijkmans et-al., 2004). In US imaging for diagnostic purposes MBs, also referred to as USCAs, are used to enhance image resolution and contrast and to assess the rate of blood flow (Schrope et-al., 1992; Nicolau et-al., 2004). The behaviour of MB's depends on the MI (Duck et al., 1998).

Nowadays, studies have combined both the visual enhancement by the MBs with their ability to maintain stable cavitation. MBs are under investigation in the drug delivery field

(Hernot and Klibanov, 2008; Hu et al., 2009), as it is known that stable cavitation can be used to stimulate membrane permeability (Dino et al., 1989). A full explanation of the effects of stable and unstable cavitation on cells, with and without MBs, is given in Section 5.1.1.2.

2.4.4 Biomedical Ultrasound Applications

2.4.4.1 Diagnostic Ultrasound

Diagnostic US refers to the imaging method called ultrasonography that utilizes transmitting and receiving US transducers. This imaging method is very straightforward and considered to be safe (Merritt, 1989). Hence it is widely used for imaging various organs and especially during pregnancy (Bricker, 2000). The principle of ultrasonic imaging is, in some ways similar to that of a bat's navigation system, where the return of a transmitted US wave is interpreted as an echo image of a surface. The typical frequencies for creation of the diagnostic images are around 2 - 20 MHz (Bluth et al, 2000). USCAs are sometimes used to enhance the quality of US imaging, mainly in echocardiography scans because blood and highly perfused tissue are highly anechogenic (Main, 2009).

2.4.4.2 Therapeutic Ultrasound

There are several ways to utilise US systems for therapeutic purposes. Some of the common therapeutic ultrasonic applications include: phacoemulsification, a method for removal of cataract using an ultrasonic tip (Packer, 2005); various dental treatments (Ustun et al., 2008; Ang et al., 2010); ultrasonic physical therapy (Roebroek et al., 1998); lithotripsy, i.e. the destruction of liver/ gallbladder/ kidney stones using a focused acoustic beam (Pengfei et al., 2011); and high intensity focused ultrasound (HIFU) surgery.

High Intensity Focused Ultrasound (HIFU) The ability of US to create focused beams, as explained in Section 2.4.1, is not only beneficial in the diagnostic field, but also the reason for the interest in HIFU for non-invasive surgery. Using a focused beam at a certain frequency, usually between 0.25 - 10 MHz, it is possible to create a sharp and accurate focus at varying distances up to many centimeters within the human body (Zhou, 2011). The acoustic beam does not harm the propagating tissues on the way to the focus nor the cells surrounding the focus, and the margins of the focus can be as little as six cells wide (Duck, 1998). In opposition to conventional surgery, where the physician needs to cut the patient's body and precisely remove tissue using a scalpel, HIFU offers the potential of a safer, more accurate, non-invasive method for the same or better outcome.

The methodology in HIFU is to heat the selected tissues to the level of necrosis (Overgaard and Suit, 1979), also known as 'ablation' (Habash et al., 2006). The thermal dose *in*

situ can be calculated through the time (t) /temperature (T) equation by Sapareto and Dewey (1984).

$$t_1 = t_0 \cdot R^{\Delta T}$$

Equation 2.12- Thermal dose

In Equation 2.12, R is a constant that can be derived from the enthalpy of the process. For tissues above 43°C, R is considered to equal approximately 0.5 (Halperin et al., 2008). According to this equation, given the temperature *in situ* one can know whether cell necrosis is achieved after a certain exposure time to US.

The effect of HIFU in tissues is not purely thermal, due to the possibility of cavitation. As mentioned previously, cavitation is a threshold-dependent, spontaneous and apparently random phenomenon which is very hard to control. The appearance of cavitation in tissue ablation procedure might have damaging effects and is usually avoided, yet some indicate that cavitation is essential for tissue ablation (Wu and Nyborg, 2006).



Figure 2.9- In-vivo liver ablation through the ribcage (InSightec, Ltd.)

Figure 2.9 depicts an ablated area in a liver. The sonications were performed in a sedated pig under MRI guidance. The main challenge was to avoid damage to the ribcage when focusing the beam. 19 sonications were performed by an ExAblate 2000 system (InSightec Ltd., Haifa, Israel) with a total energy of about 116 kJ for 377 s at $f = 1.15$ MHz. As can be seen, the ablated area appears in the image as brighter spots with an average size of a few mm. Although the first *in-vivo* application of HIFU was in the 1950s by the Fry Brothers, HIFU was not in clinical use until the 1990s due to lack of means to visualise the targeted tissue and thus target and monitor treatment. Recent developments in imaging, such as CT, MRI and US moved HIFU from the research stage into a clinical therapeutic device.

The leading imaging modalities in use for FUS surgery are US (Wu et al., 2005) and MRI (Jolesz, 2009). HIFU surgery has many therapeutic applications, especially in oncology, including: prostate cancer (Rewcastle, 2006), bone metastases (Lieberman, 2008), breast cancer

(Huber et al., 2001), pancreatic cancer (Wu et al., 2005), liver and kidney tumours (Illing, 2005). Non-oncological utilization of FUS surgery includes, for example, the ablation of uterine fibroids (UFs), a process that can dramatically increase the quality of life without the removal of the uterus (Zowall et al., 2008).

2.4.5 Magnetic Resonance guided Focused Ultrasound Surgery

The mathematical principles of MRI are complex and mainly rely on quantum mechanics. Nevertheless, those principles can be formulated using ‘quasi-classical’ techniques, which are more intuitive. Initially named ‘nuclear magnetic resonance imaging’ (NMRI) (Lauterbur, 1973), the physics behind it lies in the nucleus of the atoms, more precisely in the hydrogen atom (Purcell et al., 1945).

The nucleus of a hydrogen atom consists of a positive charge created by a single proton in a constant spinning motion. By electromagnetism, this motion creates a magnetic field which has a ‘magnetic moment’ (Bloch et al., 1946). When discussing a human body, which is filled with myriad protons spinning in different directions, the average magnetic moment without application of external magnetic field equals zero (Abragam, 1961). Under the influence of a strong external magnetic field, B_0 , the protons should theoretically align with the direction of this field (Pykett et al., 1982). In practice, this does not happen: the protons rotate around the axis of the applied external magnetic field, precessing, instead. The precessional frequency, ω_0 , of the spin is constant and depends solely on the magnitude of B_0 , as defined by the Larmor equation (Epstein, 2008).

$$\omega_0 = \gamma \cdot B_0$$

Equation 2.13- Larmor equation

where $\gamma = 2.7 \cdot 10^8$ rad/s-T also known as the gyromagnetic ratio and B_0 is the strength of the magnetic field. The protons’ rotation direction can be parallel or anti-parallel to B_0 (Wolbarst, 1999). The ratio between the parallel and anti-parallel spins depends on the strength of B_0 and temperature. The sum of the spins is the net magnetization, M_0 , which is aligned with B_0 in the equilibrium state and can be measured in units of μ Tesla. In practice, the value of M_0 is considerably lower than B_0 , e.g. by 10^6 , hence it is practically immeasurable (Brown et al., 2010). For that reason a secondary pulse, B_1 , is generated transverse to B_0 , which tilts M_0 in the direction of the diagonal axis, as illustrated in Figure 2.10. This way the signal generated by M_0 can be translated into voltage and recorded (McRobbie et al., 2003).

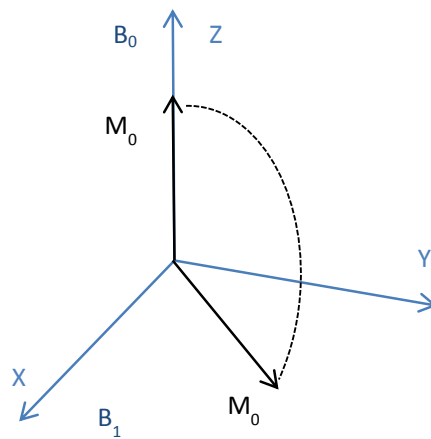


Figure 2.10- A schematic representation of M_0 under the influence of B_1

B_1 is a radio frequency (RF) wave at the Larmor frequency. M_0 will stay tilted until the end of the RF pulse. In Figure 2.10, the RF pulse presented is a 90° pulse, which tilts M_0 into the transverse axis (Bernstein et al. 2004). This is not always the case, and in order to define the wanted tilt degree (α) the following equation is needed:

$$\alpha = \gamma \cdot T_p \cdot B_1$$

Equation 2.14- Angle of M_0 tilt

where T_p is the RF pulse duration time and B_1 is the strength of RF pulse. Since α depends both on the strength of the pulse and its length, it is recommended that only the strength will be changed while the time stays constant (Brant and De Lange, 2012). The RF pulse not only tilts M_0 but also creates phase coherence between the spins; this is the principle behind spin echo (SE) imaging, allowing increases in the level of the signal, the M_0 recordable level (Suetens, 2002). Unfortunately, the spins re-phase rapidly and as a result their signal decays to zero, in a process known as Free Induction Decay (FID); therefore some additional modulations need to be performed in order to overcome this problem.

There are two types of echoes with different α values, the gradient echo (GE) and the SE (Westbrook et al., 2011). GE is usually applied with a RF pulse in which $\alpha < 90^\circ$ while, in SE, the RF pulse is transverse to Z ($\alpha = 90^\circ$). In GE, a negative gradient lobe is applied straight after the initial RF pulse, which causes a fast dephasing of M_0 , e.g. much quicker the FID. An application of a positive gradient not long after the negative one, rephases the precessing spins around the Y axis, and in that way forming the GE (Webb, 2003). In SE, the spins are left to dephase for a specific time, and a 180° (Y axis) pulse is applied. As a result, the spins flip and eventually rephase at the Y axis, creating the SE (Hashemi et al., 2010).

The spins' relaxation time highly depends on two things: the spin interaction with other spins, known as spin-spin relaxation or T_2 relaxation time, and the interaction of the spin with its environment, the spin-lattice relaxation or T_1 relaxation time. In T_2 , the spins dephase due to a small variation in the precessional frequencies of the spins they interact with. This variation occurs as a result of the accumulating effect of each spins' magnetic moment (Poustchi-Amin, 2001). When the interaction is over, they return to the Larmor frequency but with different phase angles they have attained from the interaction. There is no energy loss in T_2 relaxation and it is independent of the magnitude of B_0 . T_1 , on the contrary, is considered to be the energy the spin loses to its environment, blood flow etc., and it is dependent on the strength of the magnetic field (B_0) (McRobbie et al., 2003).

While T_2 is the de-phasing on the Y-X plane of the rotating frame of reference, T_1 is the dephasing of M_0 back to the Z axis. Since the de-phasing of the spin is much quicker, by several orders of magnitude, in the transversal plane than the dephasing in the Z axis, in a given tissue, T_1 will always be greater than T_2 (Webb, 2003).

From this it is clear that timing plays an important role in MRI. The two important features that define the desired timing in regular MRI are the echo time (TE) and repetition time (TR). TE refers to the length of the echo pulse (GE/ SE) and TR to the RF and gradient pulse recurrence time (Brant and De Lange, 2012). In SE, the images acquired rely solely on TE and TR, so that short TR and TE will result in T_1 imaging and long TR and TE in T_2 imaging, while in GE the angle of RF (α) is an important factor. If $\alpha > 50^\circ$ a T_1 weighted image will be generated, whereas if $\alpha < 40^\circ$ a T_2^* image will be generated.

It is necessary at this point, to explain about T_2^* weighted images (Weishaupt et al., 2006). While in SE there is a correction of the inhomogeneities of the magnetic field, in GE there is no consideration of that factor. Moreover, since the positive pulse only compensates for the negative one, it results in no consideration of the spin-spin relaxation as well (Suetens, 2002). The compensation of both of the things mentioned above in GE images is referred to as the 'apparent' relaxation (T_2^*) (Kuperman, 2000).

There is another optional image contrast approach named proton density (PD) weighted images. This type of imaging is rarely used, since most of the soft tissues have similar proton densities, but can be achieved via long TR and short TE in SE, or a small angle, $\alpha < 40^\circ$, and a short TE in GE (McRobbie et al., 2003).

2.4.5.1 Existing Methods of Magnetic Resonance-guided Focused Ultrasound Surgery

MRgFUS is presently considered to be the ultimate combination of non-invasive surgery and accurate real time monitoring. The main benefits of using MRI as a guiding tool for FUS surgery are the possibility for real-time thermometry and relatively high resolution 3D imaging (Wu and Nyborg, 2006).

MR-guidance has clear advantages over US guidance in treatment location planning, treatment monitoring, focal point location and thermometry (Jolesz and Hynynen, 2008). In each of these fields, US imaging lags the equivalent MR capability. For example, US lacks accuracy in margin detection of tumours in US imaging, increases uncertainty regarding the location of nerves within the treatment area, and, most importantly, lacks temperature measurement capability (Jolesz, 2009).

As previously described, FUS has many clinical applications and the mechanism of tissue ablation as a surgical tool is in use worldwide (Peters and Cleary, 2008). Further explanation on MRI thermometry and a full description of the systems in use in this work are given in Section 4.1.

2.4.5.2 Limitations

The main drawback in MRgFUS is in obtaining access to an MRI scanner. Because of the large He capacity needed to maintain the temperature of the superconducting coil that generates the magnetic field, the costs of MRI suites can go up to a few million dollars. Moreover, these highly complicated and expensive systems require frequent maintenance and servicing, which can add up to a significant sum per annum, e.g. 10% of the machine cost. Furthermore, MRI is not suitable for all patients, e.g. those who are obese and patients with implants.

From the technical point, one of the current limitations of FUS surgery is the penetration of the acoustic beam past energy absorbing features, such as bones. Bones reflect and absorb the acoustic beam much more than other tissues, which results in heating and disturbance or prevention of the focus formation. Due to the importance of these issues, there is a significant research effort to overcome this problem, focusing mainly on manipulation of the transmitting elements (Bobkova et al., 2010; Liu et al., 2010). Overcoming the challenge of focusing beyond bone also opens up the possibility for neurological treatments through the skull (Clement et al., 2000; Hynynen et al., 2004). Additional problems in the application of FUS

include the motion of the body due to breathing, and the need to ablate large volumes of tissue, e.g. large UFs, which results in long treatment times (Jolesz, 2009).

2.4.6 Magnetic Resonance guided Focused Ultrasound Surgery Systems in Drug Delivery

In recent years MRgFUS has been investigated as a guiding and localizing tool for TDD (Vaezy and Zderic, 2009). MRI guidance in USmTDD can be used to monitor the distribution of drugs and their accumulation in the target regions, by conjugation of drug carriers and MRI contrast agents, and/ or to measure temperature *in situ* for targeted drug release from thermo-sensitive carriers (Deckers et al., 2008).

MRI contrast agents are complexes that usually consist of a paramagnetic element, such as $\text{Co}^{2+/3+}$, $\text{Fe}^{2+/3+}$ or Gd^{3+} and a polymeric shell in order to reduce toxicity (Weishuapt et al., 2006). Such complexes are commercially available and are widely used in order to gain clearer MR images. The interaction of these paramagnetic materials with the protons in the body results in shorter T_1 and T_2 . MRI contrast agents are used to enhance site-specific imaging according to the organ in question. Currently, there is a great interest in the utilization of MRI contrast agents to enhance visualization and TDD (Veiseh et al., 2010; Sun et al., 2008). Recent *in-vivo* studies proved the feasibility of utilization of MRgFUS with targeted drug release from Gd-conjugated thermo-sensitive liposomes (Smet et al., 2011). Another possible implementation of such an idea is the conjugation of Gd with CD-based carriers (Battistini et al., 2008; Banerjee and Chen, 2009).

2.5 Summary

This chapter aimed to provide the necessary background for the work presented in this thesis. The broad introduction to TDD included the various existing chemical methods and mechanisms for targeting drugs in the body. CD technology was presented, with the fundamental chemical background as well as the pharmaceutical applications in TDD and the possible routes of administration. The design, characterization and chemical evaluation of CD-based drug carriers is discussed in Chapter 3. To provide background on the MRgFUS system that was utilized in this study, the basic physics and applications of both US and MRI were reviewed.

As a part of the introduction to US, the following points were discussed: acoustic fields and the general wave equation, types of cavitation and its formation, and biomedical US applications. Although the working principles of MRI involve highly complicated physics, a

general description of the mechanisms involved was included to provide basic understanding and to introduce the reader to the terminology in use. More information on the evaluation of acoustic fields and MRI thermometry is provided in Chapter 4.

2.6 References

Aboofazeli, R. et al. (1994) Investigations into the formation and characterization of phospholipid microemulsions. III. Pseudo-ternary phase diagrams of systems containing water lecithin-isopropyl myristate and either an alkanolic acid, amine, alkanediol, polyethylene glycol alkyl ether or alcohol as cosurfactant. *Int J Pharm*, 111, pp.63-72.

Abragam, A. (1961) *The principles of nuclear magnetism*. Oxford: Oxford University Press.

Al-Jamal, W. and Kostarelos, K. (2011) Liposomes: from a clinically established drug delivery system to a nanoparticle platform for theranostic nanomedicine. *Accounts Chem Res*, 44 (10), pp.1094- 104.

Allen, T.M. and Cullis, P.R. (2004) Drug delivery systems: entering the mainstream. *Science*, 303, p.1818-22.

Ang, W.T. et al. (2010) Design and implementation of therapeutic ultrasound generating circuit for dental tissue formation and tooth-root healing. *IEEE Trans Biomed Circuits Syst*, 4 (1), pp.49-61.

Apfel, R.E. and Holland, C.K. (1991) Gauging likelihood of cavitation from short-pulse low-duty cycle diagnostic ultrasound. *Ultrasound Med Biol*, 17 (2) pp. 179-85.

Ashokkumar, P.M. (2011) *Theoretical and Experimental Sonochemistry Involving Inorganic Systems*. Germany: Springer.

Astray, G. et al. (2009) A review on the use of cyclodextrins in foods. *Food Hydrocolloid*, 23, pp.1631- 40.

Azhari, H. (2010) *Basics of Biomedical Ultrasound for Engineers*. USA: John Wiley & Sons, Inc.

Bagalkot, V. et al. (2006) An aptamer-doxorubicin physical conjugate as a novel targeted drug-delivery platform. *Angew Chem Int Ed*, 45, pp.8149- 152.

Bai, J. et al. (2009) Spherical phased array by PVDF needle hydrophone. *IEEE: BMEI 09'*, pp.1-4.

Banerjee, S.S. and Chen, D-H. (2009) Cyclodextrin-conjugated nanocarrier for magnetically guided delivery of hydrophobic drugs. *J Nanopart Res*, 11, pp.2071- 8.

Battistini, E. et al. (2008) High-relaxivity magnetic resonance imaging (MRI) contrast agent based on supramolecular assembly between a gadolinium chelate, a modified dextran, and poly- β -cyclodextrin. *Chem Eur J*, 14, pp.4551- 61.

- Bergen, J.M. et al.** (2006) Gold nanoparticles as a versatile platform for optimizing physicochemical parameters for targeted drug delivery. *Macromol Biosci*, 6, pp.506- 16.
- Bernstein, M.A. et al.** (2004) *Handbook of MRI pulse sequences*. USA: Elsevier Academic Press.
- Bibby, D.C. et al.** (2000) Mechanisms by which cyclodextrins modify drug release from polymeric drug delivery systems. *Int J Pharm*, 197, pp.1–11.
- Bilensoy, E.** (2011) *Cyclodextrins in pharmaceuticals, cosmetics, and biomedicine: current and future industrial applications*. USA: John Wiley & Sons, Inc.
- Birkin, P.R. et al.** (2001) Electrochemical evidence of H[•] produced by ultrasound. *Chem Commun*, pp.2230- 1.
- Bloch, F. et al.** (1946) Nuclear induction. *Phys Rev*, 70 (7-8), pp.460- 74.
- Bluth, E.I. et al** (2000) *Ultrasound: a practical approach to clinical problems*. Italy: Thieme Medical Publishers, Inc.
- Bobkova, S. et al.** (2010) Focusing of high-intensity ultrasound through the rib cage using a therapeutic random phased array. *Ultrasound Med Biol*, 36 (6), pp.888–906.
- Boer, T. et al.** (2000) Recent innovations in the use of charged cyclodextrins in capillary electrophoresis for chiral separation in pharmaceutical analysis. *Electrophoresis*, 21, pp.3220-39.
- Brant W.E. and De Lange E.E.** (2012) *Essentials of Body MRI*. Oxford: Oxford University Press.
- Breslow, R.** (1980) Biomimetic control of chemical selectivity. *Acc Chem Res*, 13, pp.170- 7.
- Brewster, M.E. and Loftsson, T.** (2007) Cyclodextrins as pharmaceutical solubilizers. *Adv Drug Deliver Rev*, 59, pp.645- 66.
- Bricker, L. et al.** (2000) Ultrasound screening in pregnancy: a systematic review of the clinical effectiveness, cost-effectiveness and women's views. *Health Technol Asses*, 4 (16), pp.1-189.
- Brouwers, J. et al.** (2008) Supersaturating drug delivery systems: the answer to solubility-limited oral bioavailability?. *J Pharm Sci*, 9 (8), pp.2549- 72.
- Brown, M.A. et al.** (2010) *MRI: basic principles and applications*. New Jersey: Wiley-Blackwell.
- Bushmann, H-J. and Schollmeyer, E.** (2002) Applications of cyclodextrins in cosmetic products: A review. *J Cosmet Sci*, 53, pp.185-191.
- Cabral Marques, H.M.** (2010) A review on cyclodextrin encapsulation of essential oils and volatiles. *Flavour Fragr J*, 25, pp.313- 26.
- Caruthers, S.D. et al.** (2007) Nanotechnological applications in medicine. *Curr Opin Biotech*, 18, pp.26–30.
- Challa, R. et al.** (2005) Cyclodextrins in drug delivery: an updated review. *AAPS Pharm Sci Tech*, 6 (2), pp.E329- 57.

- Clement, G.T. et al.** (2000) Investigation of a large-area phased array for focused ultrasound surgery through the skull. *Phys Med Biol*, 45, pp.1071- 83.
- Crocker, M.J.** (1998) *Handbook of Acoustics*. Canada: John Wiley and Sons, Inc.
- Davies, N.M.** (2000) Biopharmaceutical considerations in topical ocular drug delivery. *Clin Exp Pharmacol P*, 27, pp.558- 62.
- Davis, F. and Higson, S.** (2011) *Macrocycles: construction, chemistry and nanotechnology applications*. United Kingdom: John Wiley & Sons Ltd.
- Davis, M.E** (2009) The first targeted delivery of siRNA in humans via a self-Assembling, cyclodextrin polymer-based nanoparticle: from concept to clinic. *Mol Pharm*, 6 (3), pp.659- 68.
- Davis, M.E. and Brewster, M.E.** (2004) Cyclodextrin-based pharmaceuticals: Past, Present and Future. *Nat Rev Drug Discov*, 3, pp.1023-35.
- Deckers, R. et al.** (2008) The role of ultrasound and magnetic resonance in local drug delivery. *J Magn Reson Im*, 27, pp.400- 9.
- Del Valle, E.M.M.** (2004) Cyclodextrins and their uses: a review. *Process Biochem*, 39, pp.1033- 46.
- Deng, W. et al.** (2007) A chemical-responsive supramolecular hydrogel from modified cyclodextrins. *Angew Chem Int Ed*, 46, pp. 5144- 7.
- Dick, D.L. et al.** (1992) Molecular encapsulation: cyclodextrin-based analogues of heme-containing proteins. *J Am Chem SOC*, 114, pp.2664- 69.
- Dijkmans, P.A. et al.** (2004) Microbubbles and ultrasound: from diagnosis to therapy. *Eur J Echocardiogr*, 5, pp.245- 56.
- Dinno, M.A. et al.** (1989) The significance of membrane changes in the safe and effective use of therapeutic and diagnostic ultrasound. *Phys Med Biol*, 34 (11), pp.1543- 52.
- Dodziuk, H.** (2006) *Cyclodextrins and their complexes: chemistry, analytical methods, applications*. Germany: Wiley-VCH Verlag GmbH & Co.
- Duck, F.A. et al.** (1998) *Ultrasound in medicine*. Great Britain: Institute of Physics Publishing.
- Ebbini, E.S. and Cain, C.A.** (1989) Multiple-focus ultrasound phased-array pattern synthesis: optimal driving-Signal distributions for hyperthermia. *IEEE T Ultrason Ferr*, 36 (5), pp.540- 8.
- Elhissi, A.M.A. et al.** (2012) Carbon nanotubes in cancer therapy and drug delivery. *Drug Deliv*, 2012, pp.1-10.
- Epstein, C.L.** (2008) *Introduction to the mathematics of medical imaging*. USA: SIAM.
- Fainerman, V.B. et al.** (2001) *Surfactants: chemistry, interfacial properties, applications*. Nederland: Elsevier.
- Feng, H. et al.** (2010) *Ultrasound Technologies for Food and Bioprocessing*. USA: Springer.

- Frömming, K.H. and Szejtli, J.** (1993) *Cyclodextrins in pharmacy*. The Netherlands: Kluwer Academic Publishers.
- Gerold, B. et al.** (2011) Laser-nucleated acoustic cavitation in focused ultrasound. *Rev Sci Instrum*, 82, pp.0449021- 9.
- Gillies E.R. and Fréchet J.M.J.** (2005) Dendrimers and dendritic polymers in drug delivery. *Drug Discov Today*, 10 (1), pp.35-43.
- Golan, D.E. et al.** (2008) *Principles of pharmacology: the pathophysiologic basis of drug therapy*. USA: Lippincott Williams & Wilkins.
- Greenwald, R.B. et al.** (2003) Effective drug delivery by PEGylated drug conjugates. *Adv Drug Deliver Rev*, 55, pp.217-50.
- Habash, R.W.Y. et al.** (2006) Thermal therapy, part 1: an introduction to thermal therapy. *Crit Rev Biomed Eng*, 34(6), pp.459- 89.
- Halperin, E.C. et al.** (2008) *Perez and Brady's principles and practice of radiation oncology*. China: Lippincott Williams & Wilkins.
- Harashima, H. and Kiwada, H.** (1996) Liposomal targeting and drug delivery: kinetic consideration. *Adv Drug Deliver Rev*, 19, pp.425- 44.
- Hashemi, R.H. et al.** (2010) *MRI: The Basics*. USA: Lippincott Williams & Wilkins.
- Hernot, S. and Klibanov, A.L** (2008) Microbubbles in ultrasound-triggered drug and gene delivery. *Adv Drug Deliver Rev*, 60, pp.1153- 66.
- Hertzberg, Y. et al.** (2010) Ultrasound focusing using magnetic resonance acoustic radiation force imaging: Application to ultrasound transcranial therapy. *Med Phys*, 37 (6), pp.2934- 42.
- Hirayama, F. and Uekama, K.** (1999) Cyclodextrin-based controlled drug release system. *Adv Drug Deliver Rev*, 36, pp.125- 41.
- Hu, Y-Z. et al.** (2009) Ultrasound microbubble contrast agents: application to therapy for peripheral vascular disease. *Adv Ther* , 26(4), pp.425- 34.
- Huang, H. et al.** (2010) Low molecular weight polyethylenimine cross-linked by 2hydroxypropylg-cyclodextrin coupled to peptide targeting HER2 as a gene delivery vector. *Biomaterials*, 31, pp.1830- 8.
- Huang, S-L.** (2006) Liposomes in ultrasonic drug and gene delivery. *Adv Drug Deliver Rev*, 60, pp.1167- 76.
- Huber, P.E. et al.** (2001) A new noninvasive approach in breast cancer therapy using magnetic resonance imaging-guided focused ultrasound surgery. *Cancer Res*,61, pp.8441- 47.
- Huo, Y. and Chen, Y.** (2001) Simulation of field characteristics of the focused axisymmetrically curved surface transducers. *IEEE T Ultrason Ferr*, 48(2), pp.445- 51.

- Hynynen, K. et al.** (2004) 500-Element ultrasound phased array system for noninvasive focal surgery of the brain: a preliminary rabbit study with ex vivo human skulls. *Magnet Reson Med*, 52, pp.100- 7.
- Illing, R.O. et al.** (2005) The safety and feasibility of extracorporeal high-intensity focused ultrasound (HIFU) for the treatment of liver and kidney tumours in a Western population. *Brit J Can*, 93, pp. 890- 5.
- Jaffe, H. and Berlincourt, D. A.** (1965) Piezoelectric transducer materials. *IEEE*, 53 (10), pp.1372- 86.
- Jain, K.K.** (2008) *Drug delivery systems*. USA: Humana Press, Springer.
- Jean-Pierre F. and Jean-Marie M.** (2004) *Fundamentals of cavitation*. USA: Kluwer Academic Publishers.
- Jolesz, F.A.** (2009) MRI-guided focused ultrasound surgery. *Annu Rev Med*, 60, pp.417- 30.
- Jolesz, F.A. and Hynynen, K.H.** (2008) *MRI-guided focused ultrasound surgery*. USA: Informa Healthcare USA, Inc.
- Jong, N.d.** (2002) Mechanical index. *J Echocardiography*, 3, pp.73-4.
- Juergen, S. et al.** (2012) *Fundamentals and applications of controlled release drug delivery*. USA: Springer.
- Julianto, T. et al.** (2000) Improved bioavailability of vitamin E with a self emulsifying formulation. *Int J Pharm*, 200, pp.53- 7.
- Karanth, H. and Murthy, R.S.R.** (2007) pH-sensitive liposomes-principle and application in cancer therapy. *JPP*, 59, pp.469- 83.
- Karsa, D. R. et al.** (1996) *Chemical aspects of drug delivery systems*. Great Britain: Royal Society of Chemistry.
- Kihara, F. et al.** (2003) In vitro and in vivo gene transfer by an optimized α -cyclodextrin conjugate with polyamidoamine dendrimer. *Bioconjugate Chem*, 14, pp.342- 50.
- Knop, K. et al.** (2010) Poly(ethylene glycol) in drug delivery: pros and cons as well as potential alternative. *Angew Chem Int Ed*, 49, pp.6288- 308.
- Kulkarni, V.S.** (2010) *Handbook of non-invasive drug delivery systems*. USA: Elsevier.
- Kuperman, V.** (2000) *Magnetic resonance imaging: physical principles and applications*. USA: Academic Press.
- Kurkov, S.V. et al.** (2011) Drug/cyclodextrin: beyond inclusion complexation. *J Incl Phenom Macrocycl Chem*, 69, pp.297–301.
- Larson, N. and Ghandehari, H.** (2012) Polymeric conjugates for drug delivery chem. *Mater*, 24 (5), pp.840–853.

- Laugier, P. and Haiat G.** (2011) *Bone quantitative ultrasound*. France: Springer.
- Lauterbur, P. C.** (1973) Image formation by induced local interactions: examples employing nuclear magnetic resonance. *Nature*, 242, pp.190- 1.
- Lawrence, M.J. and Rees, G.D.** (2000) Microemulsion-based media as novel drug delivery systems. *Adv Drug Deliver Rev*, 45, pp.89 -121.
- Lecoffre, Y.** (1997) *Cavitation: bubble trackers*. USA: A.A. Balkema Publishers.
- Leighton, T. G.** (1994) *The acoustic bubble*. Great Britain: Academic Press.
- Li, J. and Loh, X.J.** (2008) Cyclodextrin-based supramolecular architectures: syntheses, structures, and applications for drug and gene delivery. *Adv Drug Deliver Rev*, 60, pp.1000- 17.
- Li, S. and Purdy, W.C.** (1992) Cyclodextrins and their applications in analytical chemistry. *Chem Rev*, 92, pp.1457- 70.
- Li, Y. et al.** (2007) γ -Cyclodextrin: a review on enzymatic production and applications. *Appl Microbiol Biotechnol*, 77, pp.245- 55.
- Liberman, B. et al.** (2008) Pain palliation in patients with bone metastases using MR-guided focused ultrasound surgery: A Multicenter Study. *Ann Surg Oncol*, 16 (1), pp.140- 6.
- Liu, H. and Venkatraman, S.** (2012) Cosolvent effects on the drug release and depot swelling in injectable in situ depot-forming systems. *J Pharm Sci*, 101, pp.1783- 93.
- Liu, H-L. et al.** (2010) Focal beam distortion and treatment planning for transcrib focused ultrasound thermal therapy: A feasibility study using a two-dimensional ultrasound phased array. *Med Phys*, 37 (2), pp.848- 60.
- Loftsson, T. and Brewster, M.E.** (1996) Pharmaceutical applications of cyclodextrins: 1.drug solubilization and stabilization. *J Pharm Sci*, 85 (10), pp.1017- 25.
- Loftsson, T. et al.** (2007) Effects of cyclodextrins on drug delivery through biological membranes. *J Pharm Sci*, 96 (10), pp.2532- 46.
- Lu, D.R. and Øie, S.** (2004) *Cellular drug delivery: principles and practice*. USA: Humana Press Inc.
- Luque de Castro, M. D. and Capote, F. P.** (2007) *Analytical applications of ultrasound*. The Netherlands: Elsevier.
- Maarel, M.J.E.C. et al.** (2002) Properties and applications of starch-converting enzymes of the α -amylase family. *J Biotechnol*, 94, pp.137-55.
- Main, M.L.** (2009) Ultrasound contrast agents safety from anecdote to evidence. *JACC.*, 2 (9), pp.1057-9.
- Manakker, F. et al.** (2009). Cyclodextrin-based polymeric materials: synthesis, properties, and pharmaceutical/biomedical applications. *Biomacromolecules*, 10 (12), pp.3157- 75.

- Matsuda, H. and Arima, H.** (1999) Cyclodextrins in transdermal and rectal delivery. *Adv Drug Deliver Rev*, 36, pp.81–99.
- Mayer, L.D. et al.** (1986) Technique for encapsulating bioactive agents into liposomes. *Chem Phys Lipids*, 40, pp.333- 45.
- McRobbie, D. W. et al.** (2003) *MRI from picture to proton*. Cambridge: Cambridge University Press.
- Merritt, C.R.B.** (1989) Ultrasound safety: what are the issues?. *Radiology*, 173, pp.304- 6.
- Miyoshi, N. et al.** (2011) The enhancement of the oral bioavailability of γ -tocotrienol in mice by γ -cyclodextrin inclusion. *J Nutr Biochem*, 22, pp.1121- 6.
- Morfey, C.L.** (2001) *Dictionary of acoustics*. Great Britain: Academic Press.
- Moses, L.R.** (1999) Beta cyclodextrin–insulin-encapsulated chitosan/alginate matrix: oral delivery system. *J Appl Polym Sci*, 75, pp.1089- 96.
- Motoyama, K. et al.** (2009) Potential use of 2-hydroxypropyl- β -cyclodextrin for preparation of orally disintegrating tablets containing dl- α -tocopheryl acetate, an oily drug. *Chem Pharm Bull*, 57(11), pp.1206- 12.
- Mueller, P. and Adam, A.** (2012) *Interventional oncology: a practical guide for the interventional radiologist*. USA: Springer.
- Narang, A.S. et al.** (2007) Stable drug encapsulation in micelles and microemulsions. *Int J Pharm*, 345, pp.9–25.
- National Academy of Sciences** (2003) *The impact of academic research on industrial performance*. USA: The National Academies Press.
- Neppiras, E.A.** (1980) Acoustic cavitation. *Phys Rep*, 61 (3), pp.159-251.
- Nicolau, C. et al.** (2004) Evaluation of hepatocellular carcinoma using SonoVue, a second generation ultrasound contrast agent: correlation with cellular differentiation. *Eur Radiol*, 14, pp.1092- 9.
- Noltingk, B. E. and Neppiras, E. A.** (1950) Cavitation produced by ultrasonics. *Proc Phys Soc B*, 63, pp.674- 85.
- Ono, N. et al.** (2011) Reduction of bitterness of antihistaminic drugs by complexation with β -cyclodextrins. *J Pharm Sci*, 100 (5), pp.1935- 43.
- Overgaard, J. and Suit, H.D.** (1979) Time-temperature relationship in hyperthermic treatment of malignant and normal tissue in vivo. *Cancer Res*, 39, pp.3248- 53.
- Owen, S.C. et al.** (2012) Polymeric micelle stability. *Nano Today*, 7, pp.53-65.

- Paciotti, G.F. et al.** (2006) Colloidal gold nanoparticles: a novel nanoparticle platform for developing multifunctional tumor-targeted drug delivery vectors. *Drug Develop Res*, 67, pp.47-54.
- Packer, M. et al.** (2005) The physics of phaco: a review. *J Cataract Refract Surg*, 31, pp.424- 31.
- Pasut, G. and Veronese, F.M.** (2007) Polymer–drug conjugation, recent achievements and general strategies. *Prog Polym Sci*, 32, pp.933- 61.
- Pengfei, S. et al.** (2011) The Results of ureteral stenting after ureteroscopic lithotripsy for ureteral calculi: a systematic review and meta-analysis. *J Urology*, 186, pp.1904- 9.
- Peters, R.M. and Cleary, K.R.** (2008) *Image-guided intervention: technology and applications*. USA: Springer Science+ Business Media, LLC.
- Pires, A. et al.** (2009) Intranasal drug delivery: how, why and what for?. *J Pharm Pharmaceut Sci*, 12(3), pp.288- 311.
- Poustchi-Amin, M. et al.** (2001) *Principles and applications of echo-planar imaging: a review for the general radiologist*. *Imaging & Therapeutic Technology*, 21(3), pp.767-79.
- Prentice, P. et al.** (2005) Membrane disruption by optically controlled microbubble cavitation. *Nat Phys*, 1, pp.107- 10.
- Purcell, E.M. et al.** (1945) Resonance absorption by nuclear magnetic moments in a solid. *Phys Rev*, 69, pp.37- 8.
- Pykett, I.L. et al.** (1982) Principles of nuclear magnetic resonance imaging. *Radiology*, 143, pp.157- 168.
- Rajewski, R.A. and Stella, V.J.** (1996) Pharmaceutical applications of cyclodextrins. 2. in vivo drug delivery. *J Pharm Sci*, 85 (11), pp.1142- 69.
- Rasheed, A. et al.** (2008) Cyclodextrins as drug carrier molecule: a review. *Sci Pharm*, 76, pp.567-98.
- Rewcastle, J.C.** (2006) High intensity focused ultrasound for prostate cancer: a review of the scientific foundation, technology and clinical outcomes. *Technol Cancer Res T*, 5 (6), pp.619-25.
- Roebroek, M.E. et al.** (1998) The use of therapeutic ultrasound by physical therapists in dutch primary health care. *Phys Ther*, 78, pp.470- 8.
- Rozou, S. et al.** (2005) Study of structural features and thermodynamic parameters, determining the chromatographic behavior of drug–cyclodextrin complexes. *J Chromatogr*, A1087, pp.86–94.
- Saltzman, W.M.** (2001) *Drug delivery: engineering principles for drug therapy*. USA: Oxford University Press, Inc.

- Sapareto, S.A. and Dewey, W.C.** (1984) Thermal dose determination in cancer therapy. *Int J Radiat Oncol Biol Phys*, 10 (6), pp.787-800.
- Schäfer-Korting, M.** (2010) *Drug delivery*. GmbH: Springer.
- Schmid, G.** (1989) Cyclodextrin glycosyltransferase production: yield enhancement by overexpression of cloned genes. *TIBTECH*, 7, pp.244- 8.
- Schroeder, A. et al.** (2009) Ultrasound, liposomes, and drug delivery: principles for using ultrasound to control the release of drugs from liposomes. *Chem Phys Lipids*, 162, pp.1–16.
- Schropet, B. et al.** (1992) Simulated capillary blood flow measurement using a nonlinear ultrasonic contrast agent. *Ultrasonic Imaging*, 14, pp.134-158.
- Seegenschmiedt, M.H. et al.** (1995) *Thermoradiotherapy and thermochemotherapy, volume 1*. Germany: Springer-Verlag Berlin Heidelberg.
- Shah, Y.T. et al.** (1999) *Cavitation reaction engineering*. USA: Kluwer Academic.
- Shutilov, V.A.** (1988) *Fundamental physics of ultrasound*. Glasgow: Gordon and Breach Science Publishers.
- Singh, R. et al.** (2010) Characterization of cyclodextrin inclusion complexes- a review. *J Pharm Sci Technol*, 2 (3), pp.171-183.
- Smet, M. et al.** (2011) Magnetic resonance imaging of high intensity focused ultrasound mediated drug delivery from temperature-sensitive liposomes: An in vivo proof-of-concept study. *J Control Release*, 150, pp.102- 10.
- Stella, V.J. and Quanren H.** (2008). Cyclodextrins. *Toxicologic Pathology*, 36 pp. 30-42.
- Stella, V.J. and Rajewski, R.A.** (1997) Cyclodextrins: their future in drug formulation and delivery. *Pharm Res*, 14 (5), pp.556-67.
- Stella, V.J. et al.** (1999) Mechanisms of drug release from cyclodextrin complexes. *Adv Drug Deliver Rev*, 36, pp.3 –16.
- Suetens, P.** (2002) *Fundamentals of medical imaging*. USA: Cambridge University Press.
- Sun, C. et al.** (2008) Magnetic nanoparticles in MR imaging and drug delivery. *Adv Drug Deliver Rev*, 60, pp.1252- 65.
- Szabo, T.L.** (2004) *Diagnostic ultrasound imaging: inside out*. USA: Elsevier Academic Press.
- Szejtli, J.** (1985) Cyclodextrins in pesticides. *Starcwstarke*, 37 (11), pp.382- 6.
- Szejtli, J.** (1989) Downstream processing using cyclodextrins. *TIBTECH*, 7, pp.170- 4.
- Szente, L. and Szejtli, J.** (1999) Highly soluble cyclodextrin derivatives: chemistry, properties, and trends in development. *Adv Drug Deliver Rev*, 36, pp.17-28.
- Tadros, T.F.** (2005) *Applied surfactants: principles and applications*. GmbH: Wiley-VCH.
- Tadros, T.F.** (2010) *Self-organized surfactant structures*. GmbH : Wiley-VCH.

- Tadwee, K.I. et al.** (2011) Advances in topical drug delivery system: a review. *IJPRAS*, 1 (1), pp.14-23.
- Tafazzoli, M. and Ghias, M.** (2009) Structure and conformation of α -, β - and γ -cyclodextrin in solution: Theoretical approaches and experimental validation. *Carbohydr Polym*, 78, pp. 10- 5.
- Taleyarkhan, R. P. et al.** (2004) Additional evidence of nuclear emissions during acoustic cavitation. *Phys Rev*, 69, pp.0361091-11.
- Taleyarkhan, R.P. et al.** (2002) Evidence for nuclear emissions during acoustic cavitation. *Science*, 295, pp.1868- 73.
- Terao, K. et al.** (2006) Enhancement of oral bioavailability of coenzyme Q10 by complexation with γ -cyclodextrin in healthy adults. *Nutr Res*, 26, pp.503- 8.
- Thanou, M. et al.** (2007) N-sulfonato-N,O-carboxymethylchitosan: A novel polymeric absorption enhancer for the oral delivery of macromolecules. *J Control Release*, 117, pp.171- 8.
- Torchilin, V.P.** (2001) Structure and design of polymeric surfactant-based drug delivery systems. *J Control Release*, 73, pp.137–172.
- Torchilin, V.P.** (2006) *Nanoparticulates as drug carriers*. Singapore: Imperial College Press.
- Uekama, K.** (2004) Design and evaluation of cyclodextrin-based drug formulation. *Chem Pharm Bull*, 52 (8), pp.900- 15.
- Uekama, K. et al.** (1998) Cyclodextrin drug carrier systems. *Chem Rev*, 98, pp.2045- 76.
- Uekama, K. et al.** (2006) Recent aspect of cyclodextrin-based drug delivery system. *J Incl Phenom Macro*, 56, pp.3–8.
- Ustun, Y. et al.** (2008) Effects of low-intensity pulsed ultrasound on dental implant osseointegration: a preliminary report. *Eur J Dent*, 2, pp.254-62.
- Vaezy, S. and Zderic, V.** (2009) *Image-guided therapy systems*. USA: Artech House.
- Veisheh, O. et al.** (2010) Design and fabrication of magnetic nanoparticles for targeted drug delivery and imaging. *Adv Drug Deliver Rev*, 62, pp.284–304.
- Wang, M. and Thanou, M.** (2010) Targeting nanoparticles to cancer. *Pharmacol Res*, 62, pp.90-9.
- Webb, A.** (2003) *Introduction to biomedical imaging*. USA: John Wiley & Sons, Inc.
- Webb, S.** (1988) *The physics of medical imaging*. USA: Taylor & Francis Group, LLC.
- Weishaupt, D. et al.** (2006) *How does MRI work?*. New York: Springer.
- Westbrook, C. et al.** (2011) *MRI in practice*. UK: Wiley-Blackwell.
- Wolbarst, A.B.** (1999) *Looking within*. London: University of California Press.
- Wu, F. et al.** (2005) Feasibility of US-guided high-intensity focused ultrasound treatment in patients with advanced pancreatic cancer: initial experience. *Radiology*, 236, pp.1034- 40.

- Wu, J. and Nyborg, W.L-M.** (2006) *Emerging therapeutic ultrasound*. Singapore: World Scientific Publishing Co. Pte. Ltd.
- Yu, L.L. et al.** (2011) Theoretical calculation of a focused acoustic field from a linear phased array on a concave cylindrical transducer. *Chin Phys Lett*, 28 (10), pp.104302-4.
- Zanelli, C. I. et al.** (1993) Beamforming for therapy with high intensity focused ultrasound (HIFU) using quantitative schlieren. *IEEE, Ultrasonics Symposium*, pp.1233-38.
- Zhang, X. et al.** (2011) β -Cyclodextrin grafting hyperbranched polyglycerols as carriers for nasal insulin delivery. *Carbohydr Polym*, 84, pp.1419- 25.
- Zhou, J. and Ritte, H.** (2010) Cyclodextrin functionalized polymers as drug delivery systems. *Polym Chem*, 1, pp.1552- 59.
- Zhou, Y-F.** (2011) High intensity focused ultrasound in clinical tumor ablation. *World J Clin Oncol*, 2 (1), pp.8-27.
- Zowall, H. et al.** (2008). Cost-effectiveness of magnetic resonance-guided focused ultrasound surgery for treatment of uterine fibroids. *BJOG*, 11, pp.5653- 62.

CHAPTER 3 DEVELOPMENT AND CHARACTERIZATION OF A CYCLODEXTRIN- BASED DRUG CARRIER

3.1 Introduction

This chapter will discuss possible methods for synthesis of CD derivatives alongside evaluation techniques for the yield. In addition, the complexation process as well as the investigation of the guest, host and the created complex structures and reactivity via different methodologies, will be presented.

3.1.1 Chemical Modification and Cyclodextrin Derivatives

The motivation for chemical modification of CDs varies and may include improvement of their solubility in certain solvents, increase in their stereo-selectivity for specific guest molecules in host-guest complexes and the possibility to explore enzyme-catalyzed reaction mechanisms (Uekama, 2004).

When modifying CDs, two important factors must be taken into account. Firstly, one must consider the hydroxyl groups' nucleophilicity, as the initial reaction of modification will be an electrophilic attack on these groups, and secondly it is important to acknowledge the CD's ability to form complexes with the reagents in use. If a strong complex is formed, the product will be defined by the reagent, whereas in a weak complex, the product is guided by the hydroxyl group nucleophilicity. Additional important considerations in the chemical modification process are the cavity size of the CD and the solvent used for the reaction, e.g. in DMF a sulphonation reaction occurs non-selectively on all of the hydroxyl groups, whereas the same reaction in pyridine will be directed to the hydroxyl groups on the 6th position (Khan et al., 1998; Szejtli, 2004).

As previously presented in Figure 2.3, the CD's glucopyranose ring has primary hydroxyl groups on the 6th position and secondary hydroxyl groups on the 2nd and 3rd positions, wherein the hydroxyl groups on the 2nd position are the most acidic ones, and the ones on the 3rd position are the most difficult to access. The hydroxyl groups on the 6th position are the most nucleophilic and will react selectively with less reactive reagents. The intramolecular hydrogen bonds created between the hydroxyl groups on the 2nd and 3rd positions restricts their rotation while the hydroxyl groups on the 6th position rotation are free, which reduces the accessibility to the cavity from the primary face (Khan et al., 1998).

Sole substitution of the CD's hydroxyl groups (either on the second, third or sixth position) also known as monosubstitution, usually increases the CD's aqueous solubility comparing to that of the natural one and hence is used, along with other materials, to enhance drug delivery to specific sites (Tang et al, 2007). It is a challenge to synthesize such molecules, due to difficulties in selectively modifying the three different hydroxyl groups on the outer surface of the CD (Muderawan et al., 2005). Therefore, the higher the number and variety of groups to be substituted on the CD, the harder it will be to synthesize (Himeno et al, 2009). A proposed way to avoid a mixture of unwanted products is by protection of certain hydroxyl groups and thereby directing of the reaction to the desired yield (Badi et al., 2006). A newly proposed, unconventional method for selective substitution on CDs suggested utilization of power US with microwaves, which is suggested not only to yield higher amounts of a specific product, but also to dramatically shorten the reaction time (Trotta et al., 2007).

When discussing chemically modified CDs, the following two commonly used CD derivatives should be mentioned: HP- β CD and SBE- β CD. Both of these have higher water-solubility values than the natural β CD and good complexing properties. Various studies were conducted on the safety profile and toxicological effects of HP- β CD and SBE- β CD which defined them as essentially non-toxic to humans and so, at present, they are used in several Food and Drug Administration (FDA) approved products (Loftsson and Duchene, 2007). Furthermore, investigation of HP- β CD abilities in complex formation with various anti-cancer agents has shown high encapsulation levels of various drugs, especially of highly hydrophobic ones such as Taxol (Cserhfiti and Hollo, 1994). Other modifications can create charged CDs which provide additional ionic interactions for diverse applications, e.g. electrophoresis (de Boer et al., 2000).

3.1.1.1 Cyclodextrin-Based Polymers

The initial step in creation of CD-based polymers and larger scale carriers is to link CDs to one another. The basic method to create linked CDs is by substitution of the hydroxyl groups with a functional group, which due to certain chemical reactions, will become the linkage to another CD molecule, creating a dimer (Liu et al., 2002; Pham et al., 2010). The dimer can be further polymerized to create branched CDs and even CD-based polymeric networks (Auzely-Velty, 2011; Van de Manakker et al., 2009). Additionally, CD-based polymers can be achieved by coupling of the CD to an existing polymer network, copolymerizing it chemically, by radiation, or even radical reactions (Balta et al., 2008).

Unfortunately the methods discussed above usually involve toxic reagents which have limited the medical applications of the created linked CDs. Therefore, an additional method for synthesis of such molecules was developed. This method is based on utilization of the CD's

inclusion ability in order to design a specific polymer. A good example is the use of adamantine in conjunction with β CD to form CD-modified hydrogels (Deng, 2007). Furthermore, it is possible to modify this inclusion-motivated polymerization process to be selectively sensitive to ultraviolet (UV) / visible light, a specific pH level, or a certain temperature. With further modifications, macro- and nanoscale self-assembled particles have been created that have shown the ability to remain a relatively long time in the blood stream and are therefore potential drug delivery vehicles (Challa et al., 2005).

Conjugation of micelles and other CD-based polymers with magnetic particles was suggested for magnetically-guided TDD (Battistini et al., 2008; Banerjee and Chen, 2009). An additional possibility is the combination of CDs, on their own or in a complex, with liposomes. The conjugation is usually made to exploit the best properties of both drug carriers, in order to create a better drug delivery vehicle, e.g. through improvement of drug solubility by CD complex while targeting via a specially designed liposome (Maestrelli et al., 2005; Maestrelli et al., 2006; Hagiwara et al., 2006).

3.1.1.2 Peptidic Cyclodextrin Polymers

Since the 1920's, when insulin was first introduced to the market, it has changed the lives of millions. Moreover, it has shown the great potential behind peptidic drug delivery (van der Walle, 2011). The research field of peptide and protein drug delivery has developed greatly since then, yet challenges to their practical use are still to be overcome. Peptides and proteins suffer from poor absorption through the biological barriers as well as rapid clearance from the blood circulation by the plasma, which complicates their cellular delivery (Irie and Uekama, 1999).

Conjugation of CDs with various peptidic structures can offer a new platform of selective tumour therapy. The peptidic-CD type of drug carriers can exploit the ability of CDs to encapsulate anti-cancer drugs, even highly lipophilic ones, and to solubilize them in aqueous solutions while obtaining site-specific delivery via the peptidic conjugate (Schaschke et al., 2000). Moreover, the CDs are able to stabilize (Haeberlin et al., 1996) and increase the water solubility of high molecular weight peptides, even without covalently bonding to them, which can provide a larger therapeutic window with higher selectivity (Arnusch et al., 2012). In addition to cancer research, at present CD-based dimers are being studied for their ability to interrupt the peptide aggregation leading to Alzheimer's disease (Wahlström et al., 2012).

3.1.2 Production Methods of Complexes

Complexation of lipophilic guest molecules with CDs in aqueous solutions is usually a spontaneous interaction in which the guest escapes the surrounding media into the cavity of the CD.

3.1.2.1 Doxorubicin as Guest Molecule in a Cyclodextrin-based Complex

Doxorubicin (Dox), Figure 3.1, also known as Adriamycin, belongs to the anthracycline family, a well-known antibiotic drug that is widely used in anti-cancer treatments. The anthracycline type drugs are ranked among the most effective oncological treatments discovered so far. The cytotoxicity mechanism of Dox is via interaction and modification of the DNA structure by disturbance of various DNA-related processes such as replication, transcription, and repair mechanisms (Frederick et al., 1990).

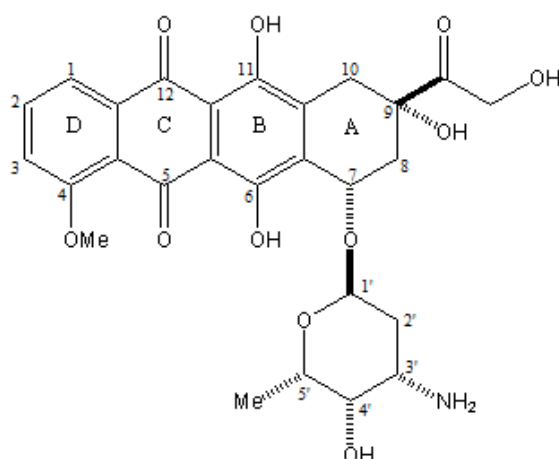


Figure 3.1- Doxorubicin (Dox)

The anthracycline type drugs are known to create reactive oxygen species (ROS) (Šimůnek et al., 2009) which have a highly cytotoxic effect that can result in various adverse side effects such as major cardiac damage (Green and Leeuwenburgh, 2002). To overcome extravasation of Dox during administration and to partially scavenge the created radicals, a delivery mechanism by DMSO was clinically tested (Lopez et al., 1999). DMSO is known to pass the dermal barrier and penetrate easily within tissues without causing irreversible damage. Due to its unique biological features, DMSO has been used in medicine since the 1960s as an analgesic, an anti-oxidant and a drug delivery vehicle (Tucker and Carrizo, 1968). Addition of DMSO to the administration of Dox can aid in rapid transfer of Dox through the tissues and

promote the drug into the blood circulation and can also reduce Dox-induced skin ulcers (Hajarizadeh et al., 1994).

Another way of preventing the creation of the ROS is through protection of the quinone group by complexation with a CD (Swiech et al., 2012). A significant drawback in the clinical efficiency of the anthracyclines is their tendency to self-aggregate (Evstigneev et al., 2006; Barthwal et al., 2008). Self-association of these drugs influences greatly their anticancer action in several ways such as causing difficulties in crossing the cell's lipid bilayer and the ability to interact with the DNA helix (Agrawal et al., 2009). It was discovered that when Dox in its monomer and dimer structures was conjugated with micelle-based carriers, the Dox monomer showed significant antitumor activity while the dimer showed no antitumor activity by itself (Nakanishi et al., 2001).

Dox has also been shown to interact with other widely consumed aromatic molecules, such as caffeine, which lowers its pharmacological activities (Piosik et al., 2002). Consequently, encapsulation of Dox inside a CD can significantly increase its medico-biological activity within the body by prevention of unwanted encapsulation to various molecules, yet maintenance of its cytotoxicity, while simultaneously lowering the potential creation of free radicals by maintaining the minimal needed dose and the protection of the quinine group from hydrolysis (Anand et al., 2012; Swiech et al., 2012).

3.1.3 Characterization of Cyclodextrins and Their Complexes

The high density of electrons located inside the CD's cavity can change the local environmental polarity affecting the electronic transitions and hence the optical behaviour of both the guest and the CD. Accordingly, inclusion complexes are widely studied by various analysis methods, such as UV-visible spectrophotometry, fluorescence, IR, and various NMR (Singh et al., 2010).

3.1.3.1 High-Performance Liquid Chromatography

Liquid chromatography (LC) is a well-established method for separation of chemical mixtures in the liquid phase by an absorbent material (McMaster, 2007). All the existing variations of this method consist of a stationary phase and a mobile phase which moves over the immobilized one (Weston and Brown, 1997; Dong, 2005). The working principle behind this technique lies in the interactions of a sample with both of the stationary and the mobile phases. In high-performance liquid chromatography (HPLC) the liquid mobile phase is pumped through the stationary phase located in a column.

The main parts of any HPLC system are a sample injector, a pump, a stationary phase column and a detector, such as an UV sensor (Dong, 2006). The initial HPLC measurements, nowadays referred to as 'normal HPLC', were performed on a hydrophilic stationary column (such as unmodified alumina or silica), allowing the hydrophobic samples to be eluted first (Jiskoot and Crommelin, 2005). Currently, it is more common to use reversed phase HPLC (RP-HPLC), which utilizes an hydrophobic stationary phase (such as octadecyl carbon chain bonded silica (C18)) with a more polar mobile phase (H₂O and methanol/ acetonitrile), this is useful especially when working with peptides (Synder et al., 2010).

3.1.3.2 Thin-Layer Chromatography

The working principle of thin-layer chromatography (TLC) also known as 'planar chromatography' is identical to that of HPLC described above. The only variation between HPLC and TLC is in the method of the sample transportation. Where, in HPLC, the sample is pressed out by a high pressure pump, in TLC the movement of the sample on the stationary phase is due to capillary forces (Kazakevich and LoBrutto, 2007). In the current work, TLC was used as a monitoring tool to follow the formation of the carrier and to distinguish it from any unwanted by-products (Caliceti et al., 2003).

3.1.3.3 Ultraviolet – Visible and Fluorescence Spectrometry

The principle of UV - visible light spectrometry is based on the interactions of photons with an electron cloud in a material. This interaction promotes the electron to a higher energy level that corresponds to a specific wavelength. Recording of the degree of absorption by the sample at different wavelengths will produce a nominal UV spectrum, being the plot of the absorbance (A) versus the wavelength (λ [nm]) (Thomas and Burgess, 2007). The energy needed to excite an electron depends on its orbital location, as presented in Figure 3.2.

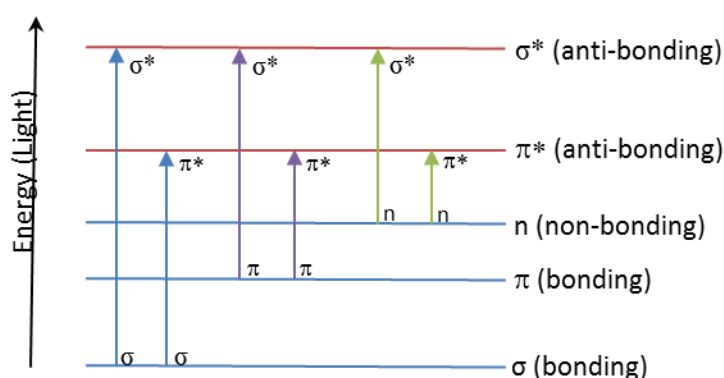


Figure 3.2- Transition between orbitals

According to the energy levels shown in Figure 3.2, mostly the n-electrons (non-bonding) and π -electrons will be excited by ultraviolet and visible light. Hence, the wavelength of absorption can indicate the character of the sample molecule (Krupadanam et al., 2001).

Since the beginning of the 1950's, CDs were discovered to be quite useful in determining the spectrophotometric properties of many compounds and materials. When the CDs form complexes with a substance and/or a colouring agent, they can modify the properties of the reagent. Examples of such changes are increased solubility and / or stability of the reagents in different solution environments, increased sensitivity of colour reactions and even improvement in their selectivity (Liu and Purdy, 1992). Various groups worldwide that have studied the interactions of α , β , and γ CD and their conjugates in host-guest complexes by spectrographic means have demonstrated the inclusion complexation formation through UV-spectroscopy. The results have shown that CDs have the ability to increase (Li et al., 2010) as well as decrease (Swiech et al., 2012) the absorption of the guest molecules.

In addition to studying various chemical changes occurring due to complexation by UV measurements, the binding constant (K_{binding}) of the created complex can be established (Wang and Eaton, 1985). K_{binding} represents the level of interaction that occurs between the guest molecule and the carrier. The widely used method for calculation of the K_{binding} is the Benesi-Hildebrand method (Benesi and Hildebrand, 1949), as described in Equation 3.1:

$$\frac{1}{\Delta A} = \frac{1}{\Delta\epsilon[G]} + \frac{1}{\Delta\epsilon[G][H]} \cdot \frac{1}{K_{\text{binding}}}$$

Equation 3.1- K_{binding} calculation via Benesi-Hildebrand method

where ΔA is the difference between the absorption of the complex and that of the free guest, $\Delta\epsilon$ is the difference in the absorption constants, $[G]$ the concentration of the guest (Dox), $[H]$ the concentration of the host (carrier) and K_{binding} is the binding constant. Following the assumption of 1:1 complex formation, one can calculate K_{binding} by plotting $1/\Delta A$ vs. $1/[H]$: the ratio of the intercept to the slope will provide the value of K_{binding} . The same calculation method could also be applied in fluorescence studies of CD inclusion complexes (Park and Song, 1989; Mukhopadhyay et al., 2005; Lu et al., 2009).

Fluorescence can be defined as the spontaneous emission of light from an electronically excited molecule. As previously described, photons have the ability to excite the electrons of substances to higher energy levels (Figure 3.2). In specific molecules, the de-excitation process results in spontaneous light emission (Valeur and Berberan-Santos, 2012).

Fluorescence spectrometry in many cases can provide more specified data than can be achieved by a UV spectrum due to its higher detection limit. The parental CDs are

spectroscopically inert, meaning that typically they will not interfere with the guest fluorescence signal. Similarly to UV spectroscopy, the CDs are able to enhance (Frankewich et al., 1991; Liu et al, 2002; Lu Z. et al., 2009) or quench (Mukhopadhyay et al., 2005) the emitted fluorescence signal of the guest molecule. In addition to tracing the fluorescent signals of the guest, the CDs can be substituted with fluorescent markers that can aid in molecular recognition of various substances (Ueno, 1996). Moreover, the formation of inclusion complexes can also provide information on the reaction of different molecules with each other, e.g. by 3D fluorescence scanning (Zhang and Xiong, 2012).

3.1.3.4 Nuclear Magnetic Resonance

The principles of nuclear magnetic resonance (NMR) were previously explained in Section 2.4.5 as the basis for MR imaging. In chemical analysis, tracking of the slight changes in the resonance frequency of certain atoms can provide insight into the structure and consistency of the investigated substance. The difference between the resonance frequency of the atom and the reference sample (usually tetramethylsilane (TMS) for ^1H and ^{13}C -NMR), divided by the precessional frequency (ω_0) (Equation 2.13) of the operating magnet is referred to as the chemical shift (δ) of the element (Balci, 2005). As the change in frequency between the sample and the reference is very small (measured in Hz) and the operating frequency of the magnet is given in MHz, the chemical shift is presented in ppm.

An important phenomenon present in NMR spectra of molecules is a split in the recorded peaks of a single atom in a molecule. This phenomenon is attributed to the spin-spin splitting that occurs as a result of atoms neighbouring the measured one. The positive and negative contributions of the neighbouring atoms contribute to the overall alteration of the applied magnetic field sensed by the measured atom and, as a result, cause a split in its NMR signal. The size of the split (in Hz) is referred to as the coupling constant (J) (Jacobsen, 2007). The intensity and type of split are defined by Pascal's triangle and dependent on the number and nature of the neighbouring spin active atoms.

NMR spectroscopy can be used not only to identify the consistency of a substance, but also to gain information on its 3D structure. Possible techniques to achieve such information are via NOESY or COSY measurements. These methods are based on tracking of changes occurring in different atoms due to irradiation at the resonance frequency of a certain atom in the molecule. Due to irradiation in COSY measurements, only the influence of covalently bonded atoms will be reordered, whereas in NOESY any atom in the spatial area of less than 5 Å will produce a signal, regardless of covalent bonding. Subtraction between the achieved readings of the two methods will yield the sole 3D interactions of unbonded atoms, which,

with proper attribution of the atoms, can indicate the 3D structure of the molecule (Holzgrabe et al., 1999).

CDs probed by NMR NMR is considered to be the most powerful and conclusive tool in identifying CD-based inclusion complexes (Fernandes, 2003). In the early 1970s, the milestones were established for the use of NMR as a complexation monitoring method. Throughout this period, it was observed by ^1H -NMR that, due to shielding of the inner cavity protons (3H, 5H) by the guest molecule, a significant upfield shift occurs. On the other hand, the hydrogen atoms located on the exterior of the cavity (2H, 4H, 6H) are generally not affected (Singh et al., 2010). Although it was initially discovered in ^1H -NMR, nowadays ^{13}C -NMR, ^{15}N -NMR, ^{31}P -NMR and ^{19}F -NMR are also in use for studies of inclusion complexes, even with solid samples (Cabral Marques, 2010).

3.1.3.5 Diffusion Ordered Spectroscopy

DOSY is an NMR-based method for discovery of the diffusion coefficient (D) of molecules in solution. The diffusion rate of molecules can indicate the dynamics of a molecule in solution and provide information on its molecular structure and organization within the medium. The working principle behind this method is in observation of the NMR signals attenuation during an applied pulsed field gradient. The recorded decay in signal corresponds to the diffusion rate of the molecule (Loening et al., 2001). In complex formations, the measurement of D can indicate the percentage of the guest encapsulation within a host molecule (Calderini et al., 2012). Equations for calculation of D, the percentage of complexation and the relation between D and M_w of the molecule can be found in Appendix i.

3.1.4 Aims and Objectives

This chapter will mainly focus on the synthesis of the novel nanocarrier utilized for *in-vitro* and possible *in-vivo* delivery of anticancer agents. The full synthesis of the monosubstituted γCD will be presented together with the chemical analysis of the yield. Moreover, the investigation of the carrier - Dox complex will be discussed and examined by various methodologies.

3.2 Materials and Methods

3.2.1 Materials

Table 3.1- Equipment and chemicals

Material	Manufacturer	Place of Origin	Notes
Equipment			
400 MHz NMR spectrometer	Bruker	USA	Model: Advance III
500 MHz NMR spectrometer	Bruker	USA	Model: Advance III
HPLC	Sedere	France	Model: SEDEX 75
UV Reader	Anthos	USA	Model: Multiread 400
Fluorescence spectrophotometer	Agilent Technologies	USA	Model: Varian Cary Eclipse
ELISA reader	Tecan	UK	Tecan infinite M200
Freeze-dryer	Labconco	USA	Model: Freezone 2.5 Plus
Reversed-phased column	Merck	Israel	Model: LiChroprep
Arguslab 4.0.1	Mark Thompson	USA	Version: v.2.1.10
Chemicals			
P ₂ O ₅	Sigma Aldrich	Israel	
γCD	Sigma Aldrich	Israel	
Amino acid derivatives	Sigma Aldrich	Israel	
Doxorubicin (Dox)	Sigma Aldrich	Israel	
Dimethylformamide (DMF)	Sigma Aldrich	Israel	
Dimethyl Sulphoxide (DMSO)	Sigma Aldrich	Israel	
Trifluoroacetic Acid (TFA)	Sigma Aldrich	Israel	
4,4-Dimethylaminopyridine (DMAP)	Sigma Aldrich	Israel	
N,N-Dicyclohexylcarbodiimide (DCC)	Fluka	Israel	
1-Hydroxybenzotriazole (HOBT)	Sigma Aldrich	Israel	
N-Boc-3-(2-naphthyl)-L-alanine	Sigma Aldrich	Israel	
Dichloromethane (CH ₂ Cl ₂)	Sigma Aldrich	Israel	
Sulphuric Acid	Sigma Aldrich	Israel	
Ninhydrine	Sigma Aldrich	Israel	
Acetone	Sigma Aldrich	Israel	
Methanol	Sigma Aldrich	Israel	
Phosphate Buffered Saline (PBS)	Sigma Aldrich	Israel	
Dimethyl Sulphoxide _{d6} (DMSO _{d6})	Sigma Aldrich	Israel	

D₂O	Sigma Aldrich	Israel	
Acetonitrile (AcN)	Sigma Aldrich	Israel	
Consumables			
96-well plates	Greiner	Austria	Polystyrene cell culture microplates with μ Clear [®] bottom
UV Cuvettes	Yavin-Yeda	Israel	4 ml volume
TLC plates	Yavin-Yeda	Israel	Silica gel 60
PLC plates	Yavin-Yeda	Israel	Silica gel 60 F254

3.2.2 Methods

3.2.2.1 Synthesis

Two isomers of the carrier were produced via the synthesis specified below, with dependence on the stereochemistry of the added amino acid derivative. The D isomer was named Ca-1688 and the L isomer Ca-1709. In this chapter the term 'carrier' refers solely to the D isomer.

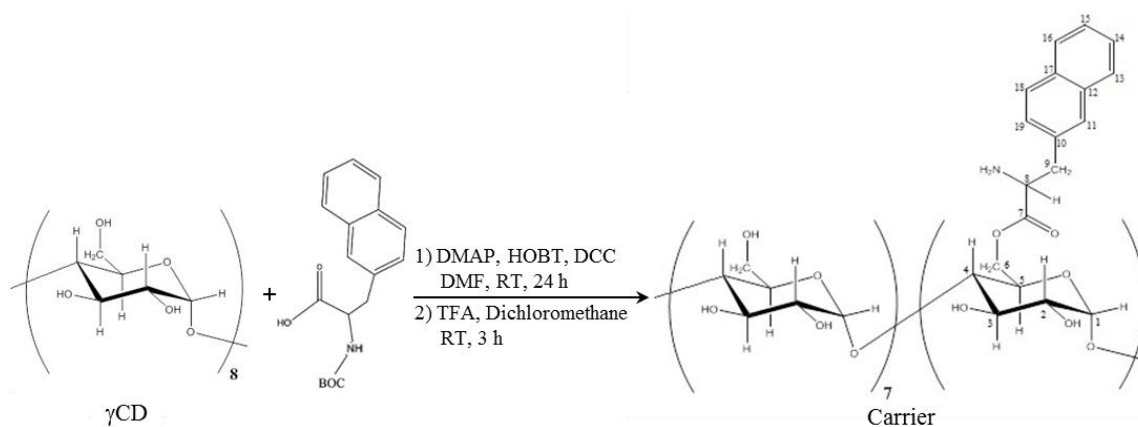


Figure 3.3- Synthesis of carriers Ca-1688 and Ca-1709

Prior to the synthesis, γ CD was dried at 110°C /0.1 mmHg in the presence of P_2O_5 for 24 h. Amino acid derivatives, DMF, DMSO, TFA, DMAP, DCC, and HOBT were used without further purification. The synthesis of the carrier in use was achieved via a two-step reaction as described in Figure 3.3. The first step was the coupling of γ CD with the N-Boc-3-(2-naphthyl)-L/D-alanine, using DDC, DMAP and HOBT in DMF and the second step was the removal of the N-protecting Boc group from the compound using CF_3COOH in CH_2Cl_2 . To couple the γ CD with the amino acid derivative, 12.97 g (10 mmol) of γ CD, 1.22 g (10 mmol) DMAP, 1.35 g (10 mmol) HOBT, 3.15 g (10 mmol) N-Boc-3-(2-naphthyl)-L/D-alanine and 4.12 g (20 mmol) DCC, were dissolved in 50 ml DMF and stirred at 25°C for 24 h.

The white precipitate was removed by filtration and the filtrate solution was added dropwise with stirring into 500 ml of hot acetone. The white solid product was then filtered and dried under vacuum. The purification of the compound was done by reversed phase column chromatography. The crude product was dissolved in 500 ml of hot water (60 - 90°C) and the resulting solution was applied to a reversed-phase column (300 g of LiChroprep RP-18, 40 - 63 μm ; 50 mm x 260 mm). The column was eluted with water (500 ml), methanol: water 20:80 (1000 ml), 40:60 (1000 ml), 60:40 (1000 ml) and 100% methanol (500 ml) at flow rate of 20 ml per min and detected by TLC. Fractions of 80 ml volume were collected. The desired yield was eluted with the mixture of methanol: water 30:70.

The removal of the protective Boc group (step 2 in Figure 3.3) was done by dissolving the yield in 20 ml TFA and 20 ml CH_2Cl_2 , and the mixture was stirred at 25°C for 3 h following which the solvent was removed by evaporation under reduced pressure (<25°C).

The residue was dissolved in 5 ml H_2O and poured into 200 ml methanol. The reason for using methanol is that, while the carrier does not dissolve in it, some impurities do, and more importantly, it can remove any traces of TFA. The white precipitate was washed three times with 100 ml acetone and then dried under vacuum at 70°C overnight. The solid product was dissolved in 20 ml of D_2O , until complete dissolution. The solution was freeze-dried for 3 days, finally affording small white crystals.

3.2.2.2 Dox Encapsulation within the Carrier

The complexation between the carrier and the guest molecule, Dox, is a spontaneous process which occurs in aqueous solutions without any external aid. Hence, the encapsulation of Dox was performed in aqueous solutions by addition of the carrier into the final Dox solution. Normally, the Dox was kept at high concentrations of 100 mM, dissolved in DMSO as a stock solution in the dark at 4°C¹. For complexation purposes the Dox was diluted at least by a factor of 1000 (maximal final concentration of DMSO in the final Dox solutions was 0.1%) in an aqueous medium (H_2O / Culture Medium) in the dark at RT.

The main reason for the utilization of DMSO as the stock solution medium is it being a well-known method for dissolving Dox (Panta e al., 2004; Lu, F. et al., 2009). In addition, in the presence of CDs it can possibly aid in the prevention of the Dox cleavage and generation of ROS (Swiech et al., 2012), and, although not very likely in the concentration used, it can potentially promote the process of drug penetration within the cells (Tucker, E.J. and Carrizo A., 1968).

¹ full description can be found in 5.2.2.6.

3.2.2.3 Chemical and Structural Analyses of the Carrier and the Created Complex

TLC The synthesis was monitored by TLC. The TLC analyses were performed on silica gel 60 TLC plates and silica gel 60 F254 PLC plates (Caliceti et al., 2003) with 1-butanol: ethanol: $\text{NH}_4\text{OH}_{\text{conc.}}$ (32% w/v aq.) [4:5:6 (v/v/v)] eluents. Spot detection was carried out by UV light and by spraying with 5% v/v concentrated sulphuric acid in ethanol, for detection of all the materials, or ninhydrine solution (0.3 g ninhydrine, 97 ml 1-butanol and 3 ml acetic acid), for detection of the free amino groups, and heating at 150°C for 5 min.

HPLC HPLC analysis was performed on a Thermo Electron instrument equipped with UV/Vis & ELSD (Sedex 75) detectors. The column in use was a Gemini 5 μm octadecyl carbon chain bonded silica (C18) (110 Å, 250-4.6 mm) mobile phase: Acetonitrile (AcN) / H_2O , with a gradient elution from 98% H_2O / 2% AcN to 10% H_2O / 90% AcN within 30 min at a constant flow rate of 1.2 ml / min (Table 3.2).

Table 3.2- HPLC elution solvents

Time (min)	H_2O (%)	AcN (%)
0	98	2
10	50	50
15	10	90
20	98	2
25	98	2

The UV signal was measured at $\lambda = 254$ nm.

Fluorescence Spectrometry For fluorescence spectrometry studies, a solution of 4 μM Dox was prepared by dilution² of the Dox in DMSO stock solution into PBS, with the final concentration of DMSO being 0.04%. To 8 ml of the final 4 μM Dox solution, 3.8 mg^1 of carrier was added to obtain the concentration of 320 μM (1:80 Dox: carrier ratio). Double dilutions of the carrier in constant 4 μM Dox were performed to obtain the following Dox: carrier ratios: 1:40; 1:20; 1:10; 1:5; 1:2.5; 1:1.25. Each solution was transferred into a 4 ml cuvette and the fluorescence was measured at $\lambda_{\text{excitation}} = 480$ nm, $\lambda_{\text{emission}} = 500 - 800$ nm (λ_{max} chosen to be 592 nm), with excitation and emission slits of 10 nm.

NMR ^1H -NMR and ^{13}C -NMR spectra of Dox, carrier and the complex at various concentrations were recorded on a 500 and 400 MHz Advance III spectrometer with

² Full equations can be found in 5.2.2.6.

deuterated DMSO (DMSO_{d6}) or deuterated water (D₂O) as a solvent. All the chemical shifts are expressed as δ units (ppm).

DOSY DOSY measurements were conducted to establish the change in D of the Dox and the carrier as a result of the complexation. For this purpose, each of the free substances and their complex were dissolved in D₂O and transferred to dedicated tubes. A series of longitudinal eddy-current delay (LED) sequences (Cohen et al., 2005; Evan-Salem et al., 2007) were applied, and the signal decays of the tested substances at 500 and 400 MHz were recorded.

3.3 Results

3.3.1 **Synthesis**

Following the purification process as described in Section 3.2.2.1, the obtained yield was 7.61 g (51%). The 49% unwanted yield consisted of about 40% starting materials and about 9% di-substituted and tri-substituted products.

3.3.2 **Chemical and Structural Analyses of the Carrier and the Complexation with Dox**

3.3.2.1 **Thin-Layer and High-Performance Liquid Chromatography**

To analyse the conjugated product of the carrier synthesis, TLC and HPLC were conducted. The TLC R_f value of the carrier was 0.5 relative to the solution described in Section 3.2.2, whereas the R_f of unsubstituted γ CD was 0.3 and the di- and tri-substituted CDs were 0.65 and 0.75, respectively. Figure 3.4 depicts the HPLC graph as detected by a UV detector, corresponding to the carrier in the stationary and mobile phases as described in Section 3.2.2.3.

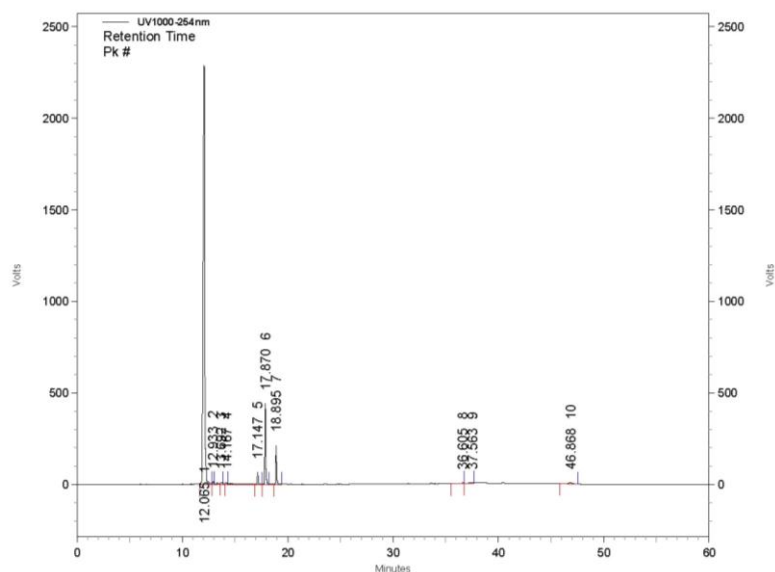


Figure 3.4- HPLC measurement of the carrier

3.3.2.2 Fluorescence Spectroscopy

The fluorescence spectrum of Dox at constant concentration with increasing concentrations of carrier was recorded and K_{binding} was calculated from the changes in the peak at 592 nm.

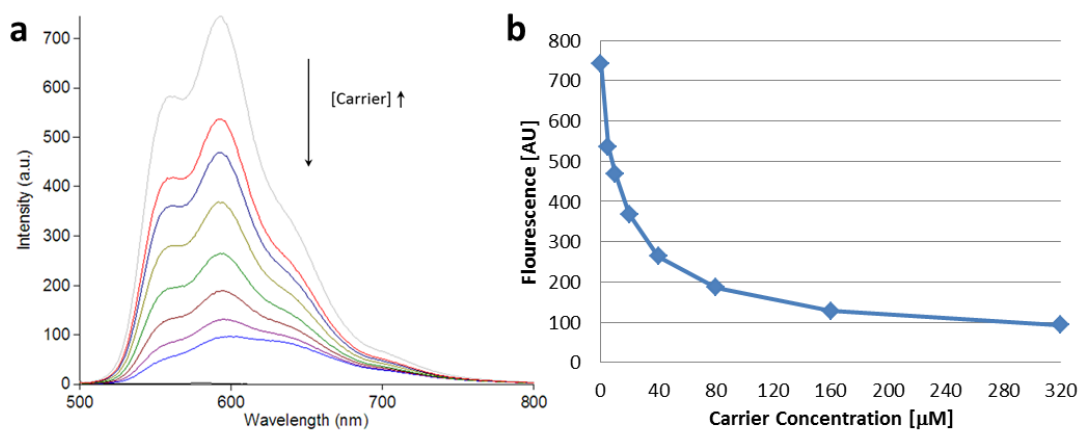


Figure 3.5- (a) Fluorescence spectrum of Dox with increasing carrier concentrations and (b) Dox fluorescence at 592 nm as a function of carrier concentration

The left side of Figure 3.5 represents the recorded fluorescence spectrum of Dox at increasing concentrations of carrier (0 - 320 μM), the right side of the figure depicts the fluorescence at the peak, 592 nm, of Dox with increasing carrier concentrations.

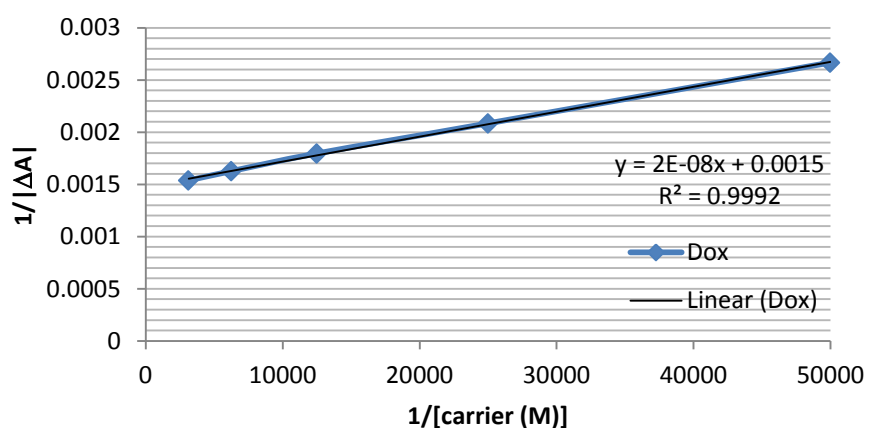


Figure 3.6- Benesi-Hildebrand plot of Dox fluorescence

In Figure 3.6, the change in the fluorescence of Dox is presented in a Benesi-Hildebrand plot, where the ratio of the intercept and the slope (equation presented top right) gives K_{binding} for the complex.

3.3.2.3 Nuclear Magnetic Resonance

$^1\text{H-NMR}$ $^1\text{H-NMR}$ measurements were conducted in different solvents for an unmodified γCD , the synthesized carrier, Dox and the complex solution of carrier and Dox. The measured spectra and the chemical shift attribution are presented in Figure 3.7- 21 and Table 3.3- 4.

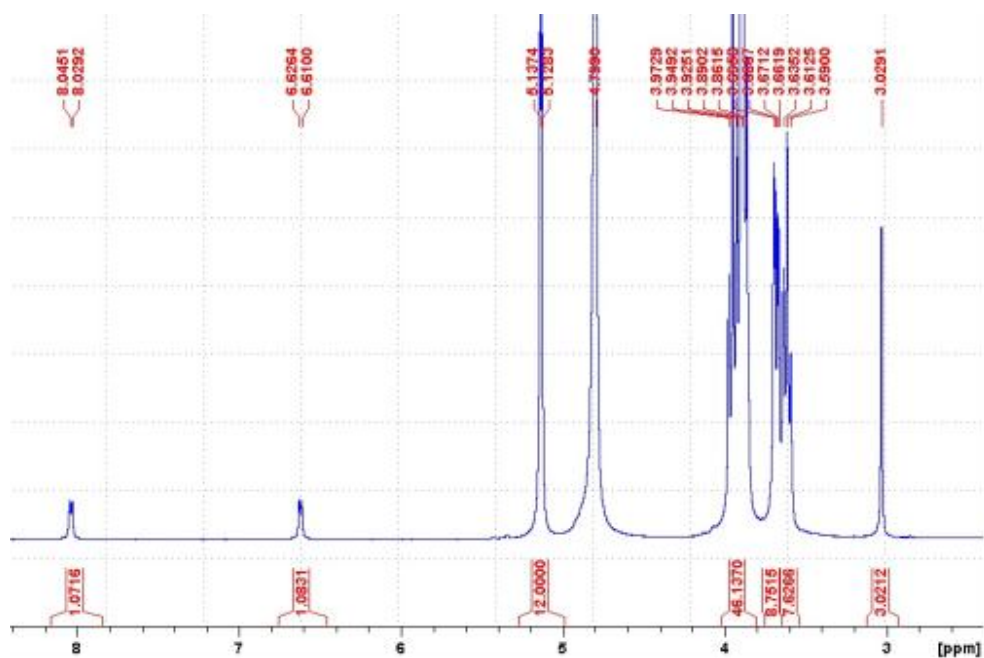


Figure 3.7- $^1\text{H-NMR}$ spectrum of γCD in D_2O

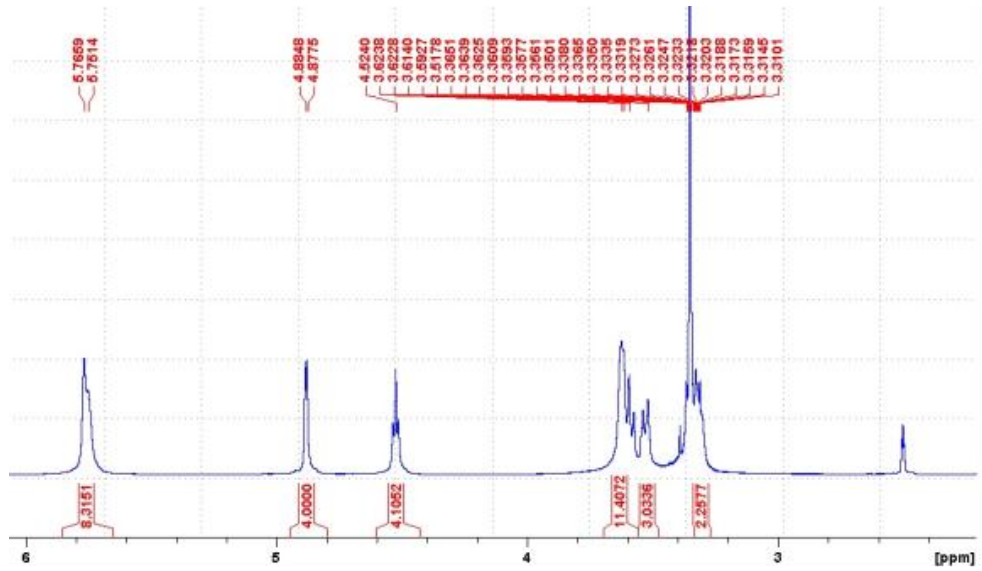


Figure 3.8- $^1\text{H-NMR}$ spectrum of γCD in DMSO

Figure 3.7 and Figure 3.8 present the measured $^1\text{H-NMR}$ spectra of 20 mM γCD performed at 400 and 500 MHz in $\text{DMSO}_{\text{d}6}$ and D_2O , respectively.

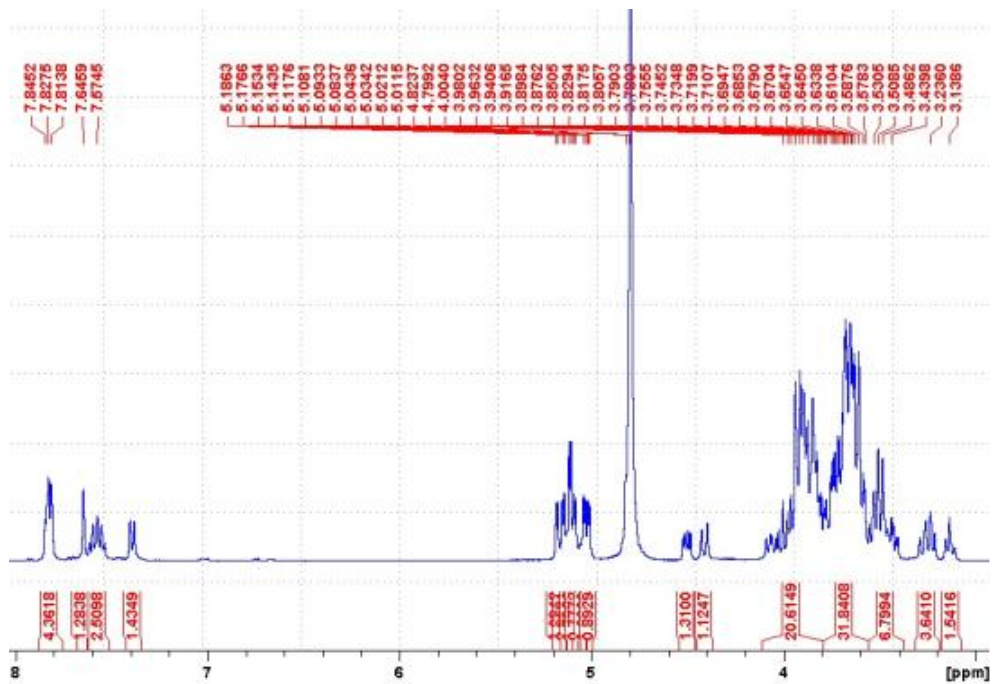


Figure 3.9- $^1\text{H-NMR}$ spectrum of the carrier in D_2O

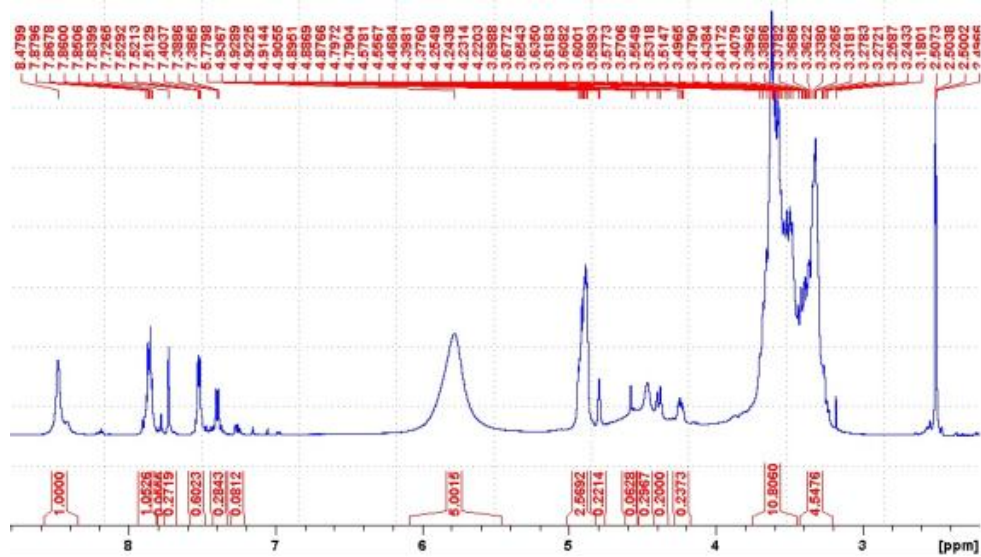


Figure 3.10- $^1\text{H-NMR}$ spectrum of the carrier in DMSO

Figure 3.9 and Figure 3.10 present the measured spectrum of $^1\text{H-NMR}$ of 20 mM carrier performed at 400 and 500 MHz in DMSO_{d6} and D_2O , respectively.

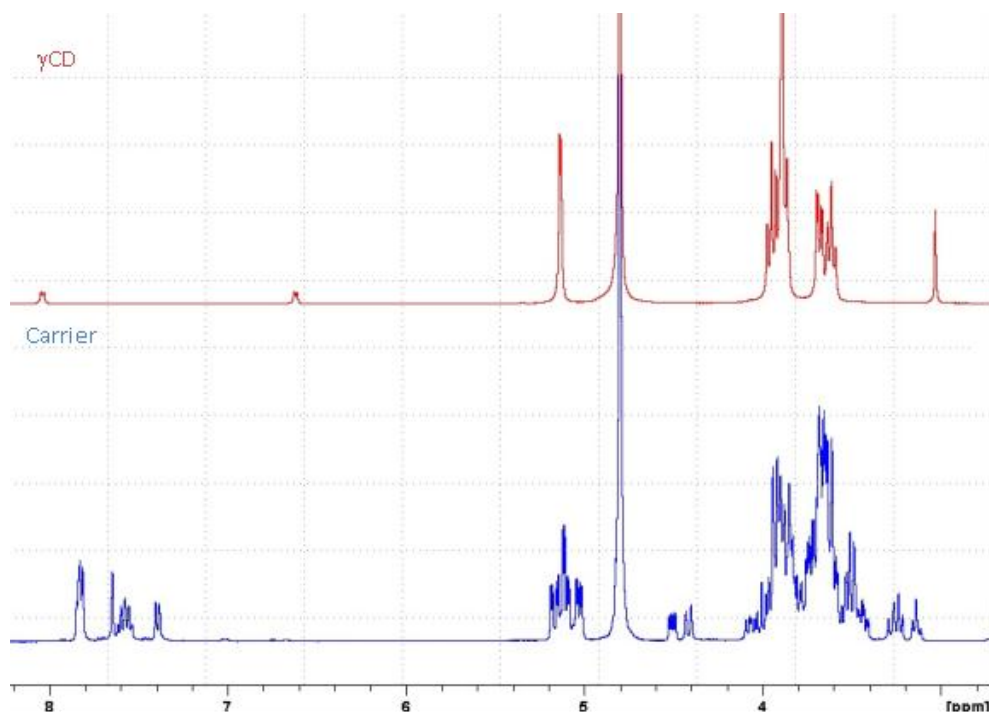


Figure 3.11- $^1\text{H-NMR}$ spectrum of γCD (top) and carrier (bottom) in D_2O

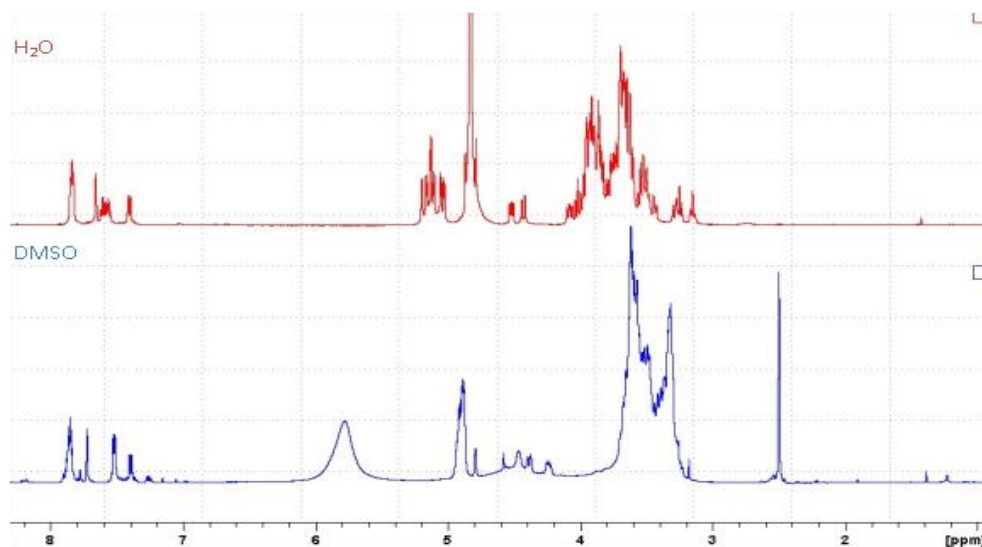


Figure 3.12- ^1H -NMR spectra of the carrier in D_2O (top) and DMSO (bottom)

For comparison, Figure 3.11 depicts both of the ^1H -NMR spectra of 20 mM γCD (top) and 20 mM carrier (bottom) performed at 400 MHz in D_2O , while Figure 3.12 depicts the ^1H -NMR spectra of 20 mM carrier in D_2O (top) and DMSO (bottom).

Table 3.3 summarizes all the observed chemical shifts of the γCD and the carrier in different solvents and concentrations (hydrogen numbering as presented in Figure 3.3).

Table 3.3- ^1H -NMR chemical shifts of γCD and the carrier

Concentration	20mM	20mM	10mM	20mM	20mM
Solvent	D_2O	DMSO	D_2O	D_2O	DMSO
Hydrogen/ δ (ppm)	γCD		Carrier		
4H (dd)	3.02	3.32	3.26	3.20	3.47
2H (dd)	3.61	3.52	3.53	3.52	3.47
6H (d)	3.68	3.62	3.70	3.68	3.47
5H (td)	3.88	4.52	3.84	3.79	3.47
3H (dd)	3.95	4.88	4.01	3.97	3.47
9H (d)			4.40	4.41	4.46
8H (dd)			4.54	4.50	4.91
1H (d)	5.13	5.76	5.13	5.10	5.78
19H (m)			7.45	7.39	7.39
15H (m)			7.67	7.57	7.51
14H (m)			7.67	7.57	7.51
11H (m)			7.73	7.65	7.73
18H (m)			7.89	7.81	7.87
16H (m)			7.91	7.83	7.87
13H (m)			7.94	7.85	7.87

In addition to the $^1\text{H-NMR}$ measurements of γCD and the carrier, $^1\text{H-NMR}$ evaluation of Dox at different concentrations and solvents was performed. The obtained spectra and chemical shifts are presented below.

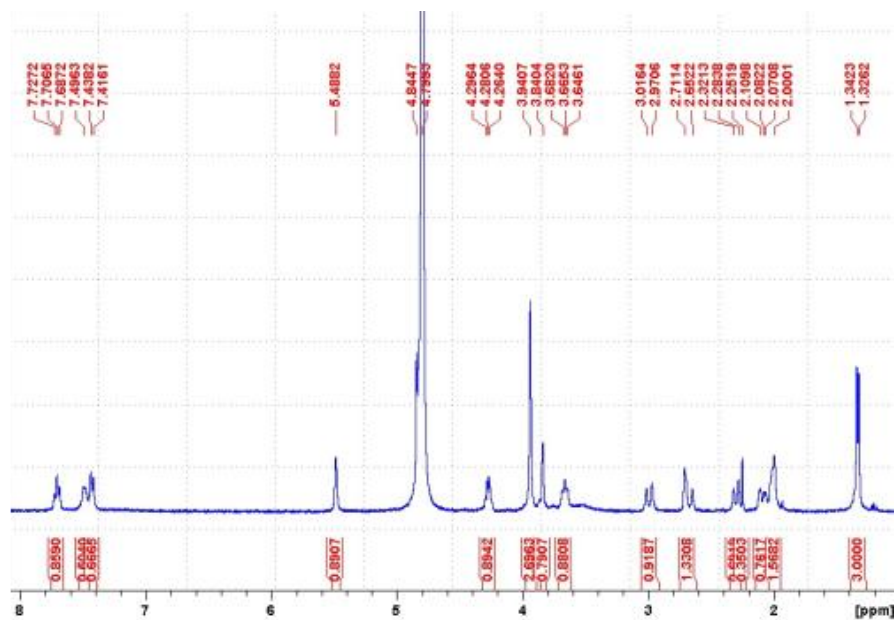


Figure 3.13- $^1\text{H-NMR}$ spectrum of Dox in D_2O

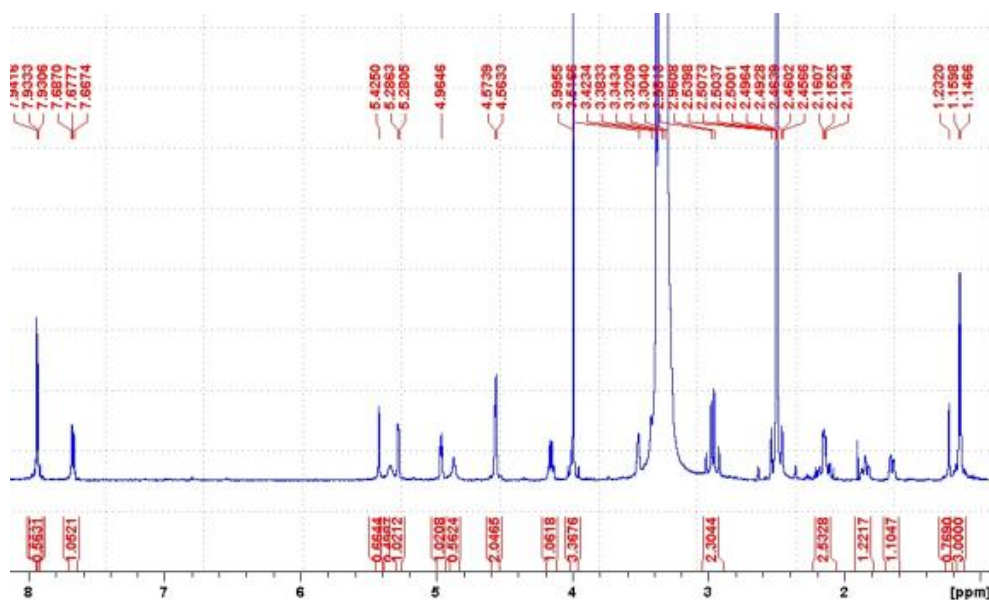


Figure 3.14- $^1\text{H-NMR}$ spectrum of Dox in DMSO

Figure 3.13 and Figure 3.14 present the measured spectrum of $^1\text{H-NMR}$ of 2 mM Dox performed at 400 MHz and 500 MHz in DMSO-d_6 and D_2O , respectively.

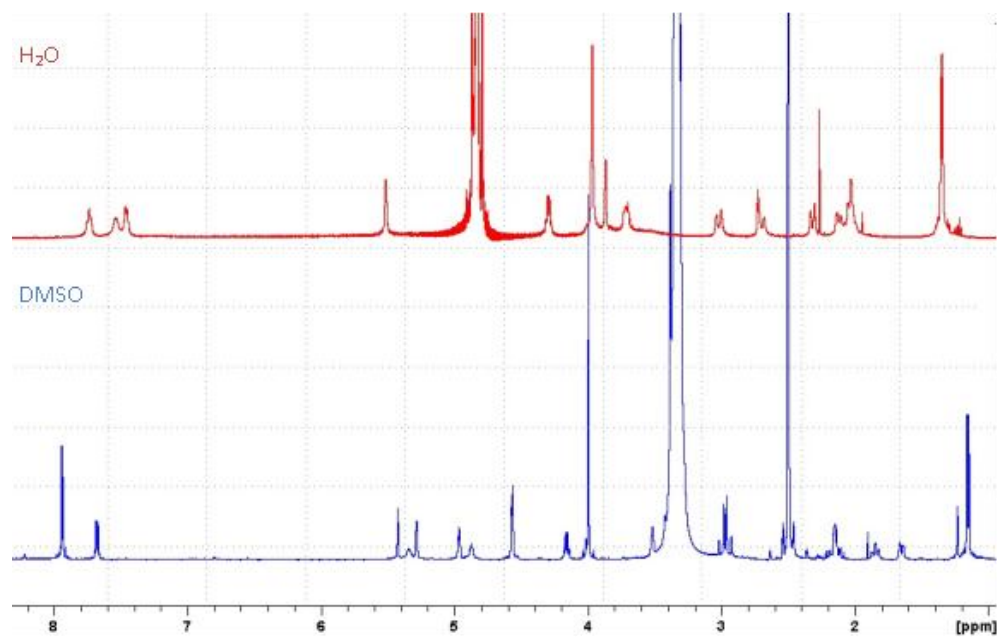


Figure 3.15- Comparison between ¹H-NMR spectra of 2 mM Dox in D₂O (top) and DMSO (bottom)

As mentioned previously, Dox has a tendency to self-aggregate above certain concentrations. This phenomenon was observed by ¹H-NMR measurements at different concentrations of Dox. Figure 3.16 compares ¹H-NMR spectra of 2 and 10 mM Dox in D₂O.

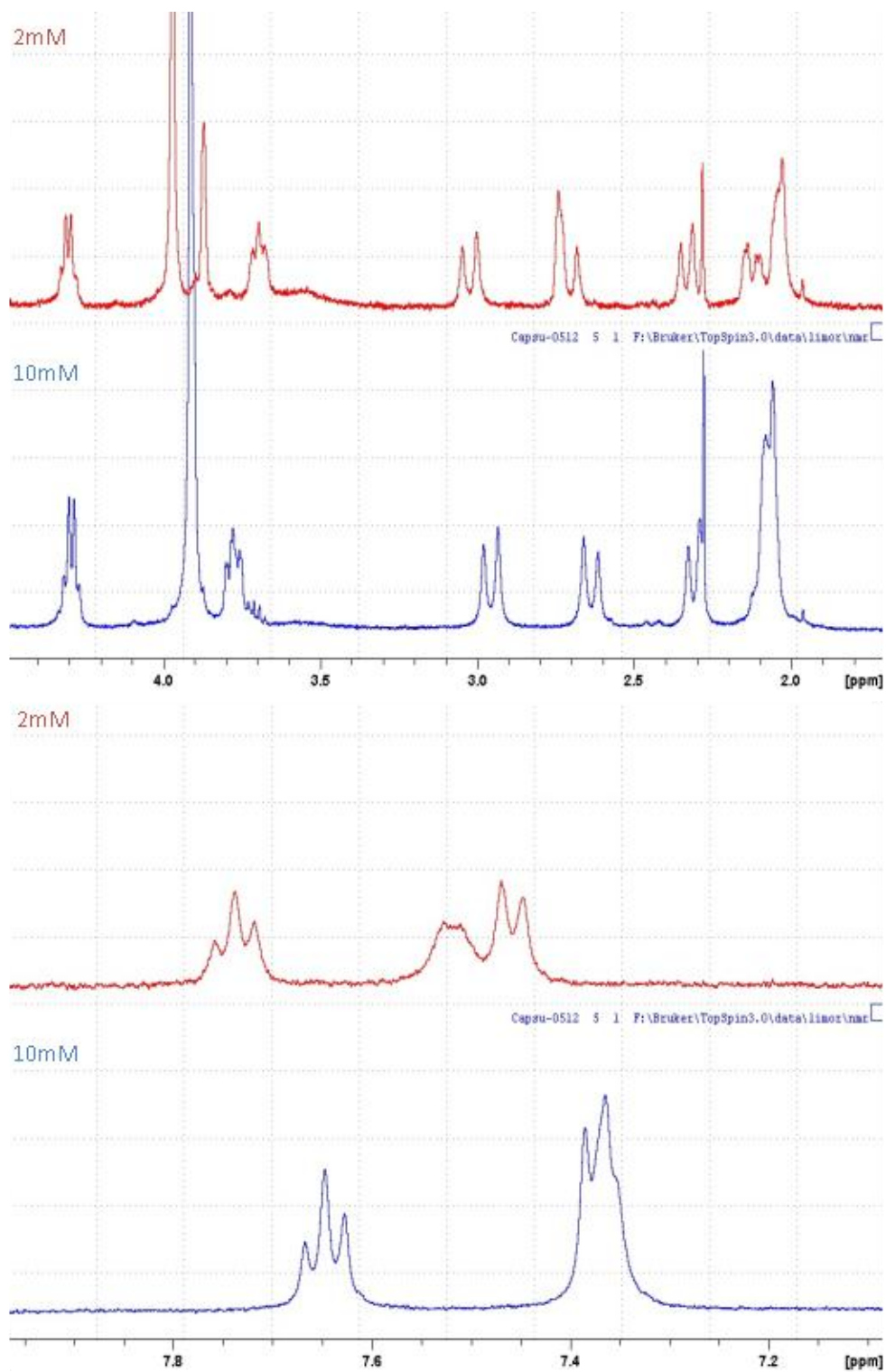


Figure 3.16- $^1\text{H-NMR}$ spectra of Dox in D_2O at 2 mM (top) and 10 mM (bottom)

Table 3.4- ¹H-NMR chemical shifts of Dox

Hydrogen/ δ (ppm)	Measurement				Literature			
	10 mM	2 mM	Δ Con .*	2 mM	Agrawal et al. (2009)	Barthwal et al. (1994)	Mondelli and Ragg (1987)	
Concentration	10 mM	2 mM	Δ Con .*	2 mM	Δ Con. 8 mM-0.01 mM *	11.5 mM	5.8 mM (1 mg/ml)	17.4 mM (30 mg/ml)
Solvent	D ₂ O	D ₂ O, 0.01% DMSO	D ₂ O	DMSO	D ₂ O	D ₂ O	D ₂ O	DMSO
5' CH ₃ (d)	1.37	1.33	0.03	1.15	0.02	1.34	1.29	1.16
2' Heq (ddd)	2.07	2.05	0.02	1.65	-0.01	2.04	1.98	1.90
2' Hax (ddd)	2.07	2.05	0.02	1.88	-0.01	2.04	2.03	1.71
8 Hax (dd)	2.30	2.14	0.17	1.88	-0.24	2.04	2.06	2.11
8 Heq (dd)	2.30	2.14	0.17	2.15	-0.28	2.28	2.28	2.18
10 Hax (d)	2.64	2.68	-0.04	2.97	-0.68	2.60	2.68	2.87
10 Heq (d)	2.96	2.99	-0.04	2.97	-0.49	2.93	2.95	2.97
3' H (td)	3.75	3.66	0.08	3.33	0.10	3.76	3.68	3.32
4' H (dd)	3.89	3.84	0.05	3.52	0.04	3.88	3.83	3.61
4 OCH ₃ (s)	3.89	3.94	-0.05	4.01	-0.30	3.88	3.90	3.97
5' H (qd)	4.29	4.47	-0.18	4.16	-0.17	4.27	4.21	4.21
7 H (dd)	4.87**	4.84 **	0.02	4.97	0.01	4.80	4.79	4.90
9 COCH ₂ OH (s)	4.87**	4.84 **	0.02	4.57	-	4.80	4.82	4.63
1' H (t)	5.50	5.49	0.02	5.28	-0.12	5.48	5.43	5.28
3 H (d)	7.37	7.43	-0.05	7.94	-0.28	7.34	7.37	7.60
1 H (d)	7.37	7.50	-0.12	7.93	-0.52	7.34	7.45	7.84
2 H (dd)	7.65	7.71	-0.06	7.68	-0.37	7.61	7.66	7.86

* Downfield shift is +ve; upfield shift is -ve. ** under the HOD peak

Table 3.4 summarizes all the observed chemical shifts of Dox in different solvents and concentrations alongside the values found in the literature. (The numbering is consistent with Figure 3.1.)

The ¹H-NMR measurements of the complex solution were performed at 1:10, i.e. 2 mM Dox and 20 mM carrier, and 1:1 Dox:carrier, i.e. 10 mM Dox and 10 mM carrier, ratios in D₂O and DMSO_{d6}. The obtained spectra are presented in Figure 3.17 to Figure 3.20.

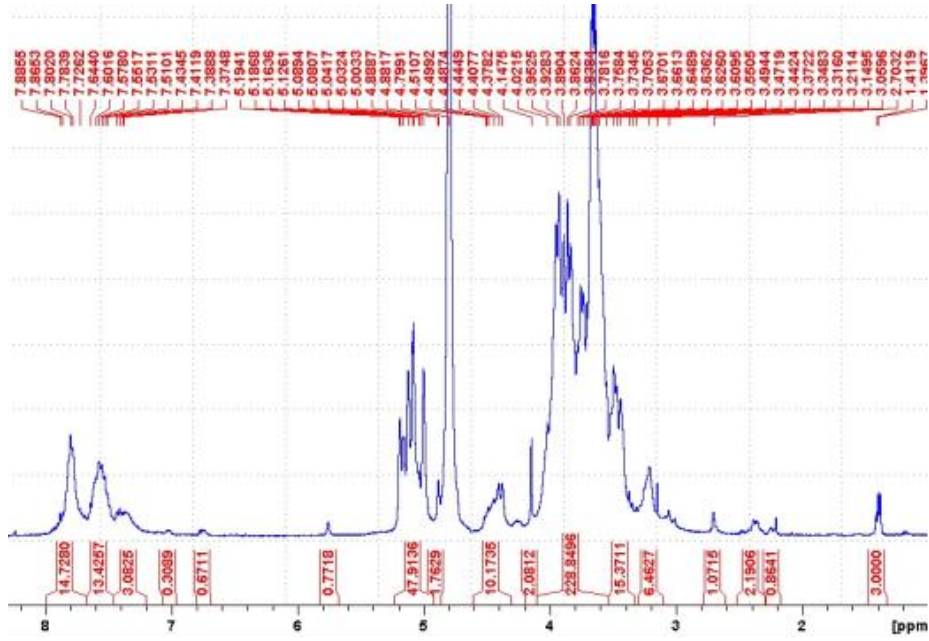


Figure 3.17-¹H-NMR spectrum 1:10 Dox:carrier complex in D₂O

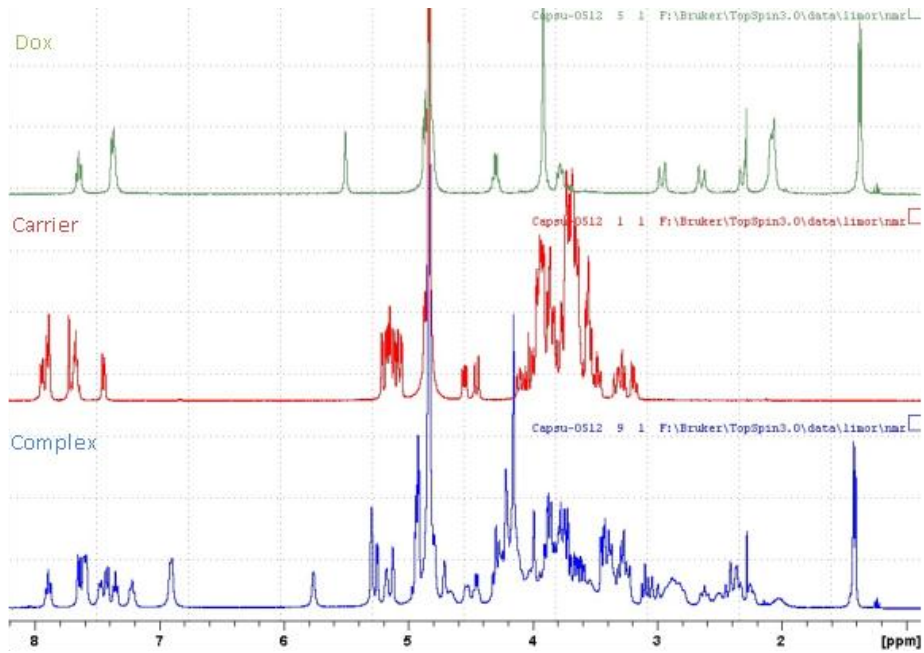


Figure 3.18-¹H-NMR spectra of Dox (top), carrier (middle) and 1:1 Dox:carrier complex (bottom) in D₂O

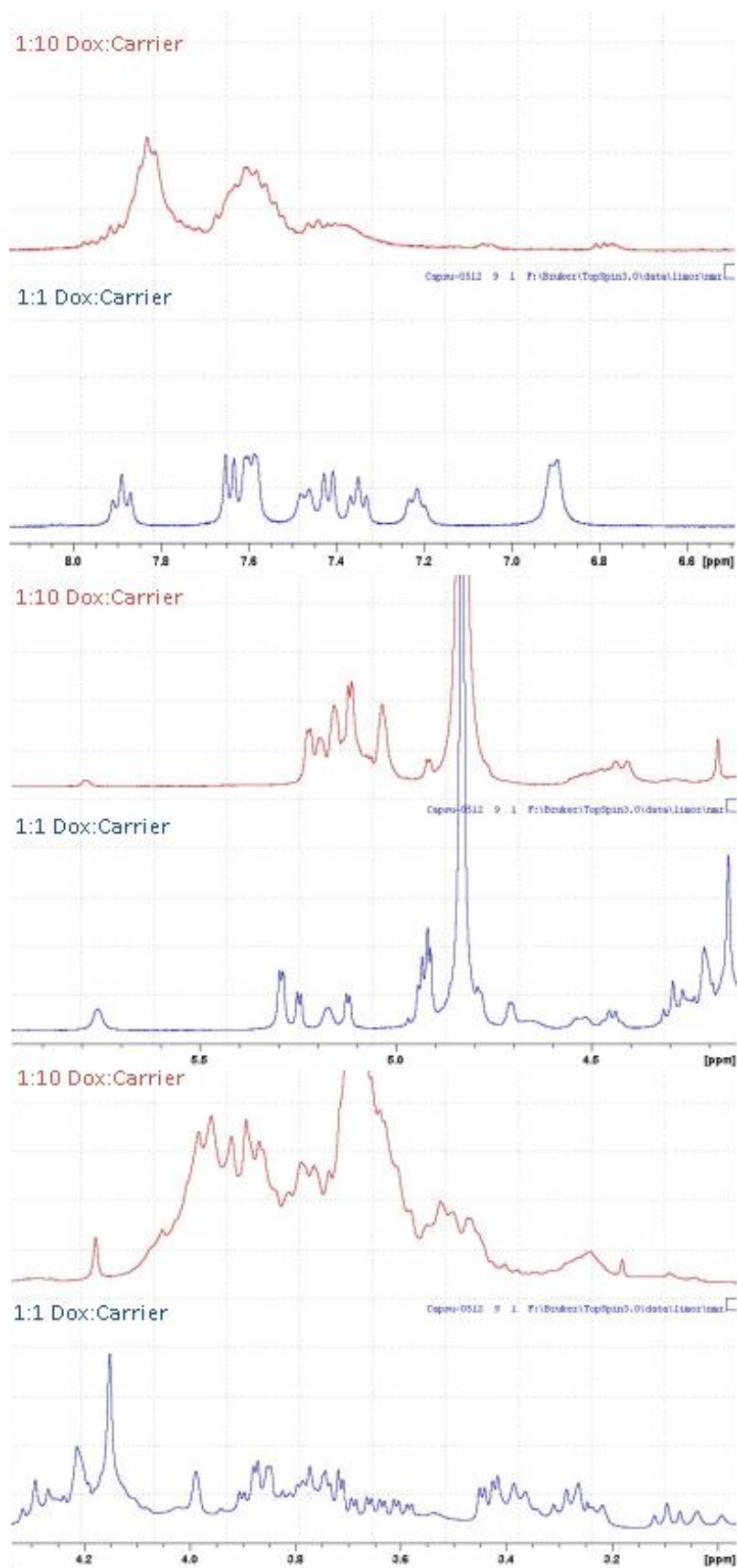


Figure 3.19- $^1\text{H-NMR}$ spectra of 1:10 Dox:carrier complex (in red) and 1:1 Dox:carrier complex (in blue) in D_2O

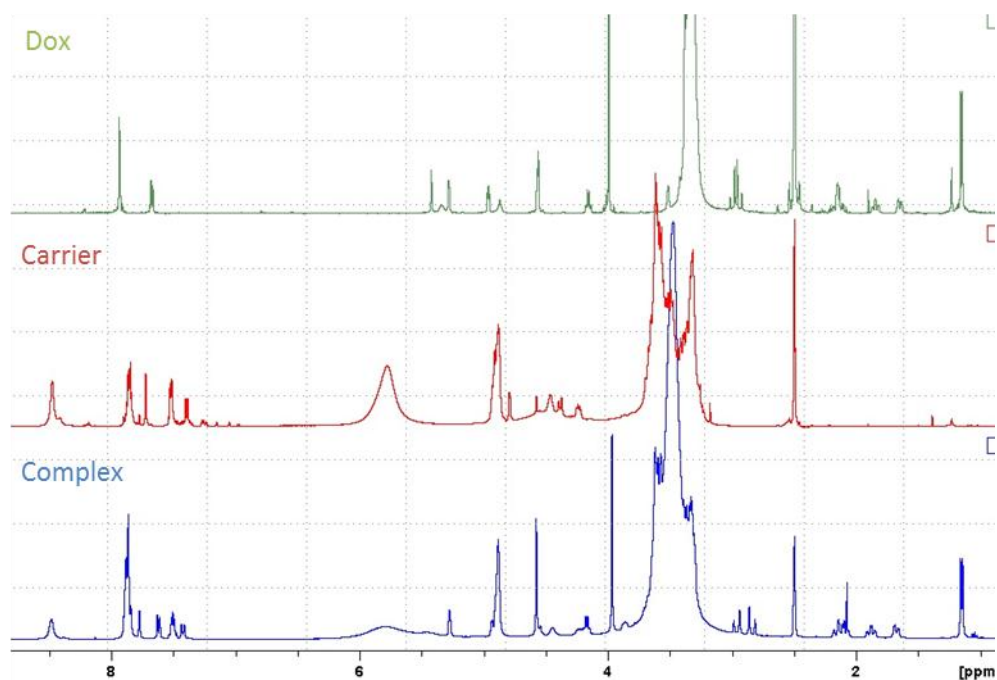


Figure 3.20- ^1H -NMR Spectra of Dox (top), carrier (middle) and 1:1 Dox:carrier complex (bottom) in DMSO

^{13}C -NMR To validate the structure of the designed carrier, ^{13}C -NMR measurements were performed.

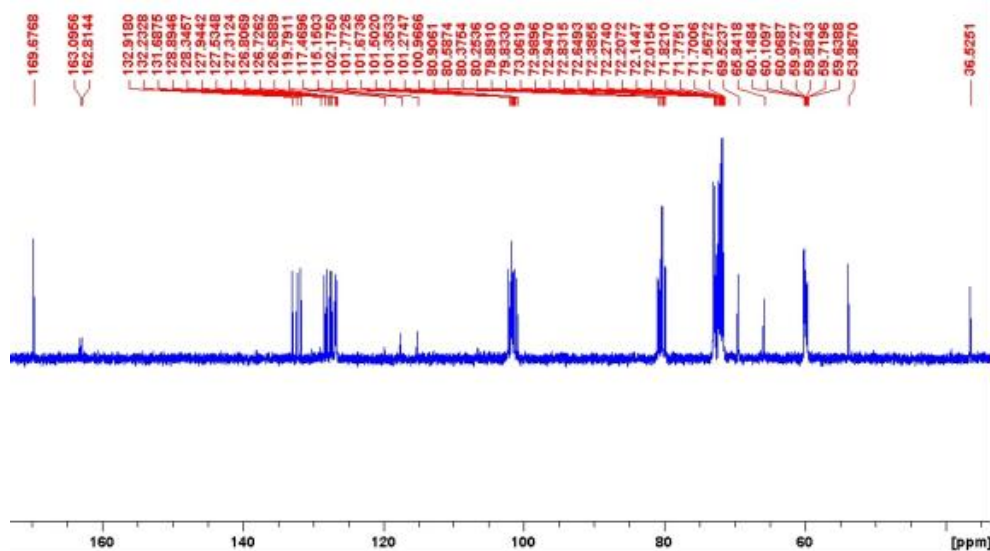


Figure 3.21- ^{13}C -NMR spectrum of the carrier

Figure 3.21 presents the measured spectrum of ^{13}C -NMR of 20 mM carrier performed at 500 MHz in D_2O . The chemical shifts of attributed carbons (numbered corresponding to Figure 3.3) in the carrier as measured by ^{13}C -NMR are summarized in Table 3.5.

Table 3.5- ¹³C-NMR chemical shifts of the carrier

Carbon num.	δ (ppm)
C9	36.53
C8	53.87
C6	59.63-60.15
C6*	65.84
C5*	69.52
C5	71.56-71.82
C2	72.01-72.38
C3	72.64-73.06
C4	79.83-80.9
C1	100.97-102.17
C15	126.59
C14	126.73
C18	126.81
C13	127.31
C16	127.53
C19	127.94
C11	128.35
C17	131.69
C12	132.23
C10	132.92
C7	169.68

* Carbon of the substituted ring

sel-NOEY, NOESY and COSY To evaluate the 3D conformation of the created complex sel-NOEY, NOESY and COSY measurements were conducted. Figure 3.22- 3.26 depict the achieved spectra.

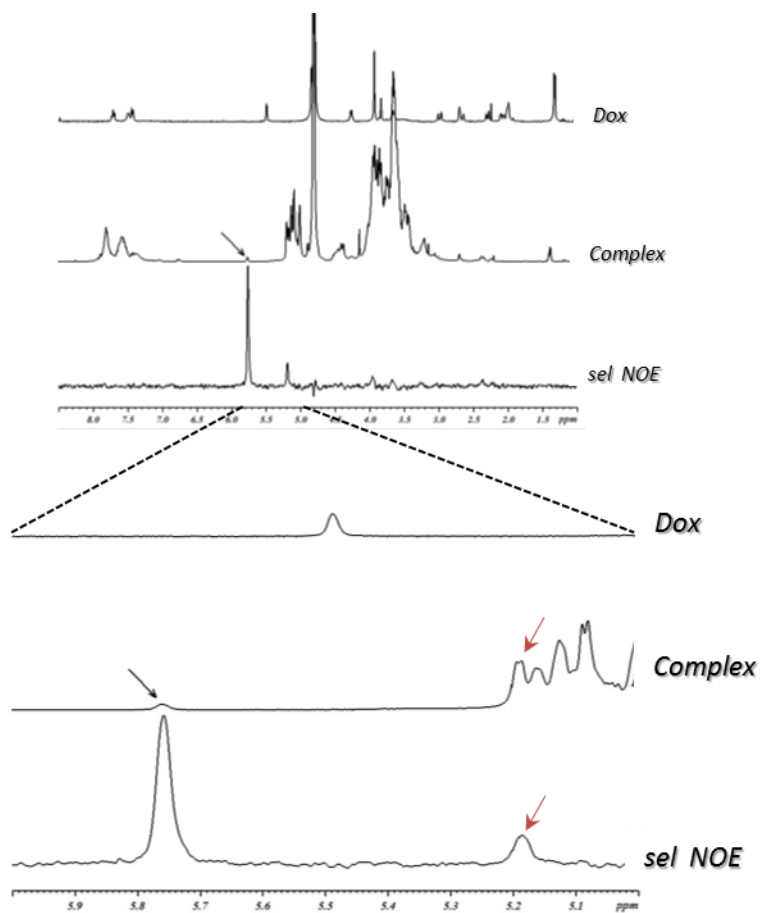


Figure 3.22- $^1\text{H-NMR}$ sel-NOE of 1:10 Dox:carrier in D_2O

Figure 3.22 depicts the $^1\text{H-NMR}$ spectra of 2 mM Dox (top), 1:10 (2 mM Dox, 20 mM carrier) Dox:carrier complex (middle) and the sel-NOE spectrum of the complex, following irradiation of the peak at 5.8 ppm (marked by black arrow).

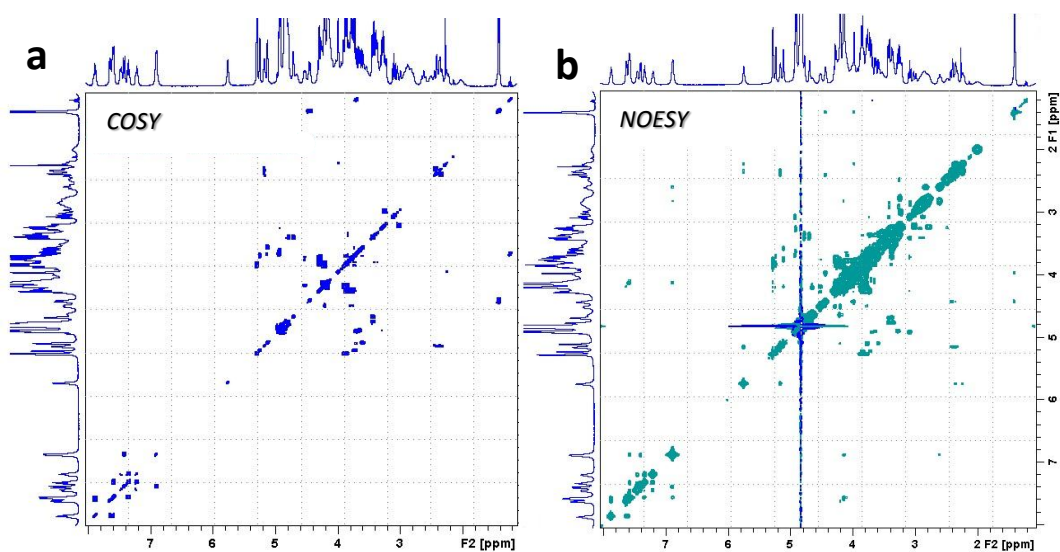


Figure 3.23- $^1\text{H-NMR}$ (a) COSY and (b) NOESY spectra of 1:1 Dox:carrier complex in D_2O

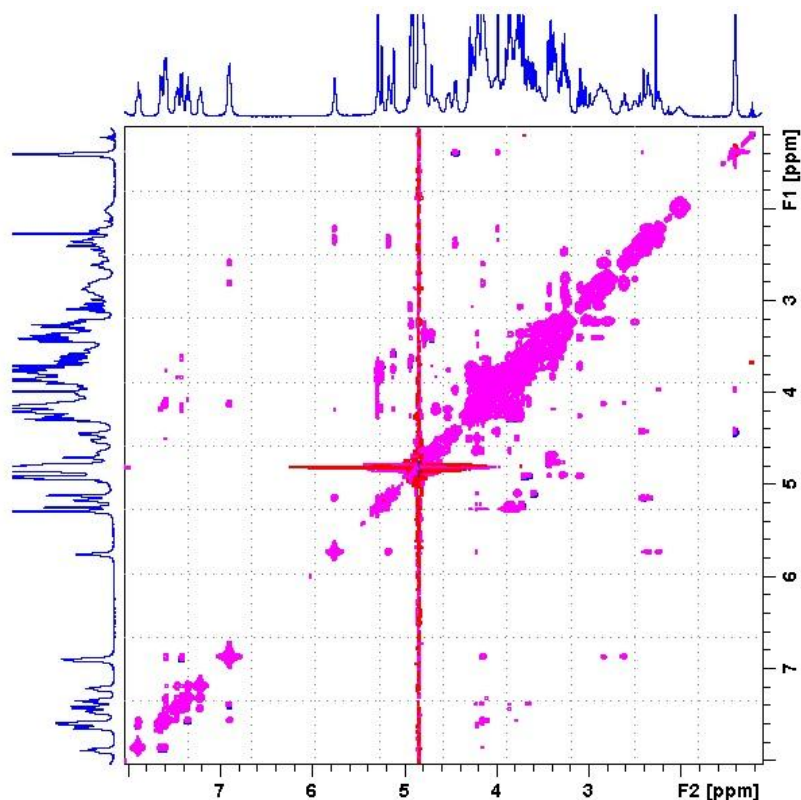


Figure 3.24- Subtraction of the COSY and NOESY spectra presented in Figure 3.23

Figure 3.23 depicts the ^1H -NMR spectra of COSY and NOESY measurements of 1:1, 10 mM Dox, 10 mM carrier, Dox:carrier complex, and Figure 3.24 depicts their subtraction. The expansion of the spectra at 5-6 and 6.8-8 ppm are presented in Figure 3.25 and Figure 3.26.

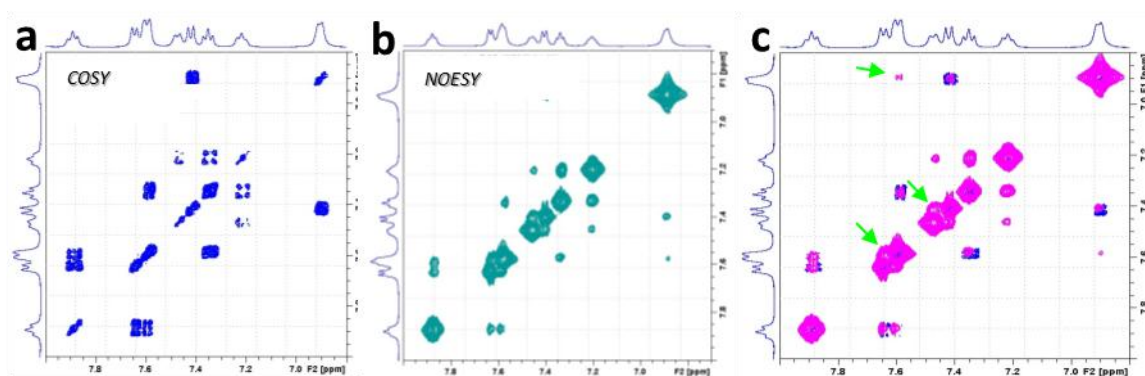


Figure 3.25- 5-6 ppm ^1H -NMR (a) COSY and (b) NOESY spectra and (c) their subtraction of 1:1 Dox:carrier complex in D_2O

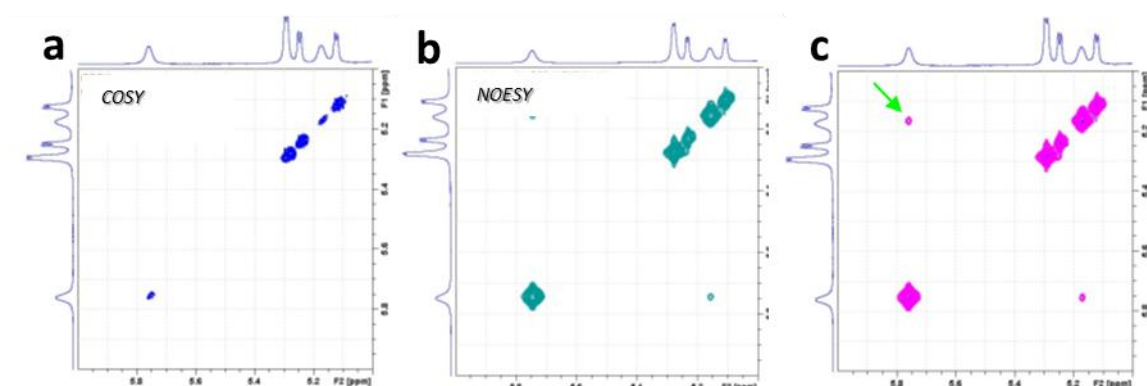


Figure 3.26- 6.8-8ppm $^1\text{H-NMR}$ (a) COSY and (b) NOESY spectra and (c) their subtraction of 1:1 Dox:carrier complex in D_2O

3.3.2.4 Diffusion Coefficient Measurements

D measurements of Dox, carrier and the complex Dox - carrier were conducted at different concentrations in aqueous solutions.

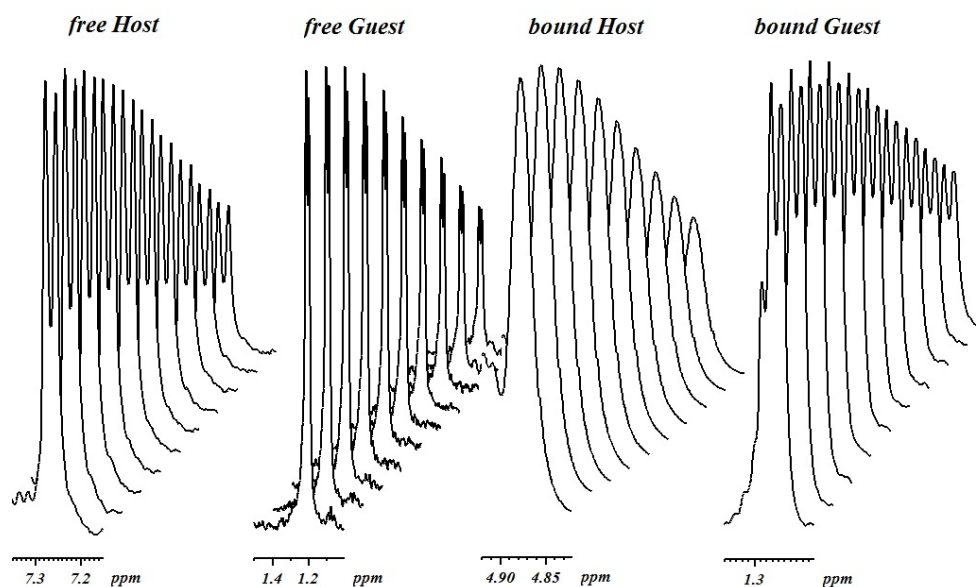


Figure 3.27- Signal decay in diffusion measurements of Dox, carrier and the complex

Figure 3.27 presents the decay in signal corresponding to the rate of diffusion for the Dox, carrier and Dox - carrier complex, and Table 3.6 summarizes the recorded D values of Dox, carrier and the Dox-carrier complex, on both the 400 and 500 MHz spectrometers, in comparison to the values found in the literature.

Table 3.6- Diffusion coefficients

D [m ² /s] *10 ⁻¹⁰	Measurement						Literature			
	1:1 Complexation Ratio		1:10 Complexation Ratio				Agrawal et al.	Viel et al.		Pessine et al.
	Dox [10mM]	Carrier [10mM]	Dox [2mM]	Carrier [20mM]	Dox [2mM]	Carrier [20mM]	Dox ⁺	Carrier*	γCD	γCD
Solvent	D ₂ O	D ₂ O	D ₂ O, 0.01% DMSO	D ₂ O	D ₂ O, 0.01% DMSO	D ₂ O				
Operating Frequency	400MHz			500MHz						
γCD	-	-	-	-	-	-	-	-	2.445*	3.15 ±0.012
Dox	1.58 ±0.01	-	1.84 ±0.04	-	1.81 ±0.03	-	1.63 ±0.21	-	-	-
carrier	-	2 ±0.02	-	1.9 ±0.02	-	1.95 ±0.03	-	2.28*	-	-
Dox+ carrier	1.85 ±0.01	1.88 ±0.01	1.86 ±0.06	1.92 ±0.01	-	-	-	-	-	-

* According to $D = 8.2 \cdot 10^{-9} \cdot M_w^{-0.49} [\text{m}^2 \text{s}^{-1}]$ (Viel et al., 2003) ** in "aggregation concentration" (Agrawal et al., 2009)

3.4 Discussion

To validate the chemical structure of the synthesized carrier, ¹H and ¹³C NMR and HPLC measurements were performed. The ¹H-NMR and in particular ¹³C-NMR spectra suggest that the chemical structure of the carrier is consistent with the desired yield being the mono-substituted γCD with an amino-acid-naphthalene moiety on a primary hydroxyl group. According to the HPLC measurement presented in Figure 3.4, the retention time of the mono-substituted carrier (83% of the product) is 12.07 min. The unwanted di-substituted and tri-substituted (14.1% in total) retention times are 17.15 min to 18.9 min, depending on the relative position of the substituents to each other. As this is a non-specific reaction, it was stopped on purpose after 50% of the reagents had reacted and carefully purified. This was done to avoid the creation of unwanted di- and tri-substitution on the γCD.

Alongside the chemical investigation of the carrier, i.e. the 'host', the guest molecule, Dox, was studied by ¹H-NMR for its chemical behaviour under various conditions, Figure 3.13 to Figure 3.16. Table 3.4 presents the chemical shifts of Dox at different concentrations in water and DMSO in comparison with the literature. All the obtained figures for the current measurements presented in Table 3.4 are in good agreement with the values found in the

literature (Mondelli and Ragg, 1987; Barthwal et al., 1994). In the $^1\text{H-NMR}$ data as well as D, as will be further discussed below, Dox is shown to self-aggregate, to some extent, at both the tested concentrations, i.e. 2 mM and 10 mM. Nonetheless, it can be noticed that there are changes in the chemical shifts of the Dox protons with higher concentration, i.e. 10 mM, which are consistent with the ones presented by Agrawal et al. (2009) when examining the self-aggregation of Dox as a function of varying concentrations from 0.01 mM to 8 mM.

To investigate the behaviour of Dox as a guest molecule in the host-guest complex with the carrier, various fluorescence and NMR measurements were conducted. It has been shown in the literature that addition of natural γCD to Dox at a ratio of up to 5000:1 can significantly stabilize Dox in aqueous solution via complex formation (Emara et al., 2000). The complex created in our study between the γCD -based carrier and Dox was monitored through fluorescence measurements based on the Dox fluorescence signal at 592 nm. This signal decays with the addition of the carrier, suggesting that, due to encapsulation, good coupling between the Dox and the γCD -naphthalene derivative is formed, allowing energy transfer between them. Therefore, the Dox excited state decays non-radiatively leading to lower fluorescence signals. According to the fluorescence studies presented in section 3.3.2.2, the main Dox fluorescence peak at 592 nm is decreased by a factor of eight as a result of the carrier addition at the maximal concentration of 320 μM . Significant encapsulation of Dox within the carrier was observed already at ratios as low as 1:1. Satisfying encapsulation was observed at 20:1 carrier:Dox ratio which therefore was applied *in vitro* (Chapter 5).

The described decrease in the intensity of Dox fluorescence peaks is in good correspondence with the literature, where it has been shown that encapsulation within a CD can significantly lower the fluorescence and absorbance signals of the guest molecule (Mukhopadhyay et al., 2005; Swiech et al, 2012). In addition, it has been shown that for these changes, the Benesi-Hildebrand method (Benesi and Hildebrand, 1949) for calculation of the binding constant, K_{binding} , can be applied (Dang et al., 1997, Mukhopadhyay et al., 2005; Swiech et al, 2012). According to these calculations, K_{binding} as indicated by the fluorescence measurements is $61944 \pm 5592.2 \text{ M}^{-1}$. This value is a factor of 310 higher than the fluorescence established K_{binding} reported by Anand et al. (2009) for the parental γCD with Dox in 1:1 complex formation. The higher value of K_{binding} can be attributed to the modification of the γCD with the naphthalene group, that potentially exhibits π - π^* interactions with the Dox's aromatic rings.

As part of the complex structure investigation, various $^1\text{H-NMR}$ measurements were conducted in different solvents. It is known that generally Dox should not exhibit

encapsulation within CDs in pure DMSO (Swiech et al, 2012). Therefore, for comparison, the complex solution $^1\text{H-NMR}$ spectra were recorded in both aqueous and DMSO solvents. Although an unavoidable amount of water was present in the DMSO solution during the $^1\text{H-NMR}$ measurements of the complex (HOD peak at 4.88 ppm in Figure 3.20), a significant difference was observed between the two solvents. In the $^1\text{H-NMR}$ spectrum of the complex dissolved in DMSO_{d6} , Figure 3.20, the superposition, although not total, of the guest and the host can be seen. The same measurement performed in an aqueous solution resulted in significant changes in the majority of the protons in both the Dox and the carrier, Figure 3.18. The variance in the movement of the peaks indicates that a different type of interaction occurs between the Dox and the carrier in the different solvents, which is consistent with assumption that water must be present for encapsulation to occur (Swiech et al, 2012).

Moreover, as can be seen in Figure 3.18, in D_2O the complex spectrum is not a superposition of the Dox and the carrier spectra, indicating that there is indeed an interaction between the two molecules. Closer evaluation of the significant amount and manner of Dox and carrier's chemical shifts in aqueous solution suggests encapsulation of Dox within the CDs cavity.

Indications for the encapsulation might be found in the upfield chemical shifts of the protons in the 3rd and 5th positions in the γCD ring, 3H and 5H - Figure 3.3, which are facing the inner space of the cone and are affected by the removal of D_2O and Dox entrance (Singh et al., 2010). Additional information obtained from the $^1\text{H-NMR}$ spectrum of the complex can indicate the orientation of the Dox within the carrier. As can be seen in Figure 3.18, the OCH_3 moiety on the 4th position of the amino sugar ring of the Dox, 4OCH_3 - Figure 3.1, is not influenced by the presence of the carrier, suggesting it is located outside the γCD cavity.

An additional important factor in the complex formation is the concentrations of the reagents and their molar ratio in solution. As can be observed in the 1:1 and 1:10 $^1\text{H-NMR}$ spectra, Figure 3.19, the latter has broader, more widely distributed peaks. This variation between the spectra suggests that, in the 1:1 solution, the created complex has a more rigid structure than with excess of the carrier. In the latter case, several carrier molecules can encapsulate a certain Dox encouraging the Dox to exhibit a faster dynamic equilibrium between the free and encapsulated forms. Additionally, the comparison of the two spectra can aid in the attribution of the peaks to the appropriate molecules. The appearance of a certain peak only in the 1:1 complex spectrum provides a strong indication that the peak belongs to Dox rather than the carrier. A good example is the peak at 6.9 ppm which appears only in the 1:1 spectrum and corresponds to Dox 3H in Figure 3.1.

Additional information on the 3D structure of the complex was achieved by sel-NOEY, NOESY and COSY measurements. In the sel-NOEY measurements, a single chosen peak was irradiated and the ^1H -NMR spectrum of the 1:10 Dox:carrier complex was recorded, where only the protons in the appropriate spatial distance produced a signal. From Figure 3.22, it can be seen that the irradiated peak at 5.76 ppm, that presumably corresponds to Dox 1'H (Figure 3.1), has a spatial interaction with a peak at 5.19 ppm. According to thorough examination of the whole 3D spectra of Dox and the carrier, the peak at 5.19 ppm can be attributed to Dox 7H, Figure 3.1, meaning that this interaction is not an indication of complexation with the carrier, but rather an intramolecular interaction of the Dox.

The same interaction of Dox 1'H and 7H, was also observed at 1:1 ratio in the NOESY and COSY measurements, presented in Figure 3.25. Subtraction of the COSY and NOESY full spectra provided the information on the non-covalently bonded protons present in proximity to each other in the 3D structure of the molecule. In the subtraction image, i.e. Figure 3.24, it can be noticed that a number of peaks that appear in the NOESY spectrum are absent in the COSY spectra, marked by purely pink colour without blue/green. The presence of these peaks does not necessarily indicate the complexation reaction, since these peaks could represent the 3D structure of the Dox / carrier on their own, Figure 3.25, but their amplitude and nature strengthen the assumption that some interactions do occur. According to the close up on the subtraction of the COSY spectrum from the NOESY one at 6 - 8 ppm, Figure 3.26, it can be seen that there is a clear spatial correlation between the peak at 6.9 ppm and the peak at 7.6 ppm. As the peak at 6.9 ppm most likely belongs to Dox 3H, Figure 3.1, which is located on the first phenyl ring next to the methyl group, marked by green arrow in Figure 3.26, and the peak at 7.6 ppm can be attributed to the carrier's naphthalene protons, this is a strong indication of π - π^* interaction between the Dox aromatic rings and the naphthalene conjugate on the carrier.

According to the overall ^1H -NMR data, it can be suggested that the encapsulation of Dox occurs in the following manner:

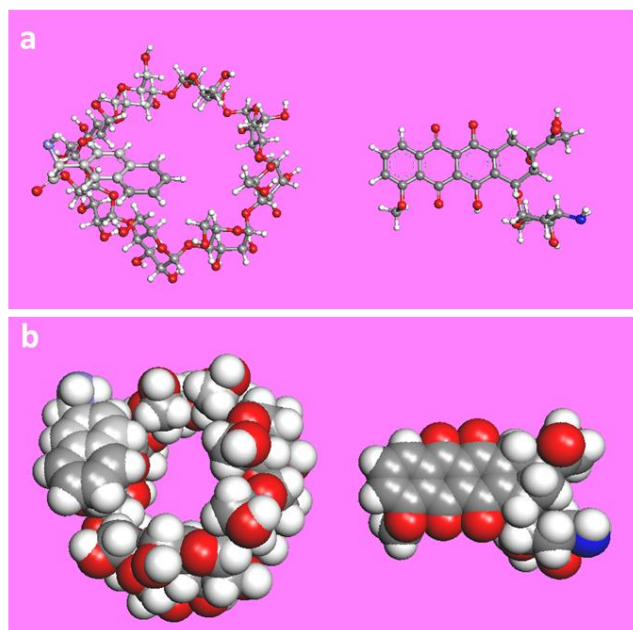


Figure 3.28- Carrier and Dox prior to encapsulation (a) ball shaped and (b) space filling style

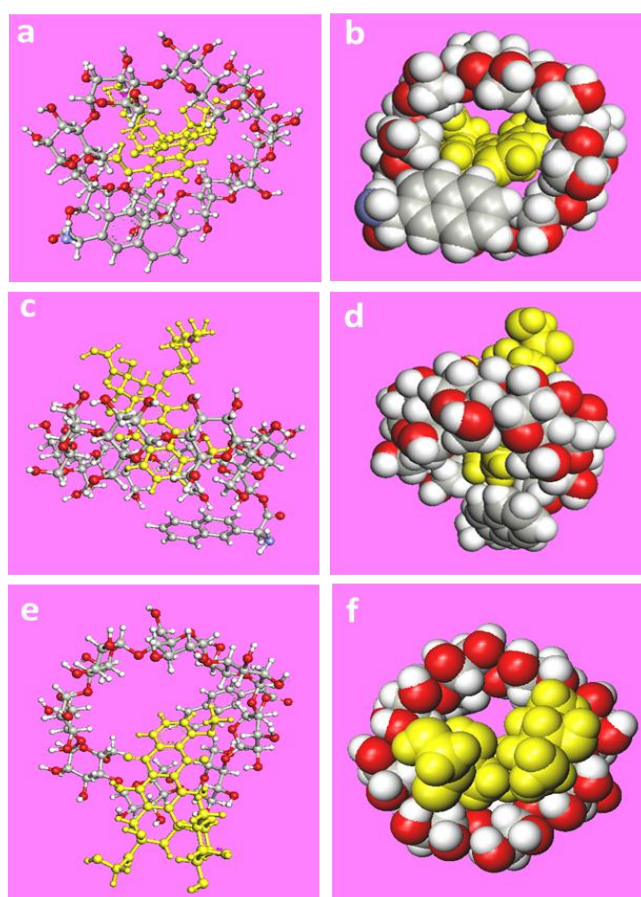


Figure 3.29- Carrier and Dox in a suggested encapsulated form (a) ball shaped primary face view, (b) space filling style primary face view, (c) ball shaped primary side view, (d) space filling style side view, (e) ball shaped secondary face view and (f) space filling style secondary face view

A suggested mechanism of encapsulation is, as can be seen from the above figures, where the Dox enters the γ CD from the secondary face with the aromatic rings forward, rings D, C and B (Figure 3.1) and forms π - π^* interactions with the naphthalene group. The D measurements of the free Dox point out the occurrence of the self-aggregation of Dox. According to M_w of Dox, 580 g/mol, and the carrier, 1494 g/mol, D of Dox should be a factor between 1.37 and 1.6 different to that of the carrier (see equations in Appendix i). Hence if the D measured for the free carrier is about 2, the corresponding value for free Dox should be around 3, and D of the 1:1 complex for both the carrier and the Dox should be around 1.78 each. In this case, the observed D value of the complex being 1.85 theoretically indicates 94% encapsulation of the Dox within the carrier, according to Appendix i.

Nevertheless, the measured value of D for free Dox was significantly lower than expected and closer to that of the carrier. This data suggests the appearance of Dox in dimer form at the measured concentration of 2 mM, which is consistent with the studies performed previously by Agrawal et al. (2009). Moreover, when a higher concentration, i.e. 10 mM, was measured an additional drop in the value of D was recorded, indicating dependence on the concentration of the solution. This is in good agreement with the suggestions of Barthelemy-Clavey et-al. (1974) that further aggregation occurs beyond the dimer form at concentrations higher than 5mM.

From Table 3.6 it can be noticed that D for both Dox and carrier in the complex solution are different from their measured values in the separate solutions. This may indicate that there is indeed a complexation between the Dox and the carrier: not only do the values differ from those of the free drug and carrier but they are also very similar to each other, 1.85 ± 0.01 and 1.88 ± 0.01 , in the combined solution which suggests they are conjugated in some way. The fact that D for Dox at the higher concentration of 10 mM is higher than that of 2 mM in the presence of the carrier may also suggest that the carrier aids in dissociation of the di/n-mers present at that concentration. According to these results it seems that the carrier-Dox interaction is stronger than the Dox - Dox interaction and therefore, through equilibrium, the complex is formed even at 'stacking concentrations' of Dox.

3.5 Conclusions

In conclusion, the overall data presented in this chapter suggest that there is an interaction between the created carrier and the chosen drug, Dox, as well as providing an indication of complex formation. Moreover, the presented data, such as the DOSY measurements, suggest that the designed carrier can potentially lower the self-aggregation of

Dox. In addition, the utilization of the carrier in combination with DMSO at physical concentrations can potentially aid in prevention of the Dox cleavage and the generation of dangerous ROS, and thus lower the harmful side-effects of Dox. The inclusive studies of the drug and the carrier structures on their own, as well as in a complex, provided strong insights into the mechanisms of interaction between them. The *in-vitro* investigation of the drug and carrier, on their own and in a complex, are presented in Chapter 5.

3.6 [References](#)

Agrawal, P. et al. (2009) Studies on self-aggregation of anthracycline drugs by restrained molecular dynamics approach using nuclear magnetic resonance spectroscopy supported by absorption, fluorescence, diffusion ordered spectroscopy and mass spectrometry. *Eur J Med Chem*, 44, pp.1437- 51.

Anand, R. et al. (2012) A close-up on doxorubicin binding to α -cyclodextrin: an elucidating spectroscopic, photophysical and conformational study. *RSC Advances*, 2, pp. 2346- 57.

Arnusch, C.J. et al. (2012) Ultrashort peptide bioconjugates are exclusively antifungal agents and synergize with cyclodextrin and amphotericin B. *Antimicrob Agents Chemother*, 56 (1), pp.1-9.

Auzely-Velty, R. (2011) Self-assembling polysaccharide systems based on cyclodextrin complexation: Synthesis, properties and potential applications in the biomaterials field. *C R Chimie*, 14, pp.167- 7.

Badi, N. et al. (2006) Synthesis of per-2,3-di-O-heptyl- β and α -cyclodextrins: a new kind of amphiphilic molecules bearing hydrophobic parts. *Tetrahedron Letters*, 47, pp.8925- 27.

Balci, M. (2005) *Basic 1H- and 13C-NMR spectroscopy*. The Netherlands: Elsevier B.V.

Balta, D.K. et al. (2008) Chemical incorporation of thioxanthone into β -cyclodextrin and its use in aqueous photopolymerization of methyl methacrylate. *J Photoch Photobio A*, 196, pp.33- 7.

Banerjee, S.S. and Chen, D-H. (2009) Cyclodextrin-conjugated nanocarrier for magnetically guided delivery of hydrophobic drugs. *J Nanopart Res*, 11, pp.2071- 78.

Barthelemy-Clavey, V. et al. (1974) Self-association of daunorubicin. *FEBS Letters*, 46 (1), pp.5-10.

Barthwal, R. et al. (1994) A 500 MHz proton NMR study of the conformation of adriamycin. *J Mol Struct*, 327, pp.201- 20.

Barthwal, R. et al. (2008) Structural elucidation of 40-epiadriamycin by nuclear magnetic resonance spectroscopy and comparison with adriamycin and daunomycin using quantum

mechanical and restrained molecular dynamics approach. *Arch Biochem Biophys*, 474, pp.48-64.

Battistini, E. et al. (2008) High-Relaxivity Magnetic resonance imaging (MRI) contrast agent based on supramolecular assembly between a gadolinium chelate, a modified dextran, and poly- β -cyclodextrin. *Chem Eur J*, 14, pp.4551- 61.

Benesi, H.A. and Hildebrand, J.H. (1949) A spectrophotometric investigation of the interaction of iodine with aromatic hydrocarbons. *J Am Chem Soc*, 71, pp. 2703- 7.

Boer, T. et al. (2000) Recent innovations in the use of charged cyclodextrins in capillary electrophoresis for chiral separation in pharmaceutical analysis. *Electrophoresis*, 21, pp.3220-39.

Cabral Marques, H.M. (2010) A review on cyclodextrin encapsulation of essential oils and volatiles. *Flavour Fragr J*, 25, pp.313- 26.

Calderini, A. et al. (2012) Host-guest interactions between dapsone and β -cyclodextrin (part I): study of the inclusion compound by nuclear magnetic resonance techniques. *J Incl Phenom Macrocycl Chem*, pp.1-10.

Caliceti, P. et al. (2003) Synthesis and physicochemical characterization of folate-cyclodextrin bioconjugate for active drug delivery. *Bioconjugate Chem*, 14, pp. 899-908.

Challa, R. et al. (2005) Cyclodextrins in drug delivery: an updated review. *AAPS PharmSciTech*, 6(2) Article 43, pp.E329-57.

Cohen, Y. et al. (2005) Diffusion NMR spectroscopy in supramolecular and combinatorial chemistry: an old parameter- new insights. *Angew Chem Int Ed*, 44, pp.520- 54.

Cserhfiti, T. and Hollo, J. (1994) Interaction of taxol and other anticancer drugs with hydroxypropyl- β -cyclodextrin. *Int J Pharm*, 108, pp.69-75.

Dang, X-J et al. (1997) Inclusion of 10-methylphenothiazine and its electrochemically generated cation radical by β -cyclodextrin in water + methanol solvent mixtures. *J Electroanal Chem*, 437, pp.53- 9.

Deng, W. et al. (2007) A chemical-responsive supramolecular hydrogel from modified cyclodextrins. *Angew Chem Int Ed*, 46, pp.5144- 7.

Dong, M.W. (2005) *Handbook of pharmaceutical analysis by HPLC*. USA: Elsevier.

Dong, M.W. (2006) *Modern HPLC for practicing scientists*. USA: John-Wiley&Sons, Inc.

Emara, S. et al. (2000) Effect of cyclodextrins on the stability of adriamycin, adriamycinol, adriamycinone and daunomycin. *Talanta*, 51, pp.359- 64

- Evan-Salem, T. et al.** (2007) Self-assembled ionophores from isoguanosine: diffusion NMR spectroscopy clarifies cationic and anionic influence on supramolecular structure. *Chem Eur J*, 13, pp.1969-77.
- Evstigneev, M.P. et al.** (2006) Complexation of norfloxacin with DNA in the presence of caffeine. *Biophys Chem*, 121, pp.84-95.
- Fernandes, C.M. et al.** (2003) Multimodal molecular encapsulation of nicardipine hydrochloride by β -cyclodextrin, hydroxypropyl- β -cyclodextrin and triacetyl- β -cyclodextrin in solution. structural studies by H NMR and ROESY experiments. *Eur J Pharm Sci*, 18, pp.285-96.
- Frankewich, R.P. et al.** (1991) Evaluation of the relative effectiveness of different water-soluble β -cyclodextrin media to function as fluorescence enhancement agents. *Anal Chem*, 63, pp.2924-33.
- Frederick, C.A. et al.** (1990) Structural comparison of anticancer drug-DNA complexes: adriamycin and daunomycin. *Biochemistry*, 29, pp.2538-49.
- Green, P.S. and Leeuwenburgh, C.** (2002) Mitochondrial dysfunction is an early indicator of doxorubicin-induced apoptosis. *Biochimica et Biophysica Acta*, 1588, pp.94-101.
- Haeberlin, B. et al** (1996) Cyclodextrins useful excipients for oral peptide administration? *Int J Pharm*, 137, pp.103-10.
- Hagiwara, Y. et al.** (2006) Preparation and pharmaceutical evaluation of liposomes entrapping salicylic acid/ γ -cyclodextrin conjugate. *Chem Pharm Bull*, 54(1), pp.26-32.
- Hajarizadeh, H. et al.** (1994) Protective effect dimethyl sulfoxide of doxorubicin in vitamin C or against skin ulceration in the pig. *Ann Surg Oncol*, 1(5), pp.411-4.
- Himeno, Y. et al.** (2009) γ -Cyclodextrins possessing an azido group and a triisopropylbenzenesulfonyl group as useful synthetic and authentic intermediates for unsymmetrically functionalized derivatives. *Tetrahedron*, 65, pp.9474-80.
- Holzgrabe, U. et al.** (1999) *NMR spectroscopy in drug development and analysis*. Germany: WILEY-VCH Verlag.
- Irie, V. and Uekama, K.** (1999) Cyclodextrins in peptide and protein delivery. *Adv Drug Deliver Rev*, 36, pp.101-23.
- Jacobsen, N.E.** (2007) *NMR spectroscopy explained: simplified theory, applications and examples for organic chemistry and structural biology*. USA: John Wiley & Sons, Inc.
- Jiskoot, W. and Crommelin, D.** (2005) *Methods for structural analysis of protein pharmaceuticals*. USA: American Association of Pharmaceutical Scientists.
- Kazakevich, Y.V. and LoBrutto, R.** (2007) *HPLC for pharmaceutical scientists*. USA: John Wiley & Sons, Inc.

- Khan, A.R. et al.** (1998) Methods for selective modifications of cyclodextrins. *Chem Rev*, 98, pp.1977-96.
- Krupadanam, G.L.D et al.** (2001) *Analytical chemistry*. India: University Press.
- Li, H. et al.** (2010) Microcalorimetric and spectrographic studies on host–guest interactions of α -, β -, γ - and M β -cyclodextrin with resveratrol. *Thermochimica Acta*, 510, pp.168–172.
- Li, S. and Purdy, W.C.** (1992) Cyclodextrins and their applications in analytical chemistry. *Chem Rev*, 92, pp.1457- 70.
- Liu, Y. et al.** (2002) Selective binding of steroids by 2,2'-biquinoline-4,4'-dicarboxamide-bridged bis(β -cyclodextrin): fluorescence enhancement by guest inclusion. *J Org Chem*, 68, pp.3687- 90.
- Loening, N.M. et al.** (2001) One-dimensional DOSY. *J Magn Reson*, 153 (1), pp.103-112.
- Loftsson, T. and Duchene, D.** (2007) Cyclodextrins and their pharmaceutical applications. *Int J Pharm*, 329, p.1-11.
- Lopez, A.M. et al.** (1999) Topical DMSO treatment for pegylated liposomal doxorubicin-induced palmar-plantar erythrodysesthesia. *Cancer Chemother Pharmacol*, 44, pp.303-306.
- Lu, F. et al.** (2009) Aqueous compatible fullerene-doxorubicin conjugates. *J Phys Chem C Nanomater Interfaces*, 113(41), pp.17768- 85.
- Lu, Z. et al.** (2009) Study of the complexation of resveratrol with cyclodextrins by spectroscopy and molecular modeling. *Incl Phenom Macrocycl Chem.*, 63, pp.295-300.
- Maestrelli, F. et al.** (2005) Preparation and characterisation of liposomes encapsulating ketoprofen–cyclodextrin complexes for transdermal drug delivery. *Intl J Pharm*, 298, pp.55- 67.
- Maestrelli, F. et al.** (2006) Effect of preparation technique on the properties of liposomes encapsulating ketoprofen–cyclodextrin complexes aimed for transdermal delivery. *Int J Pharm*, 312, pp.53-60.
- McMaster, M.** (2007) *HPLC: a practical user's guide*. USA: John Wiley & Sons, Inc.
- Mondelli, R. and Ragg, E.** (1987) Nuclear magnetic resonance conformational study of daunomycin and related antitumour antibiotics in solution. The conformation of ring A. *J Chem Soc Perkin Trans, II*, pp.15-26.
- Muderawan, I.W. et al.** (2005) A reliable synthesis of 2- and 6-amino- β - cyclodextrin and permethylated- β -cyclodextrin. *Tetrahedron Letters*, 46, pp.7905- 7.
- Mukhopadhyay, M. et al.** (2005) Excited state intermolecular proton transfer and caging of salicylidine-3,4,7-methyl amine in cyclodextrins. *J Photoch Photobio A*, 175, pp.94-9.
- Nakanishi, T. et al.** (2001) Development of the polymer micelle carrier system for doxorubicin. *J Control Release*, 74, pp.295-302.

- Panta, G.R. et al.** (2004) ATM and the catalytic subunit of DNA-dependent protein kinase activate NF- κ B through a common MEK/extracellular signal-regulated kinase/p90rsk signaling pathway in response to distinct forms of DNA damage. *Mol Cell Biol*, 24(5), pp.1823-35.
- Park, J.W. and Song, H.J.** (1989) Association of anionic surfactants with β -cyclodextrin. fluorescence-probed studies on the 1:1 and 1:2 complexation. *J Phys Chem*, 93, p.6454-58.
- Pessine, F.B.T. et al.** (2012) Review: cyclodextrin inclusion complexes probed by NMR techniques. *Magn Res Spec*, pp.237-64.
- Pham, D-T. et al.** (2010) synthesis of C6A-to-C6 A and C3 A-to-C3 A diamide linked γ -cyclodextrin dimers. *Tetrahedron*, 66, pp.2895- 8.
- Piosik, J. et al.** (2002) The modulation of xanthines of the DNA-damaging effect of polycyclic aromatic agents Part II. The stacking complexes of caffeine with doxorubicin and mitoxantrone. *Biochemi Pharmacol*, 63, pp.635- 46.
- Schaschke, N. et al.** (2000) β -Cyclodextrin/epoxysuccinyl peptide conjugates: a new drug targeting system for tumor cells. *Bioorg Med Chem Lett*, 10, pp.677- 80.
- Šimůnek, T. et al.** (2009) Anthracycline-induced cardiotoxicity: overview of studies examining the roles of oxidative stress and free cellular iron. *Pharmacol Rep*, 61, p.154- 71.
- Singh, R. et al.** (2010) Characterization of cyclodextrin inclusion complexes – a review. *J Pharm Sci Tech*, 2 (3), pp.171- 83.
- Snyder, L.R. et al.** (2010) *Introduction to modern liquid chromatography*. USA: John Wiley & Sons, Inc.
- Swiech, O. et al.** (2012) Intermolecular interactions between doxorubicin and β -cyclodextrin 4-methoxyphenol conjugates. *J Phys Chem B*, 116, pp.1765- 71.
- Szejtli, J.** (2004) Past, present, and future of cyclodextrin research. *Pure Appl Chem*, 76(10), pp.1825- 45.
- Tang, W. et al.** (2007) Facile synthesis of positively charged monosubstituted α - and γ -cyclodextrins for chiral resolution of anionic racemates. *Tetrahedron: Asymmetry*, 18, pp.1548- 53.
- Thomas, O. and Burgess, C.** (2007) *UV-Visible spectrophotometry of water and wastewater*. The Netherlands: Elsevier.
- Trotta, F. et al.** (2007) Recent advances in synthesis of cyclodextrin derivatives under microwaves and power ultrasound. *J Incl Phenom Macrocycl Chem*, 57, pp.3-7.
- Tucker, E.J. and Carrizo A.** (1968) Haematoxylon dissolved in dimethylsulfoxide used in recurrent neoplasms. *Int Surg*, 49(6), pp.516-27.

- Uekama, K.** (2004) Design and evaluation of cyclodextrin-based drug formulation. *Chem Pharm Bull*, 52 (8), p.900- 15.
- Ueno, A.** (1996) Review: fluorescent cyclodextrins for molecule sensing. *Supramol Sci*, 3, pp.31-6.
- Valeur, B. and Berberan-Santos, M.N.** (2012) *Molecular fluorescence*. Germany: Wiley-VCH.
- Van de Manakker, F. et al.** (2009) Cyclodextrin-based polymeric materials: synthesis, properties, and pharmaceutical/biomedical applications. *Biomacromolecules*, 10(12) pp.3157-75.
- Van der Walle, C.F.** (2011) *Peptide and protein delivery*. China: Elsevier Inc.
- Viel, S. et al.** (2003) Diffusion-ordered NMR spectroscopy: a versatile tool for the molecular weight determination of uncharged polysaccharides. *Biomacromolecules*, 4, pp.1843- 47.
- Wahlström, A. et al.** (2012) Specific binding of a β -Cyclodextrin dimer to the amyloid β peptide modulates the peptide aggregation process. *Biochemistry*, 51, pp. 4280- 9.
- Wang, Y. and Eaton, D.F.** (1985) Optically non-linear organic molecules cyclodextrin inclusion complexes. *Chem Phys Lett*, 120 (43), pp.441- 4.
- Weston, A. and Brown, P.R.** (1997) *HPLC and CE: principles and practice*. USA: W.B. Saunders Company.
- Zhang, H-X. and Xiong, Z-Y.** (2012) Spectroscopic study of the interactions of buflomedil to serum albumin and β -Cyclodextrin. *J Solution Chem*, 41, pp.1254- 64.

CHAPTER 4 ADAPTATION OF CLINICAL MRgFUS SYSTEM FOR IN-VITRO APPLICATION OF FUS: DESIGN AND EVALUATION

4.1 Introduction

The main focus of this chapter is to describe the design and calibration of tailor made arrangements for application of USmTDD *in vitro*. The arrangements to be discussed aim to distinguish between different US-induced physical mechanisms acting on cells. The following mechanisms must be isolated in order to explore their contribution to cellular drug uptake: stable cavitation, transient cavitation and thermal effects, including hyperthermia. According to the literature, these are the major contributors for the enhanced drug uptake in USmTDD.

Although USmTDD is a widely investigated research field, there is still a major concern regarding the repeatability and reproducibility of the results generated by the different research groups. The lack in standardization of the FUS application techniques as well as the existence of properly detailed biological protocols makes it difficult for researchers to compare their achieved data. For that purpose, three types of arrangements dealing with the heating and mechanical effects correlated to FUS application, were constructed and presented in this chapter. All the arrangements described in this work are based on clinical MRgFUS systems. This presents the possibility for researchers with accessibility to a clinical MRgFUS system to potentially exploit the presented arrangements for various USmTDD related studies. This could then create a needed standardization in the research of USmTDD that will ease the understanding and communication between researchers worldwide. Furthermore, research groups deprived of access to an MRgFUS system could still benefit from the currently presented arrangements, and especially the biological protocols described in 5.2.2, since that with proper adjustments this can still be applicable in various research environments, e.g. as shown in 5.1.1.3.

The first part of this chapter provides a concise introduction to acoustic effects that may occur in the *in-vitro* application of FUS, such as standing waves, and a description of the MRgFUS system in use, as well as the methodologies to evaluate the experimental arrangements acoustically and thermally. The second part of the chapter focuses on the materials and methods utilised to create and evaluate the arrangements; it also explains the rationale behind the design and the evolution of the arrangements to their finalised form. The

third part presents the results of the acoustic and thermal evaluation of the various arrangements and provides the discussion in the achieved data.

4.1.1 **Ultrasound**

4.1.1.1 **Transverse Acoustic Waves Propagation**

In the case studied in the present work, a cell culture growth environment in the form of a solid plastic 96-well plate was filled with various solutions in specific patterns (as described in 4.2.2) and exposed to different FUS parameters. Because of the plastic boundaries between the different wells a concern raised regarding transverse propagation of acoustic waves that may occur at the boundaries between liquid-solid or solid-solid media (Shutilov, 1988), and might influence the cells in the neighbouring wells.

Consequently, acoustic measurements were conducted to assess the acoustic power loss. According to the acoustic measurements there was only a minor loss of power caused by the presence of the plate. This may be attributed to various reasons including heating and reflection. Hence it is assumed that the appearance of transverse waves in the tested plate was negligible.

4.1.1.2 **Standing Waves**

As previously mentioned, standing waves can occur due to coherence of applied and reflected acoustic waves within certain structures and media (Repacholi and Benwell, 1982). Because the cell culture growth environment of relevance here is the bottom part of a perfectly shaped cylinder, a concern raised regarding the possibly of secondary focuses creation due to the well's behaviour as an acoustic wave guide (Redwood, 1960).

Due to the symmetry of the cylinder, application of certain acoustical parameters – which clearly were not utilised for *in-vitro* work - can create a secondary focus not far from the end of the wells in the plate by the reflected waves from the walls of the well. This is especially dangerous when working with an inverted plate where the acoustic beam is travelling through the well before reaching the cells. A schematic example of such a case is presented in Figure 4.1.

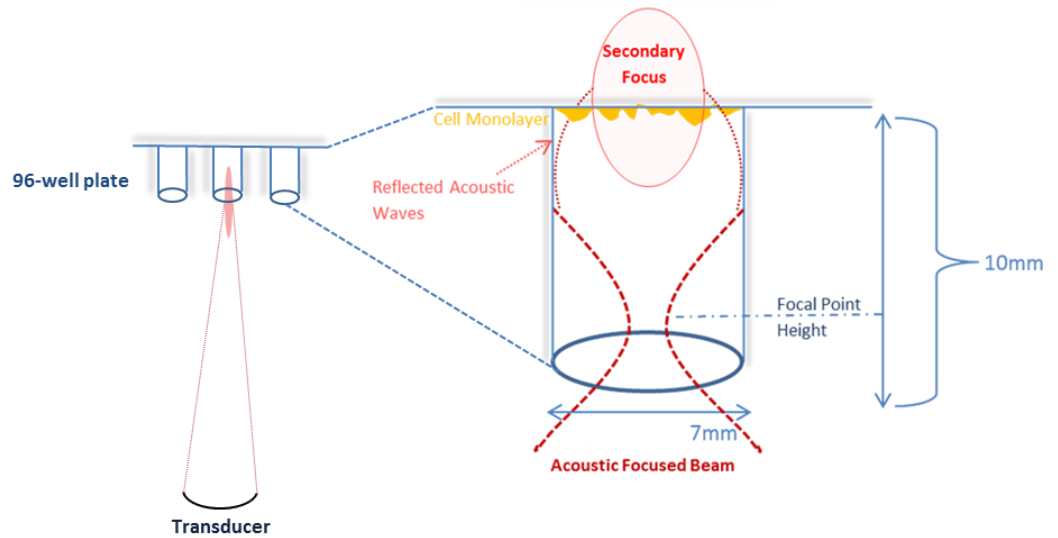


Figure 4.1- Schematic representation of a secondary focus in a well

An example of this was observed when an absorbing material was placed on top of a regularly placed plate (not inverted) to absorb the continuation of the acoustic wave after passage through the cells. For high intensities, the presence of the secondary focus in absorbing material creates bubbles on its surface. These bubbles reflect the US back into the well resulting in an additional ultrasonic beam impacting the cell monolayer and potentially creating standing waves. Even though high intensities were not used during the *in-vitro* study, to reduce the risk of standing waves in possible future studies the absorbing material was moved upwards, 10 cm over the sonicated plate.

4.1.1.3 Prediction and Evaluation of Acoustic Fields

Acoustic evaluation of the arrangement was performed to make an accurate assessment of the ultrasonic field behaviour in the different arrangements.

Hydrophones, i.e. specialised receiving transducers, are commonly used in measurements of acoustic fields. The principles of hydrophone measurements are explained in Section 2.4.1 as an explanation of generation and behaviour of an acoustic field. A hydrophone acts like an underwater microphone to record US. Its operation is similar to that of US transmitting devices, except that it is a receiver producing a voltage equivalent to the acoustic signal. Hydrophones can be made from different materials; the main two are piezoelectric and fibre-optic (Chester, 1987). Several hydrophones can be aligned together to create a multi-hydrophone (Zimmer, 2011).

The sensitivity of hydrophones depends on the frequency applied, the geometry and material of the hydrophone and the direction of the acoustic wave (Sherman and Butler, 2007). There are various shapes of hydrophones, utilized for many purposes. In this work, a

needle-shaped hydrophone (Precision Acoustics, UK) was used to perform accurate measurement inside wells of 7 mm diameter (Platte, 1985) and above the 96-well plate.

4.1.1.4 Monitoring of Cavitation

As described in Chapter 2, cavitation denotes the generation, oscillation and implosion of gas / vapour bubbles in liquid under an applied US field (Leighton, 1994). The minimal intensity of the US field that will create cavitation, also known as the cavitation threshold, depends mainly on the property of the liquid and especially its impurity. In order to assess the creation of cavitation bubbles and their behaviour, three topics must be considered:

1. The media the acoustic wave is propagating through.
2. The applied acoustic field.
3. A cavitation observation tool.

While the first two topics are rather straightforward, knowing the characteristics of the liquid and the acoustic field applied, the third is referred to as a monitoring device that usually relays the effects of cavitation (Apfel, 1984). Stable cavitation created in a constant frequency acoustic field (f) has an acoustic signature at the harmonics ($2f$, $3f$ etc.), sub-harmonics ($f/2$) and ultra-harmonics ($3f/2$) frequencies. Hence a common way to monitor stable cavitation occurrence is by measurement of the sub- or ultra-harmonics. Transient cavitation usually results in broadband noise, which can also be recorded by hydrophones (Sundaram, 2003).

4.1.2 Magnetic Resonance guided Focused Ultrasound Surgery

4.1.2.1 MRI Thermometry

The principle of MRI thermometry was introduced by Bloembergen, Purcell and Pound in 1948 and is known as 'the BPP relaxation theory' (Bloembergen et al. 1948). The basics of this theory lie in the fundamental movements of atoms: rotating, vibrating, translating, and the rapid transfer between them (order of magnitude of time: 10^{-12} sec). This is also referred to as the correlation time (τ_c) and depends on the states of matter of the molecules ($\tau_{c(\text{solid})} > \tau_{c(\text{liquid})} > \tau_{c(\text{gas})}$) and the temperature (thermal increase results in τ_c decrease) (McRobbie et al., 2003).

There are several methods to measure temperature via MRI; the majority rely on the intrinsic interactions of the spins, although the possibility of using thermosensitive contrast agents also exists (Zhang et al., 2005). The spin-based thermometry methods are based on the effects of temperature on spin distributions or the spin active nuclei interactions with each other or the lattice, and can be measured by the T_1 and T_2 relaxation times, the PD, the water

diffusion constant and the proton resonance frequency (PRF), by either spectroscopic imaging (Kuroda et al., 2000) or phase mapping. Since, in the present work, PRF phase mapping was implemented, a more detailed description of this method is given below. Further reading on other thermometry methods can be found in a review by Rieke and Pauly (2008).

Water PRF Phase Mapping Thermometry Thermal measurement with the PRF method is done by subtraction of an unknown image phase (φ_T) from a reference one, in ‘RF-spoiled’ GE sequences with T_1 weighted images. The correlation between φ_T and the temperature is described as:

$$\varphi_T = \gamma \cdot \sigma_T \cdot TE \cdot B_0$$

Equation 4.1- Image phase and chemical shift correlation

where γ is the gyromagnetic ratio, as previously mentioned in Section 2.4.5, σ_T is the chemical shift, TE is the echo time and B_0 is the strength of the magnetic field (Poorter et al., 1995). The chemical shift, σ_T , is dependent on both the inhomogeneities of B_0 , σ_0 , and the thermal contribution (σ_t) as presented in Equation 4.2:

$$\sigma_T = \sigma_0 + \sigma_t$$

Equation 4.2- Chemical shift relation to temperature

To eliminate σ_0 from the equation, and hence to obtain the temperature change, a subtraction of φ_T at a known temperature ($T_{\text{reference}}$) is applied (Ishihara et al., 1995). While TE has a linear relation with the difference between φ_T and $\varphi_{T_{\text{reference}}}$, it is in inverse correlation with signal-to-noise ratio (SNR), so the optimal time for temperature measurement is T_2^* . Because of this, temperature mapping by PRF measurement is not only relatively fast, but also has the optimal SNR (Chung et al., 1996). Moreover, PRF is considered to be more precise MRI thermometry than the other existing methods such as T_1 and D (Włodarczyk et al., 1998), even in relatively small magnetic fields e.g. 0.2 T, as has been shown by Rempp et al. (2008). An additional benefit of the PRF method is that it is almost independent of the composition of tissue (Peters and Henkelman, 2000).

Nonetheless, there are several disadvantages to this method, e.g. neglecting the B_0 dependence on temperature is not always possible, and artifacts may occur in the presence of lipids. The latter could be partially resolved by suppression of the lipid layer in the appropriate sequences, but it is still necessary to take it into account (Li et al., 2009). Although PRF is dependent on T_2^* - which consists of both T_2 and the inhomogeneities of B_0 - it can either be linear relative to B_0 , if the main contribution comes from the magnetic field, or independent of

the magnitude of B_0 , if the main temperature contribution is from spin-spin interaction. Usually, it is considered to be in linear correlation only to B_0 (Quesson et al., 2000).

One of the main applications of PRF is thermal monitoring in ablation of tissue. PRF monitoring is applied in various ablation techniques such as: laser thermotherapy in phantoms (Olsrud et al., 1998) as well as *in-vivo* (Weidensteiner et al., 2003); radiofrequency ablation (Vigen et al., 2006); microwave thermocoagulation (Vitkin et al., 1997; Morikawa et al., 2002); and in FUS ablation in clinical applications worldwide (Hynynen et al. 2001; Tempany et al., 2003).

4.1.2.2 ExAblate System Description

The main components of the ExAblate 2000 UF system (InSightec, Haifa, Israel) are presented in Figure 4.2.

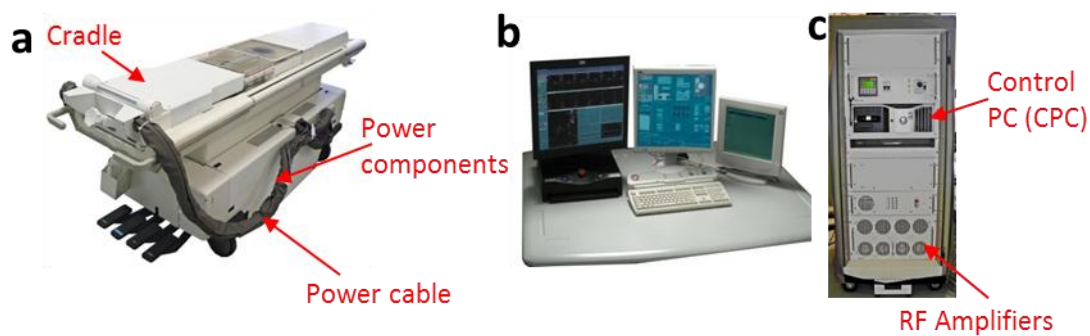


Figure 4.2- ExAblate main components: (a) cradle, (b) operator console and (c) equipment cabinet

In the UF ExAblate 2000 system, the transducer is located within the water bath in the patient table (Figure 4.3).

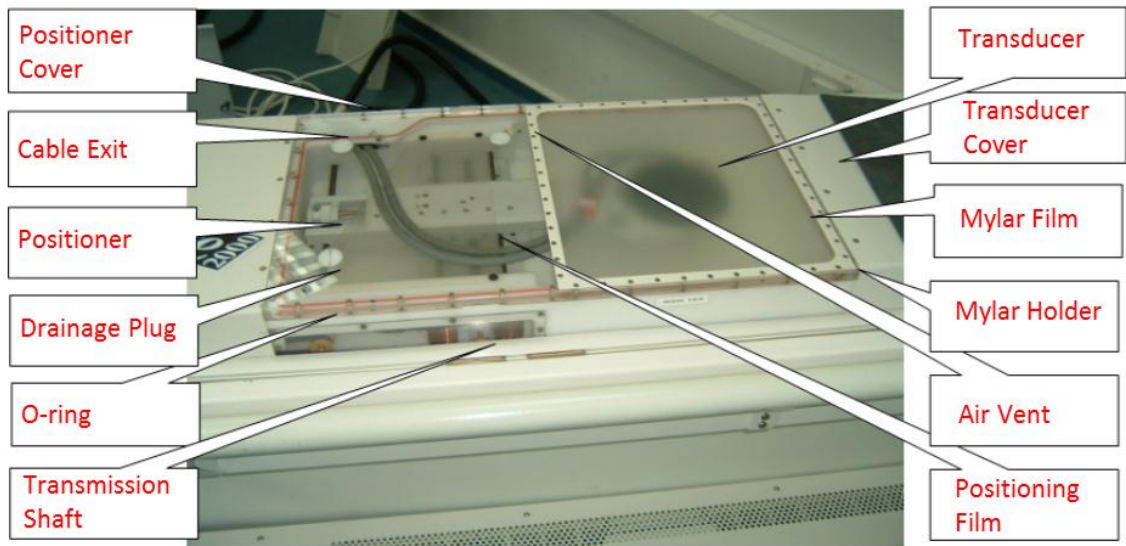


Figure 4.3- Bath components

The transducer in use in the UF system is a 208-element segmented annular curved phased array, Figure 4.4, with radius of curvature 160 mm, aperture 120 mm, and variable operating frequencies 0.95 - 1.35 MHz.

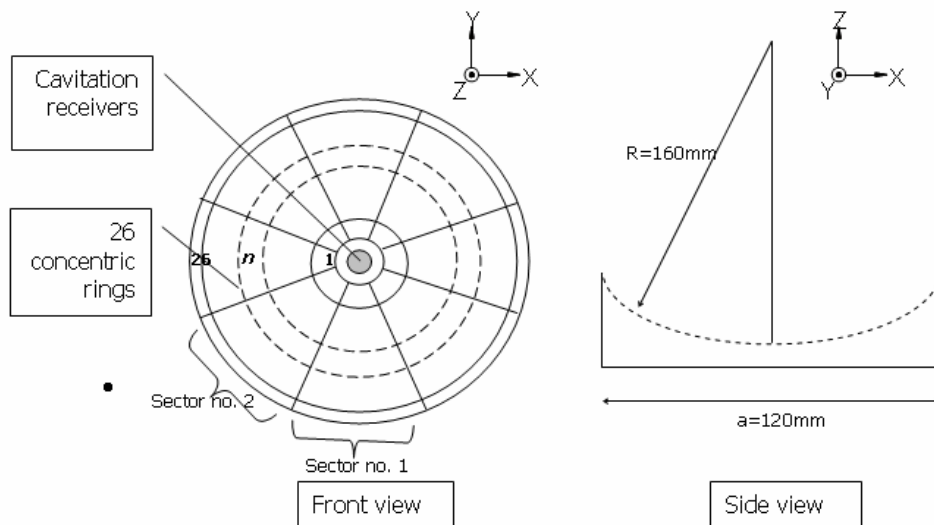


Figure 4.4- Drawing of UF transducer dimensions

The ExAblate 2100 Conformal Bone System (CBS) consists of a planar phased array transducer of 550 kHz central frequency, with approximately 1000 transmitting elements in a 74 mm square aperture. Figure 4.5 depicts the placement of the CBS transducer in the patient table as well as the dimensions of the phased array.

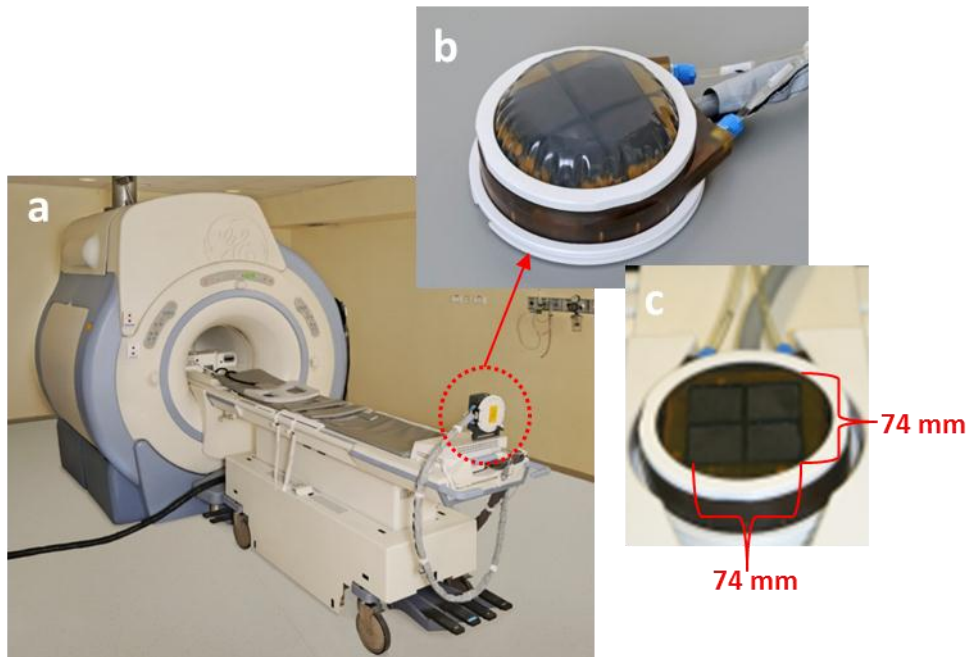


Figure 4.5- ExAblate 2100 conformal bone system (CBS): (a) connected to a MRI (b) the transducer filed with degassed water and (c) the dimensions of the transducer

4.1.2.3 Targeted Drug Delivery with ExAblate

Drug delivery with a MRgFUS system was previously introduced in Section 2.4.6. There are clear advantages in the utilization of a clinically available MRgFUS system in TDD, including beam control to minimise the damage caused by free drugs in other vital organs and the enhancement of drug effectiveness *in situ* (Jolesz, 2009). Currently one of the leading research groups investigating the application of TDD with the ExAblate system is located in Fox Chase Cancer Centre, Philadelphia, mainly focusing on delivering anticancer agents to solid tumours *in vivo* (Chen et al., 2009; Chen et al., 2010). While this research is carried out *in vivo*, the present study is mainly focused on the *in-vitro* platform in order to understand the fundamentals of USmTDD. Therefore, the arrangements were designed to apply FUS using ExAblate *in vitro*.

4.1.2.4 Challenges in Utilization of a Clinical MRgFUS System *In vitro*

The main challenge in adaptation of the clinical MRgFUS system lies in the overall complexity of the system. Because the ExAblate systems were designed and produced for clinical use, the high safety levels implemented within the arrangement and the rigidity the equipment imposes on operation introduced various difficulties. In general the ExAblate is not compatible with biological protocols; hence alterations had to be made from both sides. Moreover, MR thermometry is not possible in solid plastic cell culture plates, which required

implementation of additional thermal measurement techniques, e.g. thermal camera and thermocouples. Specific issues and their solutions are described in the results section.

4.1.3 Additional Thermal Evaluation Techniques

4.1.3.1 Thermal Camera

Thermal infrared (IR) imaging is a non-contact real time technique that is used for many purposes such as animal tracking, food quality assessment, and face recognition (Hovinen et al., 2008; Gowen et al., 2010; Socolinsky and Selinger, 2002). It is based on the assumption that all materials emit IR energy. This occurs because of molecules' movement on the surface of objects, if above absolute zero. Moreover, objects can also reflect and absorb IR energy. The IR emission depends on the temperature of the object; hence by measurement of the emission, one can determine the temperature of an object with a known emissivity value (Speakman and Ward, 1998). The correlation between the IR emission and temperature is described by the Stefane-Boltzmann law in the following equation:

$$W = e \cdot \sigma \cdot T^4$$

Equation 4.3- Stefane-Boltzmann law of energy emission as a function of temperature

where W is the emitted energy from the object (W/cm^2); σ is the Stefane-Boltzmann constant which is derived from the speed of light, Plank's constant and Boltzman's constant and equals $5.67 \cdot 10^{-8} W/m^2 \cdot K^4$; T is the temperature; and e is the material's emissivity, which equals the ratio of the material's emitted energy to that of a perfect black body. Hence, for a perfect black body, e equals 1. A perfect black body is a theoretical object that fully emits all the IR energy it receives.

A standard thermal camera consists of: the optical part i.e. a camera with various optional sets of lenses, an IR detector and an image processor. The IR detector converts the emitted energy into a signal that, after processing, will become a multilayered image in which each layer represents a certain temperature. One of the known limitations of IR imaging is its inability to measure temperature changes in transparent materials, especially plastic-based thin films, as explained by Vollmer and Mullmann (2010, Chapter 3- 3.2.1.2 Plastic Filters, and Chapter 9- 9.6.5 Plastic Foils: Selective emitters).

4.1.3.2 Thermocouples

The working principle of thermocouples is based on the fact that by introducing a temperature gradient to a conductor, a voltage is generated. The voltage can be measured by

a connection of a second, dissimilar conductor that, under the same temperature gradient, will produce a different voltage. This approach was first taken by Seebeck in 1821; utilising it, temperature differences are measured and not the absolute temperature (Morris, 2001). Hence, there is great importance in the reference temperature (T_R), which by subtraction will determine the unknown temperature (T_X). Since T_R is usually set to 0°C , the conventional method was through immersion of the wires in ice-cold water as shown in Figure 4.6.

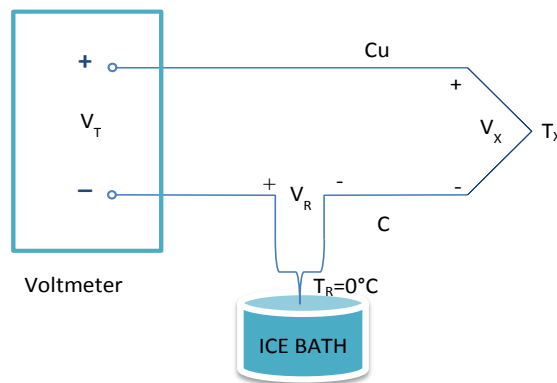


Figure 4.6- Schematic structure of a copper (Cu)- constantan (C) (T type) thermocouple

Now, the ice bath is converted to an isothermal block with a thermistor or a resistance temperature detector (RTD). The relation between the voltage measured by the voltmeter and the temperature is described by:

$$EMF = \Delta V = \Delta S \cdot \Delta T$$

Equation 4.4- Electro-motive force (EMF) as a function of thermal change

According to Equation 4.4, EMF equals the difference in voltage which also corresponds to the thermal difference multiplied by the Seebeck coefficient (S). From this equation, having two materials with different S values and a known reference temperature, T_R , the unknown temperature, T_X , can be easily calculated.

Thermocouples are frequently used because they are relatively cheap, easy to operate, and can cover a wide variety of temperatures (ASTM Committee E-20, 1981). Nonetheless, one of the thermocouple's limitations is its malfunction in an ultrasonic environment. The effects of acoustic field on thermocouple temperature measurements have been investigated since 1954 (Fry and Fry, 1954). They discovered that, because of the difference in density of the thermocouples wires and the medium they are placed in, under application of an ultrasonic field, the created motion of the thermocouples generates 'viscous heating' which is then transmitted into a false temperature reading. In other words, while thermocouples are supposed to measure the temperature of their environment, under an acoustic field they

absorb the heat generated from the viscous forces between the thermocouples and the media, which results in an artefact of a false rapid temperature increase. When the US is turned off, they re-measure the temperature of the environment, giving a true signal once again. Consequently, Fry and Fry suggested to ignore the initial rapid temperature rise and to measure the temperature from time > 0.5 s. According to Hynynen (1983) when working with focused beams the thermocouple measurements should be carried out after the ultrasonic beam is switched off. Morris et al. have referred to this approach as “wait and measure” in their thorough research of the subject (Morris et al., 2008).

In addition, the location and orientation of the thermocouples in the acoustic field is very important, as it can affect the measured temperature. Consequently, great care should be taken with the positioning of the thermocouples in acoustic environments, e.g. outside of the direct acoustic focus, for better measurements to be achieved (Hynynen, 1983). For more information on thermocouples behaviour under acoustic fields the reader is referred to a recent paper by Morris et al. (2008).

4.1.4 Aims and Objectives

A current challenge in USmTDD is the repeatability and accuracy of the experiments. Most biological research is carried out in a sterile environment under constant conditions, such as temperature and humidity. In contrast, US is a physical procedure that requires continuous physical coupling of the desired target with the transducer by immersion into degassed water or application of coupling gel. Therefore the conjunction between the two fields is complicated.

Since there were no easily available commercial tools for biological cell sonication, specially designed apparatus was created, in combination with the clinical MRgFUS system. The purpose of the bespoke arrangement was to introduce US to cells to investigate their behaviour as a result of sonication. Such apparatus could also allow differentiation between the thermal and physical effects on cells - a major issue in current cell sonication work. For this purpose, three *in-vitro* ultrasonic arrangements were developed, with two focusing on TDD via sonoporation. The MRgFUS UF apparatus allows sonication at frequencies 0.95 - 1.35 MHz in an automated manner via a prewritten computer script. The CBS arrangement, $f = 550$ KHz, increased the chance of cavitation and also presented the possibility of multi-focal sonication patterns. The third arrangement was set up to investigate the effects of US generated (mild) heating on cells. An additional heating arrangement, without FUS, was created to serve as a control for the FUS induced heating.

4.2 Materials and Methods

4.2.1 Materials

Table 4.1- Equipment and consumables

Material	Manufacturer	Place of Origin	Notes
Equipment			
1.5 Tesla MRI system	General Electric	USA	Model: Signa HDX
ExAblate 2000	InSightec LTD	Israel	UF, 0.95-1.35 MHz
ExAblate 2100	InSightec LTD	Israel	CBS, 550 kHz
Thermocouple data logger	Omega	UK	Model TC-08
Thermocouples	Omega	UK	Omega T type, 0.25 and 0.076 mm wire diameters
Fibro-optical hydrophone	Precision Acoustics	UK	
Needle hydrophone	Precision Acoustics	UK	0.5 mm diameter
Stuart Heat-Stir	Barloworld Scientific	UK	Model: CB162
Techne Dri Block	Techne	UK	Model: DB-20
IR thermal camera	FLIR	UK	Model: JADE
Consumables			
Daily quality assessment (DQA) gel phantom	ATS Laboratories	USA	
96-well plates	Greiner	Austria	Polystyrene cell culture microplates with μ Clear [®] bottom
Black 96-well plates	Greiner	Austria	Non cell culture treated black base microplates

4.2.2 Methods

4.2.2.1 Design and Construction of Sonoporation Arrangements

ExAblate UF System Currently most of the studies in USmTDD are carried out in cell suspensions (Feril Jr. et al., 2002) or in an Opti-cell environment (Eisenbrey et al., 2009; Feril Jr. et al., 2010). The latter, although having excellent visualization possibilities, fundamentally lacks an isolated control. In the current study, the effect of FUS was investigated on cell monolayers, therefore, a typical arrangement consisting of 96 isolated wells in a uniform plate (referred to as a plate henceforth) was chosen to populate the cells. This way various treatment groups could be sonicated in one plate, with positive and negative controls *in situ* for each of them. To maintain the sterility of the plate and to ensure isolation of the treatment groups, sealing film was applied on top of the plate.

The particular plate and the sealing film were chosen such that the plate has a thin base, 0.2 mm, and the seal is also thin, 0.01 mm. Moreover, the plates chosen for this work had to be opaque, preferably black, for fluorescence studies.

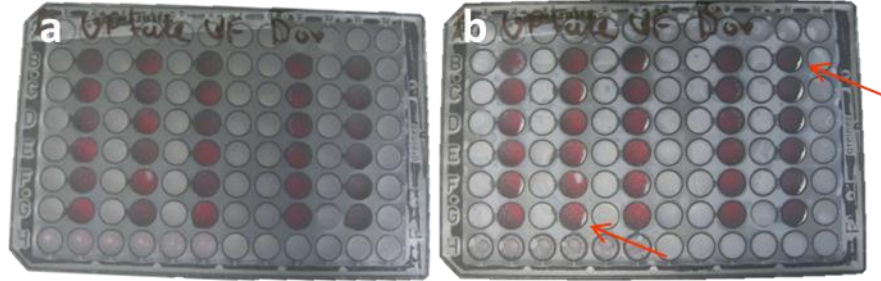


Figure 4.7- Sealed plate (a) before and (b) after sonication

Figure 4.7 depicts a sealed plate before and after sonication. It can be seen that before the sonication, all the treatment groups look approximately the same, and after the application of FUS, certain wells contain a white substance; this is MB residue (marked by red arrows). The location and order of the optimal sonication pattern (i.e. the sonication pattern having the lowest impact on the neighbouring wells) that was developed for the UF sonoporation arrangement is presented in Figure 4.8.

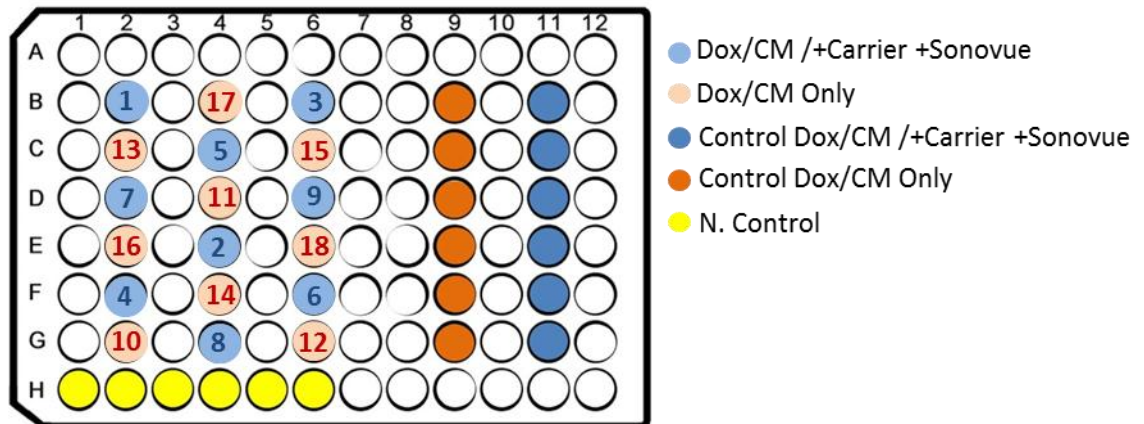


Figure 4.8- Diagram of sonication pattern and order in the UF sonoporation arrangement

According to Figure 4.8, the order of sonication of the plate is as follows: B2-E4-B6-F2-C4-F6-D2-G4-D6-G2-D4-G6-C2-F4-C6-E2-B4-E6. Since the stability of MBs is time dependent (Schneider, 1999), in this pattern all the groups that contained MBs were sonicated first and only then the groups without MBs. This specific pattern of sonication was chosen to avoid accumulating effects from neighbouring wells in the same plate as was validated by the uptake studies presented in 5.3. The plate was placed in water upside down to ensure that the MBs are in proximity to the cell monolayer because the MBs float upwards. Initially the sonication

via the UF sonoporation arrangement was conducted under MR guidance, as presented in Figure 4.9.

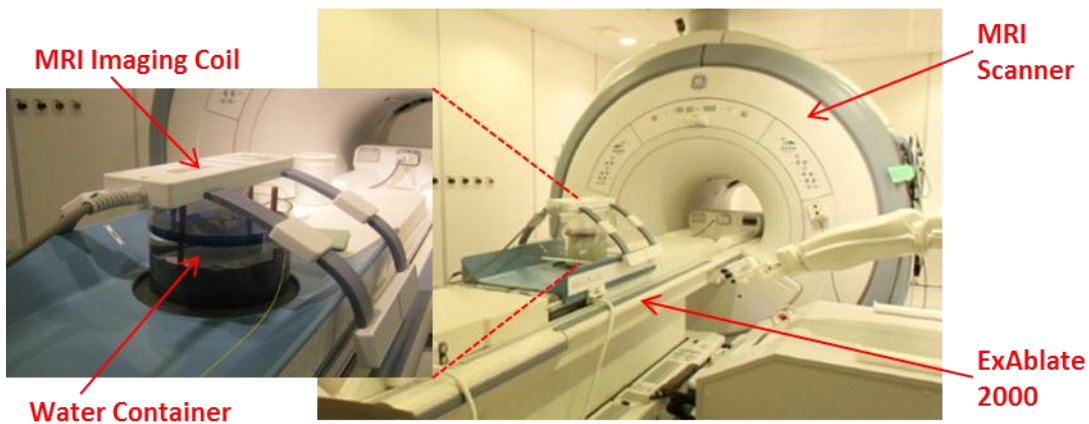


Figure 4.9- Initial UF sonoporation arrangement in MR environment

In Figure 4.9, the plate is located between the FUS source below and the imaging coil above. The plate is immersed in 3 litres of degassed water inside a dedicated container which consists of a mylar base i.e. US transparent material, plastic rings with special cut outs for placement of the plate and holes for insertion of rods to hold the absorbing material, which is placed about 5 cm above the location of the plate, Figure 4.10.

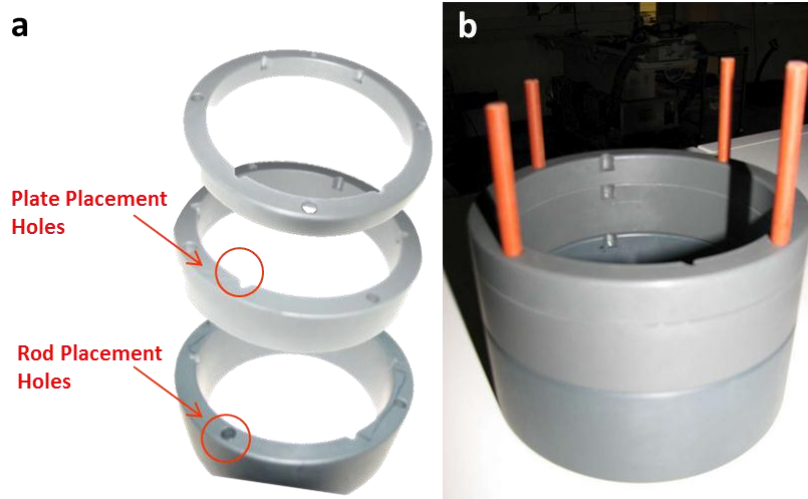


Figure 4.10- Plate holder rings (a) separated and (b) stacked

As presented in Figure 4.10, there are three sizes of rings, with dedicated cutouts for the plate positioning in each one. The heights of the rings are 20, 40 and 60 mm. The final arrangement consisted of 20 and 40 mm rings placed on top of each other at the final height of 60 mm. The FUS transducer in the ExAblate UF system is located inside a hermetically sealed water tank and is coupled to the experimental container with degassed water. The water in the container was degassed and adjusted to 30°C prior to immersion of each plate. 30°C was

the optimal temperature since it protected the cell monolayer from hypothermia yet did not cause any detachment of the sealing film. To keep the temperature constant throughout the experiment a polystyrene box was placed over it, under the imaging coil, as presented in Figure 4.11. The polystyrene box thermally isolated the experiment very effectively, with a small temperature drop of only 0.5°C - 3°C drop after 2 h in a 20°C room, and hence was implemented throughout all the UF arrangements.



Figure 4.11- UF sonoporation arrangement covered by a polystyrene box

After temperature adjustment and careful polystyrene box positioning, the apparatus was moved inside the MRI scanner. The following MRI scans were performed: 3D localizer, coronal and sagittal with field of view (FOV) = 48 and 5 mm slice thickness. No axial scans were done in order to avoid any table movement that might affect the experiment. In the ExAblate software, the spot location was chosen in the coronal slice, as shown in Figure 4.12(a) and then adjusted to the specific height using the sagittal images, Figure 4.12(b).

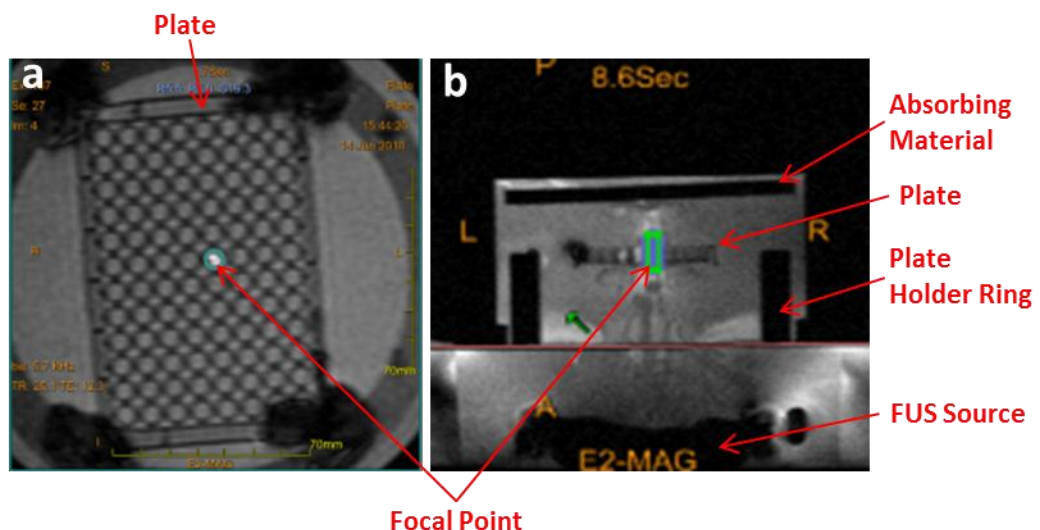


Figure 4.12- Spot planning in (a) coronal and (b) sagittal images of a plate

Spot accuracy testing in a daily quality assessment (DQA) phantom was performed on the day prior to each set of experiments. The DQA phantom is a tissue mimicking phantom

that absorbs approximately 10% of the acoustic energy for each centimetre of US propagation. During the sonications, temperature mapping scans were conducted via the ExAblate software. The thermal imaging consisted of pre-sonication scans for reference; scans during sonication, conducted in real-time with the application of FUS; and post-sonication, cooling phase, scans to follow the thermal behaviour after sonication. At first, all the experiments were conducted with the normal ExAblate software, but as the work advanced more sonication protocols were investigated that required access to the control personal computer (CPC) of the ExAblate.

Each spot location planning took about 60 s and the sonication time was 60 s on average per well, with one pre-sonication scan and an additional two post-sonication cooling phases. With typically 18 spots per plate, the total sonication time was about 45 min to an hour. The adjustment of the plate in the sonication arrangement took around 20 min on average and MRI scanning before and after the sonications together with the return of the plate to the tissue culture lab took about 20 min, so the total exposure time of each plate was approximately 1.5 h to 2 h. Such long exposure time was problematic from various points of view, both biological, e.g. the nonuniformity of cell exposure times, masking of the FUS effects (60 s in 2 h), and more basic, e.g. the low replicate number of treatments that could be done per experiment. Moreover it introduced physical issues such as the need to add pre-heated degassed water to the sonication container and availability issues with booking prolonged time of MRI suite.

An additional problem in the arrangement that has been described concerned the spot location chosen as a result of differences between the coronal and sagittal images. As previously mentioned and shown in Figure 4.12, the sonication spot was set according to the coronal images. When the sagittal images were reviewed to confirm the location of the spot and adjust its height, a 2 mm shift in the position of the spot was observed. Further investigation showed that the shift is a common phenomenon that exists in many MRI scans of purely geometrical shapes as well as human tissue (Sumanaweera et al., 1996).

Shifts in MRI can occur for various reasons including inhomogeneity of the magnetic field and the nonlinearity of the gradients. Image corrections methods are available but they often result in loss of quality in the images (Langlois et al., 1999; Wang et al., 2004). As the diameter of each well in the plate is 7 mm and the focal spot is about 2.5 mm wide, a shift of even 3 mm can result in the focus directly hitting the well wall. This was the case in several early experiments, presented in Figure 4.13. The deformation presented in the well happened as a result of a shift of the focus from the centre of the well.



Figure 4.13- Deformation in a single well due to FUS (marked in red)

To overcome all the mentioned issues, an automated script was developed that sonicated each well in the plate according to pre-established coordinates. The utilization of the automated script without the need of MRI resulted in a more accurate and efficient arrangement. The improved arrangement not only significantly decreased the experimental duration, e.g. 20 min for 60 s sonication at 18 spots, reduced from 2 h, but also eliminated the possibility of human error.

Since the sonications are performed according to specific coordinates, the experimental arrangements must be rigid to avoid any movement of the plate or wrong placement. In order to ensure repeatability in the location of the placed plate, a metal structure was attached to the ExAblate cradle to define a constant plate location, as demonstrated in Figure 4.14.

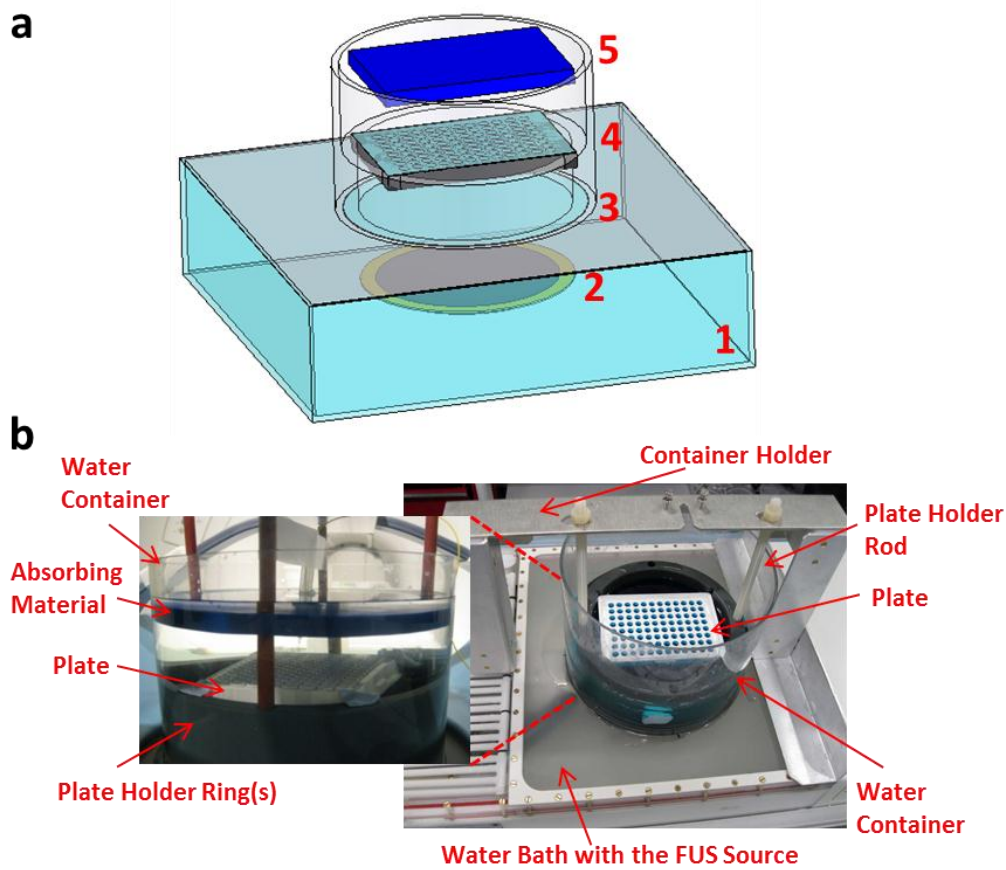


Figure 4.14- Final UF sonoporation arrangement: (a) designed model, key: 1- water bath containing FUS source; 2- FUS source; 3- degassed water container; 4- the plate; 5- ultrasound absorber material, and (b) real imaging

Ten cm above the plate an absorbing material was placed, as shown in Figure 4.14, to absorb any excess of acoustic waves and prevent their reflection from the water-air boundary. Prior to each experiment, the arm positioning was calibrated according to the location of the focus inside two pre-defined opposite wells in the plate. For this purpose, the water in the container was filled such that it reached only half of the height of a special baseless plate, following which sonication inside the wells created visually seen fountains. In the automated script utilised for sonication of the wells in the plate the following parameters were included: spot location (X, Y coordinates), the power applied, the sonication duration and the sonication mode (continuous / pulsed- Duty Cycle (DC) and Pulse Repetition Time (PRT)) as well as the frequency and the Focal Distance (FD) (Z).

After thorough acoustic evaluation, the FD was chosen to be 97 mm from the transducer, which is located exactly in the middle of the well as shown in Figure 4.15. According to the acoustic measurements, focal height of 97 mm had less effect on the

neighbouring wells than other FDs, results shown later in Figure 4.54. Full dimensions of the plate in use can be found in Appendix iii.

As previously stated, the UF transducer is a phased array with 208 elements. This type of transducer introduced the possibility of having various beam forms by manipulating different elements and hence creating different sonication patterns. After examining various beam forms, the optimum beam form was found to be when 50% of the transducer rings (Tr) are on, and 50% are off. Utilization of 50% Tr resulted in a longer and more concentrated focal point that fitted the well geometry better due to lower interference at the entrance to the well. The beam diameter and length were calculated to be 2.6 mm and 30.24 mm respectively. The calculations were done using technical notes by Olympus NDT (2008); full equations can be found in Appendix iii. Figure 4.15 is a schematic representation of the focal point inside a single well with 50% Tr at FD = 97 mm i.e. the optimal parameters as were defined by the acoustical evaluation.

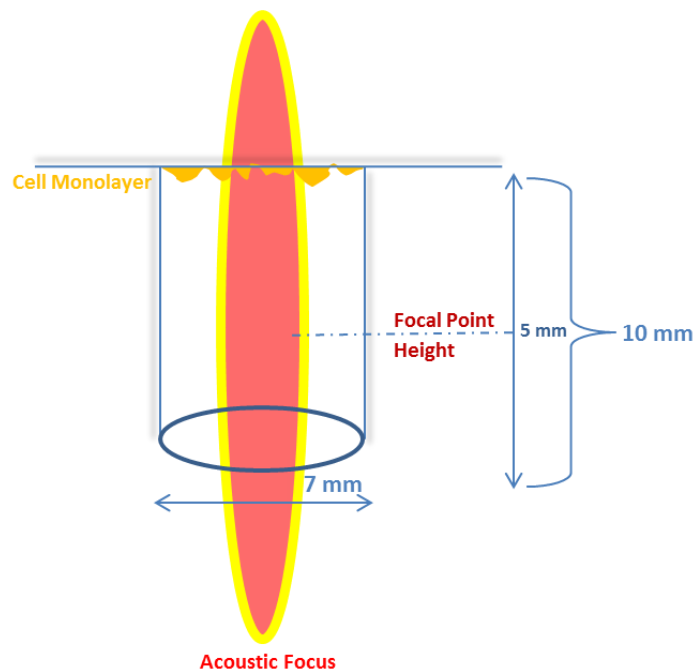


Figure 4.15- Focus within a single well in an inverted plate

The frequency of the applied FUS was set to 0.95 MHz to gain a wider focal spot and higher probability of cavitation (Maisonhaute et al., 2002).

ExAblate CBS The CBS arrangement is shown in Figure 4.16. It comprises the ExAblate 2100 phased array in its holder, a container full of degassed water, an inverted sealed plate 62 mm above the planar phased array, and an absorbing material 40 mm above the plate.

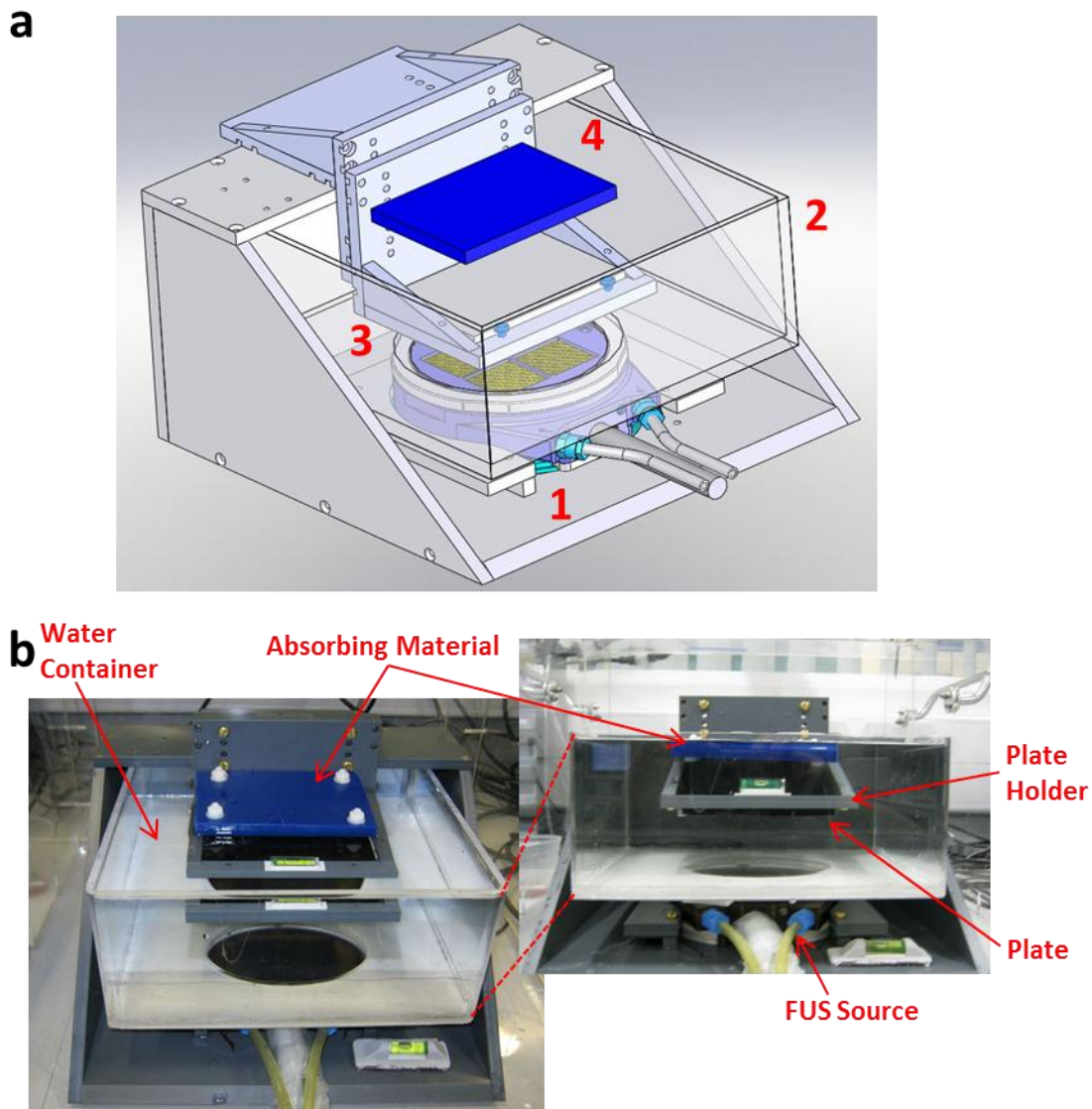


Figure 4.16- CBS sonoporation arrangement: (a) designed model, key: 1- FUS source; 2- degassed water container; 3- the plate; 4- ultrasound absorber material, and (b) real imaging

The water was pre-heated to 30°C prior to every set of experiments. The plate was sealed and placed in water upside down in the same manner as in the UF system. The phases for 16 focal points with minimal intensity distribution generation were calculated according to the iterative GS algorithm described by Hertzberg and Navon (2011). The points were selected such that each point is located inside a single well in the 96 well plates. All the spot locations in a single plate are depicted in Figure 4.17.

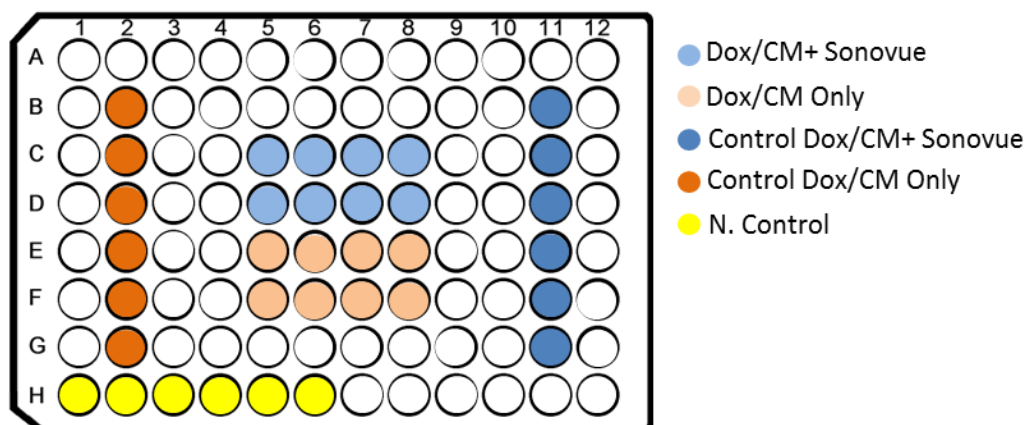


Figure 4.17- Diagram of sonication pattern in the CBS arrangement

According to Figure 4.17, all the wells in the treatment group were sonicated simultaneously with a multi-focal pattern of sonication.

4.2.2.2 Design and Construction of Heating Arrangements

As mentioned previously, the carriers in use in this work are temperature dependent and the drug release can be triggered by a temperature rise. To obtain a controlled and uniform temperature rise *in vitro*, two arrangements were created. The main one utilizes FUS as the heating source; and a control arrangement without FUS.

Heating Arrangement without Focused Ultrasound The heating arrangement without FUS consists of two heating blocks at different temperatures. On the heaters, two metal blocks of specific sizes were placed, such that only a certain part of the plate was heated, allowing control wells on the same plate. The arrangement is displayed in Figure 4.18. As can be seen, the heaters are directly heating the two metal blocks whose temperature is constantly monitored by attached thermocouples.

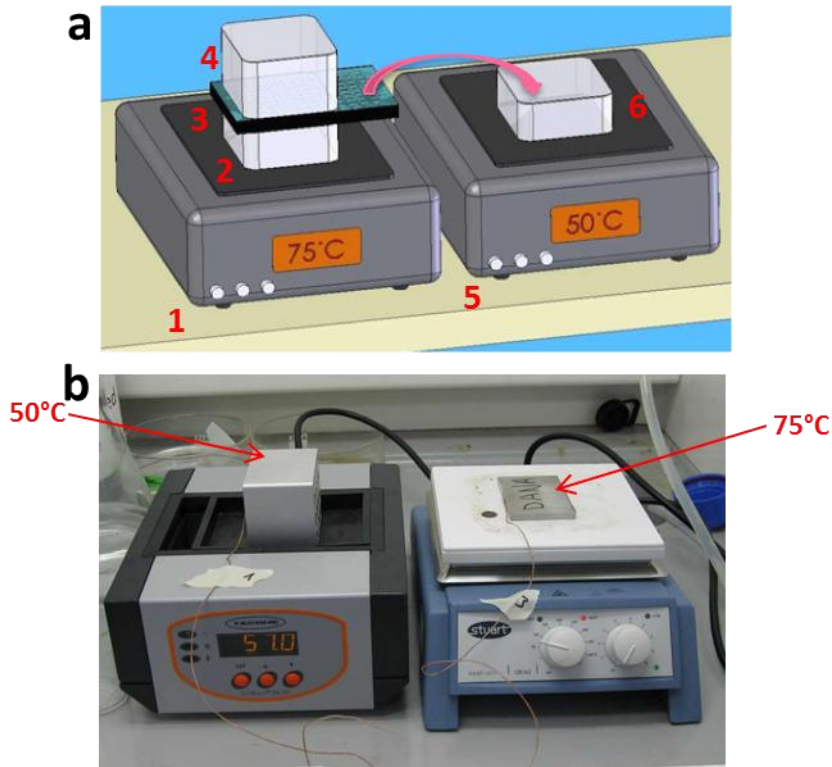


Figure 4.18- Heating arrangement without FUS: (a) designed model, key: 1- 75°C heater, 2- 75°C heating block, 3- plate, 4- top block, 5- 50°C heater, 6- 50°C heating block, and (b) real imaging

In both of the heating arrangements, the plate was placed upside down to avoid direct and non-linear heating of the cells through the plastic plate and to ensure that the solution within each well heated homogeneously. The optimal heating pattern (i.e. having the highest possible amount of treatment groups and isolated control groups) for the heating arrangement without FUS is presented in Figure 4.19. As shown in Figure 4.19, all the wells of the treatment group were heated simultaneously.

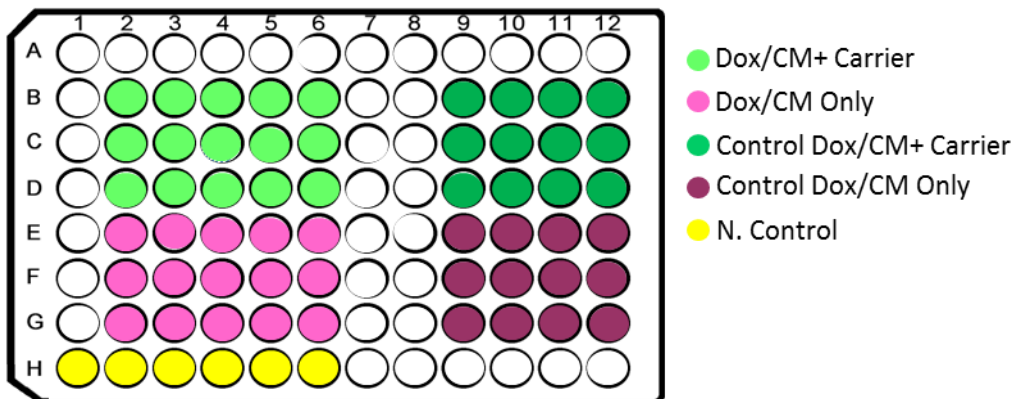


Figure 4.19- Diagram of heating pattern in the heating arrangement without FUS

ExAblate UF System Based on the previously described sonoporation configuration, FUS induced heating was tested as a possible mechanism for enhancement of cell permeability. This was investigated using a DQA phantom gel. The phantom was placed below the plate to deliver the FUS-generated heat to the proximity of the focused wells, and to partially absorb the acoustic energy propagation before reaching the well.

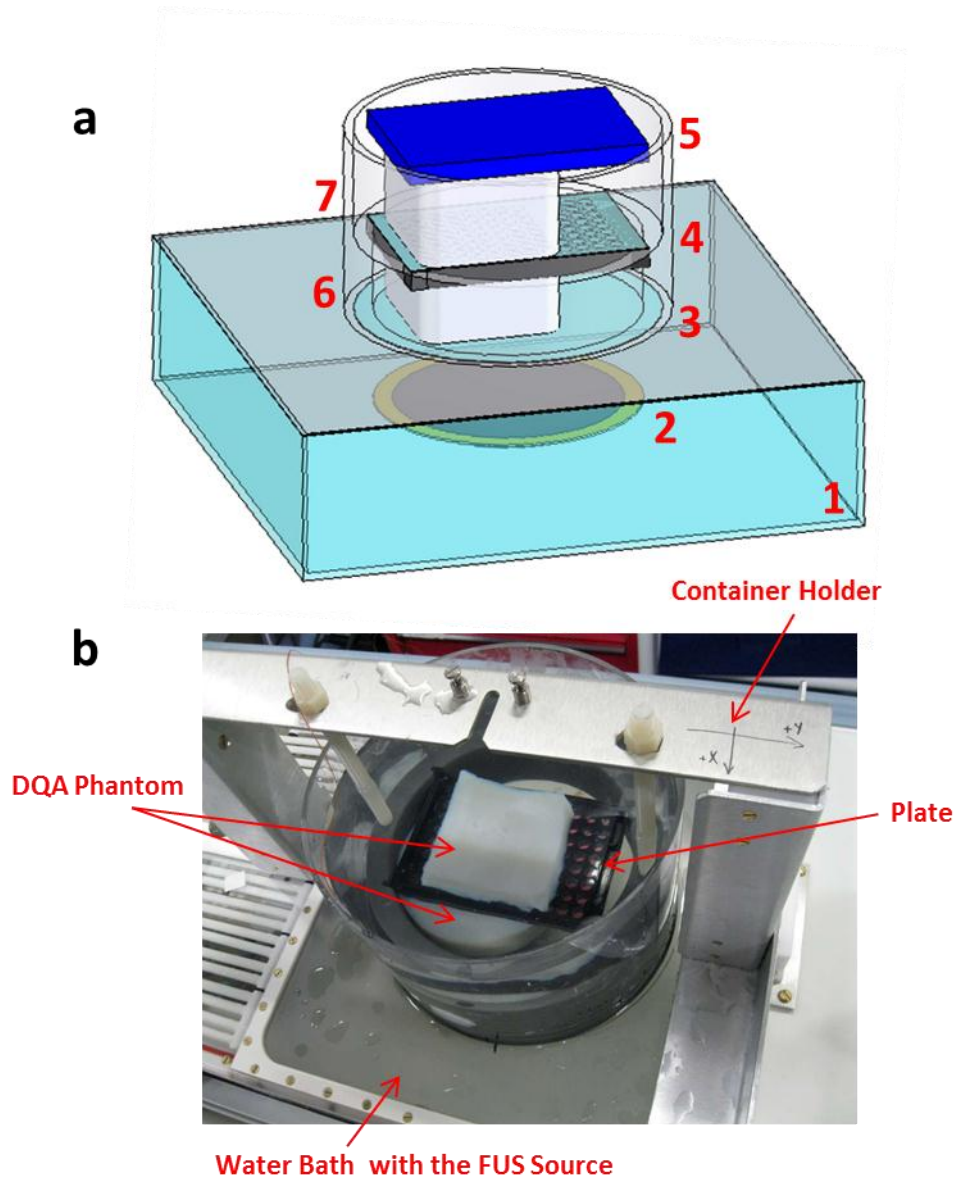


Figure 4.20- UF heating arrangement: (a) designed model, key: 1- water bath containing FUS source; 2- FUS source; 3- degassed water container; 4- the plate; 5- ultrasound absorber material 6 and 7 - lower and upper tissue mimicking phantoms, respectively, and (b) real imaging

As can be seen in Figure 4.20, the DQA phantom was placed underneath and on top of the inverted plate. In the cell culture experiments, an absorbing material was placed on top of

the upper phantom, not shown in the figure, to sustain a constant temperature in the proximity of the cells and to prevent reflection from the air. Because of the long sonication periods, about 1 h per plate, and the relatively high acoustic powers in use, the water in the container was replaced in between each plate with fresh degassed water to avoid cavitation.

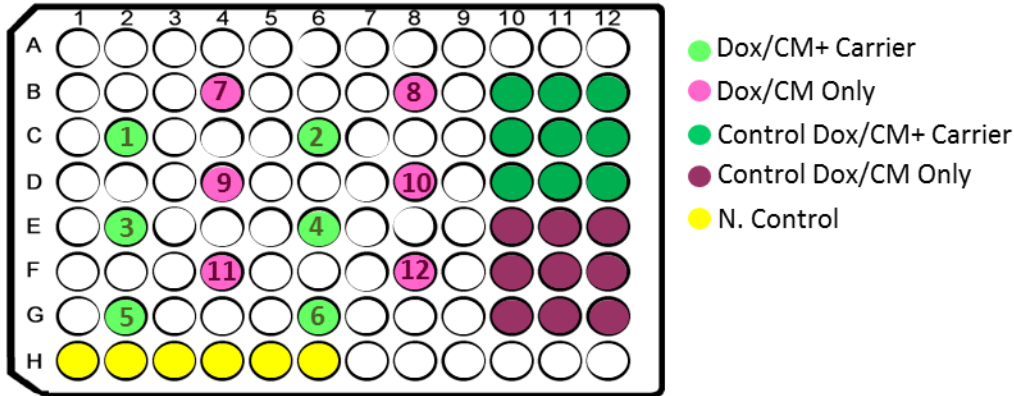


Figure 4.21- Diagram of sonication pattern and order in the UF heating arrangement

The location and order of the sonication pattern for the UF heating arrangement is presented in Figure 4.21 with a sonication order as follows: C2-C6-E2-E6-G2-G6-B4-B8-D4-D8-F4-F8. This sonication order was chosen to avoid heat accumulation by thermal isolation of each well by surrounding air filled wells. The frequency was set to 1.35 MHz to decrease the possibility of cavitation and to increase the absorption in the phantom and hence to shorten the propagation distance. Due to the CBS’s low frequency, 550 kHz, it was not considered suitable for heating purposes in the current arrangements.

4.2.2.3 Thermal Evaluation of the Apparatus

MRI The MRI thermometry in use in the present work was achieved via the software supplied with the ExAblate system. As part of the tracking of temperature rise in tissues, a graph (e.g. Figure 4.22, where green line shows average temperature in the nine pixels surrounding / including the selected pixel, red line is the temperature at the selected pixel) is recorded which represents real time temperature *in situ* based on PRF MRI thermometry.

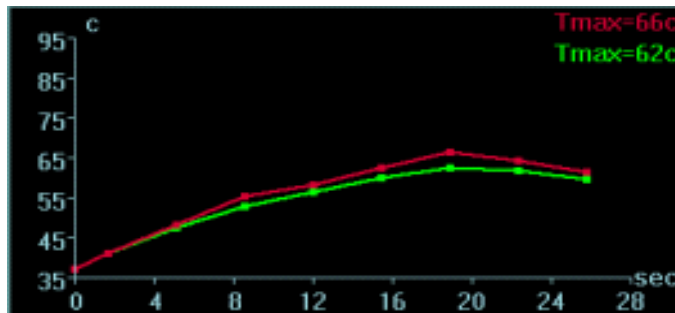


Figure 4.22- PRF temperature measurement via the ExAblate software

Thermal Camera The thermal evaluation of the UF sonoporation arrangement was performed by IR thermal camera measurements outside the MRI suite. The camera was placed above a partially submerged plate, focusing downwards on the part of the plate which is above the water level, Figure 4.23.

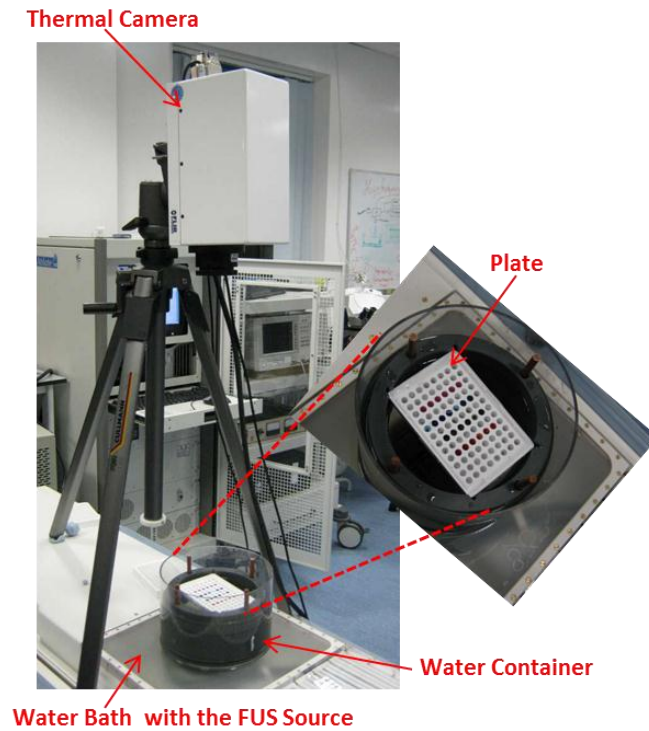


Figure 4.23- Positioning of thermal camera on the UF table

After careful positioning of the thermal camera on a tripod on the UF table, the camera was connected to a PC with Altair software (FLIR, UK) to record the thermal changes. Via the Altair software both videos and graph of temperature time dependence were created as shown in Figure 4.24.

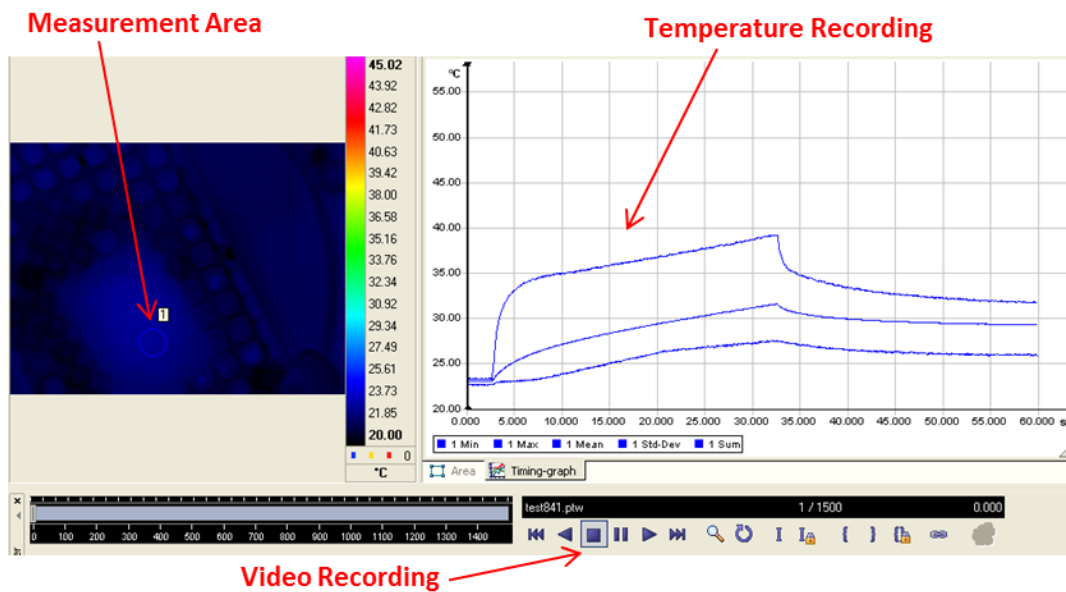


Figure 4.24- Altair software for thermal evaluation via FLIR IR thermal camera

Thermocouples The thermocouples in use in all the experiments were of type T. Type T thermocouples consist of copper, Cu, and constantan, Ni-Cu, wires. This type was chosen for its wide range of temperature measurement, -250°C - 400°C , and relatively low error, 1°C / 0.75% above 0°C ; 1°C / 1.5% below 0°C , whichever is higher in both cases (Omega, n.d.). The thermocouples were connected through a data logger to the computer. The data were recorded using Picolog software (Omega, UK). Each thermocouple was attached to the surface of the plate using a medical plaster, to keep it in a constant place yet not to interfere with the temperature measurement.

Heating without FUS The heating arrangement was based on monitoring temperature changes throughout the plate and subsequently moving it between two different heaters (Figure 4.18). To measure and record the temperature changes in the plate in real time, thermocouples were attached to the base and sealing film on the plate, as presented in Figure 4.25.

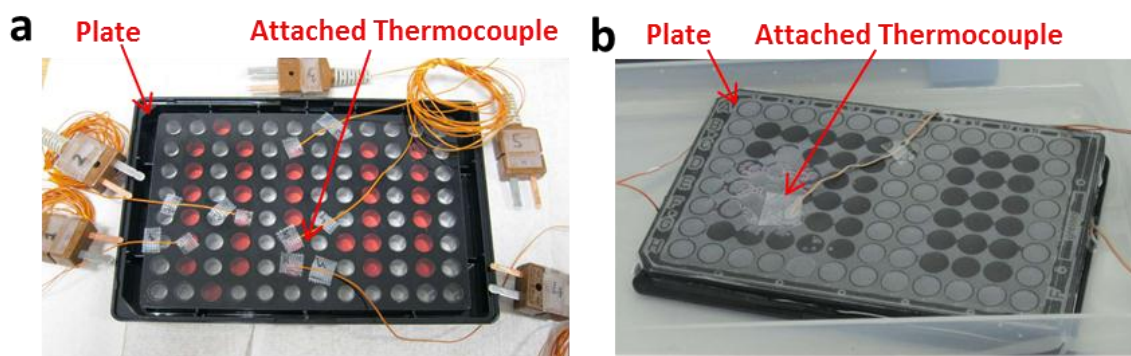


Figure 4.25- Thermocouples attached to the (a) base and (b) sealing film on a plate

UF Heating Arrangement To validate the temperature rise measured by MR thermometry, a second thermal evaluation of the heating arrangement was conducted using thermocouples. The thermocouples were attached to the plate inside and outside several wells, and the plate was placed inverted and the right way up between two DQA phantoms (Figure 4.26) in the arrangement presented in Figure 4.20.

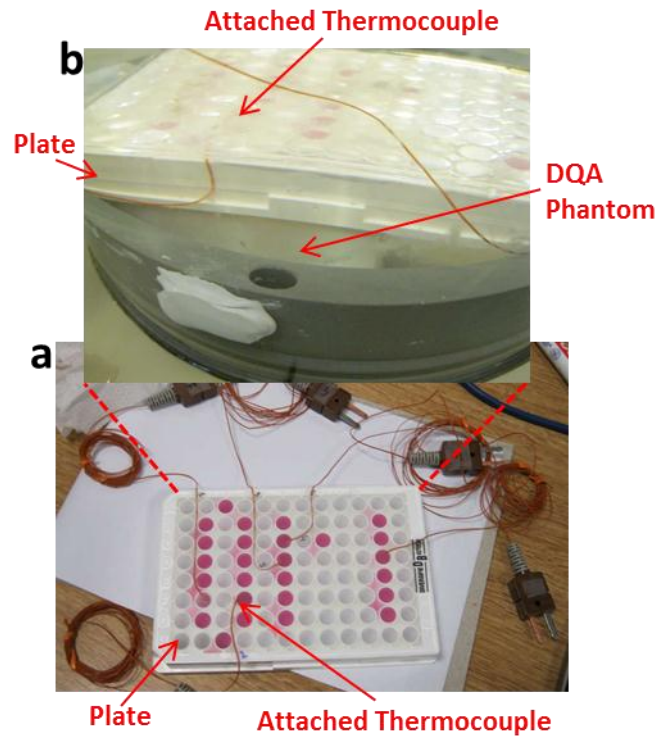


Figure 4.26- (a) thermocouples attached to a plate and (b) placed over a phantom

UF Sonoporation arrangement To ensure that no temperature rise occurred in the sonoporation arrangement, it was evaluated by thermocouples attached to the base of sonicated wells. After attachment of the thermocouples to the various wells in the plate, it was placed upside down inside the water container, as shown in Figure 4.27.

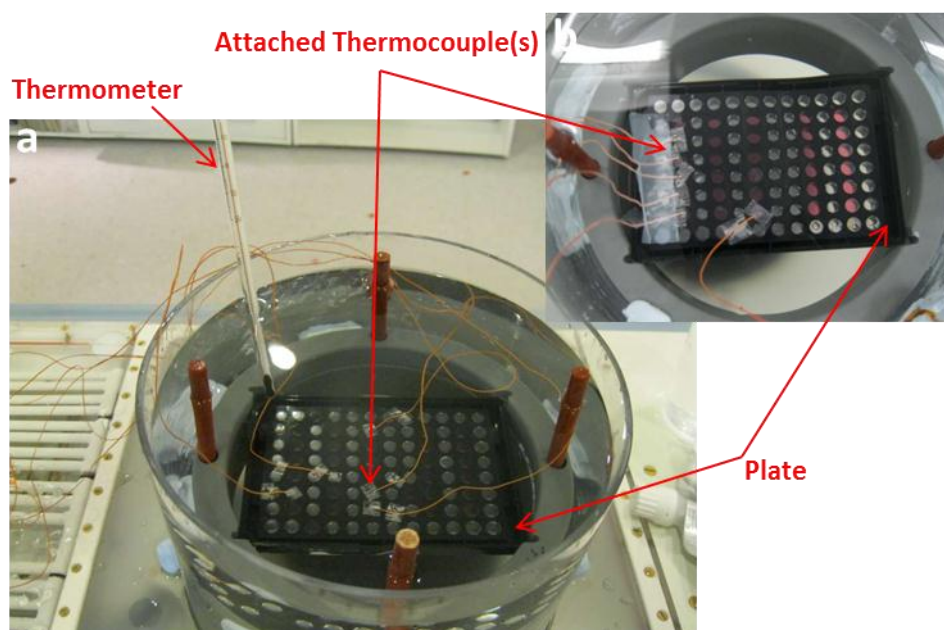


Figure 4.27- Thermocouples attached to a plate in the UF Sonoporation arrangement

As can be seen in Figure 4.27, the plate with the thermocouples attached to it was fully immersed in water. A Hg thermometer was placed in the container to validate the functioning of the thermocouples by comparison with the initial temperature in the container.

4.2.2.4 US Evaluation of the Apparatus by Hydrophone Measurements

A 0.5 mm needle hydrophone or a fibre-optic hydrophone was placed inside a bespoke positioning device with two automated degrees of freedom and a manual Z-axis. The hydrophone positioner was fixed on top of the arrangement and the acoustic properties of the plate were observed. The peak voltage from the hydrophone was recorded for each location.

US properties of the plate base and seal To evaluate the acoustic properties of the plate base and sealing, special arrangements were made with plates consisting of the plate frame and only a sealing or a base film, without any wells (Figure 4.28).

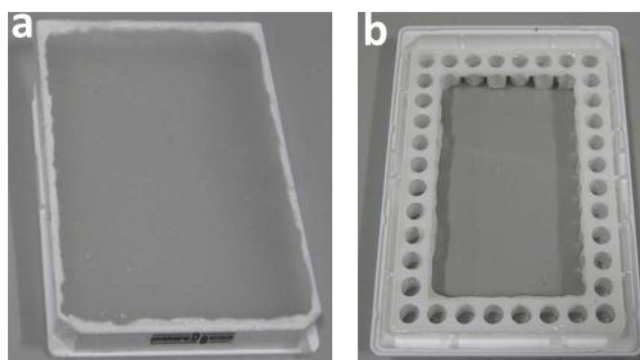


Figure 4.28- Special plates with (a) only a sealing film or (b) base attached to the plate frame

These plates were placed in the sonication arrangement, between the US source and the hydrophone, as presented in Figure 4.29.

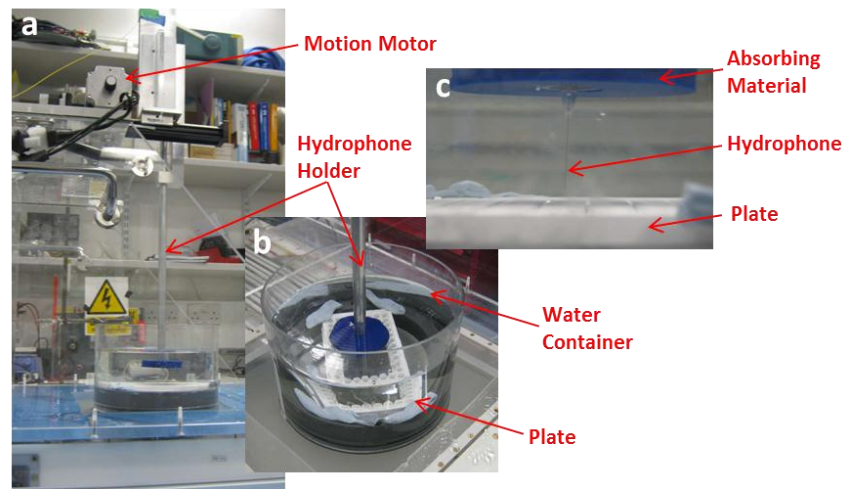


Figure 4.29- (a) the hydrophone positioner (b) scanning base part of a plate (c) hydrophone position over the plate

Figure 4.29 shows a fibre-optic hydrophone inside the hydrophone positioner, scanning the base part of a plate; similar scans were performed for the sealing film.

US Field Measurements To establish the behaviour of a focused US beam penetrating through a plate, US field measurements were done. A 0.5 mm diameter hydrophone was positioned in the same way as presented in Figure 4.29, and the US field with and without the plate was mapped as shown in Figure 4.30.

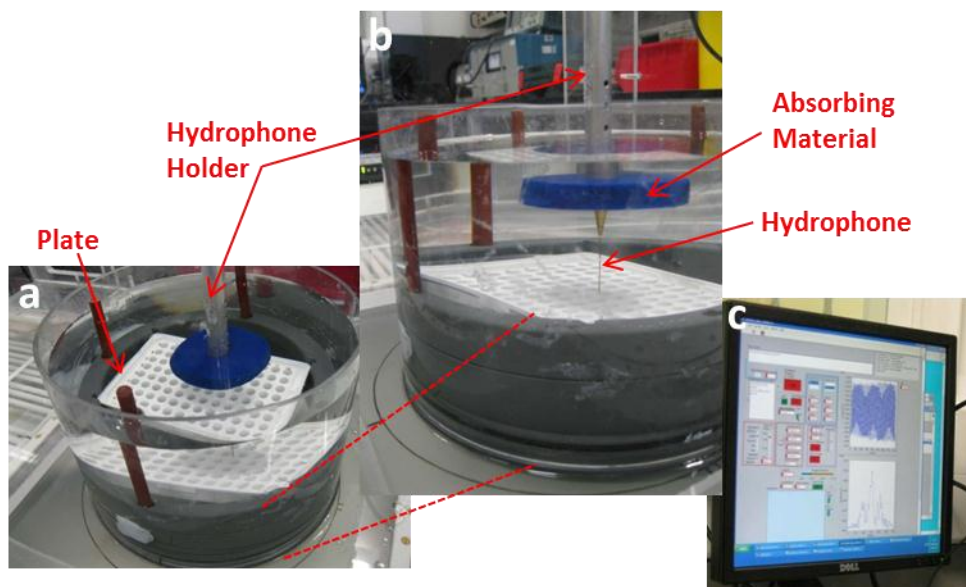


Figure 4.30- (a) US field measurements (b) positioning of the hydrophone above the plate (c) interpretation of the data using dedicated software

Figure 4.30 depicts the scan over an inverted plate. As mentioned previously all the data was interpreted via dedicated software to obtain the results shown in this manuscript.

4.3 Results

4.3.1 Thermal Evaluation

4.3.1.1 Magnetic Resonance Imaging Thermometry

The main use of MRI thermometry was in thermal evaluation of the heating arrangements with the UF system. As previously mentioned it is impossible to retrieve temperature mapping of a solid plastic material by PRF measurements, hence the temperature mapping took place in the tissue mimicking DQA phantom below and above the plate.

Prior to the sonication, positioning images were collected, with coronal, sagittal and axial scans presented in Figure 4.31 - Figure 4.32.

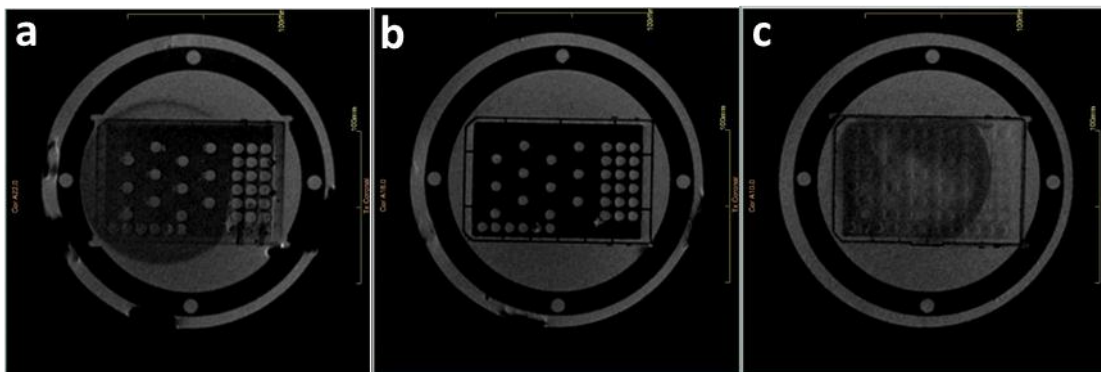


Figure 4.31- Coronal images of a plate between two DQA phantoms

Figure 4.31 represents the coronal scan of the plate placed between two phantoms at different slice heights. In the slice presented in 'a' the bottom phantom is visible, slice 'b' is in the middle of the plate, and slice 'c' shows the plate with the upper phantom. As can be seen in the figure several wells appear bright coloured whereas others remain dark. The bright wells are filled with the testing solutions and the dark wells contain air for isolation.

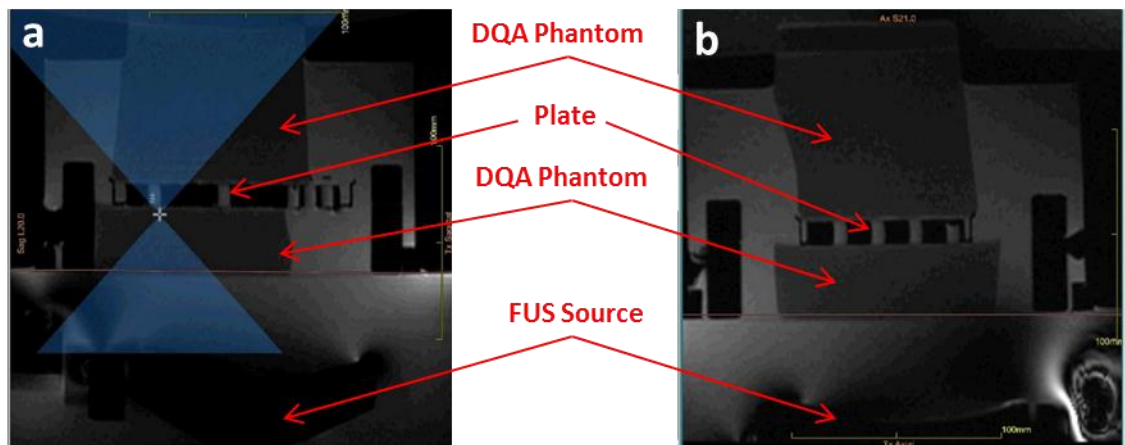


Figure 4.32- (a) sagittal and (b) axial images of a plate between two DQA phantoms

Figure 4.32 depicts the sagittal and axial scans of the plate in the UF heating arrangement. According to these scans the thicknesses of the bottom phantom, the plate and the upper phantom are 34.6 mm, 10.2 mm and 93.7 mm respectively. The sagittal scan shows the expected area of the US beam passage called the passzone.

The sonication pattern in the heating arrangement consists of two sonication modes: initial continuous sonication to achieve a fast temperature rise and a second pulsed sonication to maintain a constant elevated temperature, as presented in Figure 4.33.

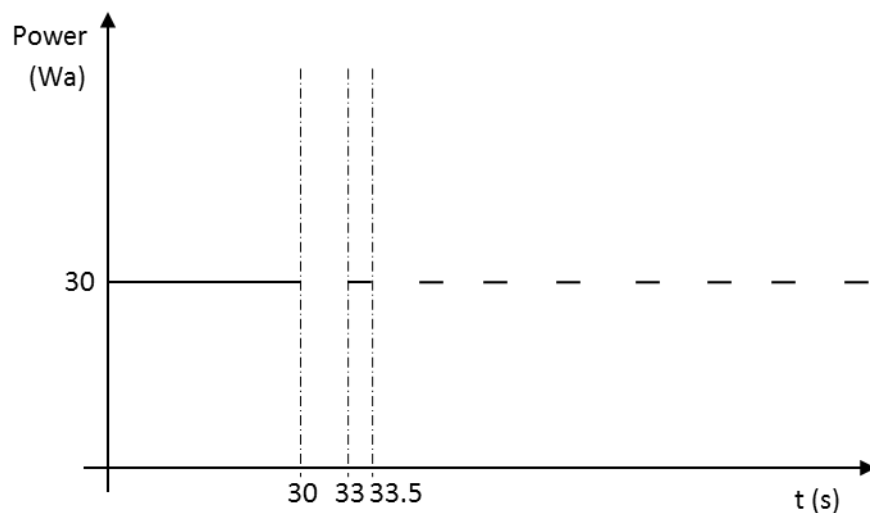


Figure 4.33- Schematic representation of the combined sonication mode

To evaluate the heating process in each well, MRI temperature mapping of the upper and lower phantoms was performed. The figure presented below correlate to real sonications on a cell monolayer inside an inverted plate with an acoustic power of 30 Watts (Wa) (i.e. the output power as defined by the ExAblate system) for 30 s continuous sonication and 30 Wa for 180 s, with 0.5 s on, 3 s off pulsed sonication.

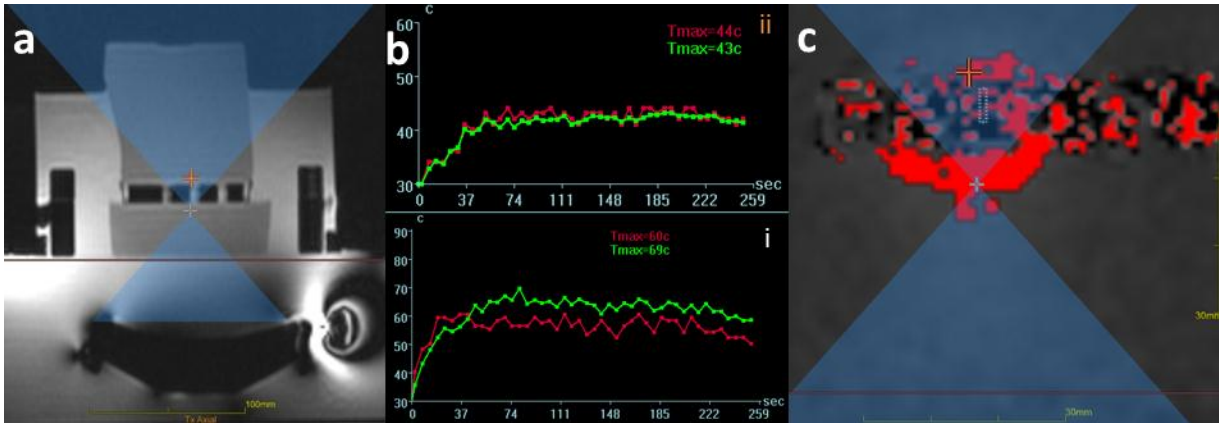


Figure 4.34- Thermal Monitoring by MRI: (a) axial MR image showing FUS induced heating arrangement, with a white and orange crosses marking the chosen pixel for temperature measurement in the lower and upper phantoms, respectively, (b) temperature graph measurement during sonication in the (i) lower and (ii) upper phantoms and (c) a thermal map, with a white and orange crosses marking the chosen pixel for temperature measurement in the lower and upper phantoms, respectively

In Figure 4.34 the thermometry of the lower and upper phantoms during a combined sonication is presented. In the temperature graph, the green line represents the average heating over the nine pixels surrounding and including the selected pixel, marked by a white/orange cross, and the red line is the temperature at the selected pixel. As can be seen in the temperature graph of the lower phantom (i), the temperature reaches an average of $65^{\circ}\text{C} \pm 2^{\circ}\text{C}$ standard deviation (Sd), which would have caused necrosis of the cell monolayer if the plate were placed the right way up and not inverted. Yet, in the upper phantom, in the proximity of the cells in the inverted position, according to temperature graph (ii), there is an average of about $43^{\circ}\text{C} \pm 2^{\circ}\text{C}$, which is the desired temperature. The fact that the lines overlay, indicates a real thermal measurement, rather than a single spot artefact.

4.3.1.2 Thermal Camera

To ensure that there is no significant heat generated in the sonoporation arrangement, temperature measurements were made with a thermal camera and thermocouples. The thermal camera was utilized to measure the heat generated on the perimeter of the well.

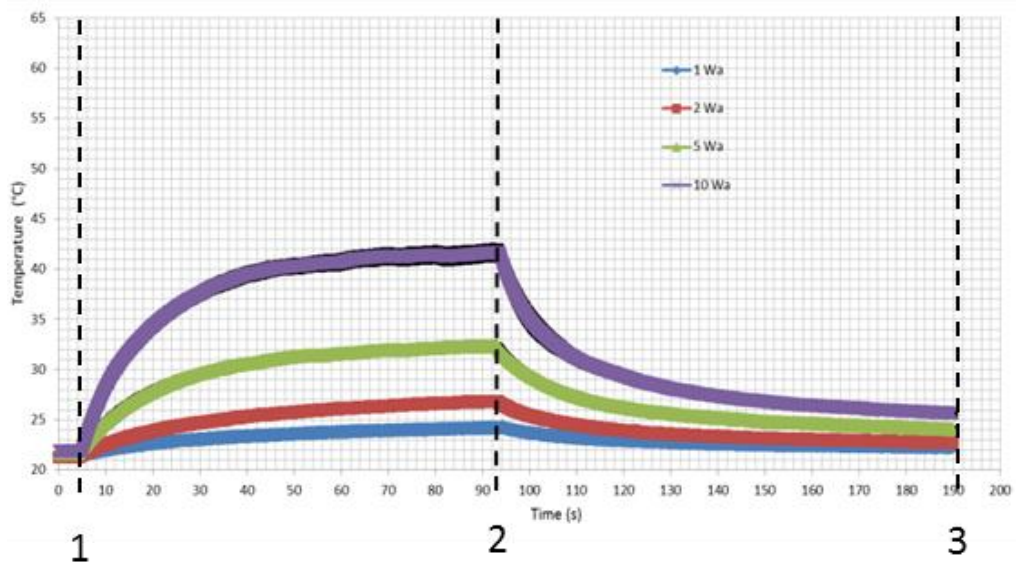


Figure 4.35- Thermal camera measurement of the well perimeter temperature of a plate

Figure 4.35 depicts measurement of temperature during sonication at the perimeter of a single well with powers 1, 2, 5 and 10 Wa, by a thermal camera. Each applied power is represented by a colour line with two black points surrounding the each line representing the sd. Consequently, lines without visible black marks in the graph have very low Sd. All the sonications were performed in an inverted plate with 50% Tr for 90 s, FD = 97 mm, $f = 0.95$ MHz. The time line is as follows: point 1- start sonication; point 2- end sonication and start cooling time; point 3- end measurements.

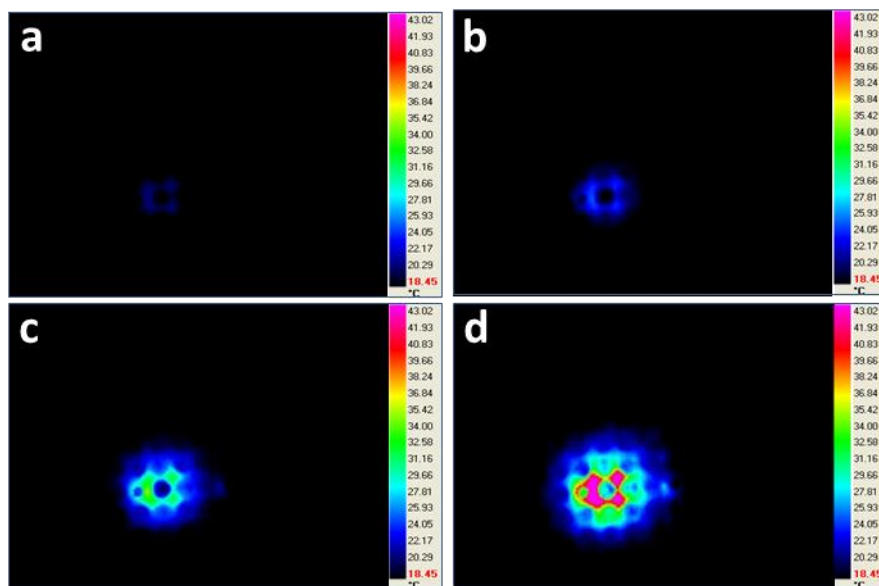


Figure 4.36- Thermal camera imaging of the well perimeter temperature of a plate at the powers (a) 1, (b) 2, (c) 5, and (d) 10 Wa

Figure 4.36 presents images of the thermal changes in the perimeter of the well as a result of 90 s sonication which correspond to the lines presented in Figure 4.35. As can be seen in Figure 4.36 heating appears only on the perimeter of the well while the inner, transparent part remains dark.

As a control for the data presented for the thin transparent base additional measurements were made in a different type of plate, the latter with a relatively thick, 1.27 mm, black base, Figure 4.37.



Figure 4.37- Black thick base plate

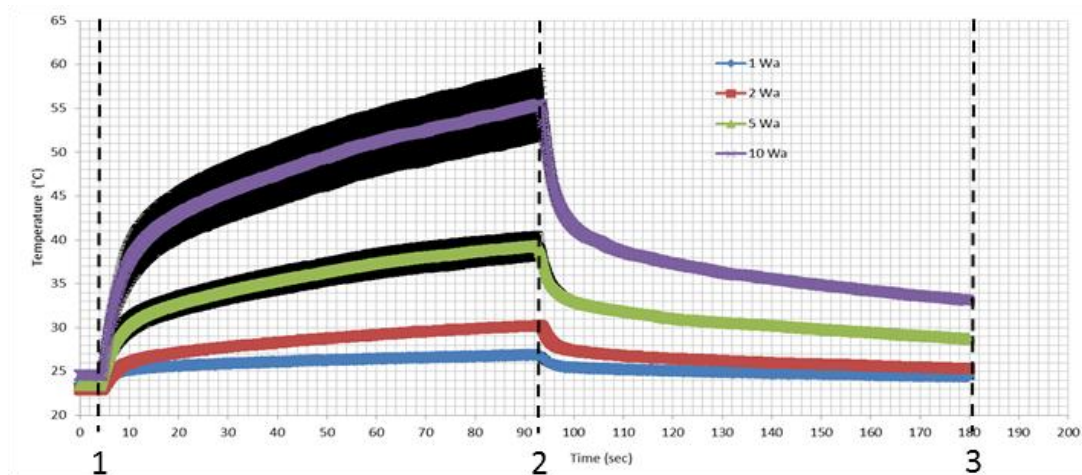


Figure 4.38- Thermal camera measurement of the well base temperature of a black thick base plate

Figure 4.38 depicts the temperature during sonication of the base part of a plate with a black thick base with the powers 1, 2, 5 and 10 Wa, by a thermal camera. The black marks surrounding the lines represent the Sd. Consequently, lines without visible black marks in the graph have very low Sd. All the sonications were performed in an inverted plate with 50% Tr for 90 s, FD = 97 mm, $f = 0.95$ MHz. The time line is as follows: point 1- start sonication; point 2- end sonication and start cooling time; point 3- end measurements.

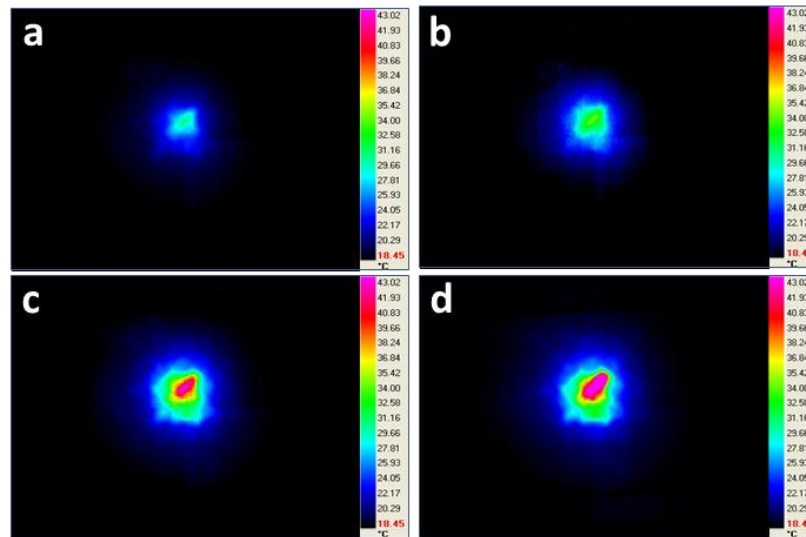


Figure 4.39- Thermal camera imaging of the well base temperature of a black thick base plate at powers of (a) 1, (b) 2, (c) 5, and (d) 10 Wa

Figure 4.39 presents images of the temperature of the base of a plate with a black thick base as a result of 90 s sonication which correspond to the lines presented in Figure 4.38. As can be seen in Figure 4.39 the heating appears on the perimeter of the well as well as in the inner part.

4.3.1.3 Thermocouples

Heating Arrangements without FUS As described in Section 4.2.2.2, the evaluation of heating without FUS is based on measurements with thermocouples. The treatment plan progressed according to the real time measurements of the temperature at the base and in the sealing film on the plate. To determine the temperature rise inside a well in the plate during the heating process, thermocouple measurements without cells were performed. Moreover, in this set of experiments, the optimal positioning of the plate, i.e. inverted and right way up, was investigated.

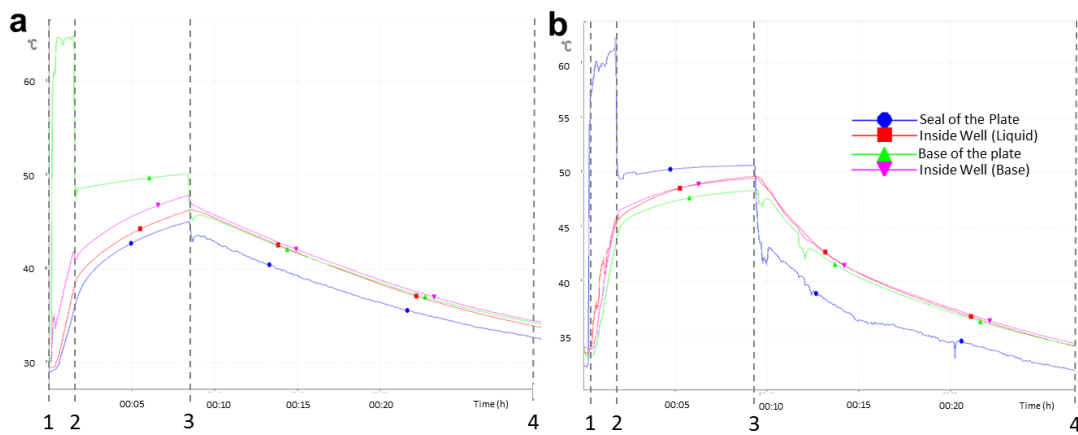


Figure 4.40-Thermocouple measurements of (a) regular and (b) inverted positioning of the plate

Figure 4.40 depicts the measurements conducted in a plate the right way up and an inverted plate where two thermocouples were placed outside the plate, on the base, green line, and seal, blue line, and another two thermocouples were placed inside a single well in the plate. The red line is the temperature of the medium inside the well and the pink line is the measurement by a thermocouple attached to the base of the well from inside of the well, measuring the temperature at the location of the cell monolayer. After establishment of optimal parameters i.e. inverted plate with 3 min exposure at 42 - 46°C, cell work was implemented.

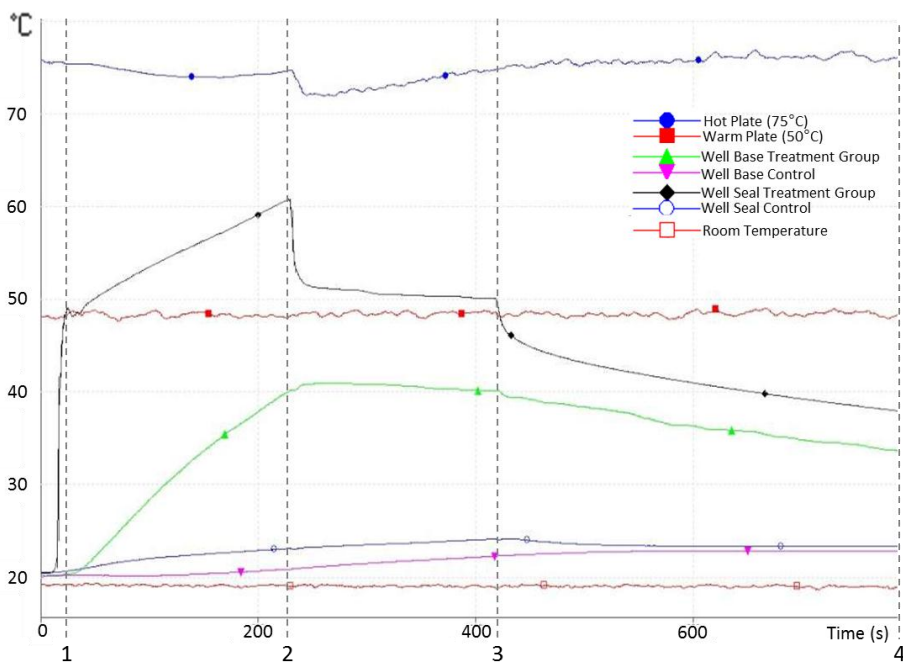


Figure 4.41- Thermocouple measurements in a heating process of an inverted plate

Figure 4.41 represents typical thermocouple measurements during heating of an inverted plate without FUS. The timeline is as follows:

- Point 1- plate placed on the hot plate at 75°C until the base, green line, reaches 42°C.
- Point 2- after the cells have reached 42°C, the plate is moved to the 50°C heater.
- Point 3- after continuous heating for 3 min on the 50°C heater, the plate was removed to cool down.
- Point 4- end of measurement.

UF Heating Arrangement The MRI thermometry of the UF heating arrangement was verified by thermocouple measurements. As mentioned in Section 4.3.1.1, the sonication pattern in the heating arrangement is a combined sonication pattern with high power continuous sonication followed by pulsed sonication to achieve a fast temperature rise and then to maintain a constant elevated temperature. To evaluate the optimal positioning of the plate, thermal measurements were performed with both regular and inverted positioning of the plate. Additional measurements were made to define the optimal sonication mode. Both types of measurements were conducted as part of the apparatus evaluation without any cells.

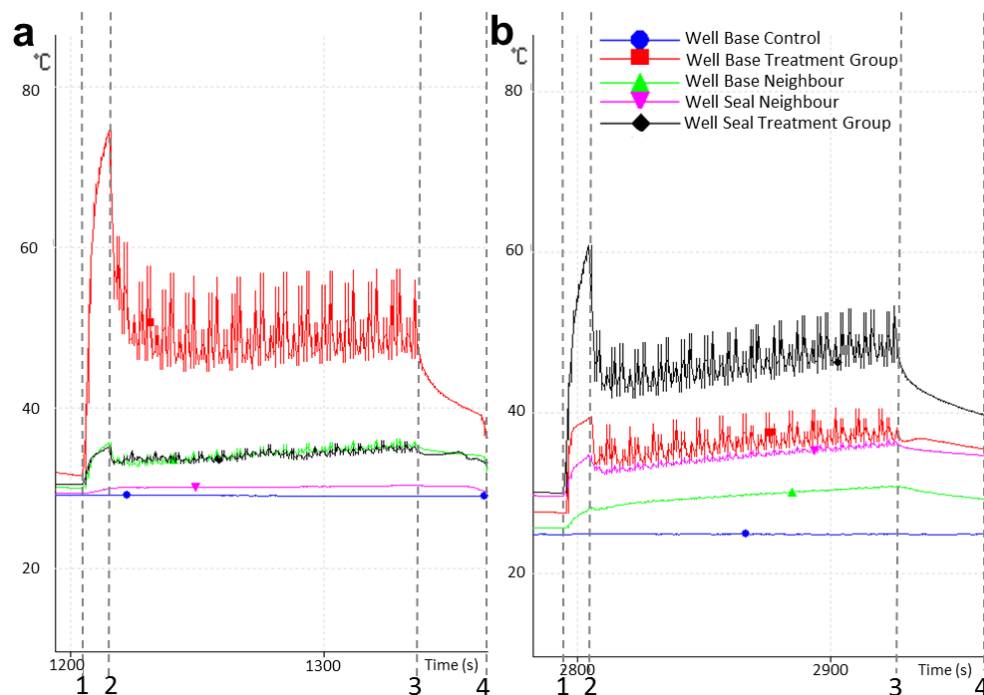


Figure 4.42- Thermocouple measurements of FUS induced heating in (a) regular and (b) inverted plates

The measurements presented in Figure 4.42 correspond to the evaluation of the positioning of the plate and compare regular and inverted positions. The timeline is as follows:

- Point 1- start of continuous, high power sonication.

- Point 2- end of continuous sonication and immediate start of pulsed sonication.
- Point 3- after a period at 42 - 46°C, the sonication is finished and the well cools down.
- Point 4- end of measurement.

The initial sonication was at a power of 20 Wa for 10 s in continuous mode followed by a second sonication of 20 Wa for 120 s in pulsed mode, 0.5 s on, 2.5 s off.

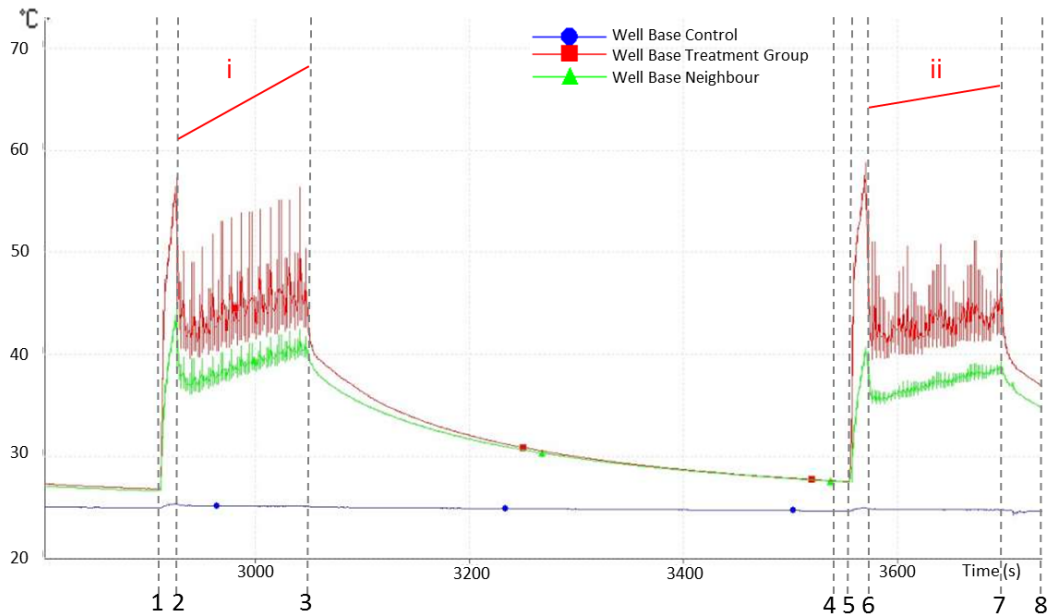


Figure 4.43- Thermocouple measurements of FUS induced heating at (i) 0.5 s on, 2.5 s off mode and (ii) 0.5 s on, 3 s off in a Plate

Figure 4.43 depicts the temperature rise as a result of two different sonication modes. The first mode is 0.5 s on, 2.5 s off, and the second is 0.5 s on, 3 s off. Both temperature rise slopes are represented in red on top of each graph. The timeline as follows:

- Point 1- start of the continuous, high power sonication.
- Point 2- end of continuous sonication and immediate start of pulsed sonication.
- Point 3- after a period at 42 - 46°C, the sonication is finished and the well cools down.
- Point 4- end of cooling period.
- Point 5- start of the continuous, high power sonication.
- Point 6- end of continuous sonication and immediate start of pulsed sonication.
- Point 7- after a period at 42 - 46°C, the sonication is finished and the well cools down;
- Point 8- end of measurement.

In the first mode the initial sonication is at a power of 60 Wa for 15 s in continuous mode followed by a second sonication of 60 Wa for 120 s in pulsed mode, 0.5 s on, 2.5 s off. In the

second mode, the initial sonication is at a power of 60 Wa for 15 s in continuous mode followed by a second sonication of 60 Wa for 120 s in pulsed mode, 0.5 s on, 3 s off.

UF Sonoporation Arrangement Following discussion in Section 4.1.3.1 regarding the accuracy of thermal camera measurements through transparent materials and for validation, additional thermal measurements were made with thermocouples in the sonoporation arrangement. The thermocouples were attached to Row 2 of wells on the base of the inverted plate (Figure 4.27) to evaluate the temperature not only in the sonicated well at the time of sonication but also in its neighbours. To establish a safety margin, the following measurements were done at a factor 15 times higher energy, 2.5 Wa for 60 s = 150 J, than the final cell sonication parameters, 1 Wa for 10 s = 10 J.

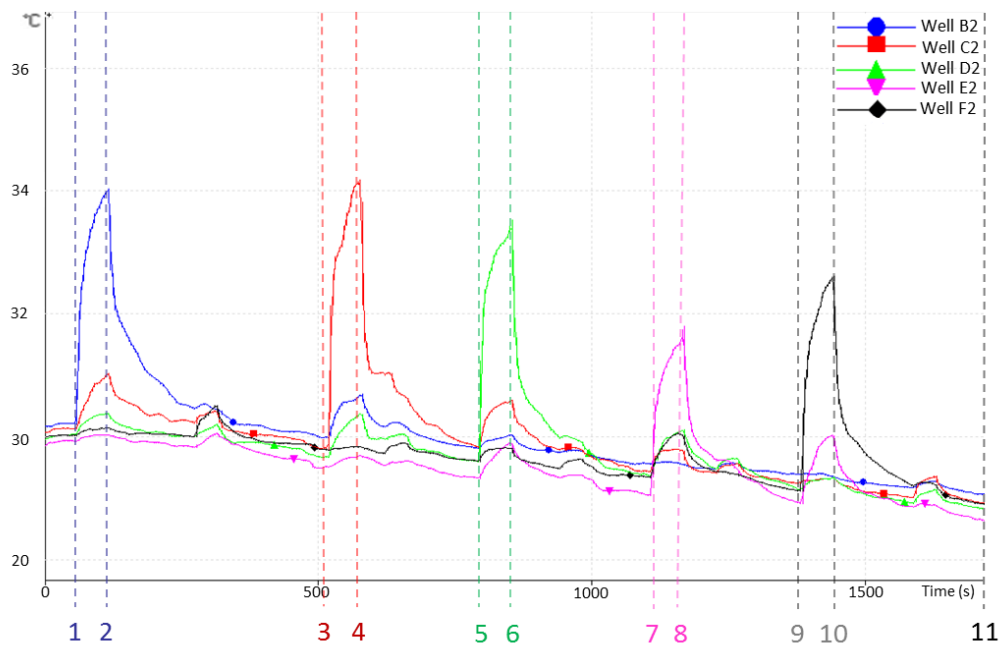


Figure 4.44- Thermocouple measurements in the UF sonoporation arrangement

The thermal measurements in Figure 4.44 were taken during a whole plate sonication using the automated script. The time line is as follows:

- Point 1- start of first sonication (well B2).
- Point 2- end of first sonication.
- Point 3- start of the fourth sonication (well C2).
- Point 4- end of fourth sonication.
- Point 5- start of the seventh sonication (well D2).
- Point 6- end of seventh sonication.
- Point 7- start of the 10th sonication (well E2).
- Point 8- end of 10th sonication.

- Point 9- start of the fourth 13th sonication (well F2).
- Point 10- end of 13th sonication.
- Point 11- end of measurement.

4.3.2 US Evaluation

4.3.2.1 US Properties of the Plate Base

The acoustic properties of the base of a plate were measured using the arrangement described in Section 4.2.2.4. All the results presented in the figures below correspond to sonication of 1 Wa at 0.95 MHz for 3 min, with the sealing film / base part located 92 mm over the transducer ($z = -5$).

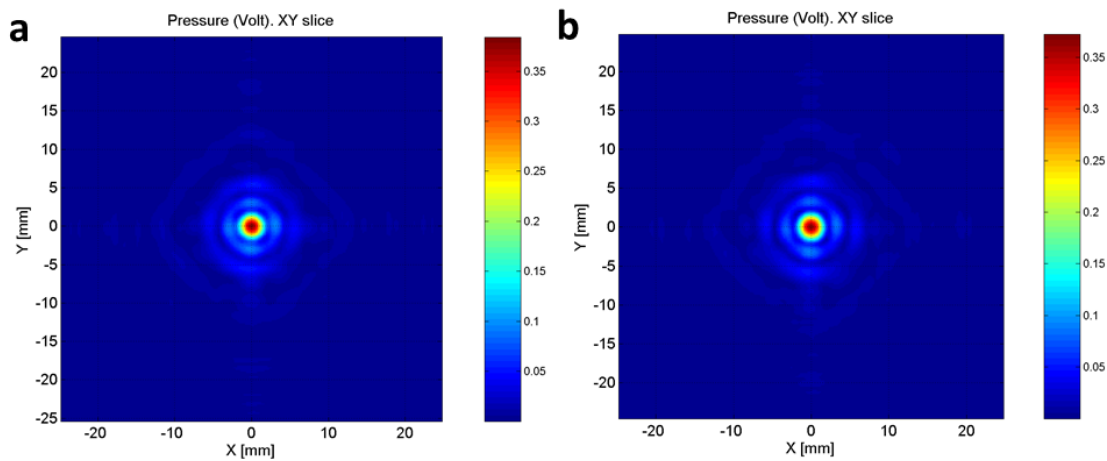


Figure 4.45- XY Slice of acoustic measurements (a) without and (b) with the base of a plate

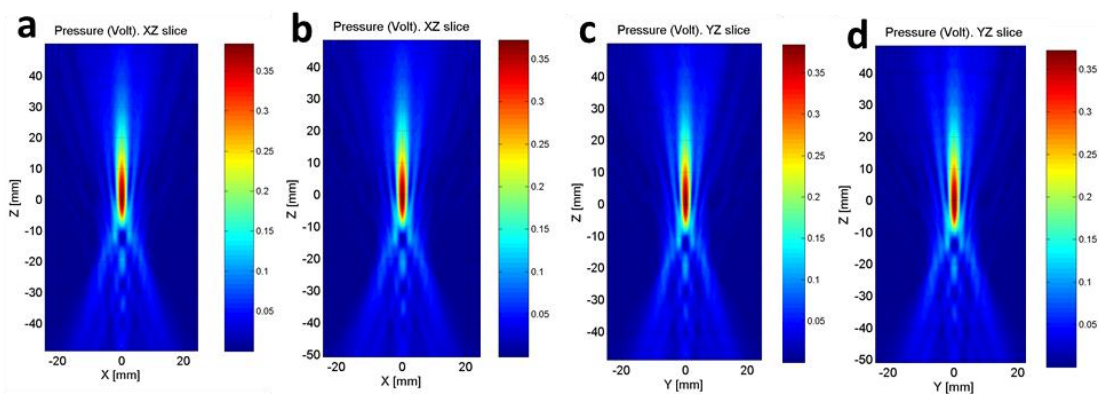


Figure 4.46- Acoustic measurements in XZ plane (a) without and (b) with base and in YZ plane (c) without and (d) with base of a plate

Figure 4.45 -Figure 4.46 show a comparison between the US field propagation in an XY slice as well as axial XZ and YZ slices, through the base of a plate and in pure degassed water without the plate.

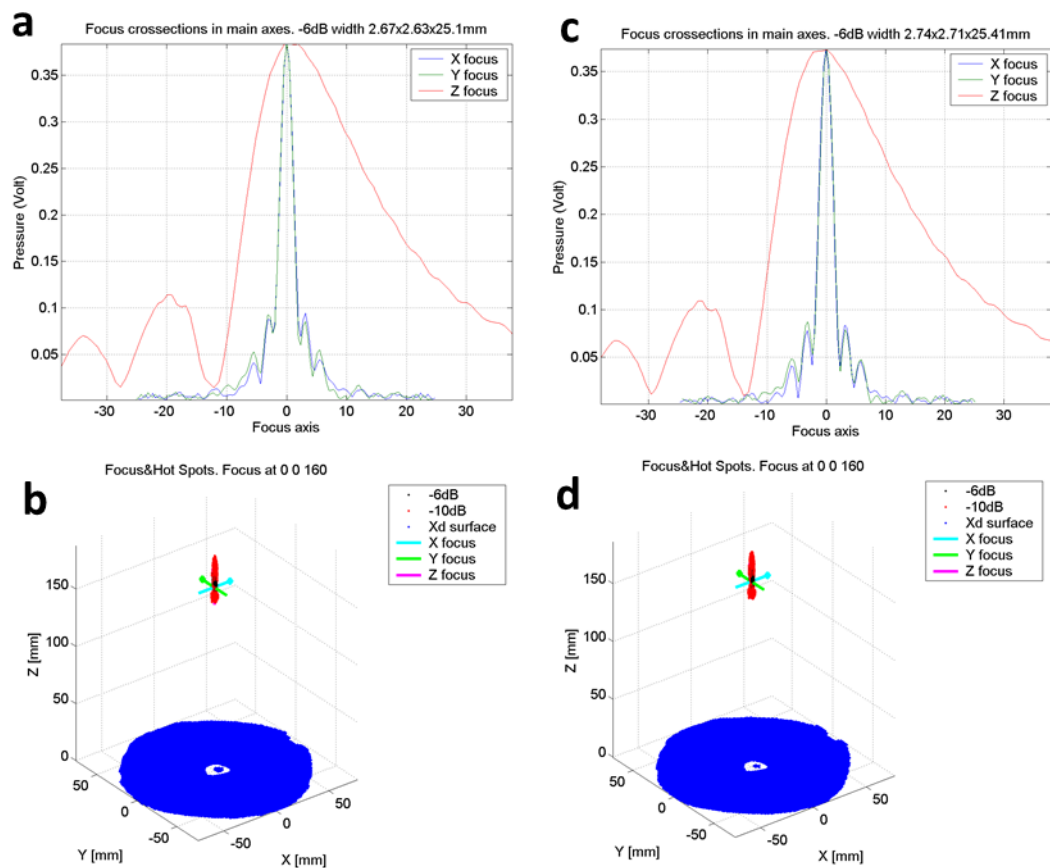


Figure 4.47- Focus cross-sections in main axes and schematic representation of the focal point without (a and b respectively) and with (c and d respectively) base of a plate

In Figure 4.47, cross-sections in the main axes at the focal point as well as a schematic representation of the focal point are presented both for the base of a plate and in pure degassed water without the plate.

4.3.2.2 Acoustic Properties of the Plate Seal

The acoustic properties of the sealing film were measured using the same arrangement as for the base, described in Section 4.2.2.4. All the results presented in the figures below correspond to 1 Wa at 0.95 MHz for 3 min.

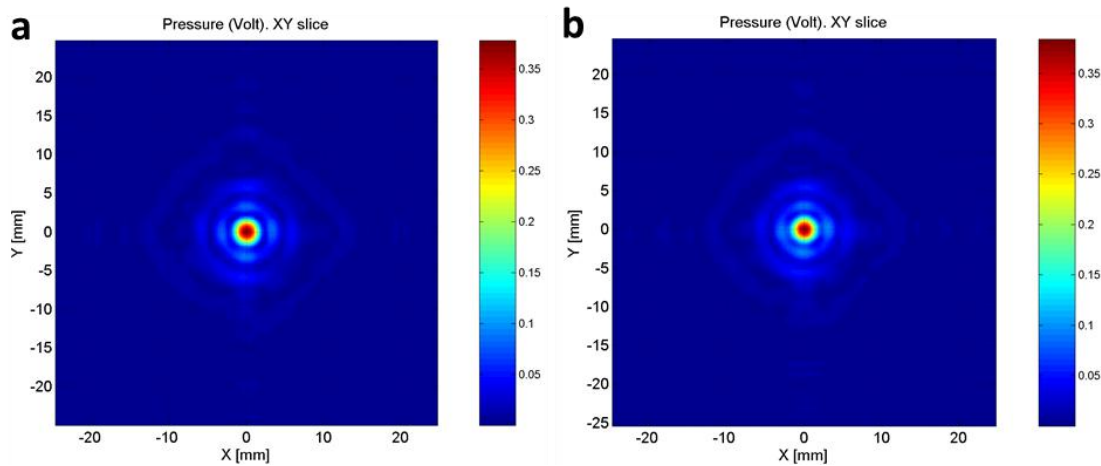


Figure 4.48- XY slice of acoustic measurements (a) without and (b) with sealing film

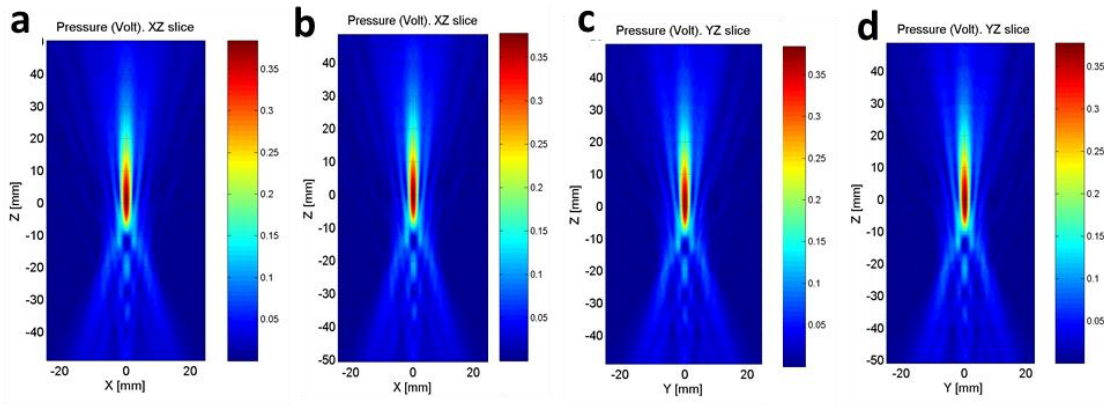


Figure 4.49- Acoustic measurements in XZ plane (a) without and (b) with sealing film and in YZ plane (c) with and (d) without sealing film

Figure 4.48 -Figure 4.49 show a comparison between the acoustic field propagation in an XY slice as well as in axial XZ and YZ slices, in degassed water and through the sealing film used to seal the plate. In Figure 4.50, cross-sections in the main axes at the focal point as well as a schematic representation of the focal point are presented both for the sealing film of the plate and in pure degassed water without the seal.

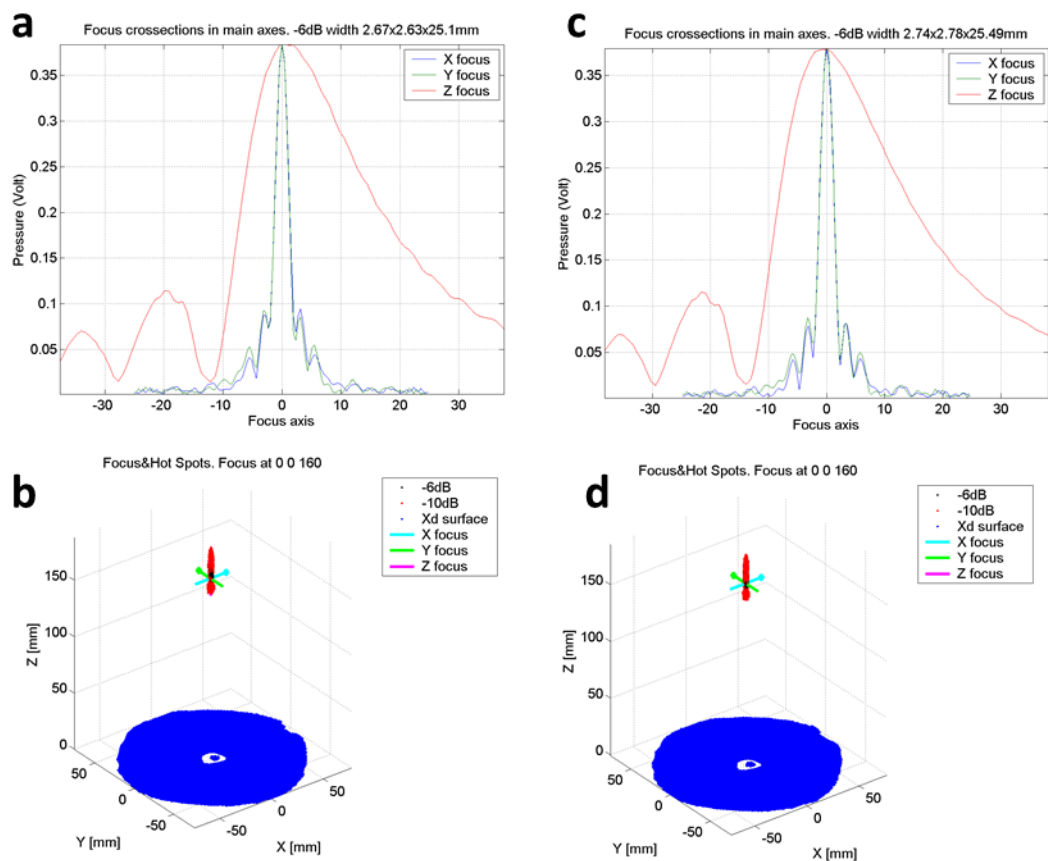


Figure 4.50- Focus cross-sections in main axes and schematic representation of the focal point with (a and b respectively) and without (c and d respectively) sealing film

4.3.2.3 Acoustic Field Measurements

UF Sonoporation Arrangement To identify the optimal sonication pattern, i.e. FD and the form of the beam, propagation of the applied acoustic field through a plate, at various parameters, was measured. As mentioned in Section 4.1.2.2, the UF transducer is a phased array consisting of 208 elements organised in 26 transducer rings (Tr), each of which can be individually adjusted for amplitude and phase and turned off and on. To define an optimal beam, various measurements were done: 100% of the Tr are on (mode 0), 50% of the Tr are on, 20% of the Tr are on, 50% of the transducer elements are in random phases, 100% of the transducer elements are in random phases, with an annular 'doughnut' shaped focus that was tested as a possibility to achieve a bigger radius of exposure. In order to observe the generated focus and to evaluate the characteristics of each beam, all the above measurements were done in the absence of the plate.

In Figure 4.51-Figure 4.54, FD = 82 mm, with a power of 1 Wa at 1.15 MHz.

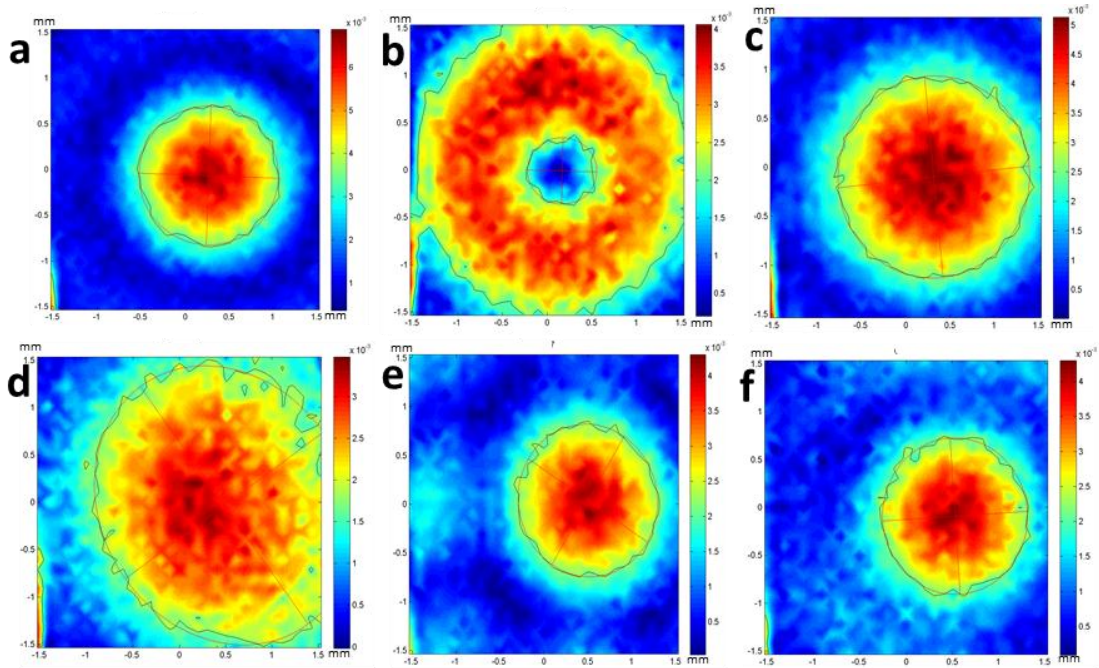


Figure 4.51- XY slice of acoustic measurements of (a) 100% Tr (b) annulus (c) 50% Tr (d) 20% Tr (e) 50% Tr random phases and (f) 100% Tr random phases

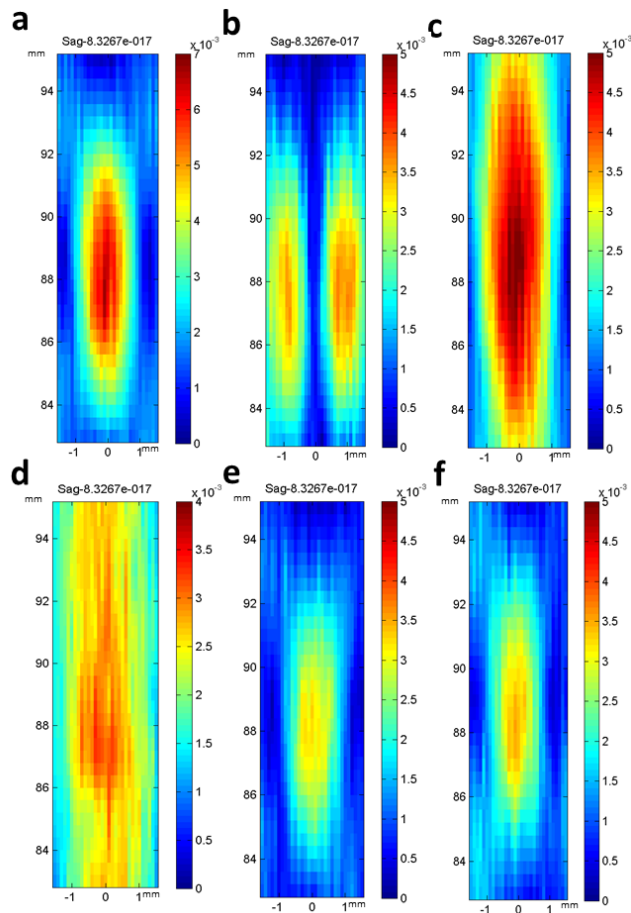


Figure 4.52- Acoustic measurements in sagittal plane at (a) 100% Tr (b) donut (c) 50% Tr (d) 20% (e) Tr 50% Tr random phases and (f) 100% Tr random phases

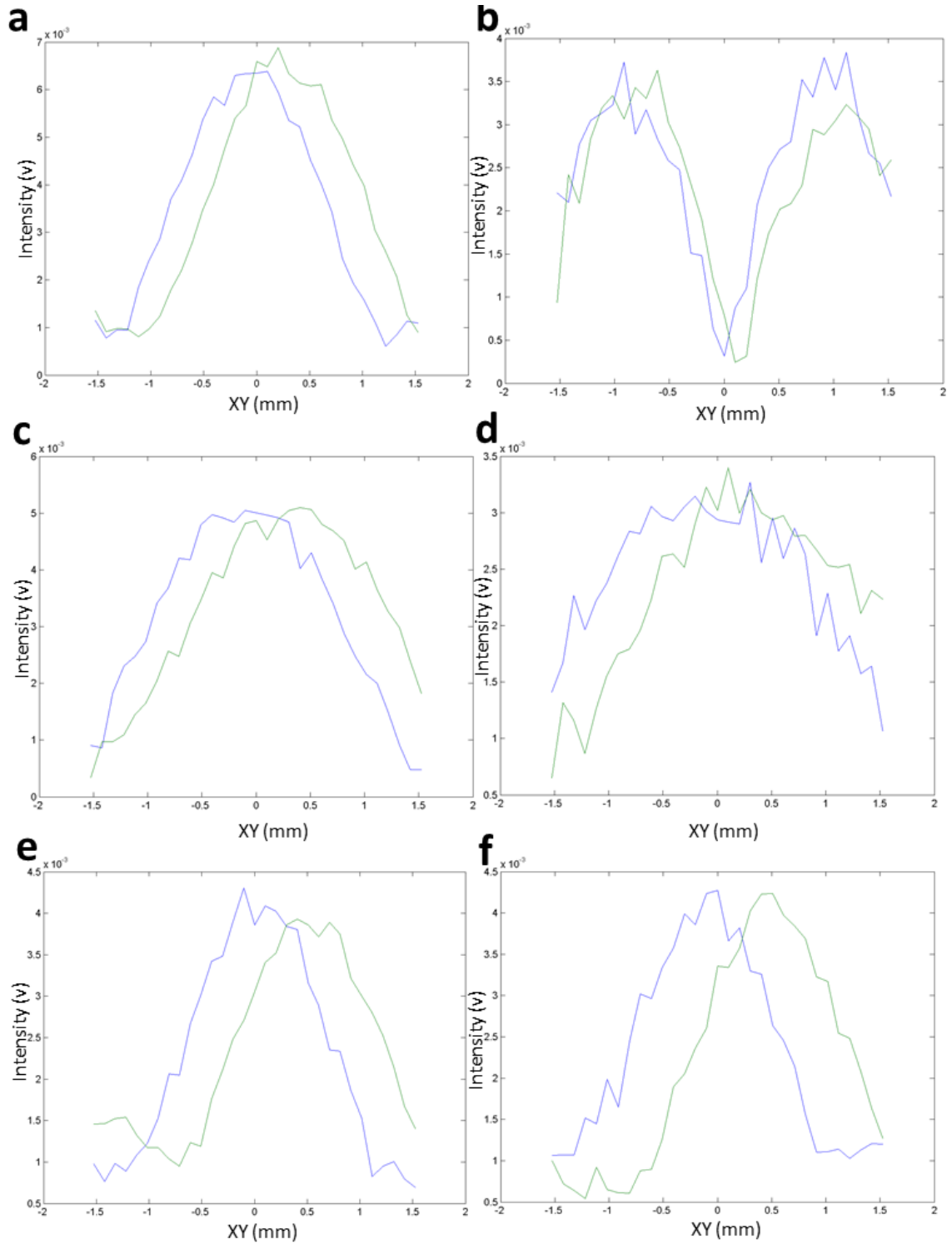


Figure 4.53- Pressure graphs with X and Y axes represented by the green and blue lines, respectively, at (a) 100% Tr (b) annulus (c) 50% Tr (d) 20% Tr 50% Tr (e) random phases and (f) 100% Tr random phases

Figure 4.51 and Figure 4.52 show the XY slice and the sagittal slice of the various acoustic beam patterns, respectively, and Figure 4.53 shows the focal pressure as a function of

distance in the XY plane. It is important to note that although the intensity scale varies between the graphs, the XY coordinates remain constant. The variation in the intensity scales is not significant in this observation, since the desired information is in the pattern of the beam.

Table 4.2- Summary of measured beam forms

Beam Form	Max Amplitude [mV]	Area [mm²]	Diameter [mm]
20% Tr	1.73	6.42	3.09
50% Tr	2.56	3.51	2.17
50% Tr with random phases	2.15	1.95	1.6
100% Tr with random phases	2.14	2.01	1.63
100% Tr	3.44	1.9	1.59

In Table 4.2 the dimensions and maximum amplitude of the focal point for the various beam forms at FD = 82 mm, are presented. The annular beam is not presented in the table because of its split focal point.

An additional issue that may influence the focal behaviour is the FD inside a well. Because of the plate geometry, as stated above, various disruptions can occur during the passage of the beam through the well. To establish the optimal height for sonication inside a single well within a plate, acoustic field measurements were performed over an inverted plate at different focal points. The hydrophone in these measurements was less than one mm from the surface of the inverted plate, meaning that the presented measurements are in close proximity to the theoretical cell location.

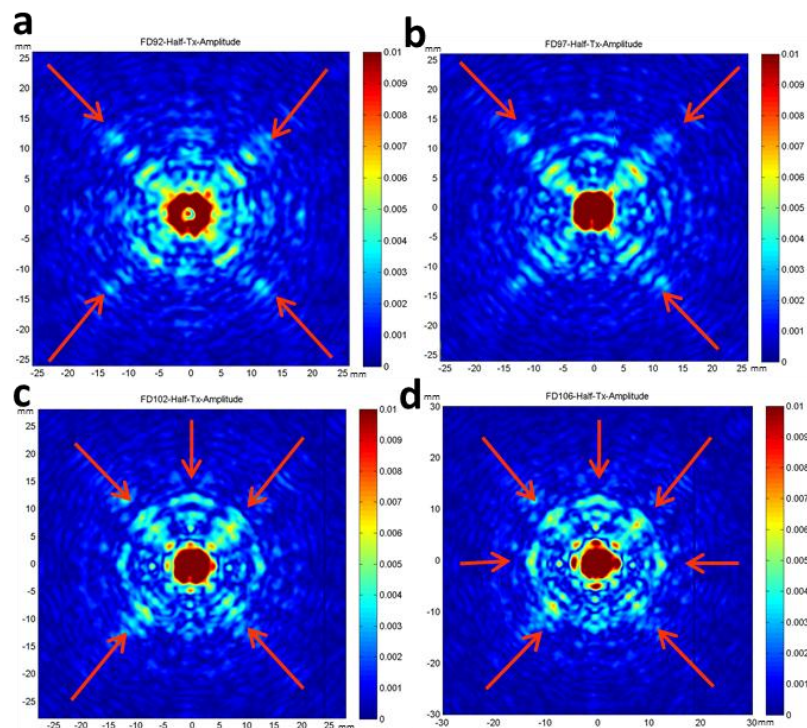


Figure 4.54- XY slice of acoustic measurements at FD of (a) 92, (b) 97, (c) 102, and (d) 106 mm

Figure 4.54 represents the acoustic measurements at different focal points performed at 50% TR with a power of 1 Wa at 0.95 MHz. The red arrows in Figure 4.54 highlight the locations of acoustic field propagation through the neighbouring wells in the plate.

UF Heating Arrangement To evaluate the effectiveness of the DQA phantom as an acoustic absorber, acoustic field measurements were conducted over the plate with the phantom present. All measurements were performed at FD = 82 mm, $f = 1.35$ MHz. Although, in cell work, the applied acoustic power was 30 W, the acoustic power chosen for the field mapping was 2 W to avoid damaging the hydrophone.

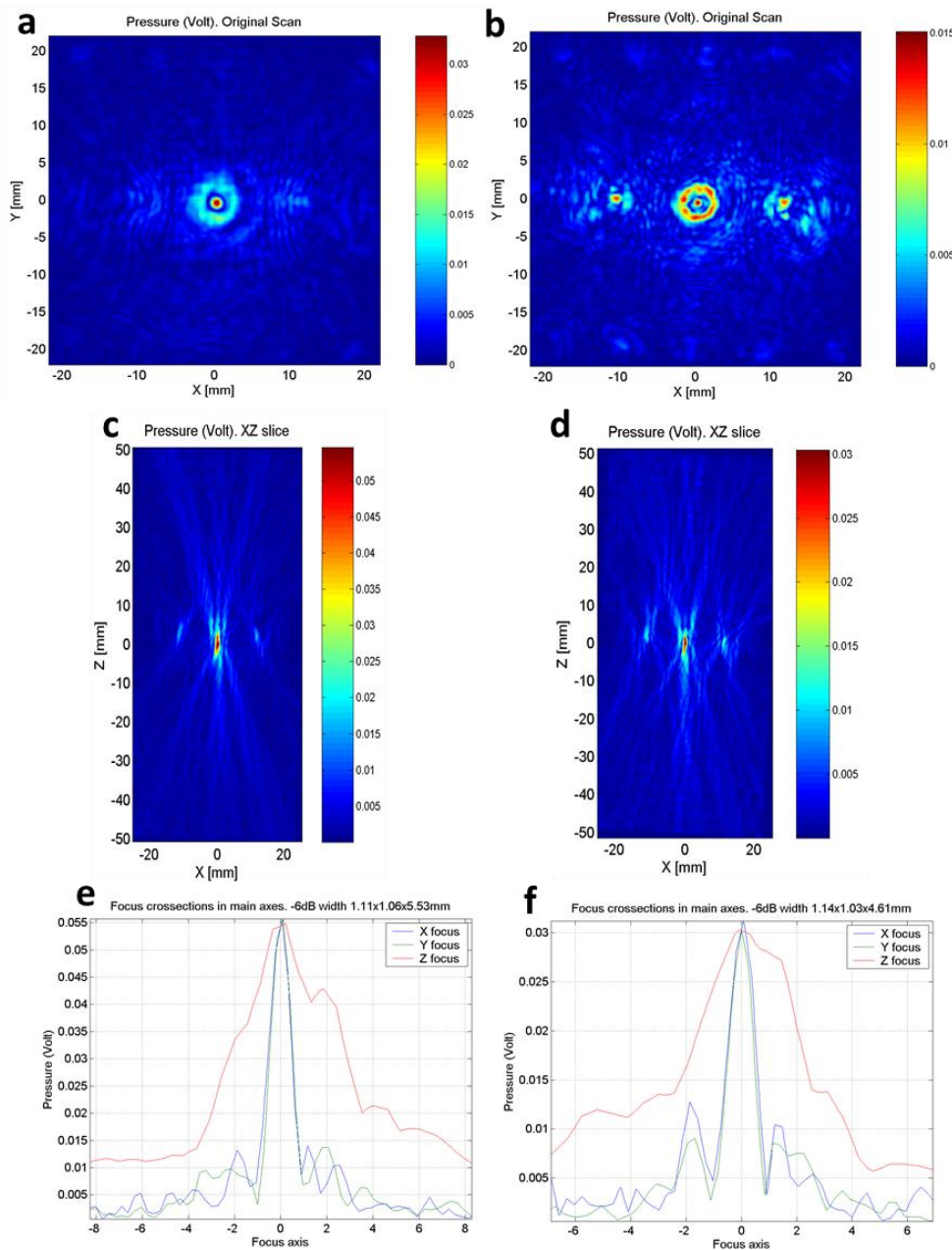


Figure 4.55- Acoustic field measurements over a plate in XY plane (a) without and (b) with a DQA phantom, in XZ plane (c) without and (d) with DQA phantom and focus cross-sections in main axes (e) without and (f) with DQA phantom below the plate

As can be seen in Figure 4.55, the acoustic field measurements over a plate on top of the phantom are approximately half the amplitude of those without any phantom.

CBS Sonoporation Arrangement To assess the uniformity of the power distribution between the 16 allocated spots in the CBS sonoporation arrangement, measurements were performed without the plate in single spot and multi-focal configurations. Measurements were also made at several heights to create 3D images of the focal points. The FD was chosen to be

62 mm- the height of the inverted plate sealing film from the transducer. This FD was chosen after careful observation of the occurrence of the US-created water fountains (described in 4.2.2.1). FD at 62 mm produced a fountain with the highest amplitude, yet with a focused structure.

The single focus acoustic measurements were performed at 0.78 Wa and for the multi-focal measurements 7.8 Wa was used to avoid cavitation at the focus. To evaluate the efficiency and uniformity (Appendix v) of the multi-focal pattern, the single spot measurements were scaled up to match the multi-focal ones. The scan value of the single well was multiplied by the square root of the applied ultrasonic load of the multi-focal sonication, i.e. $\sqrt{10}$. All measurements were done at 0.55 MHz. Figure 4.56 depicts the single spot measurement in the XY, XZ and YZ planes as well as the pressure graph of the measurement.

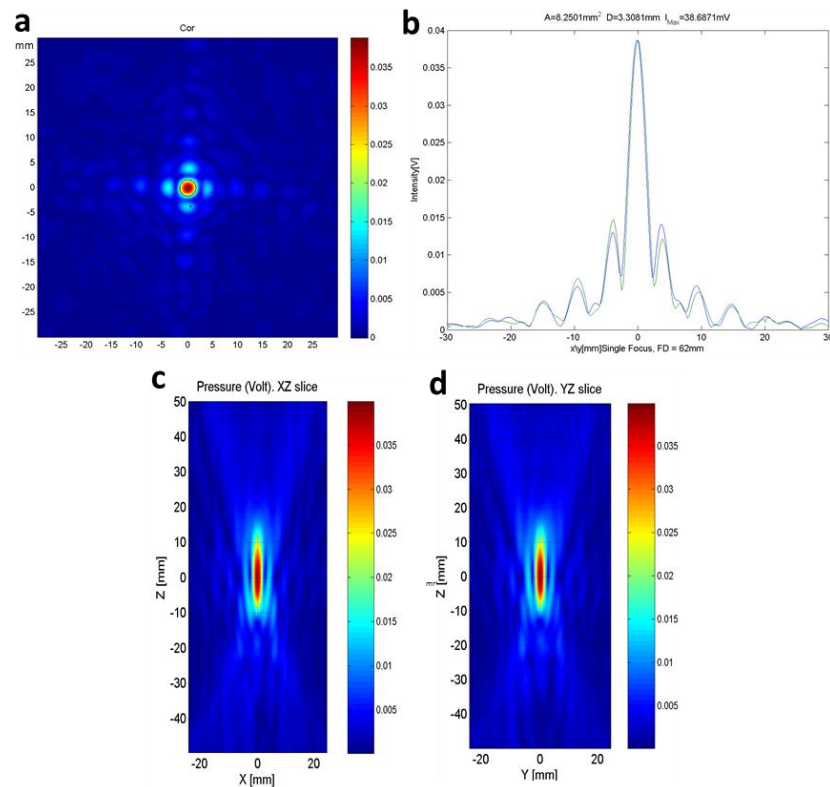


Figure 4.56- Single point acoustic measurement in (a) XY plane, (b) the focus cross-sections in main axes X and Y, green and blue, respectively, and the (c) XZ plane and (d) YZ plane

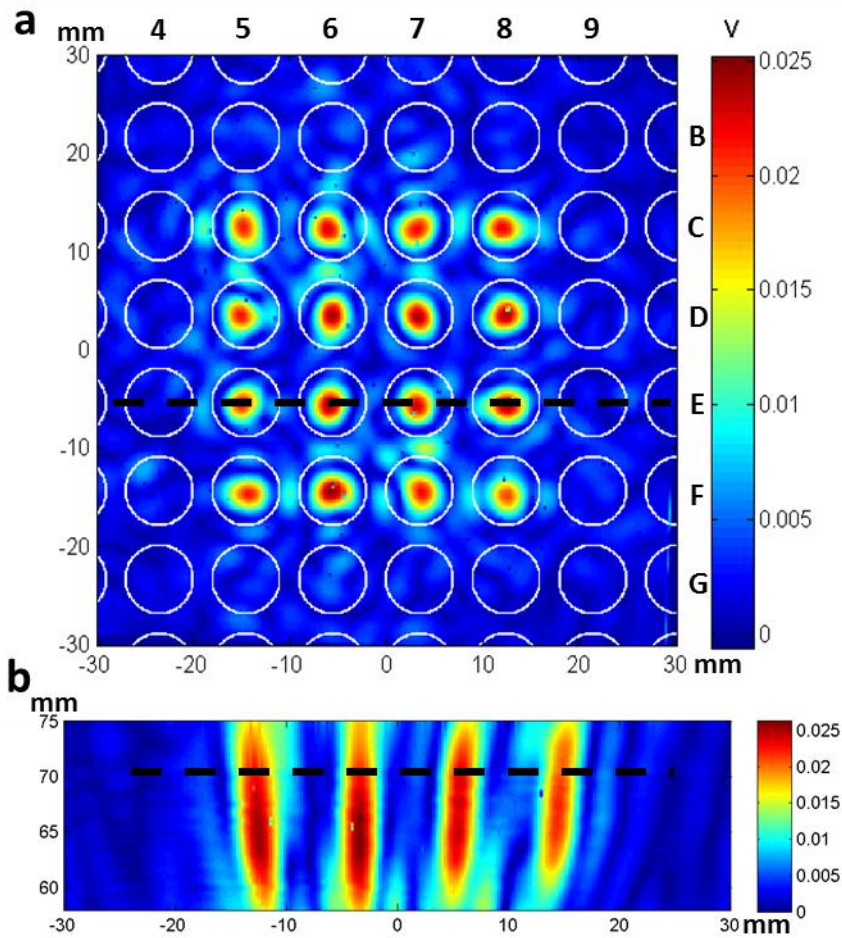


Figure 4.57- Acoustic measurement of 16- well multi-focal pattern in (a) XY and (b) XZ plane

Figure 4.57 shows the acoustic measurement in the XY plane at a height of 72 mm, marked by a black line in (b), and the acoustic measurement parallel to the beam path. The black line in (a) corresponds to the measurement plane in (b). Spot sizes measured at half the maximal pressure and locations were calculated from the acoustic field measurements. The average area over the 16 spots was $8.79 \pm 0.92 \text{ mm}^2$ and the average distance between each two spots was $9.06 \pm 0.25 \text{ mm}$ in the X direction and $9.02 \pm 0.2 \text{ mm}$ in the Y direction.

Since the frequency of the transducer is below the calibration range of the hydrophone, the hydrophone calibration constants $\beta_H (\text{V}^2\text{cm}^2/\text{W})$ and $\alpha_H (\text{V}/\text{Pa})$ were calculated according to Appendix v, to be $8.45 \pm 1.12 \cdot 10^{-5} \text{ V}^2\text{cm}^2/\text{W}$ and $7.53 \pm 0.44 \cdot 10^{-8} \text{ V}/\text{Pa}$. The adjusted acoustic pressure (MPa) for each spot in the multi focal pattern is presented in Table 4.3.

Table 4.3- Acoustic pressure measurements of the 16 points focal pattern per well inside the plate

Row/Line	5	6	7	8
C	0.279	0.253	0.279	0.279
D	0.307	0.322	0.265	0.28
E	0.244	0.293	0.33	0.323
F	0.244	0.32	0.285	0.277

The efficiency (*Eff*) and uniformity (*Uni*) were calculated according to Appendix v to be 89% and 86%, respectively.

4.4 Discussion

As presented in the previous section, three innovative arrangements for investigation of the mechanical and thermal effects of US on cells were created and evaluated by both thermal and acoustic means. The thermal evaluation of the different arrangements was done by MRI thermometry, thermal camera observation and thermocouples and the acoustic evaluation was conducted using hydrophones and multiaxis scanning systems.

Thermal camera measurements were performed to assess occurrence of unwanted heating in the sonoporation arrangement. From Figure 4.35, the average temperature rises (\pm Sd) on the perimeter of a single well from a 10 s sonication at powers of 1, 2, 5 and 10 Wa were 0.44°C (\pm 0.2°C), 1.25°C (\pm 0.35°C), 3°C (\pm 0.5°C) and 6.4°C (\pm 0.9°C), respectively. After 90 s sonication at the same powers of 1, 2, 5 and 10 Wa, temperature rises were 2.7°C (\pm 0.2°C), 5.6°C (\pm 0.3°C), 10.7°C (\pm 0.25°C) and 19.8°C (\pm 0.9°C), respectively. Figure 4.36 presents the visualization of the temperature rise in the plate due to 90 s of continuous sonication. It can be seen that the thermal distribution in the plate as a result of sonication develops from the inside of a well towards the surrounding wells. This important fact was taken into account in the order of cell sonications in each arrangement.

As mentioned in Section 4.1.3.1, there are some limitations in measurement of heating of transparent thin films. Although there is no visualization of the heating process in the base of the plate, some heating may have occurred in the transparent parts of the plate, e.g. the base and/ or the sealing film. As a control for the transparent thin base (0.2 mm) plate, a black thick (1.27 mm) base plate was sonicated and the average temperature over the well base area was recorded, with the results presented in Figure 4.38. From Figure 4.38 the temperature rises (\pm Sd) in a black thick-base plate from 10 s sonication at powers of 1, 2, 5 and

10 Wa are 1.8°C ($\pm 0.2^\circ\text{C}$), 3.7°C ($\pm 0.5^\circ\text{C}$), 8.2°C ($\pm 1.4^\circ\text{C}$), and 15.9°C ($\pm 3^\circ\text{C}$), respectively. After 90 s sonication at the same powers of 1, 2, 5 and 10 Wa, the temperature rises were 3.4°C ($\pm 0.2^\circ\text{C}$), 7.3°C ($\pm 0.5^\circ\text{C}$), 15.9°C ($\pm 1.6^\circ\text{C}$) and 30.9°C ($\pm 4.2^\circ\text{C}$), respectively.

The temperature changes in the black thick-base plate are visualized in Figure 4.39. The difference in the temperature rises ($\pm Sd$) between the transparent thin base and the black thick-base plates from 10 s sonication at powers of 1, 2, 5 and 10 Wa equal 1.4°C ($\pm 0.3^\circ\text{C}$), 2.5°C ($\pm 0.6^\circ\text{C}$), 5.2°C ($\pm 1.5^\circ\text{C}$) and 9.5°C ($\pm 3.1^\circ\text{C}$), respectively. After 90 s sonication at the same powers of 1, 2, 5 and 10 Wa, the differences were 0.63°C ($\pm 0.25^\circ\text{C}$), 1.72°C ($\pm 0.6^\circ\text{C}$), 5.18°C ($\pm 1.7^\circ\text{C}$) and 11.09°C ($\pm 4.3^\circ\text{C}$), respectively.

From these results, suggesting a difference of 1°C to 10°C difference between the two tested plates, it seems clear that the thin base plate is preferable to use in order to decrease unwanted heating. Nonetheless, for additional validation, thermocouples measurements were also made.

In the present work, thermocouple utilization for temperature measurements provided a good insight into the thermal behaviour of the created arrangements without and with FUS. In the heating arrangement without FUS, utilization of thermocouples allowed real time monitoring of the temperature rise and, by that, deciding when to move the plate to the lower temperature heater. The initial thermal evaluation of the heating arrangement without FUS generated parameters for the cell work. In the thermal measurements of the inverted and regular plates in Figure 4.40 it can be seen that there is a greater difference between the temperature of the inner well base, cell monolayer location, and the outer well base, marked by the green and pink lines, respectively, in the regular positioning of the plate compared to the inverted plate, 4 - 8°C difference and 0.5 - 2°C difference, respectively. Additionally, in the case of the inverted plate, the cells receive heat from the surrounding media rather than through the plastic base. In the latter, because of the proximity of the plastic to the cells the transmitted heat can cause a sudden, spatially nonuniform temperature rise in the cell monolayer which can result in inconsistent results and even cell death. As can be seen in the results, the heating arrangement without FUS proved to be a successful control for the FUS induced heating, simulating the same thermal behaviour. In both arrangements similar temperature profiles, consisting of a fast rise of several degrees followed by a thermally constant state, were achieved. This special pattern of local heating can be useful in local drug delivery and hyperthermia treatments (Chen et al., 2010).

The rationale behind the design of the UF heating arrangement was to utilize a commercially available US absorber material with good heat conductivity as a heat conductor

to the cell monolayer. A good candidate for such a purpose was the DQA tissue mimicking phantom. In theory, according to Appendix vi, at a height of 36 mm, the DQA phantom should absorb 41% of the transmitted intensity. In practice, according to the measurements presented in Figure 4.55, the DQA phantom absorbed slightly more, about 48%, of the acoustic intensity when placed below the plate.

The thermal evaluation of the UF heating arrangement with thermocouples provided some insights regarding the sonication modes in regular and inverted positions. At the same power, in the regular position, the temperature rise at the base of the plate, i.e. the cell monolayer location, was larger and had relatively more impact on the neighbouring wells (Figure 4.42). In the inverted position, the cells were heated through the medium in the well and hence the heat distribution was much more uniform with less potentially damaging influence on the cell monolayer. However, as can be seen in Figure 4.42, the temperature rise in the inverted plate, $\Delta \approx 10^{\circ}\text{C}$, is lower compared to the regular position, $\Delta \approx 20^{\circ}\text{C}$.

To gain a higher temperature rise in the inverted plate, greater power was applied (Figure 4.43). In the initial sonication, which provides the initial temperature rise in the plate, the power was increased from 20 Wa for 10 s with total energy of 200 J, to 60 Wa for 15 s with total energy of 900 J. Because of this increase, the mode of 0.5 s on, 2.5 s off was no longer found suitable since a constant rise in temperature appeared throughout the pulsed sonication i.e. the slope of the increase marked with the first red line in Figure 4.43. A sonication mode with longer cooling time, 0.5 s on, 3 s off, provided a more constant temperature i.e. the reduced slope of the increase marked with the second red line in Figure 4.43.

Because of concerns about cell viability the power was decreased by a factor of two in the final experiments, and the time was increased by the same factor, hence maintaining the same energy (900 J), yet with a more gradual delivery.

From Figure 4.55, it can be seen that there is some US influence on the neighbouring wells in the plate. It is important to notice that the influence on the neighbouring wells occurs at $FD = 82$ mm, regardless of the presence of a phantom. The intensity of the field in the neighbouring wells is 66% of the intensity transmitted into the target well. Consequently, to reduce the mentioned US influence and lower the level of heat transfer between wells and accumulation in neighbouring wells, the treatment group wells were separated by air-filled neighbours, Figure 4.21.

Thermocouple monitoring of heat propagation throughout the plate during heating without FUS resulted in accurate real time measurements. However, in the FUS induced heating arrangement, the use of thermocouples is rather doubtful. Although thermocouples

are in use in measuring temperature rises due to US (Dasgupta et al., 2011), the results should be carefully considered for their accuracy in an US field. As explained in Section 4.1.3.2, when the thermocouples are placed in US fields, they can produce artefacts such as a false rapid temperature rise. Nonetheless, if the initial temperature rise is ignored, according to the “wait then measure” approach (Morris et al., 2008), and with proper positioning of the thermocouples, i.e. away from the focal point, accurate data can be achieved.

In the sonoporation arrangement, the thermocouple measurements of possible heating occurrence because of sonication at 2.5 Wa for 60 s, i.e. 150 J, have shown that the maximum possible temperature rise at the base of the sonicated well is about 4°C, and 1°C in the neighbouring well (Figure 4.27). According to the thermal camera measurements, the same energy level of 150 J due to sonication of 2 Wa for 75 s, the temperature rise at the perimeter of the well was 5.2°C ±0.25°C.

These measurements were done at an energy a factor of 3 to 15 higher than the ones used in the final protocols for sonoporation cell experiments. This suggests that during the sonoporation experiments at 10 J and 50 J the temperature rise was approximately 0.26°C - 0.72°C and 1.3°C - 1.73°C, respectively. The overall thermal evaluation of the sonoporation arrangement by both thermal camera and thermocouples suggests that there is no significant temperature rise as a result of sonication at 10 J, e.g. 1 Wa for 10 s, and even at 50 J, e.g. 2 Wa for 25 s.

According to the evaluation of the US properties of the base and seal of the plate in Figure 4.45 - Figure 4.50, there is minimal absorption of US in the tested parts and hence they are suitable for sonication of cell monolayers.

Following the assessment for the optimal sonication beam, it can be seen in Figure 4.51, that the 50% Tr has a wider focal zone than 100% Tr, yet it retains the same focal shape, while at a lower excitation percentage of the transducer, e.g. 20%, the focal beam is distorted. From the sagittal slice in Figure 4.52, it can be seen that the focal point of 50% Tr is significantly longer than for 100% Tr and has higher focal intensity than for 20% Tr. According to Table 4.2, which presents the measurement at FD = 82 mm, 50% Tr has the optimal power to diameter ratio. The diameter of the focal point generated by 50% Tr is 2.17 mm, which is 40% higher than for 100% Tr and lower by 40% than for 20% TR, yet the intensity of 50% Tr is 25.6 W / cm² which is 47% higher than the 20% Tr focal intensity, 17.3 W / cm². Therefore, 50% Tr has a wider focal diameter than the nominal 100% Tr, yet it retains a relatively high intensity at the focal point compared to lower percentage of Tr. From these results, 50% Tr was chosen to be the optimal sonication pattern.

The measured values of the focal sizes at FD = 82 mm as presented in Table 4.2, are consisted with the calculation performed according to equations in Appendix iii, e.g. the focal diameter of 50% Tr at FD = 82 mm is 2.17 mm and 2.2 mm according to the measurement and the calculation, respectively. This has proven that the theoretical calculations can be used to define the focal sizes at various beam forms and parameters. According to the calculations, the focal diameter of 50% Tr at FD = 97 mm, is 2.6 mm.

To define the optimal FD, acoustic measurements at different FDs were performed, as shown in Figure 4.54. All the measurements were conducted with the optimal sonication pattern, 50% Tr. From Figure 4.54, it can be seen that at FD = 97 mm the ultrasonic pressure is the most uniform in the well. Moreover, at FD = 97 mm there is minimal effect on the neighbouring wells due to sonication, marked by red arrows in Figure 4.54.

The establishment of the CBS arrangement for cell sonication, Figure 4.16, provided the opportunity for multi-focal sonication patterns. According to the US evaluation of the multi-focal patterns it provides efficient delivery of the beam at 16 foci simultaneously. Moreover, the focal area remains the same as in the single focus case, which is still smaller than the single well area, $\varnothing = 7$ mm. The distance between every two points in the grid of the 96-well plate is 9 mm (Appendix ii), suggesting that the planned pattern hit its targets exactly. The intensity deviation of the spots was up to 7% from the average, allowing similar acoustic properties for each well. The multi-focal patterns have shown good *Eff* and *Uni* levels, both over 85%, meaning that most of the power reaches the targets in a relatively uniform pattern.

4.5 Conclusions

In this chapter the design and evaluation of the different arrangements for *in-vitro* USmTDD application, were presented. The thermal evaluation of the sonoporation arrangement confirmed that no significant heating occurred during sonication at the tested powers and energy levels that correspond to the ones used *in vitro*. The meaning of this is that during FUS application in the sonoporation arrangement any observed *in-vitro* effects will correlate solely to the US related physical effects on cells. MRI thermometry measurements of the heating generated during the application of FUS induced heating, confirmed that the designed sonication mode can be used to achieve temperature rise in a hyperthermia mode. In the heating without FUS arrangement thermocouple measurements validated that the heating mode applied without FUS is similar to the one observed in the FUS induced heating arrangement. This confirmed that the heating without FUS arrangement can be utilised as a control model for evaluation of hyperthermia related mechanisms occurring *in-vitro*. The

conducted acoustic measurements confirmed that the sealing film and base part of the plate are suitable for *in vitro* USmTDD research. Furthermore, by the acoustic evaluation of the beam propagation a specific beam pattern and focal point height were chosen for the *in-vitro* studies. The acoustic measurements in the CBS arrangement for multifocal cell sonication confirmed the uniformity and efficiency in the beam distribution within 16 focal spots.

The overall evaluation of each arrangement with several methodologies has resulted in sets of parameters for cell application in each arrangement. The results of the *in-vitro* cell work are presented in Chapter 5.

4.6 References

- Apfel, R.E.** (1984) Acoustic cavitation inception. *Ultrasonics*, July 1984, pp.167- 73.
- ASTM Committee E-20** (1981) *Manual on the use of thermocouples in temperature measurement*. Baltimore: American Society for Testing and Materials.
- Bloembergen, N. et al.** (1948) Relaxation effects in nuclear magnetic resonance absorption. *Phys Rev*, 73 (7), pp.679-712.
- Chen, L. et al.** (2009) Enhancement of drug delivery in prostate tumor in vivo using MR guided focused ultrasound (MRgHIFU). *IFMBE Proceedings*, 25, pp.342- 4.
- Chen, L. et al.** (2010) MR-guided focused ultrasound: enhancement of intratumoral uptake of [3H]-docetaxel in vivo. *Phys Med Biol*, 55, pp.7399- 410.
- Chester, A.N.** (1987) *Optical fiber sensors*. The Netherlands: Martinus Nijhof Publishers.
- Chung, A.H. et al.** (1996) Optimization of spoiled gradient-echo phase imaging for in-vivo localization of a focused ultrasound beam. *MRM*, 36, pp.745- 52.
- Dasgupta, S. et al.** (2011) Beam localization in HIFU temperature measurements using thermocouples, with application to cooling by large blood vessels. *Ultrasonics*, 51, pp.171- 80.
- Eisenbrey, J.R. et al.** (2009) Ultrasound triggered cell death in vitro with doxorubicin loaded poly lactic-acid contrast agents. *Ultrasonics*, 49, pp.628- 33.
- Feril Jr., L.B. et al.** (2010) Hypotonia-induced cell swelling enhances ultrasound-induced mechanical damage to cancer cells. *J Med Ultrasonics*, 37, pp.3-8.
- Feril Jr., L.B. et al.** (2002) Enhancement of hyperthermia-induced apoptosis by non-thermal effects of ultrasound. *Cancer Lett*, 178, pp.63–70.
- Fry W.J. and Fry R.B.** (1954) Determination of absolute sound levels and acoustic absorption coefficients by thermocouple probes. *J. Acoust. Soc. Am.*, 26, 311-7.
- Gowen, A.A. et al.** (2010) Applications of thermal imaging in food quality and safety assessment. *Trends Food Sci Tech*, 21, pp. 190-200.

- Hertzberg, Y. and Navon, G.** (2011) Bypassing absorbing objects in focused ultrasound using computer generated holographic technique. *Med Phys*, 38(12), pp.6407-15.
- Hovinen, M. et al.** (2008) Detection of clinical mastitis with the help of a thermal camera. *J Dairy Sci*, 91, pp. 4592- 8.
- Hynynen, K. et al.** (1983) Errors in temperature measurement by thermocouple probes during ultrasound induced hyperthermia. *Br. J. Radiol.*, 56, 969–70.
- Hynynen, K. et al.** (2001) MR imaging–guided focused ultrasound surgery of breast fibroadenomas. *Radiology*, 219 (1), pp. 176- 85.
- Ishihara, Y. et al.** (1995) A precise and fast temperature mapping using water proton chemical shift. *MRM*, 34, pp.814- 23.
- Jolesz, F.A.** (2009) MRI-guided focused ultrasound surgery. *Annu Rev Med*, 60, pp.417- 30.
- Kuroda, K. et al.** (2000) Temperature mapping using the water proton chemical shift: Self referenced method with echo-planar spectroscopic imaging. *Magnet Reson Med*, 43, p.220- 5.
- Langlois, S.** (1999) MRI geometric distortion: a simple approach to correcting the effects of non-linear gradient fields. *J Magn Reson Im*, 9(6), pp.821- 31.
- Leighton, T. G.** (1994) *The acoustic bubble*. Great Britain: Academic Press.
- Li, C. et al.** (2009) An internal reference model–based PRF temperature mapping method with cramer-rao lower bound noise performance analysis. *Magnet Reson Med*, 62, pp.1251- 60.
- Maisonhaute, E. et al.** (2002) Microelectrode study of single cavitation bubbles induced by 500 kHz ultrasound. *Ultrason Sonochem*, 9, pp.275- 83.
- McRobbie, D. W. et al.** (2003) *MRI from picture to proton*. Cambridge: Cambridge University Press.
- Morikawa, S. et al.** (2002) MR-guided microwave thermocoagulation therapy of liver tumors: initial clinical experiences using a 0.5 T open MR. *J Magn Reson Im*, 16, pp.576- 83.
- Morris, A.S.** (2001) *Measurement and instrumentation principles*. Great Britain: Butterworth-Heinemann.
- Morris, H.** (2008) Investigation of the viscous heating artefact arising from the use of thermocouples in a focused ultrasound field. *Phys. Med. Biol.*, 53, 4759- 76.
- Olsrud, J. et al.** (1998) MRI thermometry in phantoms by use of the proton resonance frequency shift method: application to interstitial laser thermotherapy. *Phys Med Biol*, 43 pp.2597- 613.
- Olympus NDT** (2008) Panametrics-NDT™ ultrasonic transducers. [online] Available at :< www.olympusNDT.com>

Omega (n.d.). Revised thermocouple reference tables type T reference tables N.I.S.T. monograph 175 revised to ITS-90 [online] Available at :<
<http://www.omega.com/temperature/z/pdf/z207.pdf>>

Peters, R. D. and Henkelman, R. M. (2000) Proton-resonance frequency shift MR thermometry is affected by changes in the electrical conductivity of tissue. *Magn Reson Med*, 43, p.62- 71.

Platte, M. (1985) A polyvinylidene fluoride needle hydrophone for ultrasonic applications. *Ultrasonics*, May 1985, pp.113- 8.

Poorter, J.D. et al. (1995) Noninvasive MRI thermometry with the proton resonance frequency (PRF) method: in vivo results in human muscle. *Magnet Reson med*, 33, pp. 74- 81.

Quesson, B. et al. (2000) Magnetic resonance temperature imaging for guidance of thermotherapy. *J Magn Reson Im*, 12, pp.525- 33.

Redwood, M. (1960) *Mechanical waveguides*. New York: Pergamon.

Rempp, H. et al. (2008) MR temperature monitoring applying the proton resonance frequency method in liver and kidney at 0.2 and 1.5 T: segment-specific attainable precision and breathing influence. *Magn Reson Mater Phy*, 21, pp.333- 43.

Repacholi, M.H. and Benwell, D.A. (1982) *Essentials of medical ultrasound: a practical introduction to the principles, techniques and biomedical applications*. USA: The Humana Press.

Rieke, V. and Pauly, K.B (2008) MR thermometry. *J Magn Reson Imaging*, 27(2), pp.376- 90.

Schneider, M. (1999) Characteristics of SonoVue. *Echocardiography: A Jrnl of CV Ultrasound & Allied Tech*, 16 (7, Part 2), pp.743- 6.

Sherman, C.H. and Butler, J.L. (2007) *Transducers and arrays for underwater sound*. USA: Springer.

Shutilov, V.A. (1988) *Fundamental physics of ultrasound*. Glasgow: Gordon and Breach Science Publishers.

Socolinsky, D.A. and Selinger, A. (2002) A comparative analysis of face recognition performance with visible and thermal infrared imagery. *IEEE*, 1051-4651/02, pp.212- 22.

Speakman, J.R. and Ward, S. (1998) Infrared thermography: principles and applications. *Zoology*, 101, pp. 224-232.

Sumanaweera, T. et al. (1996) Quantifying MRI geometric distortion in tissue. *MRM*, 31, pp.40-7.

Sundaram, J. et al. (2003) An experimental and theoretical analysis of ultrasound-induced permeabilization of cell membranes. *Biophys J*, 84, pp.3087- 101.

Tempny, C.M.C. et al. (2003) MR imaging-guided focused ultrasound surgery of uterine leiomyomas: a feasibility study. *Radiology*, 226 (3), pp.897-905.

- Vigen, K.K. et al.** (2006) In vivo porcine liver radiofrequency ablation with simultaneous MR temperature imaging. *J Magn Reson Im*, 23, pp.578- 84.
- Vitkin, I.A. et al.** (1997) Magnetic resonance imaging of temperature changes during interstitial microwave heating: a phantom study. *Med Phys*, 24 (2), pp.269- 77.
- Vollmer, M. and Mullmann, K.P.** (2010) *Infrared thermal imaging: fundamentals, research and applications*. Germany: Wiley-VCH.
- Wang, D. et al.** (2004) Geometric distortion in clinical MRI systems Part I: evaluation using a 3D phantom. *Magn Reson Imaging*, 22, pp.1211- 21.
- Weidensteiner, C. et al.** (2003) Real-time MR temperature mapping of rabbit liver in vivo during thermal ablation. *Magnet Reson Med*, 50, pp.322- 30.
- Wlodarczyk, W. et al.** (1998) Three-dimensional monitoring of small temperature changes for therapeutic hyperthermia using MR. *J Magn Reson Imaging*, 8, pp.165- 74.
- Zhang, S. et al.** (2005) MRI thermometry based on PARACEST agents. *J Am Chem Soc*, 127, pp.17572- 3.
- Zimmer, W.M.X.** (2011) *Passive acoustic monitoring of cetaceans*. USA: Cambridge University Print.

CHAPTER 5 FOCUSED ULTRASOUND APPLICATION ON CELLS – AN *IN-VITRO* STUDY

5.1 Introduction

USmTDD was first realized in 1974, and has been widely investigated since then (Tachibana and Tachibana, 2001). The implementation of non-invasive surgery techniques such as FUS in conjunction with a targeting moiety can produce new platforms for safe, site specific drug delivery. In this chapter a brief introduction is given on the interaction of US with living cells and current studies in this area followed by the *in-vitro* results achieved via the dedicated arrangements described in Chapter 4.

5.1.1 Therapeutic Ultrasound and Cells

US waves can propagate through soft tissues resulting in thermal and mechanical effects on the cells. Although these biophysical effects are commonly divided into two separate trends, with application of US *in vivo*, the mechanical and thermal effects occur simultaneously, and are thus inseparable (Baker et al., 2001). Nonetheless, when investigating the fundamental acoustic impacts on cells, the two effects should be isolated as much as possible from one another to accurately assess the overall bioeffects of US on cells.

5.1.1.1 Thermal Effects of Ultrasound

US generation of heating in tissues is probably the best understood mechanism of US behaviour *in vivo* (Frenkel, 2008). The thermal effects of US currently used in tissue ablation in FUS surgery are described in Section 02.4.5. Stable, controlled heating can be achieved in tissue via the application of a focused ultrasonic beam (ter Haar, 1995). Utilization of this temperature rise can allow *in situ* heating to achieve moderate hyperthermia. This is known for its ability to increase cellular uptake of anticancer drugs (Chen et al. 2010). Moreover, hyperthermia modes were investigated recently, in conjunction with MBs, to enhance cellular uptake of anticancer agents *in vivo* (Yudina et al., 2012).

5.1.1.2 Mechanical Effects of Ultrasound

Ultrasonic enhancement of cell membrane permeability using MBs is a widely investigated field of research. Enhancement of cell membrane permeability is often considered to occur via the formation of holes in the cell membrane (Ferrara, 2008). The diameters of the holes that are created determine whether the effect is reversible, for drug delivery into living

cells, or necrotic, resulting in cell death (Böhmer et al., 2009). There are two different mechanical ultrasound effects that cause cell membrane distortion - inertial and stable cavitation. During stable cavitation, bubbles oscillating in proximity to the cells produce “cellular massage” (Wu and Nyborg, 2008). Inertial cavitation is the process where bubbles imploding near the cell membrane cause “sonoporation” effects (Pitt et al., 2004).

MBs as Ultrasonic Contrast Agents Initially MBs were developed as a tool in diagnostic US. Hence, they must be small enough to go through the capillary vessels (<8 µm) (Duck et al., 1998). As research advanced, the use of MBs for therapeutic purposes became of interest (Mayer et al., 2008; Wu and Nyborg, 2008). MB consist of a gas core entrapped in a polymeric/ lipid shell of 2 – 500 nm thickness, Figure 5.1, and sizes usually vary between 1 - 8 µm with an average of about 2.5 µm.

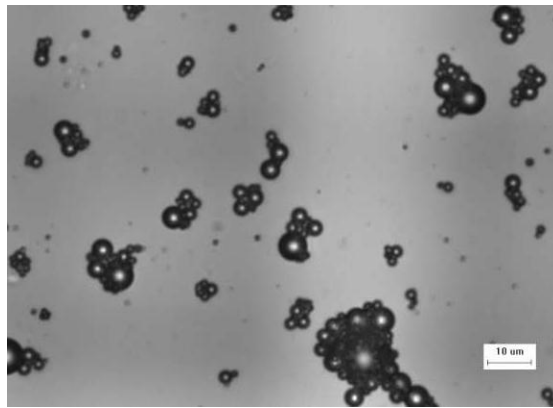


Figure 5.1- Sonovue MBs

First generation MBs had an air filled core but because of stability issues, second and third generation MBs progressed to sulphur hexafluoride (SF6)- such as the Sonovue MB, Figure 5.1, or perfluorocarbon core fillings (Hernot and Klibanov, 2008). A general estimate of the correlation between MI and MB behaviour in an US field is presented in Table 5.1.

Table 5.1- MBs deformation dependance on the MI

Mechanical Index (MI)	MB Physical Condition
Higher than 0.6	Bubble Destruction
0.6	Stable Cavitation State: Non-linear Oscillation, Backscattering at Various Frequencies (sub-harmonics, ultra-harmonics etc.)
0.3	
0.1	Linear Oscillations: Inversely Proportional to Pressure, Linear Backscattering
0.05	

There is an inverse correlation between the MB diameter and the resonance frequency (Greis, 2004). At the average Sonovue MB size of 2.5 μm , the measured resonance frequency is about 3 MHz, while for slightly larger bubbles, of 4 μm diameter, it is around 1.6 MHz (Meer et al., 2004). Formulations of MBs are constantly under development and testing for their potential contribution to site specific drug delivery (Tinkov et al., 2010). Recent studies have shown that the use of Sonovue MBs can increase cell permeability *in vitro* in the presence of US (Yudina et al., 2010). The advantages of using such commercially available MBs are both safety, as the MBs are approved for clinical use with rare adverse side effects (Bokor et al., 2001; Stewart and Sidhu, 2006), and to provide already investigated background (Greis, 2004).

5.1.1.3 Current Trends in USmTDD Research *in vitro*

In today's research, US is being explored for various drug delivery methodologies such as gene therapy, drug release from vehicles such as liposomes (Schroeder et al., 2009), nanocarriers, micelles (Husseini and Pitt, 2008) etc., protein delivery, and small structured chemical drug delivery (Pitt, 2004), with nominal frequencies being 1 MHz and 500 KHz for drug and gene delivery (Mitragotri, 2005). There are several mechanisms by which US can aid TDD. Some of the approaches are based on ultrasonic modification of the cell layers, whereas others utilize US as a drug release stimulus from vehicles by thermal or mechanical effects. When discussing sonoporation as a TDD method, numerous data were collected in the past two decades and have been summarised in many reviews indicating the on-going interest in this field (Byl, 1995; Tachibana and Tachibana, 2001; Bekeredjian et al., 2005; Polat et al., 2011).

Referring to the experimental data described in the literature for cell poration, several setup related principles become apparent:

- I. US exposure is mostly done in cell suspensions (Ashush et al., 2000; Sundaram et al., 2003; Karshafian et al., 2009).
- II. Sonications are carried out in a dedicated chamber (Guzman et al., 2001; Feril Jr. et al., 2002), in an Opti-cell environment (Eisenbrey et al., 2009; Feril Jr. et al., 2010) or in wide petri-dishes (Conti et al., 2004; Hundt et al., 2009).
- III. Most of the acoustic sources in use are bespoke transducers (Yudina et al., 2010; Wang et al., 2010).

The decision to work in cell suspension is very attractive. While it may seem the straightforward way to introduce US into cells due to the relative simplicity of handling cells in suspension, this model is significantly far from cellular structures *in vivo*. Although cell

monolayers can rarely mimic accurately the *in-vivo* system, they are much closer to real cell behaviour in existing tissue.

When applying US to cells, especially into a cell monolayer, the sonication chamber is highly important. From an acoustical point of view it must be transparent to US propagation, without attenuation, with good coupling to the transducer, preferably by degassed water. Moreover, the excess acoustic energy propagating outside the chamber is also important since, without a proper acoustic absorber, e.g. absorbing material or excess water, the energy can be reflected back into the chamber. Any reflection from the chamber walls or other components should be taken into consideration in the construction and evaluation stages of the arrangement. From a biological point of view, the chamber should be sterile to allow healthy cell growth, sealed for the time of exposure, yet accessible for cell handling and, most important, with isolated control groups.

When working in a single chamber environment, it is practically impossible to achieve isolated control groups undergoing the same conditions. Although the Opti-cell chamber is designed for cell work, and is also US transparent, it lacks this isolated control, which positions it in this work as a purely optical observation tool with outcomes presented below. Figure 5.2 depicts the effects of sonication by the ExAblate 2000 UF system on A375m cells observed in an Opti-cell chamber at different powers. As can be seen, at the lower power of 5 Wa there is no visual difference due to sonication, whereas at the higher power of 20 Wa there is a detached cell agglomerate.

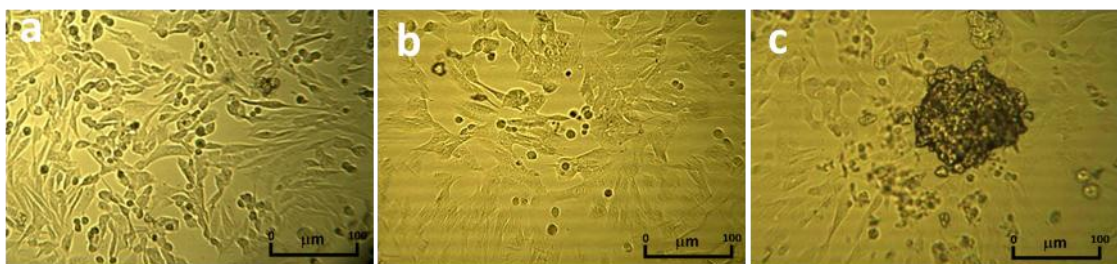


Figure 5.2- 5 Wa continuous sonication for 20 s (a) prior to sonication, (b) after sonication (c) after 20 Wa continuous sonication

Although it is clear from Figure 5.2(c) that there is significant destruction of the cell monolayer, since the Opti-cell is a unitary chamber there is no possibility to assess the scale of damage to the cells due to FUS application.

In addition to the importance of the cell environment, the type of US source also has an impact on the final results achieved in sonoporation. Furthermore, the lack of proper monitoring of the applied US may result in inaccurate conclusions.

As a part of the search for the optimal cell sonication arrangement in the presented work, a dedicated cell sonicator was tested, as shown in Figure 5.3.

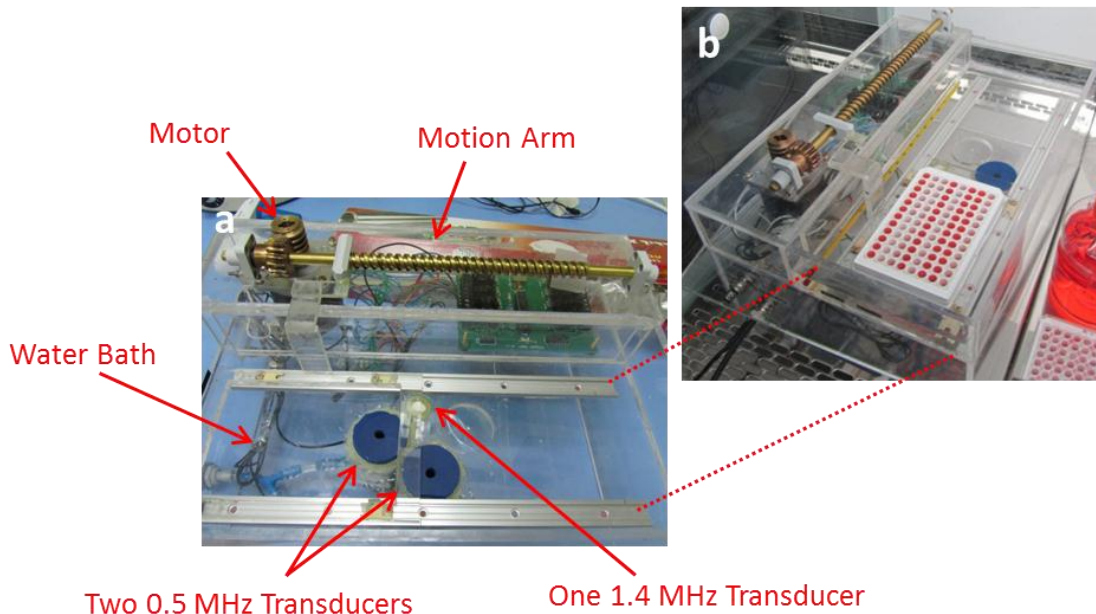


Figure 5.3- Bespoke cell sonicator (a) without and (b) with a plate

Although the *in-vitro* cell sonicator has the potential to become a useful instrument for investigation of USmTDD, in practice proper monitoring tools such as input and output data of all the sonication parameters, cavitation detection and thermal isolation are still under development.

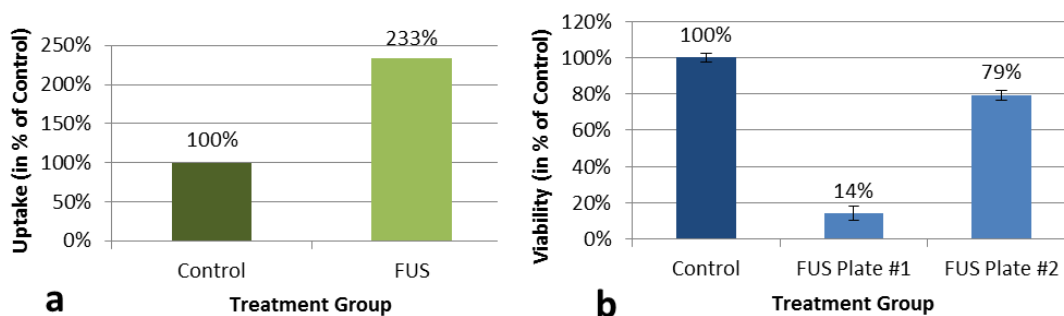


Figure 5.4- (a) uptake of Dox and (b) viability of MCF7 cells without and with FUS

Early Dox uptake results from this system looked promising, such as an increase by a factor of 2.3 compared with non-sonicated cells, in a single point measurement, as shown in Figure 5.4, but unfortunately this data had poor repeatability. As previously mentioned, because of the cylindrical shape of the wells, a secondary focus is created. In the bespoke cell sonicator an absorbing material was placed on top of the plate to absorb any excess of acoustic waves. In practice, air bubbles created on the surface of the absorbing material

reflected the acoustic energy back into the well, creating possible standing waves, acoustic streaming and additional foci. All of these phenomena are hard to monitor in a relatively simple cell sonicator; therefore, it caused an inconsistency in the achieved results and no possibility to draw reliable conclusions on the mechanism of cell behaviour due to FUS.

An additional example of the lack of consistency in results from such a system can be seen in the viability studies presented in Figure 5.54b. This represents the viability summary for two plates sonicated with the same FUS parameters and under the same experimental conditions. As can be seen from the values in Figure 5.4, although in each plate the results seem consistent, $Sd = \pm 4\%$, there is a factor of 5.6 difference between the two tested plates.

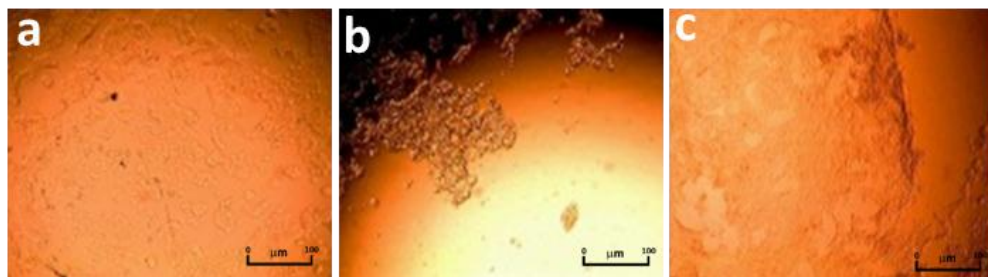


Figure 5.5- MCF7 cells (a) control without FUS (b) FUS plate #1 and (c) FUS plate #2

Figure 5.5 presents the cell images corresponding to the treatment groups in Figure 5.4. As can be seen for the cell images, there is indeed a major variation between the cells after sonication in the two different plates, where in Figure 5.5(b) except for a single cell agglomeration, the well is empty of cells, and in Figure 5.5(c) there is a relatively intact cell monolayer. The cell images correspond to the viability values presented in Figure 5.4b, where the wells in plate #1 are mostly empty of viable cells, $14\% \pm 4\%$, and the wells in plate #2 contain up to $79\% \pm 4\%$ viable cells. These variations are attributed to the random occurrence of cavitation. To overcome this problem and achieve more uniform results, MBs were used as cavitation nuclei in later work.

FUS Induced Heating for TDD An additional means of US facilitated TDD is via a local temperature rise. Hyperthermia can assist in the process of drug delivery both as a release mechanism from drug carriers (Kost et al., 1989; Schroeder et al., 2009) as well as to increase the cellular permeability (Feril Jr. et al., 2002). All the qualifications regarding the design of the sonoporation arrangement mentioned above apply for thermal application of US as well. Furthermore, the utilization of US induced hyperthermia requires accurate temperature monitoring (Moonen, 2010).

5.1.2 Aims and Objectives

The aim of this chapter is to demonstrate the feasibility and efficiency of the arrangements created with the ExAblate clinical MRgFUS system for *in vitro* applications. Despite the fact that application of US behavioural studies to clinical environments is generally conjectural (Baker et al., 2001), the results achieved *in vitro* may serve as a fundamental baseline for studies *in vivo*.

5.2 Materials and Methods

5.2.1 Materials

Table 5.2- Materials for *in-vitro* work

Material	Manufacturer	Place of Origin	Notes
<u>Equipment</u>			
1.5 Tesla MRI system	General Electric	USA	Model: Signa HDX
ExAblate 2000	InSightec LTD	Israel	UF, 0.95-1.35 MHz
ExAblate 2100	InSightec LTD	Israel	CBS, 550 kHz
Tecan infinite	Tecan	UK	Model M200
Stuart Heat-Stir	Barloworld Scientific	UK	Model: CB162
Techne Dri Block	Techne	UK	Model: DB-20
Thermocouple data logger	Omega	UK	Model TC-08
Thermocouples	Omega	UK	Omega T type, 0.25 and 0.076 mm wire diameters
<u>Cell Culture</u>			
MCF7 cell line	ATCC	USA	
A375m cell line	ATCC	USA	
<u>Consumables</u>			
Daily quality assessment (DQA) gel phantom	ATS Laboratories	USA	
96-well plates	Greiner	Austria	Polystyrene cell culture microplates with μ Clear [®] bottom
Black 96-well plates	Greiner	Austria	Non cell culture treated black base microplates
Cell culture flasks	TPP	UK	75 cm ²
Titer Tops™ sealing film	ESM	USA	
Opti- cell	NUNC	Denmark	
Syringe filters	Thermoscientific	UK	Pores diameter of 0.2 mm

Sonovue®	Bracco	Italy	
Chemicals			
Roswell Park Memorial Institute (RPMI) 1640 medium	Gibco Invitrogen	UK	
Dulbecco's Modified Eagle Medium (DMEM)	Gibco Invitrogen	UK	
Fetal Bovine Serum (FBS)	Gibco Invitrogen	UK	
Penicillin Streptomycin (P/S)	Gibco Invitrogen	UK	(5000 I.U./ml, 5000 lg/ml)
Dimethyl Sulfoxide (DMSO)	Gibco Invitrogen	UK	
Trypsin- Ethylenediaminetetraacetic acid (EDTA)	Gibco Invitrogen	UK	0.05%
Membrane Integrity Kit	Invitrogen	UK	
Phosphate Buffered Saline (PBS)	Oxoid	UK	
Sodium Dodecyl Sulfate (SDS)	Sigma Aldrich	UK	
Bovine Serum Albumin (BSA)	Sigma Aldrich	UK	
Bicinchoninic acid (BCA) and Cu(II)	Sigma Aldrich	UK	
3-(4,5-Dimethylthiazol-2-yl)-2,5-diphenyltetrazolium bromide (MTT)	Sigma Aldrich	UK	
Doxorubicin (Dox)	Discovery	UK	

5.2.2 Methods

5.2.2.1 Cell Growth and Maintenance

The two cancer cell lines used in this study were MCF-7, human breast cancer cells, ATCC HTB-22, and A375m, human melanoma cells, ATCC CRL 1619. The cells were cultured in complete medium (CM), as monolayers in 75 cm² cell culture flasks in humidified air with 5% CO₂ at 37°C. Twice each week, the cell cultures were subcultured. Each flask was washed with 10 ml of Phosphate Buffered Saline (PBS) to remove any dead cell and remains of old media.

Straight after washing, the cells were detached using 1.5 ml of trypsin-ethylenediaminetetraacetic acid (EDTA) 0.05% and heated for 5 min at 37°C. Ten ml of 37°C pre-heated CM was added and the cells were transferred into 15 ml Eppendorf tubes and centrifuged for 5 min at 750 rpm. The CM was removed and the cells were re-suspended in 10 ml fresh CM. 1.5 ml of the solution was re-seeded in a new flask with an additional 15 ml CM. For US exposure experiments, 15,000 cells per well in 100 µL CM were seeded in 96-well plates three days in advance to reach confluence on the day of the experiment.

5.2.2.2 Evaluation of Drug Uptake into Cells

The uptake of Dox into both cell lines was investigated using fluorescence intensity measurements. Prior to the FUS / heating application, the medium in each well was replaced

with 420 μL of various solutions, as described in the appropriate plate descriptions for each arrangement in Figure 4.8, Figure 4.17, Figure 4.19 and Figure 4.21, and the plates were sealed using Titer-Tops® sealing film. Following sonication, the cells were washed twice with 100 μL of PBS. The PBS was removed and the cells were lysed using 0.5% SDS. The total fluorescence intensity of each well in the plate was measured under the conditions in Table 5.3:

Table 5.3- Fluorescence measurement parameters

Parameter	Value
Excitation wavelength	485 nm
Emission wavelength	592 nm
Excitation bandwidth	20 nm
Gain	100
Number of flashes	25
Integration time	20 μs
Temperature	Room temperature (RT)

The fluorescence readings were normalized by total protein amount using the BCA method (Smith et al., 1985). The uptake of Dox was calculated as:

$$\text{Uptake \%} = \frac{\left(\frac{\text{Dox Fluorescence [RFU]}_{\text{sample}}}{\text{Total Protein Amount } [\mu\text{g}]_{\text{sample}}} \right)}{\left(\frac{\text{Dox Fluorescence [RFU]}_{\text{control}}}{\text{Total Protein Amount } [\mu\text{g}]_{\text{control}}} \right)} \cdot 100$$

Equation 5.1- Uptake calculation

5.2.2.3 Cell Viability Evaluation

The viability of cells after US exposure was measured using MTT 3-(4,5-dimethylthiazol-2-yl)-2,5-diphenyltetrazolium bromide- a colorimetric assay that determines the cell enzymatic activity (Gerlier and Thomasset, 1986). Prior to the FUS / heating application, the medium in each well was replaced with 420 μL of various solutions, as described in the appropriate plate descriptions for each arrangement in Figure 4.8, Figure 4.17, Figure 4.19 and Figure 4.21, and the plates were sealed using Titer-Tops® sealing film. Following sonication, the cells were washed twice with 100 μL of PBS. 100 μL of fresh CM was added and the cell viability was determined immediately for cell loss studies or incubated at 37°C in 5% CO_2 for 24 h for cell recovery studies.

At the end of the incubation period, 20 μL of MTT was added, and the cells were incubated at 37°C in 5% CO_2 for an additional 3 h, after which all the liquid was removed and 100 μL of DMSO was added to dissolve the Formazan- an artificial chromogenic product created by the reduction of the tetrazolium salt (MTT) (Cole, 1986; Twentyman and Luscombe, 1987). The plate was shaken linearly in the Elisa plate reader at 1 mm for 50 s and the Formazan absorbance was measured at 550 nm. The cell viability was calculated with

$$\text{Cell Viability \%} = \left(\frac{\text{MTT Absorbance}_{\text{sample}} - \text{Background}}{\text{MTT Absorbance}_{\text{control}} - \text{Background}} \right) \cdot 100$$

Equation 5.2- Cell viability calculation

5.2.2.4 Membrane Integrity

A membrane integrity test was conducted to quantify the levels of membrane permeability due to US application (Cho et al., 2002). In the presence of MBs, US is known to increase cell membrane permeability. Therefore, measurement of lactate dehydrogenase (LDH) levels released from leaking membrane into the media can indicate the levels of membrane permeability achieved by US. A membrane integrity assay was conducted using the CytoTox-ONE kit according to its nominal protocol. The level of resofurin, which is proportional to the amount of LDH, was measured by fluorescence intensity. Prior to US application, the medium in each well was replaced with 420 μL of various solutions, as described in the appropriate plate descriptions in Figure 4.8, and the plates were sealed using Titer-Tops® sealing film.

Following sonication, the plate was centrifuged at 2000 rpm for 10 min to spin down any cells present in the media. 50 μL of the medium in each well were transferred into a new black 96-well plate and an equivalent amount of resazurin reagent was added. After an incubation period of 10 min at RT, the stop solution was added and the fluorescent signal was measured with an excitation wavelength of 560 nm and emission wavelength of 590 nm. The fluorescence readings were normalized by the total protein amount using the BCA method (Smith et al., 1985). The membrane permeability was calculated with

$$\text{Membrane Permeability \%} = \frac{\left(\frac{\text{LDH [RFU]}_{\text{sample}} - \text{Background}}{\text{Total Protein Amount } [\mu\text{g}]_{\text{sample}}} \right)}{\left(\frac{\text{LDH [RFU]}_{\text{control}} - \text{Background}}{\text{Total Protein Amount } [\mu\text{g}]_{\text{control}}} \right)} \cdot 100$$

Equation 5.3- Membrane permeability calculation

5.2.2.5 Cell Total Protein Estimation: The Bicinchoninic Acid Assay

The estimation of the total protein located in each well after treatment, was quantified as noted using a BCA assay. BCA (Bicinchoninic Acid) forms a complex with Cu(I) that results in a purple solution with maximum absorbance at 562 nm. Cu(I) appears in the solution as a result of reduction from Cu(II) after reaction with proteins. This is a highly sensitive protein concentration-dependent reaction (Smith et al., 1985).

Following the fluorescence measurement of the plate, 150 μ L of the cell solution in each well were transferred into a new plate and 50 μ L of BCA Working Reagent (WR) were added to the individual wells. Additionally, each plate contained a duplicate of a standard curve and triplicate of background, i.e. 150 μ L of 0.5% SDS with 50 μ L of the BCA WR. After addition of the BCA WR the plates were shaken linearly at 1 mm for 30 s and incubated at 37°C in 5% CO₂ for 1 h. At the end of the incubation time the absorbance of the plate was measured at 562 nm.

The final protein quantity in the samples after deduction of the background was derived from the average standard curve for each plate. Since the BCA assay does not have an end point, it is important to have a standard curve for each plate to accurately assess the amount of protein in each sample. Unfortunately, the BCA assay standard curve supplied in the kit was not compatible with the tested samples. It consisted of Bovine Serum Albumin (BSA) at significantly higher concentration than the samples in a plate and hence the measurements were at the noise level of the standard curve. Moreover, the supplied BSA was dissolved in a different solvent than the samples resulting in a need for different background and was thus generally incomparable. Consequently, the BSA standard curve was adjusted to the specific needs of the experiments. The final standard curve solutions consisted of BSA in 0.5% SDS, the same as the cell sample, with linearly increasing concentration from 6.25 μ g/ml to 400 μ g/ml.

5.2.2.6 Solution Preparation

PBS (Phosphate Buffered Saline) Five tablets of PBS were dissolved in 500 ml of purified water in RT and the solution was autoclaved. The solution was kept at RT before opening, and after opening was stored in a fridge.

Complete Media (CM) CM consists of Roswell Park Memorial Institute (RPMI) 1640 medium for A375m and Dulbecco's Modified Eagle Medium (DMEM) for MCF-7 supplemented with 10% Fetal Bovine Serum (FBS) and 1% Penicillin Streptomycin (5000 I.U./ml, 5000 Ig/ml). The solution was stored in a fridge.

MTT (3-(4,5-Dimethylthiazol-2-yl)-2,5-diphenyltetrazolium bromide) 250 mg of the MTT salt was added to 50 ml PBS, final concentration 5 mg/ml. The solution was stirred using a magnetic stirrer until all solid was dissolved. The solution was filtered using a 0.2 mm filter, then aliquoted into Eppendorf tubes in 5 ml/tube ratio and kept frozen until use.

Sodium Dodecyl Sulphate (SDS) Solution For the final concentration of 0.5% SDS in H₂O, 500 mg of SDS was dissolved in 1 L purified water. The solution was kept at RT.

Bovine Serum Albumin (BSA) To achieve a concentration of 400 µg/ml (mother solution), 400 mg BSA was dissolved in 1 L of SDS 0.5%, as described in Section 5.2.2.5. Solutions of 200, 100, 50, 25, 12.5, and 6.25 µg/ml, were created by dilution of the mother solution with 1:1 volume of 0.5% SDS. All solutions were kept in a fridge.

Preparation of the BCA Assay Reagent The BCA WR consisted of Cu(II) sulphate pentahydrate 4% solution and BCA solution of 1:8 ratio, freshly prepared on the day of the experiment.

Dox Solution Dox was kept in stock solution consisting of DMSO at a concentration of 100 mM, referred to as 'stock solution'. The amount of Dox was weighted according to the following calculation:

$$G = M_w \cdot C \cdot V$$

Equation 5.4- Weight dependence on concentration and volume

where G is the mass, M_w is the molecular mass, C is the concentration, and V is the volume of the final solution. Therefore to prepare a 100 mM solution in 1 ml of DMSO, 58 mg of Dox was weighed. On the day of the experiment, the Dox concentration in CM was adjusted according to

$$C_1 \cdot V_1 = C_2 \cdot V_2$$

Equation 5.5- Correlation between volumes and concentrations

where C stands for concentration, and V for volume. According to Equation 5.5, to convert 100 mM of Dox in DMSO into a volume of 50 ml with a final concentration of 25 µM of Dox in CM (referred to as 'final solution'), one must take 12.5 µl of the stock solution. Each stock solution was kept refrigerated for no longer than 3 months and the final solutions were always prepared freshly on the day of experiment.

Carrier (Ca-1709) Solutions Solutions of Ca-1709 were prepared in media with and without Dox depending on the experiment. The ratio between the Ca-1709 and Dox was 20:1. Hence when a concentration of 25 µM of Dox was used, the Ca-1709 concentration was 500 µM. The Ca-1709 was added to the final Dox solution. The weight of Ca-1709 was

calculated according to Equation 5.3. For the desired concentration of 500 μM at a volume of 50ml, 37.35 mg of Ca-1709 was added to the Dox solution/CM at RT. The final solutions were vortexed for 1 min and used immediately. For viability studies, all the solutions were filtered using 0.2 mm filters.

Dox with Sonovue MB Solution The Sonovue MBs were prepared on the day of the experiment according to the manufacturer's instructions and kept in an ice bath during the experiment. 0.5 ml of the Sonovue solution was added to 10 ml of Dox or CM solutions, to reach the final concentration of 4.7%, i.e. $4 \cdot 10^6$ bubbles/well.

5.2.2.7 Sonication and Heating Protocols

UF Sonoporation Arrangement The plate layout for cell sonication in the UF sonoporation arrangement is presented in Figure 4.8. From there it can be seen that wells B - G in rows 2, 4 and 6 were sonicated and wells B - G in rows 9 and 11 were control wells with no sonication. Line H1 - 6 was a negative control, meaning it did not undergo any treatment and was not subjected to FUS. For cellular drug uptake experiments, Section 5.2.2.2, the following solutions were used: Dox with Sonovue MBs, Dox only, and negative control, line H1 - 6, that consists of 100 μl of the existing CM filled with an additional 320 μl of fresh CM. For the viability and membrane integrity studies, CM with and without Sonovue MBs was used. Following the sealing of the plate, it was placed in its dedicated location in the water container, Figure 4.14. The temperature of the water in the container was preset to 30°C. After positioning the plate, the polystyrene thermal isolation box was placed over the apparatus and the sonications were performed according to the prepared protocol. All the sonications were performed at the optimal sonication configuration for the UF sonoporation arrangement i.e. 50% Tr at FD = 97 mm. Immediately after sonication, the plate was returned to the culture hood and treated according to the protocols in Section 5.2.2.

CBS Sonoporation Arrangement The plate layout for cell sonication in the CBS sonoporation arrangement is presented in Figure 4.17. From there it can be seen that wells C - G in rows 5 - 8 were sonicated and wells B - G in rows 2 and 11 were control wells with no sonication. Line H1 - 6 was a negative control, meaning it did not undergo any treatment and was not subjected to FUS. For cellular drug uptake experiments, Section 5.2.2.2, the following solutions were used: Dox with Sonovue MBs, Dox only, and negative control, line H1 - 6, that consists of 100 μl of the existing CM filled with an additional 320 μl of fresh CM. For the viability studies, CM with and without Sonovue MBs was used. Following the sealing of the plate, it was placed in its dedicated location in the water container, Figure 4.16. The temperature of the water was preset to 30°C. After positioning the plate, the cells were

subjected to FUS using the multi-focal sonication pattern. All the sonications were performed at the optimal FD = 62 mm. Immediately after sonication, the plate was returned to the culture hood and treated according to the protocols in Section 5.2.2.

UF Heating Arrangement The plate description for cell sonication in the UF heating arrangement is presented in Figure 4.21. From there it can be seen that wells C, E and G in rows 2, 4, 6 and 8 were sonicated, while wells B - G in rows 9 - 11 were control wells with no sonication. Line H1 - 6 was a negative control, meaning it did not undergo any treatment and was not subjected to FUS. For cellular drug uptake experiments, Section 5.2.2.2, the following solutions were used: Dox with Ca-1709, Dox only, and negative control, line H1 - 6, that consists of 100 μ l of the existing CM filled with an additional 320 μ l of fresh CM. For the viability studies, CM with and without Ca-1709 was used. Following the sealing of the plate, it was placed in its dedicated location in the water container, Figure 4.20, with DQA phantom above and below. The temperature of the water in the container was preset to 30°C. After positioning the plate, the polystyrene thermal isolation box was placed over the apparatus and the sonications were performed according to the prepared protocol. All the sonications were performed at the optimal sonication configuration for the UF heating arrangement i.e. 50% Tr at FD = 82 mm. Immediately after sonication, the plate was returned to the culture hood and treated according to the protocols in Section 5.2.2.

Heating without FUS The plate description for cell sonication for heating without FUS is presented in Figure 4.17. From there it can be seen that wells C, E and G in rows 2 - 6 were subjected to heat, while wells B - G in rows 9 - 12 were control wells without heating. Line H1 - 6 was a negative control meaning it did not undergo any treatment and was not heated. For cellular drug uptake experiments, Section 5.2.2.2, the following solutions were used: Dox with Ca-1709, Dox only, and negative control, line H1 - 6, that consists of 100 μ l of the existing CM filled with an additional 320 μ l of fresh CM. For the viability studies, CM with and without Ca-1709 was used. Following the sealing of the plate, it was placed on top of the heating blocks as shown in Figure 4.18. Immediately after heating, the plate was returned to the culture hood and treated according to the protocols in Section 5.2.2.

5.3 [Results](#)

5.3.1 **Sonoporation with UF System**

To evaluate the efficiency of the UF sonoporation arrangement for cell sonication, uptake, viability and membrane integrity studies were conducted.

5.3.1.1 The Influence of FUS on Dox Uptake

Following the construction and evaluation of the apparatus, fine tuning of the sonication parameters was performed to establish the optimal sonication powers and patterns.

Investigation of Various Sonication Powers To find the optimal power for enhancement of Dox cellular uptake, sets of sonications were performed. The power levels of the various sonications conducted were chosen such that there could be comparison between various sonication times with the same power, e.g. 1 Wa for 50, 25 and 10 sec; the same sonication times with different powers, e.g. 25 s with 1 and 2 W; and the same applied energy in different modes, e.g. 50 J by 2.5 Wa for 20 s and 1 Wa for 50 sec.

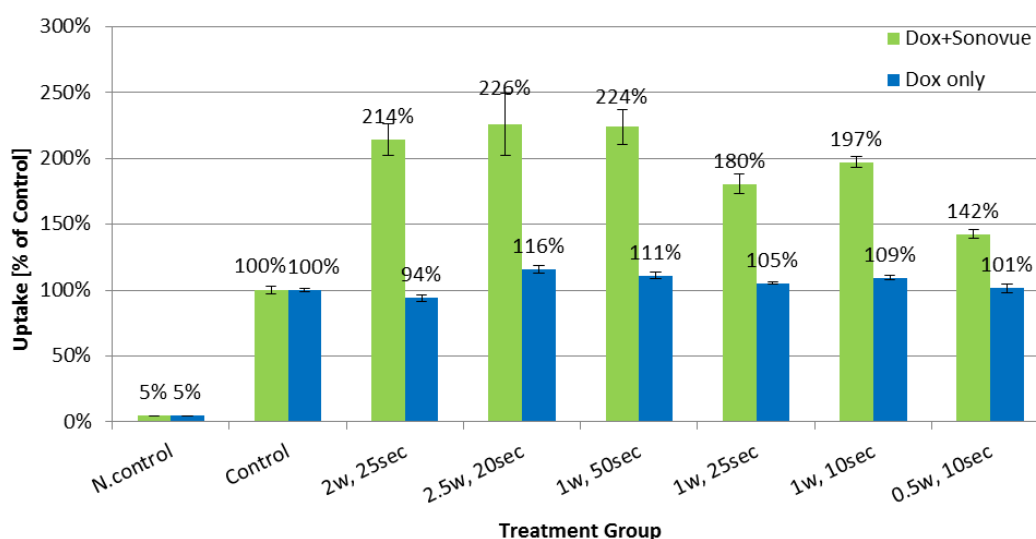


Figure 5.6- Uptake of Dox into MCF7 Cells at Various Sonication Parameters

Figure 5.6 depicts the Dox uptake, as a % of control \pm standard error (Se), into MCF7 cells, with and without Sonovue MBs, at the various sonication powers and energy levels presented in Table 5.4.

Table 5.4- Applied US powers in Dox uptake studies

	Total Energy [J]	Pressure [MPa]	Mechanical Index (MI)
2 W, 25 sec	50	0.75	0.77
2,5 W, 20 sec	50	0.84	0.86
1 W, 50 sec	50	0.53	0.54
1 W, 25 sec	25	0.53	0.54
1 W, 10 sec	10	0.53	0.54
0.5 W, 10 sec	5	0.37	0.38

Table 5.4 summarises the power levels tested for their potential in enhancement of drug uptake, together with their pressure and MI (as calculated according to Equation 2.10). To avoid destructive implosion of the MBs, all the power levels were chosen such that $MI < 0.9$. Figure 5.7 represents the Dox uptake, as % of control $\pm Se$, into A375m cells with and without Sonovue MBs at the optimal sonication power of 1 Wa for 10 sec.

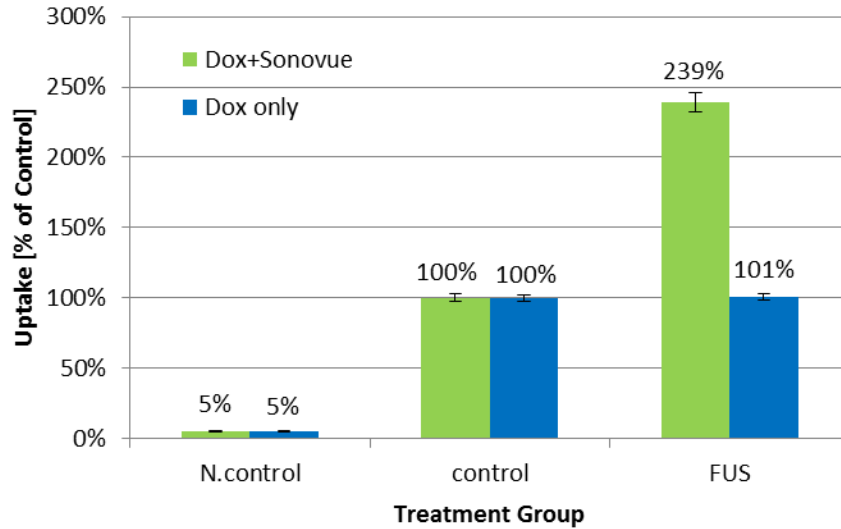


Figure 5.7- Uptake of Dox into A375m cells at 1 Wa for 10 s

Establishment of Optimal Sonication Pattern To define the best sonication pattern (i.e. the sonication pattern having the lowest impact on the neighbouring wells) as presented in Figure 4.8, the uptake of Dox was examined as a function of the sonication pattern.

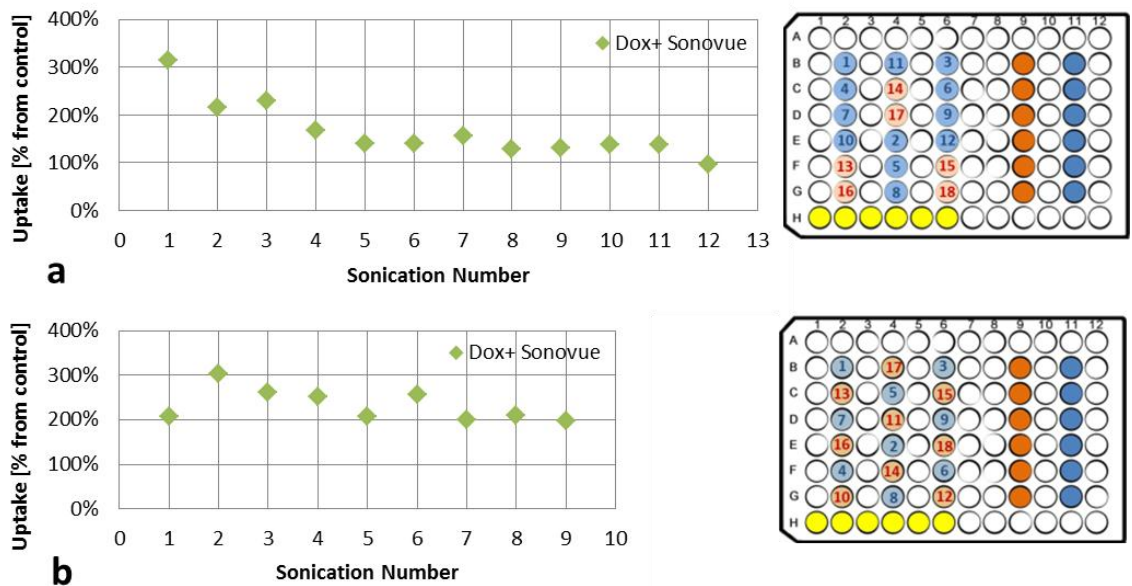


Figure 5.8- Location dependence of Dox uptake into MCF7 cells at 2 Wa for 25 sec

Figure 5.8 presents the Dox uptake, as a % of control, into MCF7 cells at 2 Wa for 25 s in correspondence with the sonication number, as appears in the plate description.

5.3.1.2 The Influence of Focused Ultrasound on Cell Viability

Viability assays were conducted to evaluate the level of irreversible membrane damage which results in cell death due to the application of FUS. The viability assays were done at two time points, immediately after the sonication and at 24 h follow up. The immediate viability studies were conducted to evaluate the amount of cell loss due to FUS, while the 24 h studies indicated the recovery level of the remaining cells. Additionally, viability studies were done at higher power to serve as a safety margin.

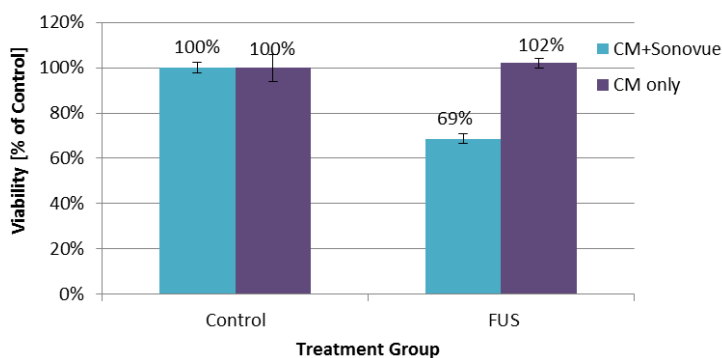


Figure 5.9- High power viability assessment in MCF7 cells 24 h after sonication

Figure 5.9 represents the viability, as % of control \pm Se, for studies conducted 24 h after sonication to assess the impact of US on cells at the relatively high power of 2.5 Wa for 20 s for safety purposes. The viability, as % of control \pm Se, immediately and 24h after 1 Wa for 10 s sonication, of MCF7 and A375m cells, is presented in Figure 5.10.

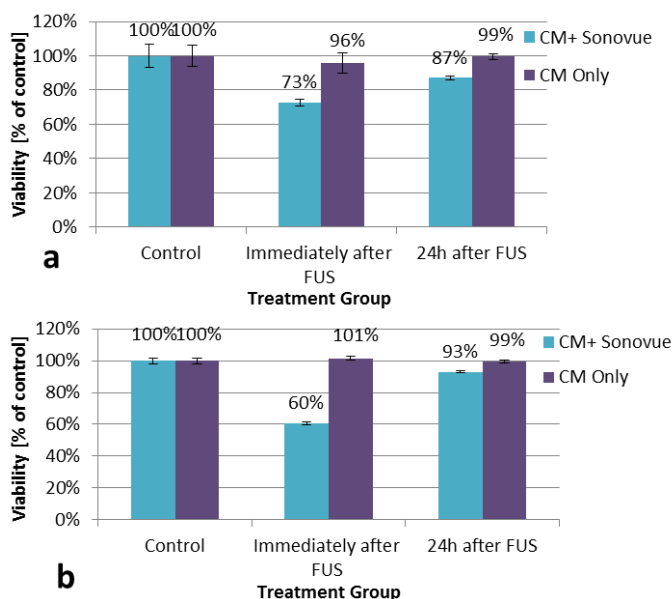


Figure 5.10- Viability of (a) MCF7 and (b) A375m cells immediately and 24 h after sonication

5.3.1.3 Membrane Integrity Studies

To help establish the mechanism of uptake enhancement by MBs, the membrane integrity of the cells was assessed.

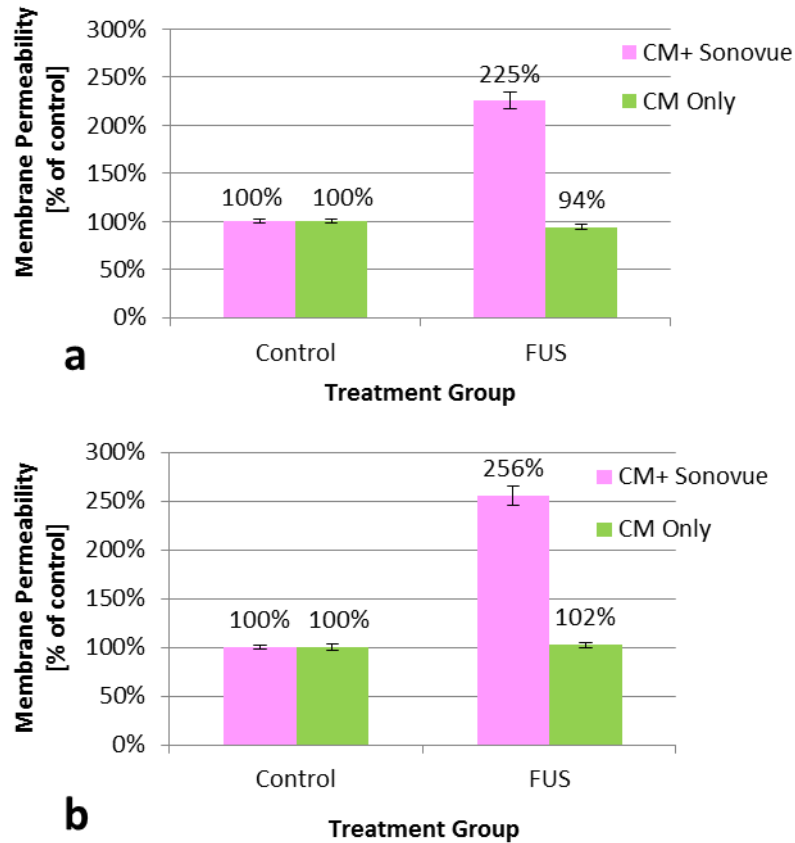


Figure 5.11- Membrane integrity due to FUS in (a) MCF7 and (b) A375m cells

Figure 5.11 shows the membrane permeability, as % of control \pm Se, of MCF7 and A375m cells as defined in Equation 5.3, at a power level of 1 Wa for 10 s exposure.

5.3.2 Sonoporation with Conformal Bone System

To examine the accuracy *in vitro* of the CBS arrangement, multi-focal sonication pattern, uptake and viability studies were conducted.

5.3.2.1 Dox Uptake in a Multi-Focal Sonication Pattern

To find the optimal power for enhancement of Dox cellular uptake, set of sonications at different powers were performed.

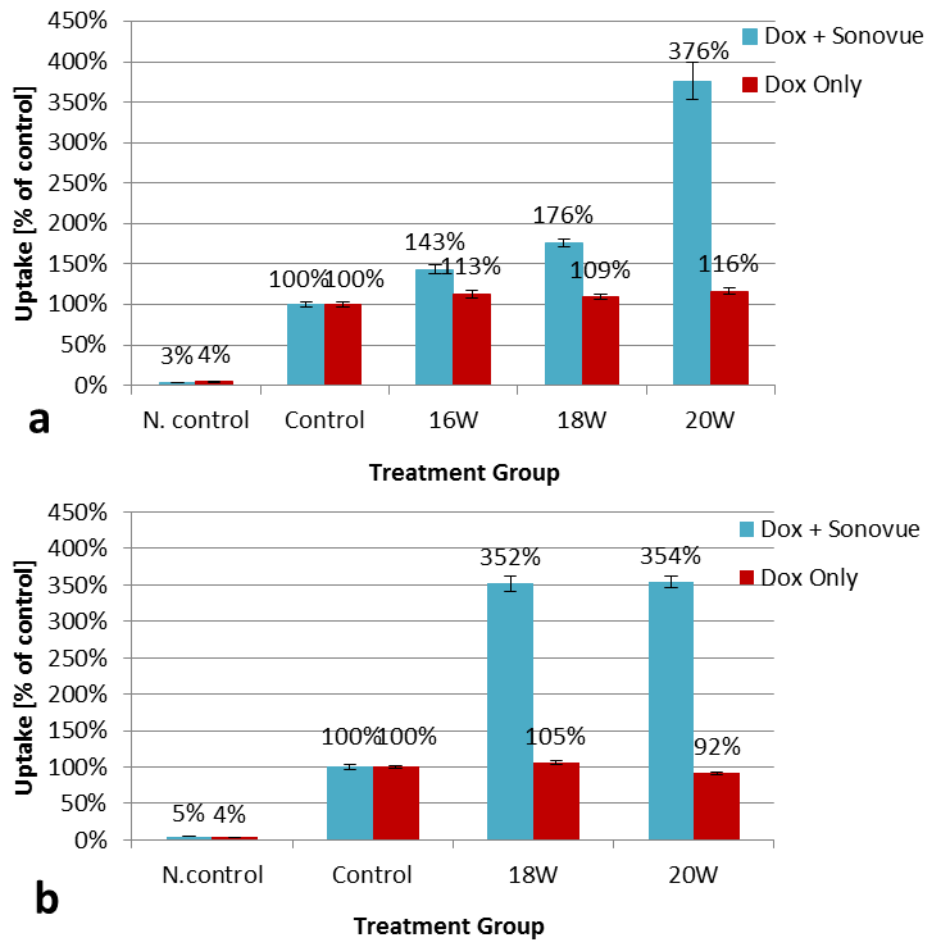


Figure 5.12- Uptake of Dox into (a) MCF7 and (b) A375m cells with a multi-focal sonication

Figure 5.12 shows the Dox uptake, as % of control \pm Se, into MCF7 and A375m cells with sonication of 16, 18 and 20 Wa for 10 s using a multi-focal sonication pattern.

Table 5.5- Average acoustic pressure and MI for different powers

	Pressure [MPa]	Mechanical Index (MI)
16 W	0.43 \pm 0.03	0.58 \pm 0.04
18 W	0.46 \pm 0.03	0.62 \pm 0.04
20 W	0.48 \pm 0.02	0.65 \pm 0.04

Table 5.5 summarizes the average acoustic pressure and MI of the 16 points on the cell level for different acoustic power levels.

a	1	2	3	4	
C	284% ($\pm 33\%$)	255% ($\pm 15\%$)	284% ($\pm 25\%$)	399% ($\pm 68\%$)	Dox+ Sonovue
D	351% ($\pm 34\%$)	514% ($\pm 77\%$)	551% ($\pm 56\%$)	393% ($\pm 71\%$)	
E	97% ($\pm 17\%$)	100% ($\pm 9\%$)	94% ($\pm 12\%$)	98% ($\pm 13\%$)	Dox Only
F	95% ($\pm 10\%$)	100% ($\pm 14\%$)	100% ($\pm 8\%$)	95% ($\pm 11\%$)	
b	1	2	3	4	
C	349% ($\pm 39\%$)	353% ($\pm 41\%$)	386% ($\pm 32\%$)	377% ($\pm 31\%$)	Dox+ Sonovue
D	397% ($\pm 36\%$)	481% ($\pm 72\%$)	455% ($\pm 41\%$)	375% ($\pm 31\%$)	
E	94% ($\pm 6\%$)	91% ($\pm 4\%$)	96% ($\pm 5\%$)	87% ($\pm 4\%$)	Dox Only
F	95% ($\pm 6\%$)	91% ($\pm 5\%$)	93% ($\pm 4\%$)	88% ($\pm 7\%$)	
c	1	2	3	4	
C	0.609	0.652	0.629	0.636	
D	0.619	0.689	0.698	0.682	
E	0.624	0.697	0.660	0.692	
F	0.610	0.711	0.627	0.575	

Figure 5.13- Average within each well of Dox uptake into (a) MCF7, (b) A375m cells and (c) the MI, with 20 Wa multi-focal sonication

Figure 5.13 depicts the Dox uptake averages, as % of control \pm Se, into MCF7 and A375m within each well of the 16 wells simultaneously sonicated at an applied power of 20 Wa. The MI is presented at the same power in the equivalent locations.

5.3.2.2 Cell Viability Studies in a Multi-Focal Sonication Pattern

Viability studies were conducted to establish the impact of the multi-focal pattern on the cell monolayer. Figure 5.14 depicts the viability as % of control \pm Se, immediately and after 24h, due to sonication of 20 Wa for 10 s in MCF7 and various power levels in A375m cells, respectively.

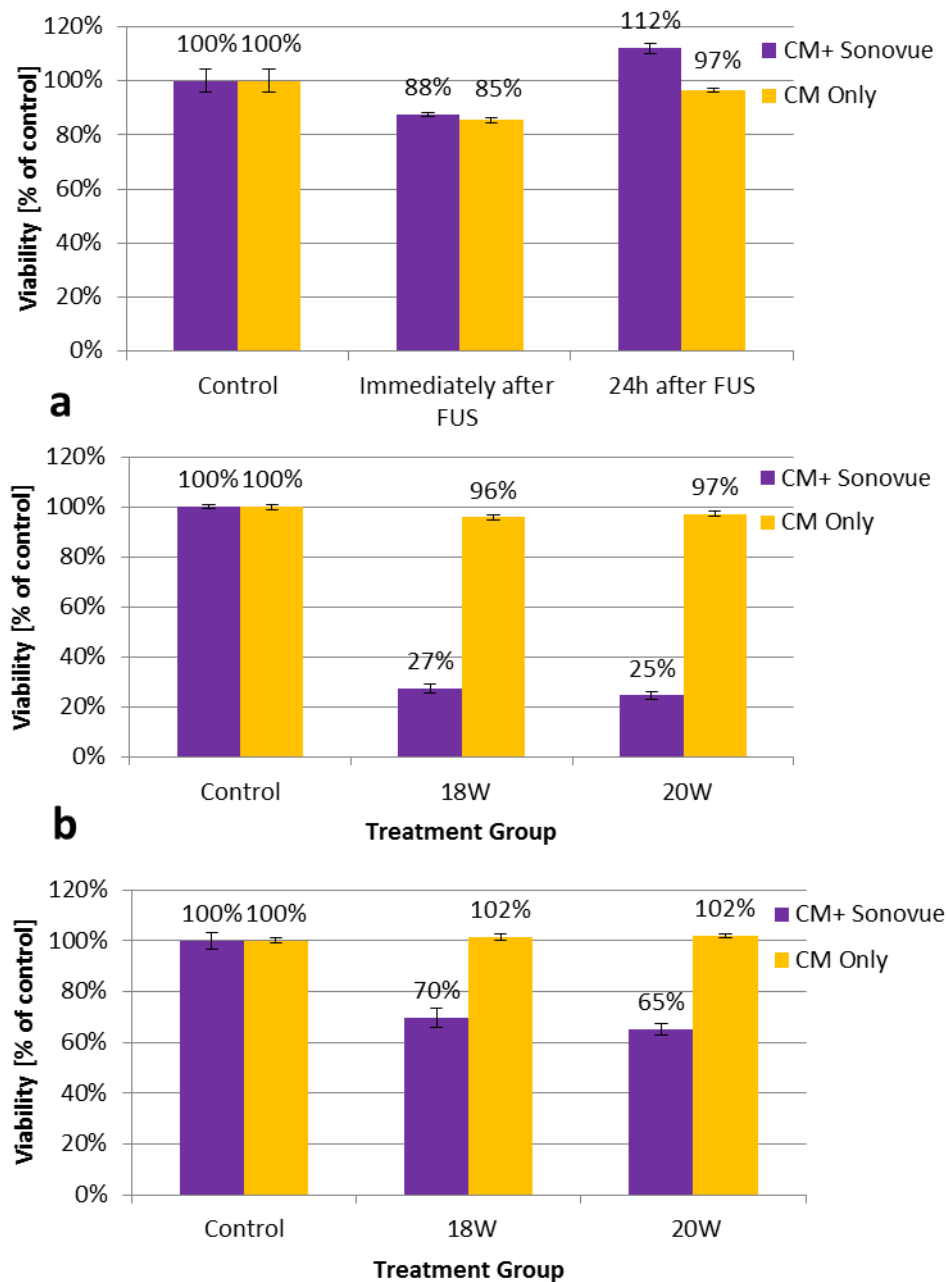


Figure 5.14- Viability of (a) MCF7 cells after 20 W multi-focal sonication and A375m cells (b) immediately and (c) 24 h after multi-focal sonication at various powers

5.3.3 Sonoporation and Heating Influence on Encapsulated Drug Uptake and Cell Viability

The novel nanocarrier, Ca-1709, presented in this work was tested for its ability to release the encapsulated drug upon an US trigger. The application of FUS in the presence of Ca-1709 was examined in the sonoporation arrangement and in the heating arrangements which are more realistically linked to possible applications *in vivo*.

5.3.3.1 Sonoporation Influence on Encapsulated Drug Uptake

Drug release from Ca-1709 due to MB-mediated cavitation was studied in the UF sonoporation arrangement. The same conditions as in the free drug sonoporation studies were applied, i.e. 50% Tr at FD = 97 mm. Figure 5.15 and Figure 5.16 depict the Dox uptake, as % of control \pm Se, into MCF7 and A375m, at various power levels, in the presence of Ca-1709 with and without Sonovue MBs.

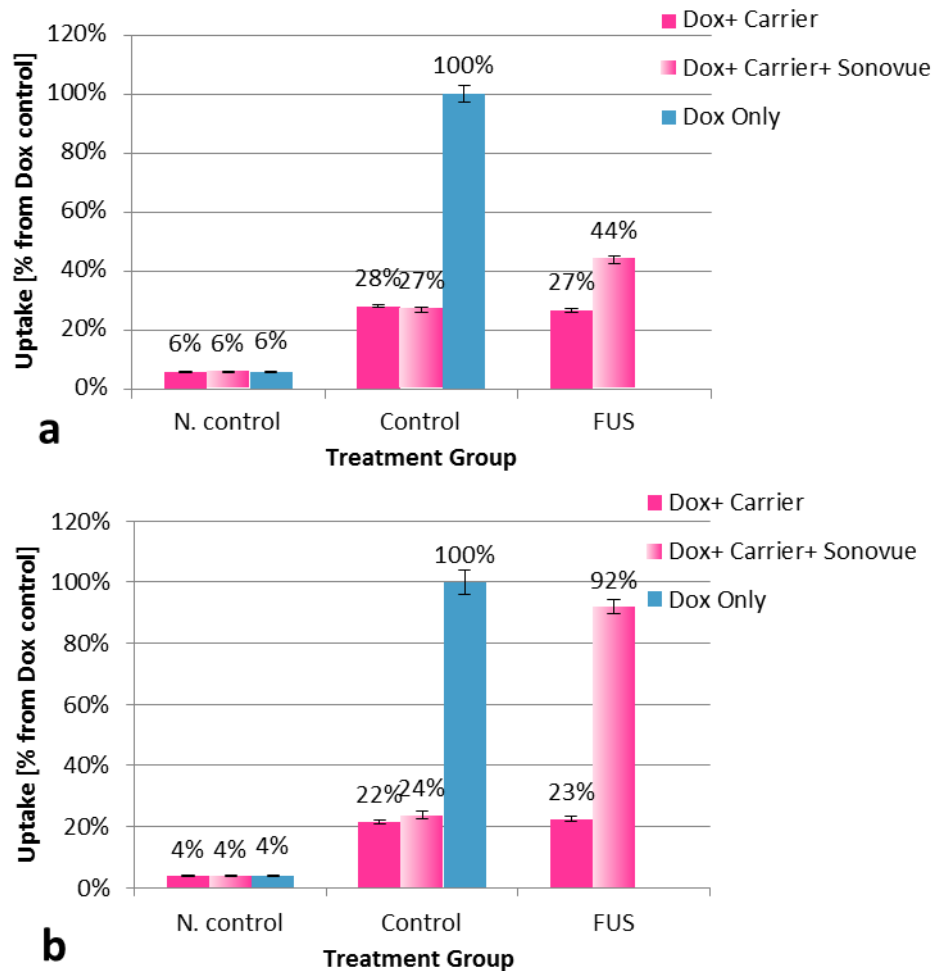


Figure 5.15- Dox uptake into (a) MCF7 and (b) A375m cells in the presence of Ca-1709

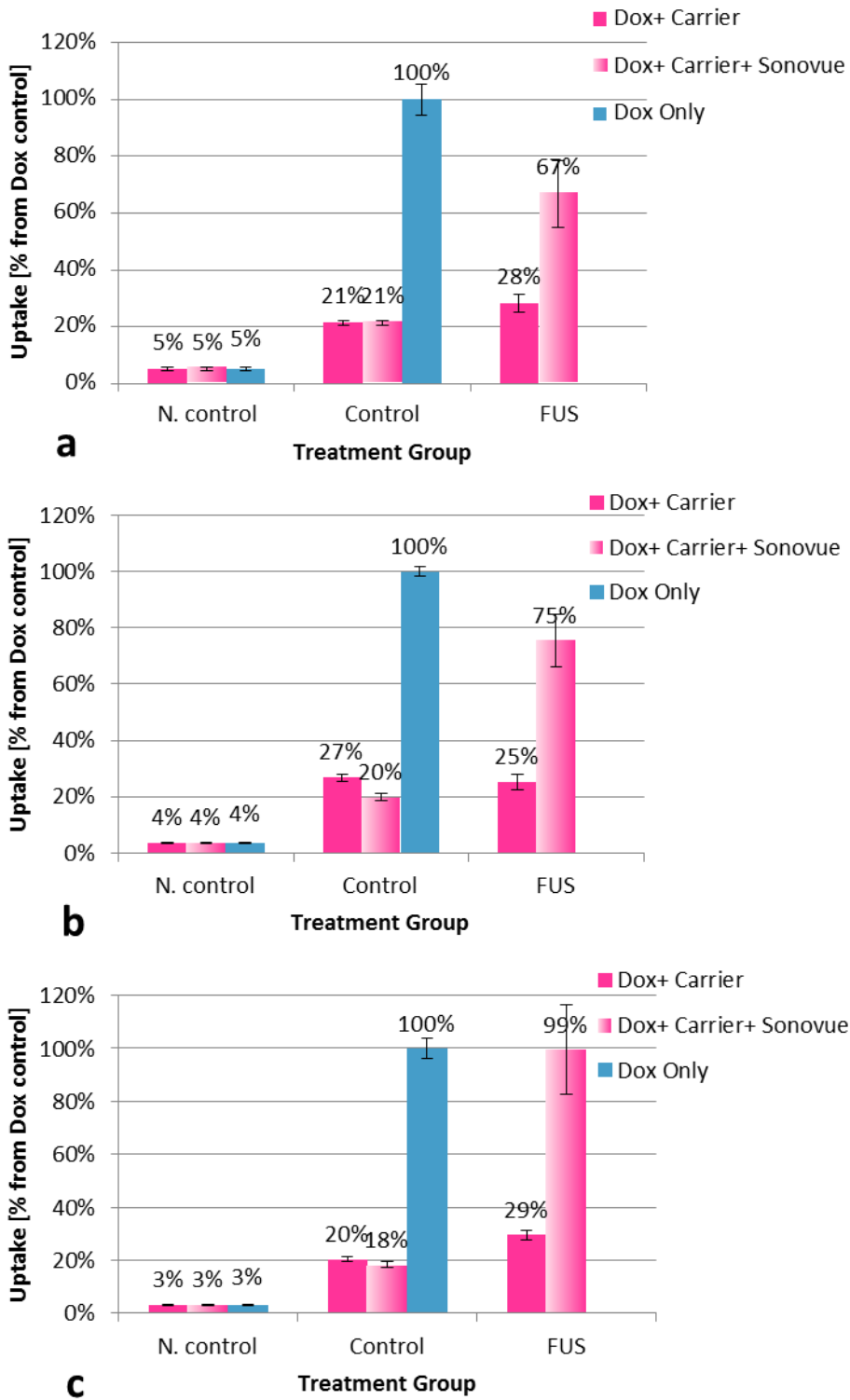


Figure 5.16- Dox uptake into MCF7 cells in the presence of Ca-1709 at (a) 1 Wa for 33 s, (b) 1 Wa for 50 s and (c) 2 Wa for 25 s

5.3.3.2 Heating without Focused Ultrasound Influence on Encapsulated Drug Uptake and Cell Viability

To establish the influence of heating on the mechanisms of drug penetration within cancer cells, uptake and viability studies were conducted.

Dox Uptake in the Presence of Ca-1709 According to the protocol described in Section 5.2, each plate was placed on a 70°C heater until the base of the plate reached 42°C; immediately, the plate was moved to the 50°C heater for what was referred to as ‘the heating time’. The fluorescence of the plate was measured and the uptake as a percentage of the Dox-only control \pm Se, is presented in Figure 5.17 -Figure 5.18.

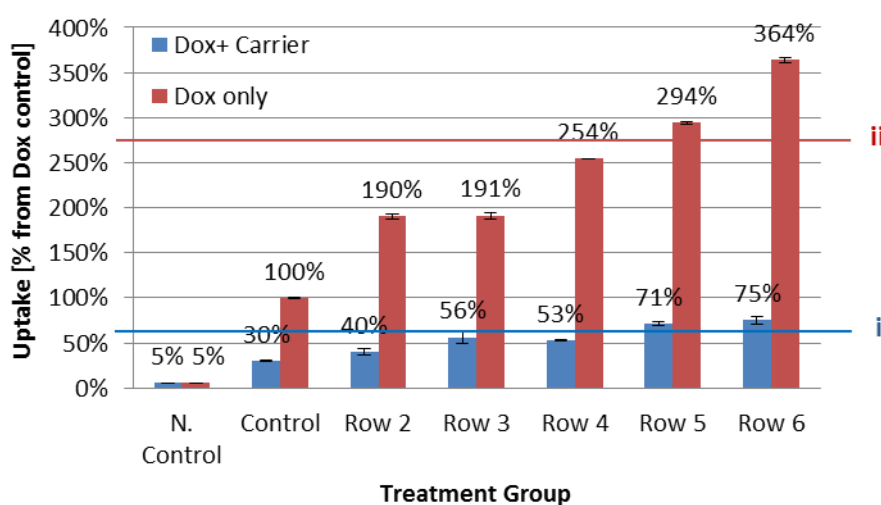


Figure 5.17- Uptake of Dox into MCF7 cells in different rows after 3 min heating of a non-inverted plate

Figure 5.17 depicts the Dox uptake into MCF7 cells as a result of 3 min heating in each row of a non-inverted plate. Line (i) represents the average of Dox only, whereas line (ii) represents the average of Dox + carrier. Figure 5.18 depicts the Dox uptake into MCF7 and A375m cells in an inverted plate, as result of 3 and 6 min heating.

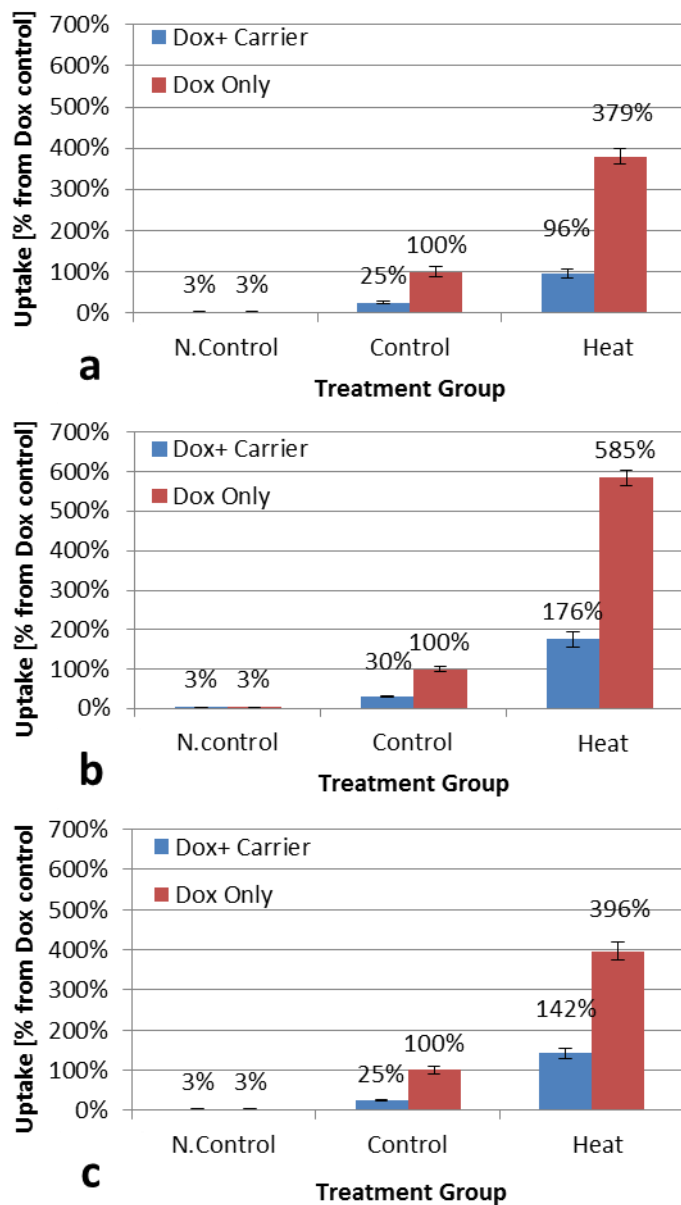


Figure 5.18- Uptake of Dox into MCF7 cells after (a) 3 and (b) 6 min and (c) into A375m cells after 3 min heating

Cell Viability in the Presence of Ca-1709 To establish the effect of heating on the cells, viability measurements were conducted. The viability of both cell lines is presented in Figure 5.19 and Figure 5.20.

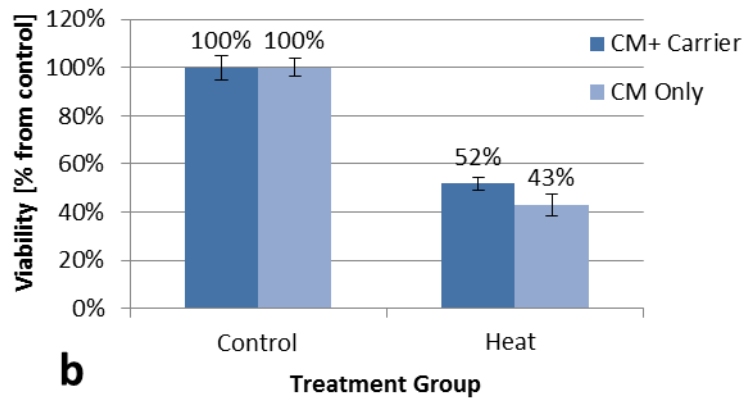
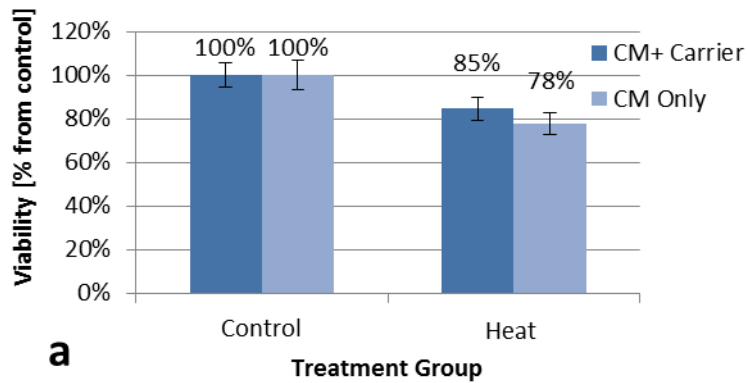


Figure 5.19- Viability of MCF7 cells after 24 h as a result of (a) 3 and (b) 6 min heating

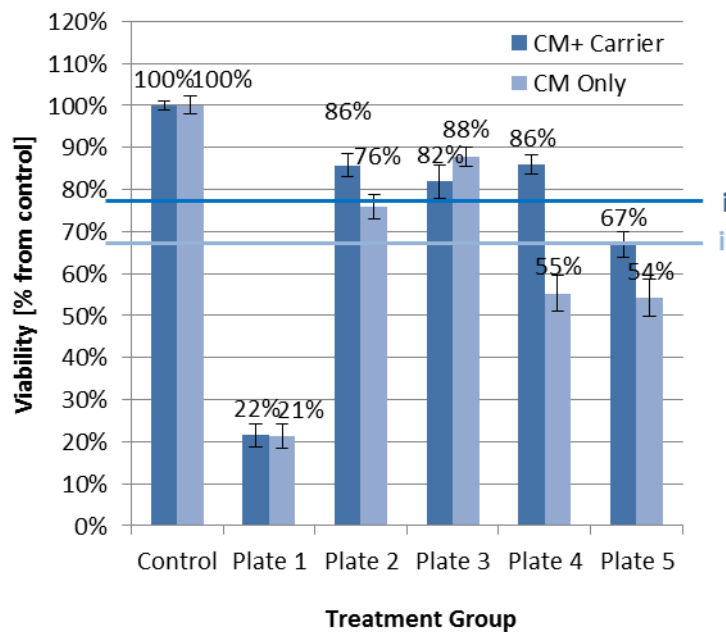


Figure 5.20- Viability of A375m cells after 24 h as a result of 3 min heating in 5 plates

Figure 5.19 presents the viability, in % of control \pm Se, of MCF7 after 3 and 6 min of heating, whereas Figure 5.20 depicts the viability, in % of control \pm Se, of A375m cells after

3 min heating of five different plates. Line (i) represents the average viability without Ca-1709 between plates 2 - 5, whereas line (ii) represents the average viability with Ca-1709 between plates 1 - 5.

5.3.3.3 Focused Ultrasound induced Heating Influence on Encapsulated Drug Uptake and Cell Viability

To evaluate the efficiency of FUS induced heating in cellular uptake of free and encapsulated drug within cancer cells and to define the cellular damage, uptake and viability studies were conducted. All the sonications were performed at the optimal sonication configuration for the heating arrangement of 50% Tr, FD = 85 mm.

Dox Uptake in the Presence of Ca-1709 The uptake as a percentage of the Dox-only control \pm Se, of free and encapsulated Dox at various sonication parameters are presented in Figure 5.21 and Figure 5.22.

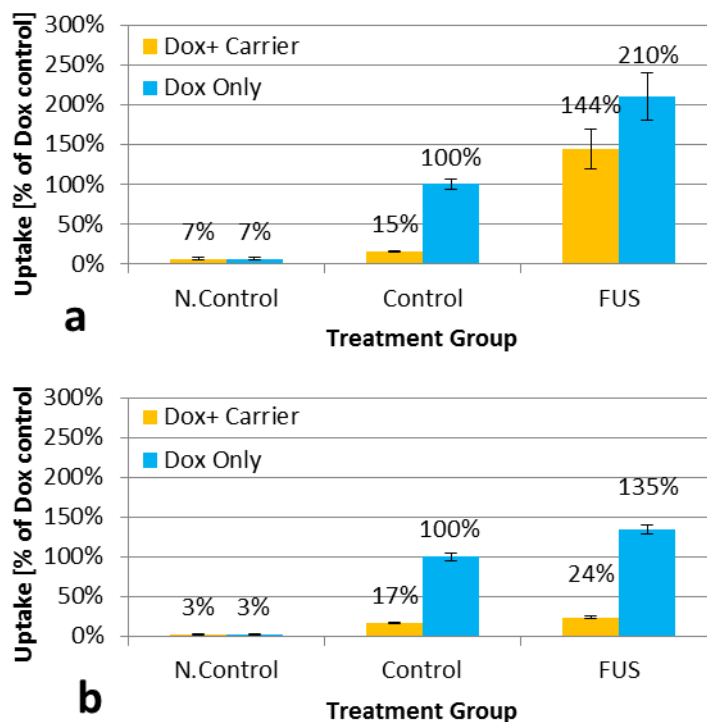


Figure 5.21- Uptake of Dox into MCF7 cells after FUS induced heating with (a) 30 Wa for 30 s and (b) 30 Wa for 20 s

Figure 5.21 presents the Dox uptake into MCF7 cells due to continuous sonication of (a) 30 Wa for 30 s and (b) 30 Wa for 20 s. In each case it was followed by a pulsed sonication of 30 Wa for 180 s, 0.5 s on and 3 s off.

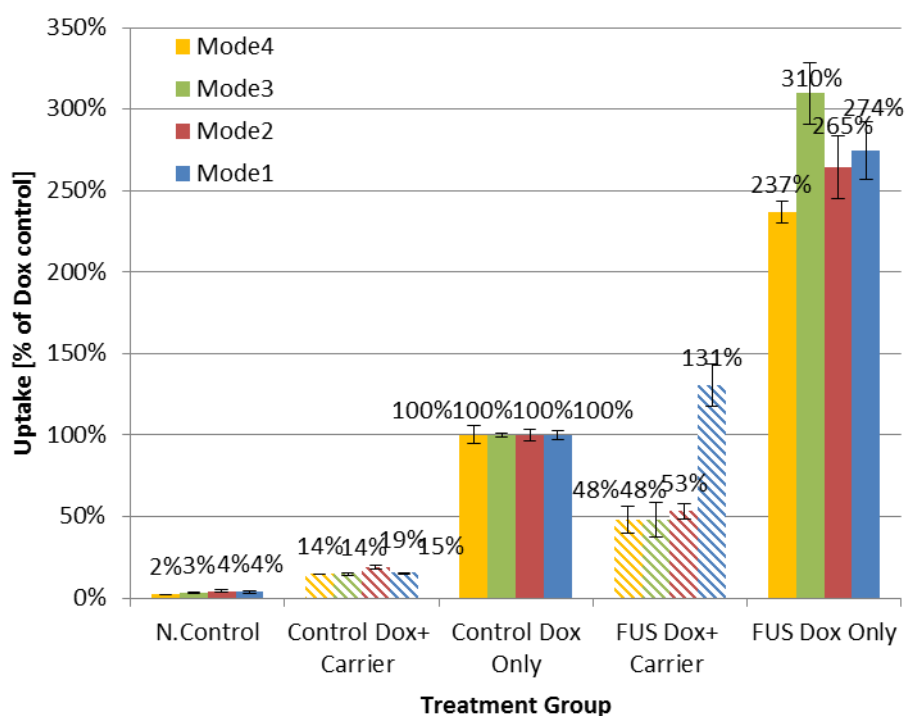


Figure 5.22- Uptake of Dox into A375m cells after FUS induced heating (see text for Mode details)

Figure 5.22 presents the Dox uptake into A375m cells due to continuous sonication as follows:

- Mode 1- 30 Wa for 30 s followed by a pulsed sonication of 30 Wa
- Mode 2- 30 Wa for 20 s followed by a pulsed sonication of 30 Wa
- Mode 3- 20 Wa for 45 s followed by a pulsed sonication of 20 Wa
- Mode 4- 15 Wa for 60 s followed by a pulsed sonication of 15 Wa

In each case, the pulsed sonication was 180 s, 0.5 s on and 3 s off.

Cell viability in the Presence of Ca-1709 Figure 5.23 depicts the viability, in % of control \pm Se, of MCF7 cells due to continuous sonication of 30 Wa for 30 s followed by a pulsed sonication of 30 Wa for 180 s, 0.5 s on and 3 s off.

Figure 5.24 depicts the viability, in % of control \pm Se, of A375m cells due to continuous sonication under different conditions. In each case, the pulsed sonication was 180 s, 0.5 s on and 3 s off.

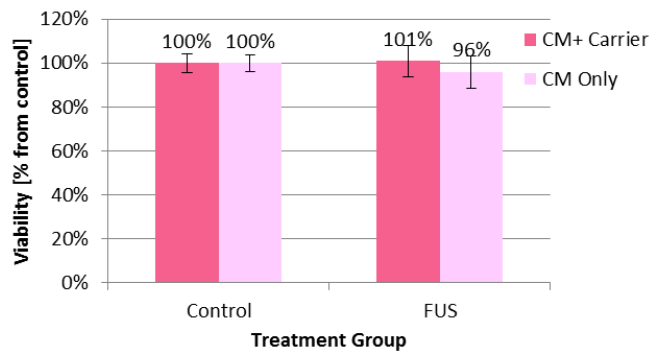


Figure 5.23- Viability of MCF7 cells 24 h after FUS induced heating

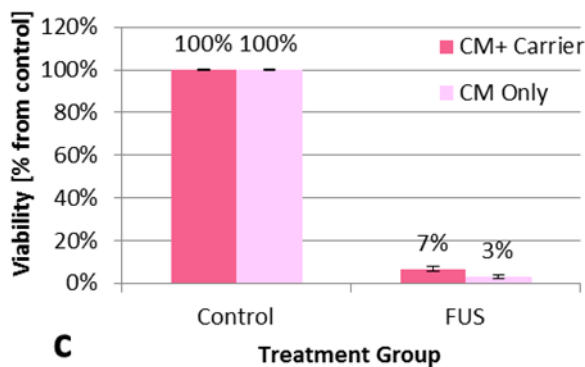
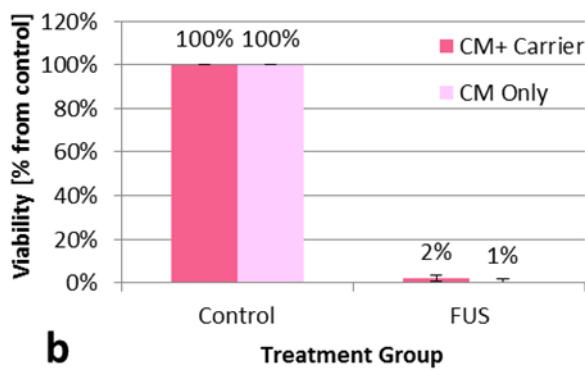
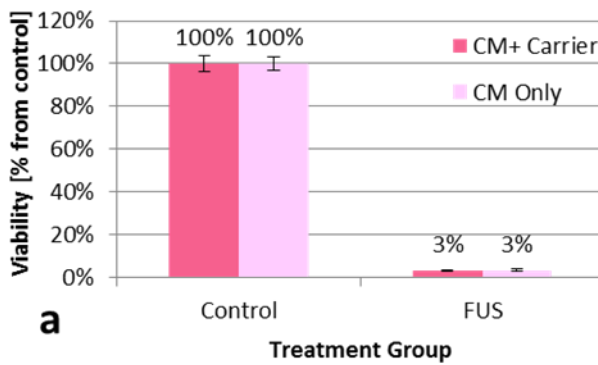


Figure 5.24- Viability of A375m cells 24 h after FUS induced heating (a) 30 Wa for 30 s followed by a pulsed sonication of 30 Wa, (b) 20 Wa for 45 s followed by a pulsed sonication of 20 Wa, and (c) 15 Wa for 60 s followed by a pulsed sonication of 15 Wa

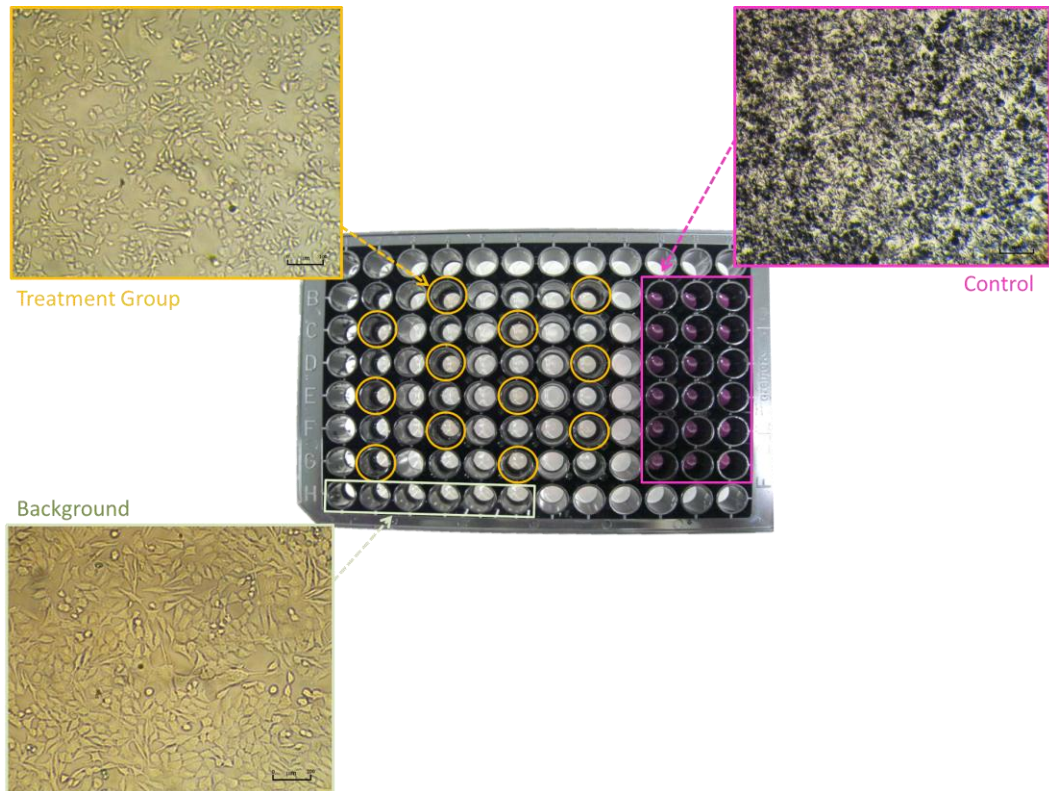


Figure 5.25- A375m cells viability plate following FUS induced heating

Figure 5.25 depicts the A375m cells plate after FUS induced heating at 30 Wa for 30 s, with representative images of the cells from the treatment, control and background groups.

5.4 Discussion

As the UF sonoporation arrangement was the first to be established for *in-vitro* application, a major baseline study was carried out with it, including tuning of the parameters and definition of the optimal sonication patterns.

The initial fundamental research was designed to discover the optimal sonication parameters by scanning possible sonication powers, times and energy levels. Since the half-life of Sonovue during sonication at 1 MHz was shown to be as low as 41 s (Tinkov et al., 2009), sonication times longer than 50 s were considered irrelevant and hence were not tested.

As can be seen in Figure 5.6, all the applied powers except the lowest one, of 0.5 Wa, caused a factor of 2 increase in Dox uptake with no major difference between them. This indicates that the MB activity is a threshold dependent phenomenon. Consequently the chosen power was the lowest, yet beneficial, sonication power level of 1W at the shortest sonication time of 10 sec.

In addition to the definition of the optimal sonication parameters, the sonication order was investigated. The sonication order in the plate is very important due to the fragility of the

MBs. In both the sonication patterns, the treatment groups containing MBs were sonicated first. In Figure 5.8 the top sonication pattern, (a), was planned to have the most of treatment groups with MBs. In this pattern it was established that there is an influence on the bubbles in the neighbouring wells. From Figure 5.8(a) it can be seen that after the fourth sonication, the uptake is significantly lower than the first three sonications, e.g. in sonication number three, the uptake value is 230% of the control whereas in sonication five it is only 139%. This could suggest that the bubbles imploded prior to the sonication as a result of the acoustic power impinging on the neighbouring wells.

At the same power, in a pattern that isolates the MB treatment groups by Dox only groups, Figure 5.8(b), the uptake of Dox in the presence of MBs is more uniform, e.g. in sonication number three, the uptake value is 261% of the control and in sonication five it is 207%, averaging 233% \pm 12%. Although three replicates of the MB treatment group were swapped by the Dox only group, the latter sonication pattern proved to be the most uniform, with the highest repeatability.

To assess the impact of FUS application on cells in the presence of MBs, viability studies were conducted. The safety margin was chosen to be the highest applied power, i.e. 2.5 Wa for 20 sec. As can be seen in Figure 5.9, sonication at this power causes significant cell damage, 31% \pm 2%, even after a 24 h recovery period. When applying 1 Wa for 10 s the viability increases. As seen in Figure 5.10, immediately after application of FUS there is a significant cell loss, 27% \pm 2% in MCF7 and 40% \pm 1% in A375m, yet after recovery period of 24 h there is a smaller percentage of cell death, 13% \pm 1% in MCF7 and 7% \pm 1% in A375m. This indicates that the remaining cells after sonication are fully functioning and dividing normally.

Membrane integrity tests were conducted to gain better understanding of the mechanism of uptake enhancement by MBs in acoustic environment. The membrane integrity assay quantified the level of LDH present in the media due to leaking cell membranes. Accordingly it was possible to evaluate the membrane permeability achieved by FUS application. As can be seen in Figure 5.11, in both cell lines there is doubling of the permeability of the membrane due to FUS in the presence of MBs and no significant change without MBs. These data correspond to the uptake values at 1W for 10 s, shown in Figure 5.6 and Figure 5.7, being double the control for the MB group and without a major difference in the Dox only treatment group. From the membrane integrity results it can be concluded that the mechanism of enhanced cellular uptake via sonoporation is achieved specifically by the Sonovue.

Development of the CBS sonoporation arrangement introduced the possibility of multi-focal sonication. Utilization of multi-focal patterns can significantly lower the treatment period and may thus contribute towards repeatability of results. To define optimal sonication parameters, several power levels were tested and the uptake and viability were recorded.

MCF7 cells show strong power dependence both from the uptake and the viability evaluation. The uptake $376\% \pm 23\%$, of Dox within the MCF7 cells after sonication of 20 Wa was higher than at powers of 18 Wa, $176\% \pm 5\%$, and 16 Wa, $143\% \pm 5\%$, Figure 5.12. Figure 5.13 presents the uptake as an average in each well location, rather than over the whole treatment group, at the applied power of 20 Wa. As can be seen from Figure 5.13, there is a variation within MB treatment groups between the different wells of up to a factor of 2.19 in MCF7 cells and 1.38 in A375m cells. The same figure presents the MI at the same locations as the average uptake in Figure 5.13. The sudden increase in uptake at a power of 20 Wa, together with the large variation in the uptake values between the individual wells, may indicate the occurrence of a threshold-related phenomenon influencing the cell monolayer.

A possible existing threshold is reported to be between stable and transient cavitation (Leighton, 1997; Brennen, 1995). As explained previously, stable cavitation is a process in which a MB, or a cloud of MBs, undergoes steady state oscillation during the application of ultrasound, expanding during negative pressure peaks and shrinking during positive pressure peaks. The oscillations can be either linear i.e. the bubble changes its size equally in every direction or non-linear, i.e. the bubble is no longer spherical and may take different oscillation shapes. The presence of stable cavitation in proximity to cells also causes micro-streaming. This produces large shear forces on the cells, contributing to increased membrane permeability. Stable cavitation generates an acoustical signature that depends on the type of oscillation and appears as harmonic and sub-harmonic peaks of the transmitted frequency.

Transient cavitation, in contrast, is a process in which, during the expansion stage under negative pressure, a bubble can no longer sustain itself and violently implodes. During such an event, a jet may be formed towards a nearby surface. This jet can be considered as a micro-needle, rupturing the cell membrane. Transient cavitation has a broadband acoustical signature in the frequency domain.

Stable cavitation in the presence of MBs is reported to occur for $0.3 < MI < 0.6$ (Wu and Nyborg, 2008; Hernot and Klivanov, 2008). Moreover, it was reported by Hung et al. (2011) that application of US with $MI = 0.6$ causes Sonovue MB destruction *in vivo*. In the present experiments, the cavitation activity was not directly measured. Therefore, because of the uptake behaviour, it was assumed that stable cavitation occurred during application of 16

Wa and 18 Wa of acoustic power and a mixture of the two phenomena during the application of 20 Wa of acoustic power, resulting in higher values and variability in the drug uptake results.

According to the viability studies there was a minor impact on the immediate viability of the MCF7 cells with, $12\% \pm 1\%$, and without, $15\% \pm 4\%$, MBs as a result of sonication at 20 Wa for 10 s in the multi-focal pattern. The recovery studies 24 h after sonication indicate a full recovery of the MCF7 cells with, $112\% \pm 3\%$, and without, $97\% \pm 2\%$, MBs at the same power. Consequently, 20 Wa for 10 s was taken as the optimal protocol for MCF7 cell sonication.

When a power of 20 Wa was applied to the A375m cell line, the viability results indicated significant cell damage in the presence of MBs, $75\% \pm 2\%$ immediately after sonication and $30\% \pm 2\%$ following 24h recovery. Lower power showed no significant improvement in the viability, demonstrating that there is no major difference in the impact on uptake and viability in the range of the applied powers, Figure 5.12 and Figure 5.14.

When comparing the uptake achieved in the CBS arrangement to that of the UF system, the CBS multi-focal sonications appear to have a stronger effect on the uptake of Dox into MCF7 cells, even at lower MI. An explanation for this can be found in the significantly lower total exposure time to Dox. In the CBS arrangement, the exposure time equals the sonication duration, e.g. 10 s, whereas in the UF sonoporation arrangement with the same sonication duration, the total sonication time equals at least 10 min, which includes 10 s sonication in 18 wells and additional transducer movement time. The additional time following the sonication in a specific well creates a masking effect of the FUS impact on the cells.

To evaluate the efficiency of FUS as a drug release stimulus from the Ca-1709 nanocarrier, both sonoporation and heating experiments were conducted. During sonoporation, the cells were exposed to FUS in the presence of encapsulated drug with and without MBs. According to the uptake studies, Figure 5.15, at a power of 1 Wa for 10 s in the presence of MBs, the uptake of Dox into A375m was increased by a factor of 3.83, resulting in almost equivalent amounts of Dox penetrating the cells as in the free Dox control. Nonetheless, in MCF7 at the same power, no significant increase in uptake was recorded. An increase in the applied power realised a significant increase in uptake, up to a factor of 5.5 at a power of 2 Wa for 25 s, Figure 5.16. A suggested mechanism for the cell uptake increase is via penetration of the encapsulated drug into the cells due to increased cell membrane permeability achieved by the MBs.

To establish the effect of heat with and without FUS on the cellular drug uptake of the free and encapsulated Dox, a set of experiments was conducted in two dedicated

arrangements. While it is clear that the plate should be placed inverted in the sonoporation arrangements in order to retain the buoyant MBs in proximity to the cells, the rationale behind the inverted plate in the heating arrangement is to achieve a uniform heating effect throughout the plate. As can be seen in Figure 5.17, placing a non-inverted plate on the heaters results in a different uptake in each row in the plate. This can be explained simply by the fact that the cells receive the heat straight from the hot plate in a nonuniform pattern which results in various levels of uptake increase. Moreover, during heating in a non-inverted plate, the cells are heated while the solution of the free or encapsulated drug inside each well remains at RT. This is also indicated by the relatively low average increase in uptake of the heated encapsulated Dox treatment group, $29\% \pm 6\%$, compared to an inverted plate, $71\% \pm 10\%$, Figure 5.18(a).

At the same exposure time of 3 min to heating without FUS in an inverted plate, the uptake values of encapsulated Dox and free Dox into MCF7 were $96\% \pm 10\%$ and $379\% \pm 18\%$, respectively. The viability values following 3 min heating without FUS of an inverted plate were $85\% \pm 5\%$ with carrier and $78\% \pm 7\%$ without carrier, Figure 5.19(a). Doubling of the heating exposure time to 6 min without FUS resulted in a factor of 1.83 increase in the uptake of the encapsulated Dox, $176\% \pm 19\%$, and 1.54 in the uptake of the free Dox, $585\% \pm 20\%$, according to Figure 5.18(b). Nevertheless, the viability of MCF7 cells following the longer exposure time of 6 min significantly decreased by a factor of 1.63 with carrier and 1.81 without carrier to values of $52\% \pm 3\%$ with carrier and $43\% \pm 4\%$ without the carrier, Figure 5.19(b).

The uptake of encapsulated and free Dox into A375m cells as a result of 3 min heating without FUS was $142\% \pm 12\%$ and $396\% \pm 9\%$, respectively, Figure 5.18(c). As presented in Figure 5.20 the average viability, excluding plate 1, of A375m at the same exposure time is $80\% \pm 5\%$ with carrier and $68\% \pm 8\%$ without carrier.

According to the overall results of uptake and viability studies, the optimal duration for heating cells to achieve significant uptake increase yet maintain low viability damage, is 3 min. Moreover, heating for 2 min at exactly 43°C (or if the temperature is $42.5 - 43^{\circ}\text{C}$, for up to 4 min) is described in the literature as 'the optimal thermal dose' for cancer therapy (Saparfto and Dewey, 1984). In view of that, the FUS induced heating exposure time was set to 3 min, and consequently in the validation setup without FUS as well. In both arrangements the cells were subjected to a rapid temperature rise followed by sustained moderate heat treatment. Whereas the duration of the initial temperature rise in the heating without FUS was decided in real-time due to thermocouple monitoring, in the FUS induced heating, a predefined power and duration must be applied.

In the search for the optimal FUS induced heating parameters, several power levels were applied for various durations. The following initial powers were tested in A375m cells for their potential of drug uptake increase: 30 Wa for 30 s (900 J); 30 Wa for 20 s (600 J); 20 Wa for 45 s (900 J); and 15 Wa for 60 s (900 J). From the uptake values presented in Figure 5.22, while there were some effects on the free Dox uptake at all the power levels, only at the highest power of 30 Wa for 30 s (900 J) was there an increase in the uptake of the encapsulated Dox. Moreover, the length of the initial continuous sonication has a major impact on the uptake of the free and especially the encapsulated Dox in MCF7 cells, as can be seen from Figure 5.21. A 10 s reduction in the initial sonication duration resulted in insufficient heating to produce an increase of the Dox uptake into MCF7 cells.

According to Figure 5.23 there is no major impact on the viability of MCF7 cells, $101\% \pm 7\%$ with and $96\% \pm 7\%$ without carrier, due to FUS induced heating at the maximum applied power level of continuous 30 Wa for 30 s followed by pulsed 30 Wa sonication for 180 s, 0.5 s on 3 s off. After sonication at the same power, A375m cells had shown no substantial viable signals, $3\% \pm 0.42\%$ with and $3\% \pm 0.4\%$ without carrier, Figure 5.24(a). Furthermore, even at lower power levels there was no significant improvement in the viability of A375m cells, Figure 5.24(b,c). In general, lack of viable signals indicates complete cell death in the measured area. As a result of cell death in a monolayer of cells, the cells detach from the base surface and float in the surrounding media. Yet, in the case discussed above, where the cells have not shown any viable signal due to FUS induced heating, there was no cell detachment, Figure 5.25.

As can be seen in the viability studies without FUS, Figure 5.20, there is a great variation between the different plates that undergo the same 3 min heating process. It can be seen that in plate 1 the amount of damage to the cells is significantly higher, 78%, than in the average of all the other plates, 32%. The fact that this phenomenon occurred occasionally in the heating without FUS, as well as in the FUS induced heating, suggests that it is related to the heating process, with some threshold dependence, rather than to any excess US that might propagate during the FUS induced heating process. Consequently, a suggested explanation of this phenomenon might be heat-induced arrest in the metaphase of the cell cycle or disability to satisfy the spindle assembly checkpoint (Rieder and Maiato, 2004) which will not necessary lead to cell death (Erenpreisa et al. 2000; Erenpreisa and Cragg, 2001).

Since the 1960s wide research has been carried out on the topic of thermal effects on cancer cells *in vitro* (Levine and Robbins, 1976). These studies indicate that a temperature rise in cultured cells results in manipulation of their mitotic cycle (Abu-absi and Srienc, 2002). Most

of the phases in the mitotic cycle respond to thermal changes similarly to other biochemical reactions, in which there is an increase in the chemical reactivity until a certain optimal temperature is reached, which is then followed by a decrease due to denaturation of the proteins involved in the process (Sisken et al., 1965). Although MCF7 cells are known to be relatively more resistant to hyperthermia (Lee et al., 1994) than other cell lines, the large variance between the viability of MCF7 and A375m cells emphasizes once more the diverse impact of heating on different cell lines (Cavaliere et al., 1967; Michalakis et al., 2005).

As can be seen throughout all the viability studies, the presence of Ca-1709 does not influence the viability of cells, Figure 5.19 and Figure 5.23, and at times even appears to contribute to the total cell viability, Figure 5.20. The slight increase of viability in the presence of Ca-1709 may be due to the CDs ability to stimulate the dehydrogenase cell activity (Al-Omar et al., 1999). These results indicate that the nanocarrier Ca-1709 has no cytotoxicity at applied concentrations of 500 μM .

In both of the heating arrangements, with and without FUS, a significant increase in the uptake of encapsulated drugs was observed. This rise in the amount of Dox present within the cells because of heating indicates two possible mechanisms. The first is release from the encapsulation due to the heat sensitivity of the carriers, and the second is that the encapsulated drug penetrates as it is into the cells due to heat-enhanced membrane permeability. The latter explains the rise in the uptake of the free Dox. In heating without FUS the rise in uptake of free Dox is significantly higher than in the FUS induced heating, e.g. a factor of 2.5 in MCF7 cells, Figure 5.18a and Figure 5.21a. Opposing this, the rise in uptake of encapsulated drug is similar, i.e. A375m cells, Figure 5.22, or higher i.e. 1.8x in MCF7 cells, Figure 5.18a and Figure 5.21a, with FUS induced heating rather than heating without FUS. These results suggest that the possible mechanisms of uptake increase in heating without FUS are heat-induced membrane permeability, as indicated by the free Dox uptake values, with potential drug release, whereas in the FUS induced heating, it is mainly attributed to the first mechanism where the drug is released from the encapsulation due to the temperature increase, indicated by the higher encapsulated Dox uptake results.

5.5 Conclusions

In this chapter the *in-vitro* applications of all the ExAblate arrangements were presented. The potential of Sonovue as a membrane permeability enhancing tool was confirmed in both UF and CBS sonoporation arrangements. The significant increase in uptake in both cell lines alongside relatively high viability results has confirmed that the membrane

rupture is a reversible and non-permanent process (Böhmer, M.R. et al. 2009), which does not lead directly to cell necrosis. In addition, moderate heating was shown to be highly beneficial in drug release and cellular uptake increase of free and encapsulated drug. Possible *in-vivo* implementation of the achieved results is outlined in Chapter 6.

5.6 References

Abu-absi, N.R. and Srienc, F. (2002) Instantaneous evaluation of mammalian cell culture growth rates through analysis of the mitotic index. *J Biotechnol*, 95, pp.63-84.

Al-Omar, A. et al. (1999) Complexation study and anticellular activity enhancement by doxorubicin-CD complexes on a multidrug-resistant adenocarcinoma cell line. *Bioorg Med Chem Lett*, 9, pp.1115- 20.

Ashush, H. (2000) Apoptosis induction of human myeloid leukemic cells by ultrasound exposure. *Cancer Res*, 60, pp.1014- 20.

Baker, K.G. et al. (2001) A review of therapeutic ultrasound: biophysical effects. *Phys Ther*, 81(7), pp.1351- 8.

Bekeredjian, R. et al. (2005) Use of ultrasound contrast agents for gene or drug delivery in cardiovascular medicine. *J Am Coll Cardiol*, 45(3), pp.329-35.

Böhmer, M.R. et al. (2009) Ultrasound triggered image-guided drug delivery. *Euro J Radiol*, 70, pp.242- 53.

Bokor, D. et al. (2001) Clinical safety of SonoVue™, a new contrast agent for ultrasound imaging, in healthy volunteers and in patients with chronic obstructive pulmonary disease. *Investigative Radiology*, 36(2), pp.104- 9.

Brennen, C. (1995) *Cavitation and Bubble Dynamics*. UK: Oxford University Press.

Byl, N.N. (1995) The Use of Ultrasound as an enhancer for transcutaneous drug delivery: phonophoresis. *Phys Ther*, 75 (6), pp.539- 53.

Cavaliere, R. et al. (1967) Selective heat sensitivity of cancer cells. *Cancer*, 20(9), pp.1351- 81.

Chen, L. et al. (2010) MR-guided focused ultrasound: enhancement of intratumoral uptake of [3H]-docetaxel in vivo. *Phys Med Biol*, 55, pp.7399- 410.

Cho, C-W. et al. (2002) Ultrasound-induced mild hyperthermia as a novel approach to increase drug uptake in brain microvessel endothelial cells. *Pharmaceut Res*, 19(8), pp.1123- 9.

Cole S.P.C. (1986) Rapid chemosensitivity testing of human lung tumor cells using the MTT assay. *Cancer Chemother Pharmacol*, 17, pp.259- 63.

Conti, L. et al. (2010) Effects induced in cells by ultrasound revealed by ATR-FTIR spectroscopy. *Vib Spectrosc*, 52, pp.79- 84.

- Duck, F.A. et al.** (1998) *Ultrasound in medicine*. Great Britain: Institute of Physics Publishing.
- Eisenbrey, J.R. et al.** (2009) Ultrasound triggered cell death in vitro with doxorubicin loaded poly lactic-acid contrast agents. *Ultrasonics*, 49, pp.628–633.
- Erenpreisa, J. and Cragg, M.S.** (2001) Mitotic death: a mechanism of survival? a review. *Cancer Cell Int*, 1(1), pp.1-7.
- Erenpreisa, J. et al.** (2000) Arrest in metaphase and anatomy of mitotic catastrophe: mild heat shock in two human osteosarcoma cell lines. *Cell Biol Int*, 24(2), pp.61–70.
- Feril Jr., L.B. et al.** (2002) Enhancement of hyperthermia-induced apoptosis by non-thermal effects of ultrasound. *Cancer Lett*, 178, pp.63- 70.
- Feril Jr., L.B. et al.** (2010) Hypotonia-induced cell swelling enhances ultrasound-induced mechanical damage to cancer cells. *J Med Ultrasonics*, 37, pp.3-8.
- Ferrara, K.W.** (2008) Driving delivery vehicles with ultrasound. *Adv Drug Deliver Rev*, 60, pp.1097- 102.
- Frenkel, V.** (2008) Ultrasound mediated delivery of drugs and genes to solid tumors. *Adv Drug Deliver Rev*, 60, pp.1193- 208.
- Gerlier D. and Thomasset N.** (1986) Use of MTT colorimetric assay to measure cell activation. *J Immunol Methods*, 94, pp.57-63.
- Greis, C.** (2004) Technology overview: SonoVue. *Eur Radiol Suppl*, 14(8), pp.11-15.
- Guzman, H.R. et al.** (2001) Ultrasound-mediated disruption of cell membranes. I. quantification of molecular uptake and cell viability. *J Acoust Soc Am*, 110(1), pp.588-596.
- Hernot, S. and Klibanov, A.L.** (2008) Microbubbles in ultrasound-triggered drug and gene delivery. *Adv Drug Deliver Rev*, 60, pp.1153- 66.
- Hundt, W. et al.** (2009) The effect of high intensity focused ultrasound on luciferase activity on two tumor cell lines in vitro, under the control of a CMV promoter. *Ultrasonics*, 49, pp.312- 8.
- Hung, SH. et al.** (2011) A simple method for quantifying ultrasound-triggered microbubble destruction. *Ultrasound Med Biol*, 37(6), pp.949-57.
- Husseini, G.A. and Pitt, W.G.** (2008) Micelles and nanoparticles for ultrasonic drug and gene delivery. *Adv Drug Deliver Rev*, 60, pp.1137- 52.
- Karshafian, R. et al.** (2003) Sonoporation by ultrasound-activated microbubble contrast agents: effect of acoustic exposure parameters on cell membrane permeability and cell viability. *Ultrasound in Med Biol*, 35(5), pp.847- 60.
- Kost, J. et al.** (1989) Ultrasound-enhanced polymer degradation and release of incorporated substances. *Proc Natl Acad Sci*, 86, pp. 7663- 66.

- Lee, Y.J. et al.** (1994) Mechanisms of mild hyperthermia-induced cytotoxicity in human prostatic carcinoma cells: perturbation of cell cycle progression and DNA fragmentation. *J therm Biol*, 19(5), pp.305-13.
- Leighton, T. G.** (1994) *The acoustic bubble*. Great Britain: Academic Press.
- Levine, E.M. and Robbins, E.B.** (1976) Differential temperature sensitivity of normal and cancer cells in culture. *J Cell Physiol*, 76, pp.373- 80.
- Mayer, C.R. et al.** (2008) Ultrasound targeted microbubble destruction for drug and gene delivery. *Expert Opin Drug Deliv*, 5(10),pp.1121-38.
- Meer, S.M. et al.** (2004) The resonance frequency of SonoVue™ as observed by high-speed optical imaging. IEEE Ultrason Ferr Joint 50th Anniversary Conference, pp.343- 5.
- Michalakos, J. et al.** (2005) Micromolar taxol, with or without hyperthermia, induces mitotic catastrophe and cell necrosis in HeLa cells. *Cancer Chemother Pharmacol*, 56, pp.615- 22.
- Mitragotri, S.** (2005) Healing sound: the use of ultrasound in drug delivery and other therapeutic applications. *Nature Reviews Drug Discovery*, 4, pp.255-60.
- Moonen, C. et al.** (2010) Ultrasound-triggered image-guided therapy. *MedicaMundi*, 54(1), pp.40- 5.
- Pitt, W.G. et al.** (2004) Ultrasonic drug delivery- a general review. *Expert Opin Drug Deliv*, 1(1), pp.37-56.
- Polat, B.E.** (2011) Ultrasound-mediated transdermal drug delivery: mechanisms, scope, and emerging trends. *J Control Release*, 152, pp.330- 48.
- Rieder, C.L. and Maiato, H.** (2004) Stuck in division or passing through: what happens when cells cannot satisfy the spindle assembly checkpoint. *Developmental Cell*, 7, pp.637- 51.
- Saparfto, S.A. and Dewey, W.C.** (1984) Thermal dose determination in cancer therapy. *Int J Radiation Oncology Biol Phys*, 10 (6), pp.787-800.
- Schroeder, A. et al.** (2009) Ultrasound triggered release of cisplatin from liposomes in murine tumors. *J Control Release*, 137 (1), pp.63- 8.
- Sisken, J.E. et al.** (1965) Effects of temperature on the kinetics of the mitotic cycle of mammalian cells in culture. *Exp Cell Res*, 39, pp.103- 16.
- Smith P.K. et al.** (1985) Measurement of protein using bicinchoninic acid. *Anal Biochem*, 19, pp.76-85.
- Stewart, V.R. and Sidhu, P.S.** (2006) New directions in ultrasound: microbubble contrast. *Brit J Radiol*, 79, pp.188- 94.
- Sundaram, J. et al.** (2003) An experimental and theoretical Analysis of ultrasound-induced permeabilization of cell membranes. *Biophys J*, 84, pp.3087- 101.

- Tachibana, K. and Tachibana, S.** (2001) The use of ultrasound for drug delivery. *Echocardiography*, 18(4), pp.323- 8.
- Ter Haar, G.** (1995) Ultrasound focal beam surgery. *Ultrasound Med Biol*, 21 (9), pp.1089- 100.
- Tinkov, S. et al.** (2009) Characterization of ultrasound-mediated destruction of drug-loaded microbubbles using an improved in vitro model. *Appl Acoust*, 70, pp.1323- 9.
- Tinkov, S. et al.** (2010) New doxorubicin-loaded phospholipid microbubbles for targeted tumor therapy: Part I- Formulation development and in-vitro characterization. *J Control Release*, 143, pp.143- 50.
- Twentyman P.R. and Luscombe M.** (1987) A study of some variables in a tetrazolium dye (MTT) based assay for cell growth and chemosensitivity. *Br J Cancer*, 56, pp.279-285.
- Wang, P. et al.** (2010) Mitochondrial damage in nasopharyngeal carcinoma cells induced by ultrasound radiation in the presence of hypocrellin. *B J Ultrasound Med*, 29, pp.43- 50.
- Wu, J. and Nyborg, W.L.** (2008) Ultrasound, cavitation bubbles and their interaction with cells. *Adv Drug Deliver Rev*, 60, pp.1103- 16.
- Yudina, A. et al.** (2010) Evaluation of the temporal window for drug delivery following ultrasound-mediated membrane permeability enhancement. *Mol Imaging Biol*, 13, pp.239- 49.
- Yudina, A. et al.** (2012) In vivo temperature controlled ultrasound-mediated intracellular delivery of cell-impermeable compounds. *J Control Release*, doi:10.1016/j.jconrel.2012.04.018.

CHAPTER 6 CONCLUSIONS AND IMPLEMENTATION OF RESEARCH: TOWARDS CLINICAL TRIALS

6.1 Introduction

This is the concluding chapter of the thesis and includes a summary of the key results achieved in the three main research areas presented in Chapters 3, 4 and 5, respectively. Chapter 3 focused on the creation through chemistry and the chemical investigation of a CD-based carrier and its complexation with Dox, Chapter 4 presented the design and evaluation of *in-vitro* research environments based on a clinical MRgFUS system for investigation of the mechanical and thermal effects associated with US application, and Chapter 5 discussed the outcomes of the *in-vitro* application of the investigated drug, Dox, both in free and encapsulated forms, in the various FUS application arrangements. Here the final outcomes of each chapter as well as the overall conclusions will be discussed.

In addition, this chapter describes the early stages in translation of the achieved knowledge of USmTDD mechanisms from the *in-vitro* studies in the *in-vivo* platform. Consequently, the second part of this chapter will discuss the current trends in research of USmTDD *in vivo* and present some preliminary *ex-vivo* results as part of the preparation for the *in-vivo* stage.

6.2 Conclusions of Research

This thesis has described the synthesis and evaluation of a novel TDD drug carrier and its implementation *in vitro* in specially designed and constructed *in-vitro* arrangements for investigation of mechanical and thermal effects of USmTDD, as well as in an additional heating arrangement, as validation of FUS induced heating.

The novel drug carrier employed in this work is based on the CD technology. It consists of a truncated-cone-shaped sugar molecule, γ CD, which is covalently bonded to an amino acid derivative with a naphthalene moiety. The synthesis of the carrier as described in Chapter 3, was done by a two step reaction where the first step was coupling of γ CD with a Boc-naphthalic-amino acid, and the second step was the removal of the N-protecting Boc group from the wanted yield- a monosubstituted γ CD. The reaction was monitored by TLC and HPLC to confirm the generation of the desired compound. The final yield, in the form of small white

crystals, was 51%. The created CD-based carrier was spectroscopically evaluated by ^1H - and ^{13}C -NMR, which provided evidence supporting the intended structure.

The designed carrier was aimed to be a potentially successful drug vehicle for delivery of Dox via a complexation reaction. The behaviour of the cytotoxic agent, Dox, in different solutions and concentration was studied by ^1H -NMR and DOSY measurements. Under the applied conditions, Dox has exhibited the well-studied phenomenon of self-aggregation, also referred to as “stacking”, with dependence on the concentrations tested.

The examination of Dox in the complexation reaction with the carrier was investigated via fluorescence and NMR. According to the fluorescence studies, where a significant decrease in the Dox signal was recorded with dependence on the carrier concentration, K_{binding} of the created complex was approximately $62,000 \text{ M}^{-1}$. This value is significantly higher than K_{binding} of Dox to the unmodified γCD (Anand et al., 2012). This could be attributed to the formation of π - π^* interactions between the Dox and the naphthalene moiety of the carrier. This was also evident in 3D NMR studies conducted, where a correlation was suggested between the protons of the Dox's aromatic rings and those of the naphthalene.

This data, together with the other 3D and 2D NMR studies, have suggested a possible encapsulation conformation presented in Figure 3.29. The overall chemical analysis of the carrier and Dox, on their own as well as in a complex, aid in understanding of their behaviour in various media, as well as validating their chemical structures and, most importantly, their roles in complex formation.

To examine the potential of the CD-based drug carrier in delivering Dox into cancer cells via USmTDD, several *in-vitro* arrangements were constructed. As the main goal in the *in-vitro* studies was to evaluate individually the mechanical and thermal effects of FUS during USmTDD, two different types of FUS application arrangements were designed.

The first, dealing with mechanical effect on the cells, utilised low power FUS in the presence of MBs to generate controlled stable cavitation. This was done in two arrangements allowing different frequencies and sonication patterns, including multi-focal ones.

The second US mediated effect, i.e. *in-situ* temperature rise, was studied in an arrangement including tissue mimicking phantoms in specially crafted shapes, to provide mild heating in order to produce hyperthermia in proximity to the cells. To validate the impact of FUS induced heating on the cell monolayer; an additional arrangement was designed, generating heating without FUS. All the USmTDD arrangements were constructed on clinical MRgFUS systems. The main arrangements for investigation of USmTDD for both its mechanical and thermal effect were constructed on the ExAblate 2000 system (InSightec, Haifa, Israel),

referred to as the UF system. An additional arrangement was created using the ExAblate 2100 system (InSightec, Haifa, Israel), for application of multi-focal sonication patterns to the cells and is referred to as the CBS arrangement.

To validate the accuracy and proper functioning of all the discussed arrangements, thorough thermal and acoustical evaluation were conducted and reported in Chapter 4. According to the thermal evaluation of the sonoporation experiment by both thermal camera and thermocouples, it was confirmed that there is no significant temperature rise as a result of sonication at the *in-vitro* applied energies of 10 and 50 J. This confirms that during sonication to achieve sonoporation, the mechanical effects of US were observed rather than thermal effects.

The performed acoustic measurements verified that the base and seal parts of the tested 96-well plate produce minimal absorption of acoustic power and are thus suitable for USmTDD research. Moreover, the acoustic evaluation also defined the optimal shape, size and height of the focal spot for *in-vitro* application. This resulted in the following parameters as the optimum sonication pattern: single focus with an average size of about 2 mm with $Tr = 50\%$ at $FD = 97$ mm at applied frequency $f = 0.95$ MHz. The sonications were performed in an automated manner via a prewritten computer script.

In addition to the single spot sonication, a multi-focal pattern was examined for simultaneous sonication at several locations. Using the ExAblate 2100 CBS transducer, it was possible to sonicate simultaneously 16 different wells in the same plate. According to the acoustic evaluation, the multi-focal sonication pattern was highly efficient and accurate, with both values over 85% (Gourevich et al., 2012).

Alongside the sonoporation arrangements, a FUS induced heating arrangement was constructed, together with a control experiment without FUS. Both were evaluated for application of temperature-induced TDD. MRI thermometry as well as thermocouples, was used to define the optimal sonication pattern for application of FUS induced heating *in-vitro*. The established heating protocol for FUS induced heating *in vitro* consists of a continuous sonication to produce a rapid temperature rise, followed by 3 min stable heating in a pulsed mode of 0.5 s on, 3 s off. In the experiment on heating without FUS, a similar heating pattern was applied where initially the plate was placed on a higher temperature heater (75°C) to achieve the rapid temperature rise, and then moved to stable heating for 3 min on a 50°C heater.

All of the above arrangements were utilised in *in-vitro* studies with the outcomes presented in Chapter 5. The mechanical effects of FUS application were evaluated in both the

UF and the CBS arrangements. According to the *in-vitro* studies performed on the UF sonoporation arrangement, in the presence of Sonovue MBs, the uptake of Dox into human cancer cells is increased by a factor up to 2.4, while the viability of the cells remained high, i.e. viability values were above 85% after 24 h recovery. Moreover, the membrane integrity test results were in line with the uptake values suggesting that the increased uptake of Dox is due to increased cell membrane permeability caused by the MBs.

In the CBS arrangement, the uptake of Dox was increased by a factor of up to 4 compared to the non-sonicated control. Yet greater cell damage, resulting in lower viability values, was observed in both cell lines. Comparing these results with those achieved in the UF sonoporation arrangement, it appears that the multi-focal sonication pattern has a greater impact on the uptake of Dox. This could be explained by the significantly lower total exposure time to Dox, i.e. 10 min in the UF and 10 s in the CBS experiments. This additional time following the sonication might mask the effect of the FUS on the cells.

The thermal effect of FUS was investigated using the UF system, and also validated with an experiment involving heating without FUS. Heating at what is described in the literature as 'the optimal thermal dose' for cancer therapy (Saparfto and Dewey, 1984), i.e. 2 - 4 min at about 43°C, resulted in an increase in the cellular uptake of Dox by a factor of 4 in both cell lines. Whereas previously, the viability studies were only slightly different between the two cancer cell lines, A375m and MCF7, in the FUS induced heating the viability values varied greatly between the two tested cell lines, where in the MCF7 cells they were over 85%, yet only about 33% in the A375m cells. A suggested explanation for this low viability signal might be heat-induced arrest in the metaphase of the cell cycle or inability to satisfy the spindle assembly checkpoint (Rieder and Maiato, 2004) which will not necessary lead to cell death (Erenpreisa et al. 2000; Erenpreisa and Cragg, 2001).

In addition to the described *in-vitro* investigation of increased Dox uptake by the mechanical and thermal effects of FUS, the ability of the designed carrier to encapsulate and release the Dox, *in vitro*, via the same mechanisms, was established.

According to the *in-vitro* evaluation of the complex, the carrier successfully encapsulated the Dox resulting in inhabitation of 80% of Dox penetration within the cancer cells. The tested release mechanisms using mechanical and thermal triggers, was found to be successful in achieving close to 100% release of Dox as compared to the control.

Via the sonoporation mechanism the uptake of encapsulated Dox in the presence of MBs was increased by a factor of 5.5, resulting in almost equivalent amounts of Dox penetrating the cells as in the free Dox control. A suggested mechanism for the cell uptake

increase is via penetration of the whole complex into the cells due to increased cell membrane permeability achieved by the MBs, followed by dissociation within the cell itself.

Thermal effects of FUS have resulted in increased factors of up to 9.6 in the uptake of the encapsulated Dox into the cells. This was validated using the heating without FUS arrangement, where an increase by a factor of 5.7 was recorded. These increases in the Dox uptake due to heating suggest two possible mechanisms. The first is the release from the encapsulation due to the heat sensitive feature of the carriers, while the second possible mechanism is that the encapsulated drug translocates across the cell membrane due to heat enhanced membrane permeability. Although the probability is that both of the described mechanisms act simultaneously, it can be postulated from the achieved results that the possible mechanisms of uptake increase in the heating treatment without FUS is due to the heat induced membrane permeability, as indicated by the free Dox uptake values, with potential drug release, whereas in FUS induced heating it is mainly attributed to the first mechanism where the drug is released from encapsulation, as indicated by the higher encapsulated Dox uptake results.

The carrier was verified to be non-toxic at the tested concentrations of 500 μ M, as confirmed by all the performed viability studies.

In conclusion, the presented arrangements for *in-vitro* investigation of USmTDD were proved to be successful in achieving the desired goals of a well monitored, reliable research environment with high repeatability, able to differentiate between the thermal and mechanical effects of FUS. In addition, the *in-vitro* results confirmed the designed nanocarrier as a promising drug delivery vehicle for USmTDD for controlled release by both temperature and cavitation.

While the fundamental objective behind this work was the establishment of a properly monitored sonication arrangement for *in-vitro* studies, the obvious development to the *in-vivo* stage and clinical trials was kept in mind. As previously explained, all of the arrangements were constructed on the ExAblate system - a commercially available, clinically approved device for MRgFUS. Although the translation from *in-vitro* work into *in-vivo* research is not straightforward, a good *in-vitro* background can contribute greatly to the success of *in-vivo* outcomes. Consequently, the work reported here provides a baseline for potential *in-vivo* TDD research using the ExAblate system, which can then lead to clinical applications.

6.3 USmTDD *In vivo*

Many research groups worldwide are currently examining the potential of USmTDD *in vivo*. As previously mentioned, two bioeffects can occur due to sonication of tissues: cavitation and increased temperature, which are related to the mechanical and thermal effects of US, respectively. Although generally these effects can happen simultaneously, and neither of them can be entirely eliminated in the application of FUS, proper tuning of the parameters can provide relatively well isolated effects. Even though, in the current *in-vivo* USmTDD research, both the mechanical (Rosenthal et al., 2004) and thermal (Grüll and Langereis, 2012) effects of US are under investigation, the latter are considered safer and more clinically applicable.

Although the application of cavitation-enhanced drug delivery *in vivo* is rather problematic due to rapid fluid conduction through the vascular system (Pitt et al., 2004), researchers have shown some promising results in tumour regression with a combination of drug delivery vehicles with MBs in the presence of US (Rapoport et al., 2009). Additional *in-vivo* research suggests that, via the mechanical effects of USmTDD *in vivo*, a reduction in neointima formation with significantly lower drug doses can be obtained (Phillips et al., 2012) or an increase in drug delivery via the BBB (Lewis et al., 2011). A possible combination of the mechanical effects of US and an *in-situ* temperature increase showed promising results *in vivo* in the intracellular delivery of cell-impermeable molecules (Yudina et al., 2012).

The possibility to achieve *in-situ* hyperthermia via application of FUS presents an improved mechanism over the conventional methods of heat generation in tissues. These include utilization of water baths- which provide only superficial heating; microwaves emitting electromagnetic radiation; and invasive catheters. Application of FUS induced heating is a non-invasive method, with deep tissue penetration and a good safety profile (Staruch et al., 2011). Currently, the main research platform for US induced thermal effects is thermally triggered drug release from liposomes, especially under MRI guidance (Grüll and Langereis, 2012). US induced temperature increases have produced a significant increase in the drug delivery of anticancer agents into tumour sites in various *in-vivo* models such as mice (Chilkoti et al., 2002; Chen et al., 2010) and rabbits (Ranjan et al., 2012).

All types of *in-vivo* USmTDD require an imaging modality (Vaezy and Zderic et al., 2009). A variety of possible imaging techniques is available to monitor the application of US *in vivo*. At times, the delivery mechanism suggests a certain imaging method, e.g. the use of ultrasonic contrast agents as membrane permeability enhancers (Rapoport et al., 2009) or conjugation of MRI contrast agents in the drug delivery vehicle (Deckers et al., 2008) can lead to the choice of US or MRI as the preferred imaging modality. There are several advantages for

using MRI as the imaging techniques in USmTDD *in vivo*: not only does it offer high resolution image guidance in TDD, but also real time thermal mapping (Moonen et al., 2010).

6.3.1 Aim and Objectives

As a part of the final goal to reach clinical trials, this section outlines a possible *in-vivo* study protocol as an outcome of the work achieved and presented in this thesis.

As a first stage towards *in-vivo* experiments, several *ex-vivo* experiments were conducted towards the end of the work reported here. The phrase ‘*ex-vivo*’ in this context refers to deceased animals of the same species as planned to be used *in vivo*. The first stage in the proposed *in-vivo* studies will focus on the feasibility of FUS as a drug release stimulus *in situ*. In terms of protocol, the *in-vivo* studies, and hence the preliminary *ex-vivo* studies will be based on healthy mice injected with encapsulated or free drugs intravenously, that will undergo a set of sonications under MRI guidance. The target sonication location is the quadriceps muscle. This is an external tissue which makes accessibility easier. An additional benefit is that the quadriceps muscles on the second leg can be used as an intrinsic control in the same animal, which significantly reduces the number of sacrificed animals.

In *in-vivo* work, following the experimental protocol as described above, the aim will be to show the *in-situ* absorption of drugs released from the carriers. This could be achieved by a measurement of fluorescence intensity, similarly to the *in-vitro* work, from the sonicated muscle, in comparison with the non-sonicated control.

6.3.2 Materials and Methods

Table 6.1- Materials for *ex-vivo* work

Material	Manufacturer	Place of Origin	Notes
1.5 Tesla MRI system	General Electric	USA	Model: Signa HDX
ExAblate One	InSightec Ltd.	Israel	0.95-1.35 MHz
Single Channel Surface Coil	InSightec Ltd.	Israel	5 GP- Breast Coil
<i>Ex-Vivo</i> Tissue	Science in Action Ltd.	Israel	Deceased Mice
DQA Phantom	ATS Laboratories	USA	
Gel Pad	InSightec Ltd.	Israel	
Veet® Hair Removal Cream	Reckitt Benckiser	France	

All the *ex-vivo* studies were performed in Sheba Medical Centre, Israel. For the *ex-vivo* experiments, deceased mice were brought to Sheba after being sacrificed in Science in Action Ltd. (Building 3, Weizmann Science Park, Israel). Transportation took 1 h from the time of death. Upon arrival, Veet® hair removal cream was placed on the lower part of each mouse,

with a focus on the quadriceps muscles, as shown in Figure 6.1. Each mouse was covered with the hair removal cream twice, for 10 min at a time, to achieve maximal depilation.



Figure 6.1- Deceased mice (a) on their arrival, (b) covered with Veet shaving cream, and (c) after the second fur removal

The experimental arrangement consisted of a gel pad, 5 GP breast coil and a plastic ring, all placed on top of the FUS source in the ExAblate UF table. The coil was wrapped in cling film to keep it dry and sterile, and placed on top of the gel pad. Inside the coil, a round plastic circle was placed to contain the water needed for sonication. The arrangement is shown in Figure 6.2.

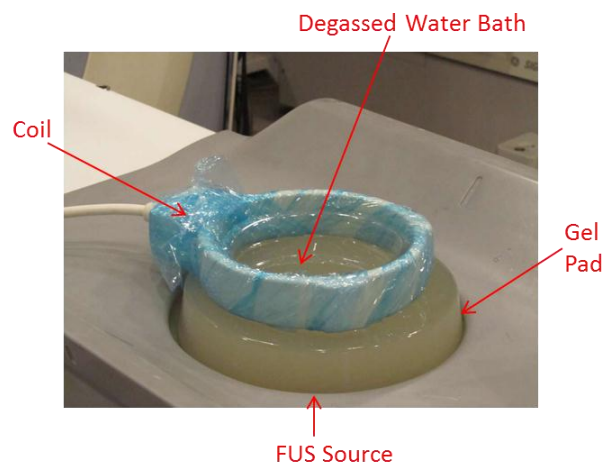


Figure 6.2- Arrangement for FUS application *ex-vivo* and *in-vivo*

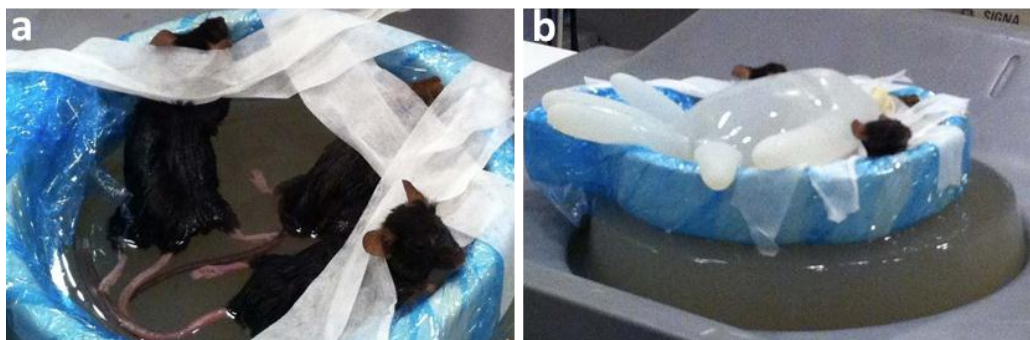


Figure 6.3- Positioning of mice (a) inside breast coil (b) covered with a glove full of warm water

The shaved mice were wiped of any excess fur and placed inside the ring. Figure 6.3 presents the placement of the mice in the experiment, such that their upper body parts are on top of the coil, for breathing *in vivo*, and the lower part on the gel pad soaked with water for US exposure. The heads and front feet of the mice were held by medical tape to the coil. A glove filled with warm water was placed on top of the mice to secure their location and, in future when dealing with live mice, to prevent hypothermia.

To create and evaluate a combined sonication mode which includes both continuous and pulsed sonications, additional experiments in a DQA phantom were performed.

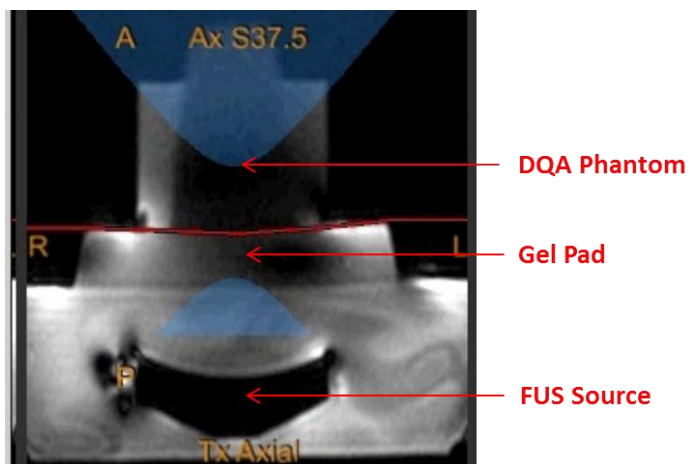


Figure 6.4- DQA phantom arrangement

Figure 6.4 presents the DQA phantom arrangement for sonication mode validation, consisting of a DQA phantom placed inside the 5GP breast coil, on top of the gel pad in the same manner as the *ex-vivo* tissues.

6.3.3 Results

6.3.3.1 Magnetic Resonance Imaging

The first set of MRI parameters was based on those of Chen et al. (2010) with adjustment to local experimental arrangements. A GE 3D localizer sequence was used for quick localization. The coronal images were obtained (T2-weighted, FSE) with the following parameters: TR/TE = 3180/96.3 ms; bandwidth: 10.4 kHz; FOV = 20 × 20 cm; matrix: 384 × 384; Number of Excitations (NEX): 4; slice thickness: 2.0 mm/1.0 sp; number of slices: 8; frequency direction: SI; and spatial resolution: 0.52 mm. The total duration of the scan was 5 min 37 s. The sagittal and axial images were taken with similar parameters, except the following: FOV = 14 × 14 cm; number of slices: 24, which prolonged the scanning time to 17 min 13 s for sagittal, and 20 min 6 s for axial.

Since the sonication planning was done solely on the coronal images, and due to the long axial and sagittal scanning times, in further *ex-vivo* and *in-vivo* experiments it was decided to perform only the MRI coronal imaging and ExAblate calibration scans. Additional optimization of the imaging parameters was performed to achieve minimal scanning time yet without major impact on the image quality. Therefore, NEX was reduced to two instead of four, which shortened the coronal scanning time to 2 min 52 s.

6.3.3.2 Sonication

The first sonications were done to define the spot accuracy, feasibility of hitting the targeted area and to have the maximal optional temperature increase for a given applied power. Figure 6.5 depicts the sonication location of continuous and pulsed sonications. The temperature rise following these sonications is presented in Figure 6.6.

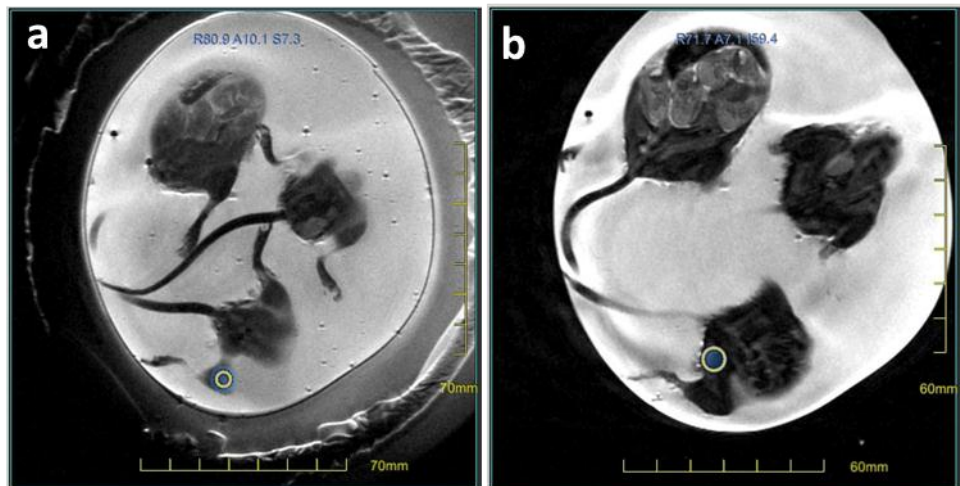


Figure 6.5- Spot location of the (a) continuous and (b) pulsed sonication

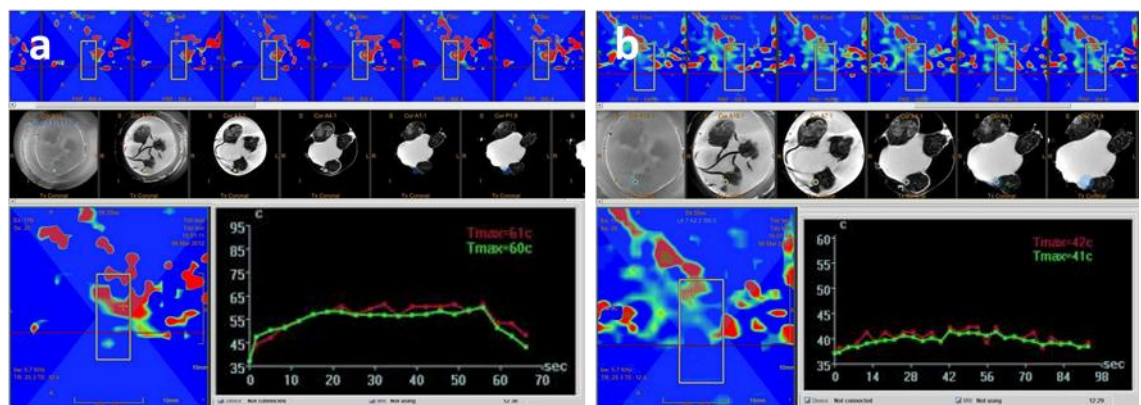


Figure 6.6- Sonication at 4 Wa in (a) continuous and (b) pulsed sonication

Figure 6.6 presents the PRF thermal measurements at the sonication locations presented in Figure 6.5. The sonication parameters were 4 Wa for 60 s continuous sonication,

and 4 Wa for 60 s, 0.5 s on, 2.5 s off in a pulsed mode. It is important to notice that all the red areas outside the yellow rectangle in Figure 6.6 are artefacts and should be ignored.

The creation and evaluation of a combined sonication pattern, similar to the one explained in Section 4.3.1.1, was initially performed in a DQA phantom, in the arrangement described in Figure 6.4. The final combined sonication mode for hyperthermia *in vivo* consists of 10 s continuous sonication and 45 s pulsed (0.5 s on, 2.5 s off) as schematically presented in Figure 4.33.

As part of the sonication investigation, an additional heating pattern was tested: the annular focus. Using beam manipulation, the same power was applied in an annular focus, presented in Chapter 4, and the temperature was recorded via PRF measurement. Figure 6.7 and Figure 6.8 depict the PRF thermometry of the normal and annular foci in a DQA phantom due to sonication in the described hyperthermia mode with powers of 4 and 16 Wa, respectively.

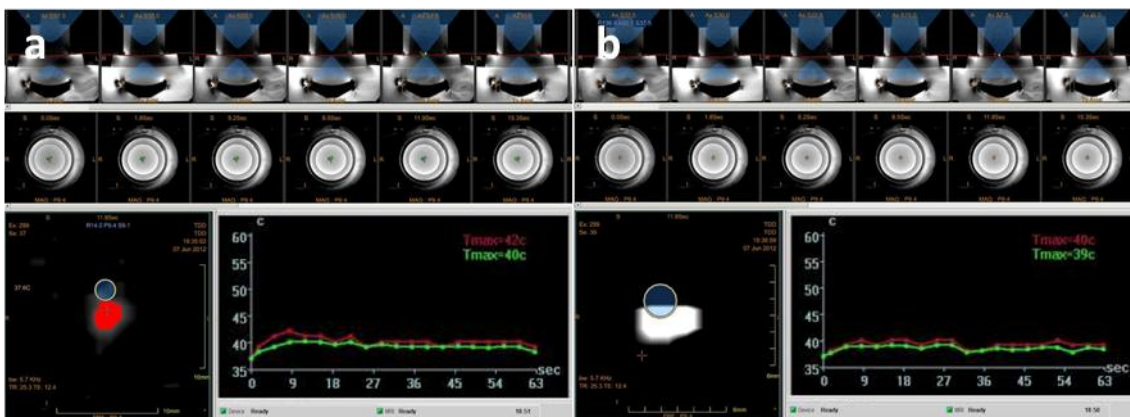


Figure 6.7- PRF thermometry measurement at the (a) normal and (b) annular foci in DQA phantom at a power of 4 Wa

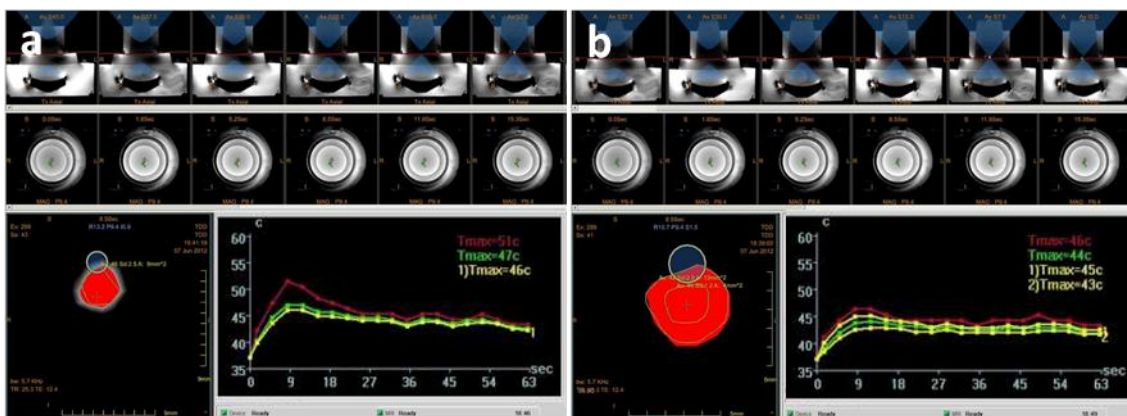


Figure 6.8- PRF thermometry measurement at the (a) normal and (b) annular foci in DQA phantom at a power of 16 Wa

The testing of the previously described hyperthermia sonication mode was performed in *ex-vivo* mice tissues to examine its ability to cause temperature increase *in situ*.

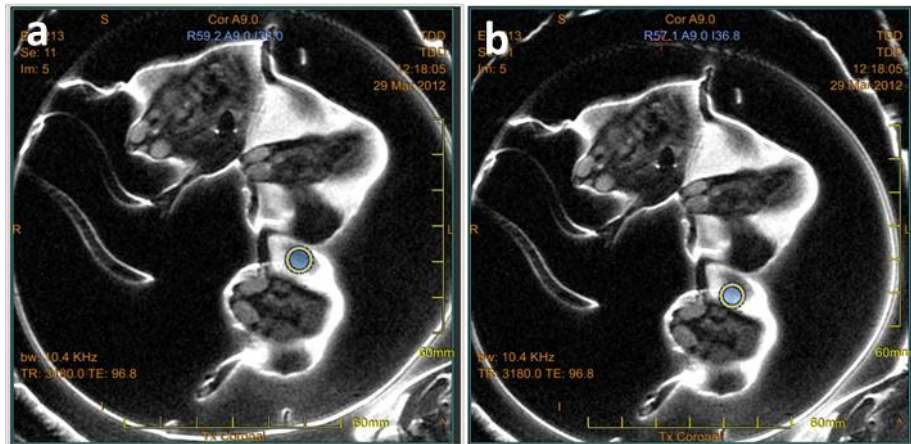


Figure 6.9- Spot location of the (a) normal and (b) annular foci

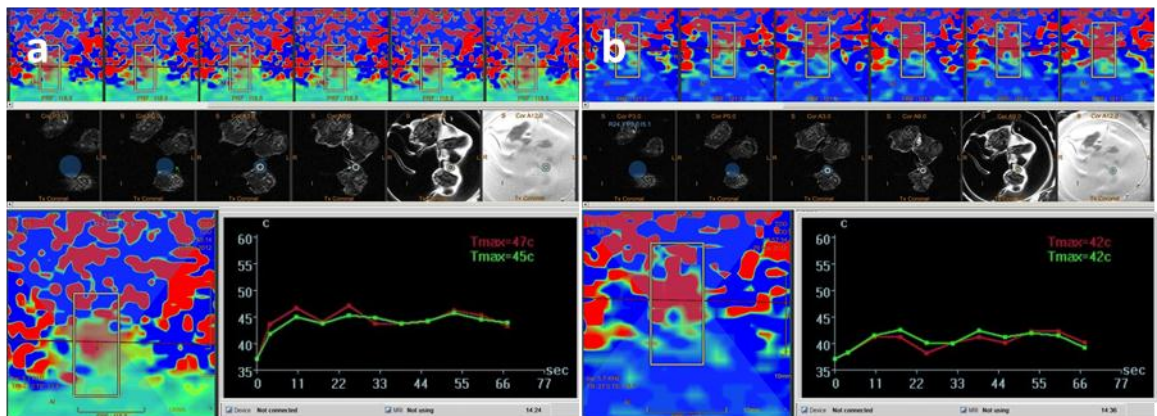


Figure 6.10- PRF thermometry measurement at the (a) nominal and (b) annular shaped spots in *ex-vivo* tissue

Figure 6.10 depicts the PRF thermometry at the sonication location presented in Figure 6.9, for the normal and annular foci. The sonication parameters were 4 Wa for 10 s continuous sonication immediately followed by 4 Wa pulsed sonication for 45 s, 2.5 s off, 0.5 s on. As before, all the red areas outside the yellow rectangle are artefacts and should be ignored.

6.3.4 Discussion and Conclusions

The *ex-vivo* model provided many important insights such as creation of a tailor-made arrangement to the species in use, the handling of the animals, and proper positioning in the experimental arrangements, definition of optimal imaging parameters, establishment of optimized sonication modes and patterns, and examination of the feasibility of conducting work *in vivo* according to the anaesthesia time window that will apply.

The quality of the MR imaging is crucial in MRgFUS, especially when dealing with small animals. Moreover, in this work it is extremely important, since the focus location is in the quadriceps muscle, which is almost impossible to detect on the MRI. The width of the entire leg is between 7 to 9 mm. Due to the time frame dictated by the anaesthesia, the scans need to be as short as possible, yet their resolution should remain high in order to accurately locate the sonication spot. Optimization of scanning parameters is presented in Section 6.3.3.1. From these results, the optimized imaging parameters total time frame is adjusted to as little as 34 s.

As an initial step for testing the protocols for both continuous and pulsed sonications, Figure 6.6, were examined for their ability to create a temperature increase in the quadriceps muscle. As can be seen in Figure 6.6(a) the increase due to the 4 Wa continuous sonication is about 24°C. Since the aim is an increase of 4°C to 7°C, there is a need to lower the power by a factor of four to six. This can be achieved via a pulsed mode similar to the one utilized in the *in-vitro* studies. In the application of FUS *in vitro*, the accumulating heat in the plastic was greater than in the *ex-vivo* tissue, hence a longer cooling interval between the sonications was applied (0.5 s on, 2.5 s off instead of 0.5 s on, 3 s off). Sonication at the same power of 4 Wa, in pulsed mode is presented in Figure 6.6(b).

Although the temperature increase was significantly lower, the long heating time prior to the stable state needed to be shortened. This could be achieved via the combination of two sonication modes, the same as *in vitro*. A first continuous sonication for a short time period achieves an initial rapid temperature increase that can then be followed by a pulsed sonication in order to sustain the temperature at a specific level. Consequently, a dedicated sonication mode was created that consists of 10 s continuous sonication and 45 s with 2.5 s off and 0.5 s on, pulsed sonication. This mode was examined initially in a DQA phantom to evaluate its efficiency.

As can be seen in Figure 6.7, at a power of 4 Wa, there is no significant temperature rise in either sonication pattern, i.e. single spot or annular. Therefore the same mode was tested at a power of 16 Wa, where a different thermal rise can be seen in both sonication patterns, Figure 6.8. In the normal single spot sonication, following sonication of 16 Wa with the combined mode, a maximal thermal increase of 10°C was recorded. The area of 7°C temperature increase is 9 mm², as defined by the yellow line in Figure 6.8a. In the annular sonication patterns, the same applied power resulted in a 3°C lower maximum temperature increase, i.e. 7°C. The area of 7°C temperature increase is 4 mm² as defined by the inner yellow line in Figure 6.8(a), whilst the area of 4°C increase is 13 mm² as defined by the outer yellow line in Figure 6.8(b).

From these results it is clear that an annular focus lowers the maximal temperature rise at the focal point, while creating a broader focal zone. This was further confirmed in the *ex-vivo* studies. Figure 6.10 depicts the application of 4 Wa in the combined sonication mode in deceased mice at the locations indicated in Figure 6.9, in two sonication patterns: single spot, i.e. normal and annular. From Figure 6.10, it can be seen that the combined sonication pattern was successful in both its targets: a fast temperature rise followed by a stable heating mode. The application of the annular focus results in a wider focal zone with lower temperature rise, $45 - 7^{\circ}\text{C} \pm 0.9^{\circ}\text{C}$ in the normal focus compared to $42^{\circ}\text{C} \pm 0.9^{\circ}\text{C}$ in the annular case, Figure 6.10.

The specific sonication shape of the focal point as indicated by the temperature rise *in situ* is somewhat similar to an annulus, whereas the central point of the annulus remains relatively cool. This introduces a possibility of a wider, more uniform pattern of sonication which may be applied in order to cover larger areas with fewer sonications. The difference between the temperature rises in the DQA phantom and those in the *ex-vivo* tissues with application of the same acoustic power of 4 Wa, may be attributed to several physical differences between the tissue mimicking phantom and the deceased mice.

The sonication location in the *ex-vivo* studies in this work was chosen to be the quadriceps muscles as it would be the primary study subject in the first stage of *in-vivo* trials. A mouse leg is about 8 mm wide in the region of the quadriceps muscles and includes the muscles, bones and various blood vessels. Therefore it is not a perfect tissue the DQA phantom is mimicking but rather a complicated combination of tissues. Consequently, in the *ex-vivo* tissues there may be greater absorbance, e.g. in the bone, and different heat distribution due to air or stiffness variation in the subject area.

As can be seen from Figure 6.10, with both spot shapes there is a relatively slow temperature decrease after the end of sonication. This can be attributed to the fact that there is no blood flow in the *ex-vivo* mice for rapid *in situ*-cooling. The significant temperature decrease that can be seen in Figure 6.6, i.e. from $60 - 61^{\circ}\text{C} \pm 0.9^{\circ}\text{C}$ to about $44 - 42^{\circ}\text{C} \pm 0.9^{\circ}\text{C}$, is due the difference from room temperature (RT).

When working in an *in-vivo* arrangement, especially dealing with small species such as mice, the duration of the experiment is highly important. The anaesthesia period dictates a working window of a maximum of 45 min. While in the *ex-vivo* experiments the possibility of sonication of three mice under the same imaging procedure was suggested, *in-vivo* it may be necessary to scan and sonicate each mouse individually. Part of the *ex-vivo* goal was to provide a timed procedure for MRI-guided mouse sonication and to optimize the timeline to fit in the

anaesthesia window. The final minimum exposure time for a single mouse was achieved to be as low as 21 min, comprising: 10 min for temperature adjustment and positioning of the mouse within the experiment, 2 min 52 s coronal scan, 70 s per sonication i.e. 10 s continuous sonication + 45 s pulsed sonication + 5 cooling phases = 3 s x 5, x number of sonications per leg, 4 in average = 4 min, and 3.5 min for retrieval of the mouse from the MRI environment to the laboratory.

To conclude the initial preparation for *in-vivo* studies reported in this chapter, the results have proved the feasibility to apply the achieved *in-vitro* knowledge in an *in-vivo* research platform. Although practical application for *in-vitro* research is sometimes difficult, in this work it was shown that emerging *in-vitro* sonication protocols may be used in *in-vivo* models to achieve local hyperthermia. Following the proof of concept in healthy mice, the same platform could be used for treating tumour-bearing mice and larger species, with the ultimate goal of reaching clinical trials.

6.4 References

- Anand, R. et al.** (2012) A close-up on doxorubicin binding to α -cyclodextrin: an elucidating spectroscopic, photophysical and conformational study. *RSC Advances*, 2, pp. 2346- 57.
- Chen, L. et al.** (2010) MR-guided focused ultrasound: enhancement of intratumoral uptake of [3H]-docetaxel in vivo. *Phys Med Biol*, 55, pp. 7399- 410.
- Chilkoti, A. et al.** (2002) Targeted drug delivery by thermally responsive polymers. *Adv Drug Deliver Rev*, 54, pp.613- 30.
- Deckers, R. et al.** (2008) The role of ultrasound and magnetic resonance in local drug delivery. *J Magn Reson Im*, 27, pp.400- 9.
- Gourevich, D. et al.** (2012) Ultrasound mediated Targeted Drug Delivery generated by Multifocal Beam Patterns: An in-vitro Study. *Ultrasound Med Biol*, Accepted 24.10.12.
- Grüll, H. and Langereis, S.** (2012) Hyperthermia-triggered drug delivery from temperature-sensitive liposomes using MRI-guided high intensity focused ultrasound. *J Control Release*, 161, pp. 317-27.
- Erenpreisa, J. and Cragg, M.S.** (2001) Mitotic death: a mechanism of survival? a review. *Cancer Cell Int*, 1(1), pp.1-7.
- Erenpreisa, J. et al.** (2000) Arrest in metaphase and anatomy of mitotic catastrophe: mild heat shock in two human osteosarcoma cell lines. *Cell Biol Int*, 24(2), pp.61–70.

- Lewis, G.K. et al.** (2011) Time-reversal techniques in ultrasound-assisted convection enhanced drug delivery to the brain: technology development and in vivo evaluation. *Proc Meet Acoust*, 10(11), pp.020005- 31.
- Moonen, C. et al.** (2010) Ultrasound-triggered image-guided therapy. *MedicaMundi*,54(1), pp.40- 5.
- Phillips, L.C. et al.** (2010) Focused ultrasound-mediated drug delivery from microbubbles reduces drug dose necessary for therapeutic effect on neointima formation- brief report. *Arterioscler Thromb Vasc Biol*, 31, pp.2853- 5.
- Pitt, W.G. et al.** (2004) Ultrasonic drug delivery- a general review. *Expert Opin Drug Deliv*, 1(1), pp.37- 56.
- Ranjan, A. et al.** (2012) Image-guided drug delivery with magnetic resonance guided high intensity focused ultrasound and temperature sensitive liposomes in a rabbit Vx2 tumor model. *J Control Release*, 158, pp.487- 94.
- Rapoport, N.Y. et al.** (2009) Controlled and targeted tumor chemotherapy by ultrasound-activated nanoemulsions/microbubbles. *J Control Release*, 138, pp.268-76.
- Rieder, C.L. and Maiato, H.** (2004) Stuck in division or passing through: what happens when cells cannot satisfy the spindle assembly checkpoint. *Developmental Cell*, 7, pp.637- 51.
- Rosenthal, I. et al.** (2004) Sonodynamic therapy- a review of the synergistic effects of drugs and ultrasound. *Ultrason Sonochem*, 11, pp.349- 63.
- Saparfto, S.A. and Dewey, W.C.** (1984) Thermal dose determination in cancer therapy. *Int J Radiation Oncology Biol Phys*, 10 (6), pp.787-800.
- Staruch, R. et al.** (2011) Localised drug release using MRI-controlled focused ultrasound hyperthermia. *Int J Hyperthermia*, 27(2) pp.156- 71.
- Vaezy, S. and Zderic, V.** (2009) *Image-guided therapy systems*. USA: Artech House.
- Yudina, A. et al.** (2012) In vivo temperature controlled ultrasound-mediated intracellular delivery of cell-impermeable compounds. *J Control Release*, doi:10.1016/j.jconrel.2012.04.018.

Appendices

i. Diffusion Coefficient (D) Calculations

$$D = \frac{k_B T}{6\pi\eta R_s}$$

k_B = Boltzmann constant (J/K)

T= Temperature (°K)

η = Dynamic Viscosity (N s/m²)

R_s = Stokes Radius (m)

$$\sqrt[3]{\frac{M_{w_j}}{M_{w_i}}} = \frac{D_i}{D_j} = \sqrt[2]{\frac{M_{w_j}}{M_{w_i}}}$$

M_w = Molecular Weight (g/mol)

$$D_{obs} = D_{free} \cdot P_{free} + D_{complexed} \cdot P_{complexed}$$

D_{obs} = Measured Diffusion Coefficient of the Complex (m²/s)

D_{free} = Diffusion Coefficient of the free guest (m²/s)

P_{free} = Population fraction of the free guest (m²/s)

D_{free} = Diffusion Coefficient of the complexed guest (m²/s)

P_{free} = Population fraction of the complexed guest (m²/s)

$$P_{free} = 1 - P_{complexed}$$

P_{free} = Population fraction of the free guest (m²/s)

P_{free} = Population fraction of the complexed guest (m²/s)

$$P_{complexed} = \frac{D_{obs} - D_{free}}{D_{complexed} - D_{free}}$$

D_{obs} = Measured Diffusion Coefficient of the Complex (m²/s)

D_{free} = Diffusion Coefficient of the free guest (m²/s)

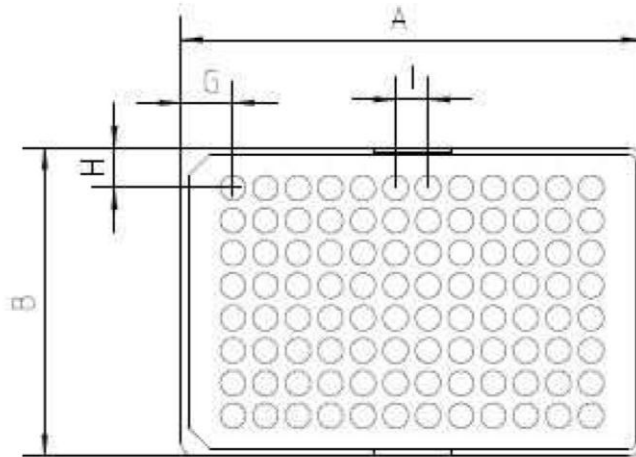
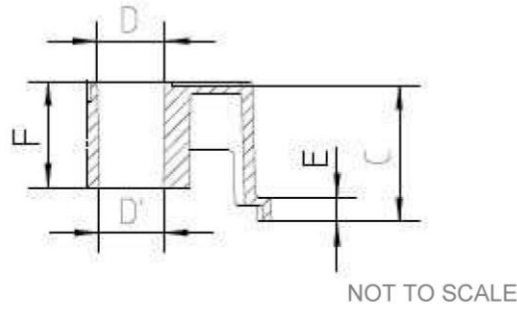
P_{free} = Population fraction of the free guest (m²/s)

D_{free} = Diffusion Coefficient of the complexed guest (m²/s)

P_{free} = Population fraction of the complexed guest (m²/s)

ii. **Dimensions of 96-well plate (Greiner Bio-One, UK)**

AC-9600024/ 96120096	CUSTOMER DRAWING	Page 1 of 2
Revision 01	lumox™ Multiwell, 96 Well, PS	
	Item-No. 9600 0024 / 9612 0096	



Cat.-No.	Description	A	B	C	D	D'	E	F	G	H	I
9600 0024	lumox™ Multiwell	127.8 ± 0.2	85.5 ± 0.2	14.4 ± 0.1	∅ 6.96	∅ 6.58	2.5	10.9	14.38	11.24	9.0
9612 0096	lumox™ Multiwell	127.8 ± 0.2	85.5 ± 0.2	14.4 ± 0.1	∅ 6.96	∅ 6.58	2.5	10.9	14.38	11.24	9.0

All dimensions in mm

Customer drawing subject to change without notice!

Prior Issue	Drawn	Approved	Released	CONFIDENTIAL: Information contained in this document or drawing is confidential and proprietary to Greiner Bio-One GmbH. This document may not be reproduced for any reason without written permission from Greiner Bio-One GmbH. All rights of design, invention, and copyright are reserved.
Revision 01	Date September 6, 2005	Date September 6, 2005	Date September 6, 2005	
Date September 6, 2005	Name F. Falter	Name F. Sonntag	Name F. Sonntag	

iii. **Beam dimensions calculations**

$$N = \frac{Ap^2 \cdot f}{4 \cdot c \cdot 10^3}$$

N = Near Field Distance (mm)

Ap = Aperture (mm)

f = Frequency (Hz)

c = Speed of Sound (m/sec)

$$S_f = \frac{FD}{N}$$

S_f = Normalized Focal Length

FD = Focal Distance (mm)

N = Near Field Distance (mm)

$$B_l = N \cdot S_f \cdot \left(\frac{2}{1 + \frac{S_f}{2}} \right)$$

B_l = Beam Length (mm)

S_f = Normalized Focal Length

FD = Focal Distance (mm)

N = Near Field Distance (mm)

$$B_d = 0.2568 \cdot Ap \cdot S_f$$

B_d = Beam Diameter (mm)

Ap = Aperture (mm)

S_f = Normalized Focal Length

iv. **The Efficiency (Eff) and the Uniformity (Uni) calculations**

$$Eff = \frac{1}{I_{Single}} \sum_m I_m$$

I_{single} = The intensity at a single spot measurement (W/cm^2)

I_m = The intensity at a single spot in a multi focal measurement (W/cm^2)

$$Uni = 1 - \frac{I_{max} - I_{min}}{I_{max} + I_{min}}$$

I_{max} = The maximal intensity at a single spot in a multi focal measurement (W/cm^2)

I_{min} = The minimal intensity at a single spot in a multi focal measurement (W/cm^2)

v. **Hydrophone Calibration constants β_H (V²cm²/W) and α_H (V/Pa) and calculations**

$$\beta = \frac{\sum_{ij} A_{ij} dx \cdot dy}{W_{ac}}$$

A_{ij} = the measured peak voltage (mv)

$dx \cdot dy$ = the acoustic field measurements steps (mm)

W_{ac} = the applied acoustic load (W)

α_H was derived from β_H according to:

$$\alpha_H = \sqrt{\frac{\beta_H}{Z}}$$

Z = acoustical impedance of water

vi. **Attenuation of Ultrasound Waves in Tissues**

$$I = I_0 \cdot e^{-\alpha \cdot dz \cdot f}$$

I = intensity in the point of interest (W/cm²)

I_0 = applied intensity i.e. power on the transducer (W/cm²)

α = absorption coefficient (Np/mm)

dz = the propagation distance (mm)

f = acoustic field frequency (MHz)